

# **First-principles Modeling of the Surface Reactivity of Transition Metals with Perturbed Electronic Properties**

by  
Hongliang Xin

A dissertation submitted in partial fulfillment  
of the requirements for the degree of  
Doctor of Philosophy  
(Chemical Engineering)  
in The University of Michigan  
2011

Doctoral Committee:

Associate Professor Suljo Linic, Chair  
Professor Phillip E. Savage  
Associate Professor Anton Van der Ven  
Professor Robert M. Ziff

*“Science is the belief in the ignorance of experts.”* by Richard Feynman

© Hongliang Xin 2011  
All Rights Reserved

This dissertation is dedicated to my wife, Dongjuan Dai, whose endless support made this research possible, and to my son, Alvin D. Xin, who was born during my thesis writing.

## ACKNOWLEDGEMENTS

Many people have contributed to the completion of this dissertation. I would first like to thank my advisor Prof. Suljo Linic for his guidance and support throughout my PhD studies. His critical thinking of fundamental research and passion for solving energy and environmental problems challenging the modern society inspired me to pursue scientific careers consistently.

I would also like to thank my dissertation committee: Prof. Phillip E. Savage, Prof. Anton Van der Ven and Prof. Robert M. Ziff. I really appreciate the help from Prof. Savage for being supportive of my PhD studies. I am very thankful to Prof. Van der ven and Prof. Ziff for helping me with Monte Carlo simulations.

I am very glad to have the opportunity to work with so many brilliant individuals in our group. Most of the presented experimental data were obtained in close collaboration with Dr. Neil Schweitzer and Dr. Phillip Christopher. I am very grateful for their support of my work and for many insightful discussions.

I would like to thank Cluster Administrators of Hades including Siris Laursen, David Ingram, Matthew Morabito, Paul Hernley, Timothy Van Cleve. I have been extensively using our cluster for computational work in the last six years. Without their care and support, none of my work would be possible.

The financial support of this work by DOE is gratefully acknowledged.

Finally, I would like to express all thankfulness to my friends and family, especially to my lovely wife, Dongjuan Dai, for her endless love and support.

## TABLE OF CONTENTS

<b>DEDICATION</b> . . . . .	<b>ii</b>
<b>ACKNOWLEDGEMENTS</b> . . . . .	<b>iii</b>
<b>LIST OF FIGURES</b> . . . . .	<b>vii</b>
<b>LIST OF TABLES</b> . . . . .	<b>xi</b>
<b>CHAPTER</b>	
<b>I. General Introduction</b> . . . . .	<b>1</b>
1.1 Microscopic View of Heterogeneous Catalysis . . . . .	2
1.2 Understanding the Kinetics of Catalytic Reactions . . . . .	3
1.2.1 Transition State Theory . . . . .	3
1.2.2 The Sabatier Principle . . . . .	6
1.3 Universal Relationships for Estimating Bond Energies . . . . .	7
1.3.1 The Brønsted-Evans-Polanyi Relationship . . . . .	8
1.3.2 Linear Scaling Relationship . . . . .	9
1.3.3 Group Additivity . . . . .	10
1.4 Research Philosophy . . . . .	11
1.5 Suggested Readings . . . . .	12
1.6 Scope of the Thesis . . . . .	13
<b>II. Density Functional Theory</b> . . . . .	<b>15</b>
2.1 Fundamental Principles . . . . .	16
2.1.1 The Hohenberg-Kohn Theorems . . . . .	17
2.1.2 The Kohn-Sham Equations . . . . .	18
2.1.3 Relating Electronic Energies to Thermodynamic Properties . . . . .	22
2.1.4 Electronic Properties of Transition Metal Surfaces . . . . .	24
2.2 Tight-Binding Approximation for Understanding of Surface Chemisorption . . . . .	25
2.2.1 Hammer-Morikawa-Nørskov Two-Level Interaction Model . . . . .	25
2.2.2 Newns-Anderson Model . . . . .	28
2.2.3 Hammer-Nørskov <i>d</i> -band Model . . . . .	32
<b>III. The General Theoretical Framework for Understanding Variations in the Surface Reactivity of Transition Metals</b> . . . . .	<b>35</b>
3.1 Introduction . . . . .	35
3.2 Detailed Derivation of the General Theoretical Framework . . . . .	37
3.3 Physical Interpretation and Computational Evaluation of Contributing Terms . . . . .	43
3.3.1 Electronic Orbital Interaction . . . . .	43
3.3.2 Dipole-dipole Interaction . . . . .	44

3.3.3	Dipole-induced-dipole Interaction . . . . .	46
3.4	Various Forms of Perturbation . . . . .	47
3.4.1	Alloying with Impurity Elements . . . . .	48
3.4.2	Doping of Substrates with Chemical Promoters . . . . .	49
3.4.3	Imposing Stimuli for Electronic Excitations . . . . .	50
3.5	Summary . . . . .	51
<b>IV. Alloying with Impurity Elements . . . . .</b>		<b>52</b>
4.1	Introduction . . . . .	52
4.2	Relating the Geometric Structure of Alloys to Their Electronic Properties . . . . .	53
4.2.1	Experimental Details . . . . .	54
4.2.2	Computational Details . . . . .	59
4.2.3	Challenges for Predicting Variations in Surface Reactivity of Alloys . . . . .	61
4.2.4	Measurement of Geometric Structure . . . . .	64
4.2.5	Measurement of Electronic Structure . . . . .	65
4.2.6	Fundamental Mechanisms of the <i>d</i> -band Center Shift . . . . .	68
4.2.7	<i>sp</i> -band Contribution to the Chemical Bonding . . . . .	71
4.3	Exceptions to the General Trend Predicted by the <i>d</i> -band Model . . . . .	74
4.3.1	Computational Details . . . . .	75
4.3.2	Surface Phenomenon in Contradiction to the General Understanding of the <i>d</i> -band Model . . . . .	75
4.3.3	Two-Level Interaction Model . . . . .	77
4.3.4	Fundamental Mechanisms Associated with this Surface Phenomenon . . . . .	81
4.3.5	Generality of this Surface Phenomenon . . . . .	84
4.4	Potential Application of the Model for Alloy Catalyst Design . . . . .	85
4.4.1	Computational Details . . . . .	86
4.4.2	Pt-Containing Electrocatalysts Design for Fuel Cell Applications . . . . .	87
4.4.3	Prediction of Adsorbate Bond Distance to the Surface . . . . .	90
4.4.4	Simple Models for the Prediction of <i>d</i> -band Center of Alloys . . . . .	92
4.4.5	Rapid Screening of Pt-Containing Multimetallic Electrocatalysts . . . . .	94
4.5	Summary . . . . .	98
<b>V. Doping of Substrates with Chemical Promoters . . . . .</b>		<b>100</b>
5.1	Introduction . . . . .	100
5.2	Computational Methods . . . . .	103
5.2.1	DFT Calculations . . . . .	103
5.2.2	Ab-Initio Atomistic Thermodynamics . . . . .	104
5.2.3	Metropolis Monte Carlo Simulation . . . . .	105
5.3	Fundamental Mechanisms that Govern Alkali Promotion . . . . .	107
5.3.1	Cs Promotion on O <sub>2</sub> Dissociation . . . . .	107
5.3.2	Alkali-Modified Electronic Properties of Metal Surfaces . . . . .	108
5.3.3	Fundamental Understanding of Alkali Promotion Mechanism . . . . .	114
5.4	Extend Insight from DFT to Catalytic Relevant Conditions . . . . .	123
5.4.1	Oxidation States of the Substrate under Relevant Catalytic Conditions . . . . .	126
5.4.2	Stabilization of Oxygen Species by Alkali Promoters . . . . .	129
5.4.3	Consequence and Mechanism of Subsurface Oxygen Formation on the Surface Reactivity . . . . .	137
5.5	Summary . . . . .	140
<b>VI. Imposing Stimuli for Electronic Excitations . . . . .</b>		<b>142</b>
6.1	Introduction . . . . .	142

6.2	Experimental Phenomenon . . . . .	145
6.3	Theoretical Approaches . . . . .	146
6.3.1	Non-adiabatic Newns-Anderson Model . . . . .	147
6.3.2	Linear-Expansion $\Delta$ SCF-DFT for Excited States . . . . .	150
6.4	Local Heating of Metal Surfaces due to Photon Absorption . . . . .	153
6.4.1	Two-Temperature Model . . . . .	153
6.4.2	Ultra-short Laser Pulses vs. Continuous Light Wave . . . . .	155
6.5	Development of Finite-Temperature Electron Scattering Model . . . . .	157
6.6	Fundamental Understanding of Oxygen Dissociation Induced by Multiple Stimuli . . . . .	161
6.6.1	Power Law Dependence of $O_2$ Dissociation Rate on Light Intensity . . . . .	162
6.6.2	Enhanced Quantum Efficiency due to Phonon Excitation . . . . .	164
6.6.3	Characteristic Features for Electron-driven Surface Reactions . . . . .	165
6.6.4	Interpretation of Power Law Exponent $n$ . . . . .	167
6.6.5	Sensitivity Analysis of the Model . . . . .	169
6.7	Insight into the Efficiency and Selectivity of Electron-Mediated Surface Reactions . . . . .	170
6.7.1	Critical Role of Electronic Resonance Energy . . . . .	171
6.7.2	Electronic Factors Determining Resonance Energies of Simple Adsorbates . . . . .	172
6.8	Summary . . . . .	174
<b>VII.</b>	<b>Conclusions . . . . .</b>	<b>177</b>
	<b>BIBLIOGRAPHY . . . . .</b>	<b>183</b>

## LIST OF FIGURES

### Figure

1.1	(a) The microscopic view of catalytic reactions on metal surfaces. (b) Potential energy diagram of a catalytic reaction vs. non-catalytic reaction . . . . .	2
1.2	Schematic illustration of volcano relationship between catalytic activity of transition metals for oxygen reduction reactions as a function of oxygen species binding energies . . . . .	7
2.1	Schematic illustration of the comparison between Schrödinger and DFT views of many-body problems . . . . .	16
2.2	Schematic illustration of Kohn-Sham implementation of DFT . . . . .	21
2.3	Schematic illustration of band formation . . . . .	24
2.4	(a) Perturbation view of two orbital interactions (b) Standard interaction diagram of two orbital interactions . . . . .	25
2.5	Simple case of interaction between adsorbate state $\epsilon_A$ with metal $d$ -state $\epsilon_B$ . . . . .	27
2.6	Schematic illustration of interaction between adsorbate orbital with the $d$ -band of the substrate within Newns-Anderson model . . . . .	28
2.7	Interaction between adsorbate state with metal $d$ -states based on the Newns-Anderson model with varying (a) $d$ -band width (b) coupling strength (c) $d$ -band center . . . . .	33
3.1	Variations in the binding energy of adsorbate A due to the perturbation of electronic properties of the substrate from $M$ to $\tilde{M}$ . . . . .	38
3.2	Schematic illustration of electronic orbital interaction . . . . .	44
3.3	Schematic illustration of dipole-dipole interaction . . . . .	45
3.4	Schematic illustration of dipole-induced-dipole interaction . . . . .	47
3.5	Perturbations of electronic properties of transition metal surfaces due to (a) alloying with impurity elements, (b) doping of substrates with chemical promoters, (c) imposing stimuli for electronic excitations . . . . .	48
4.1	Schematic illustration of x-ray absorption spectroscopy technique . . . . .	56
4.2	(a) Schematic illustration of XANES (b) Schematic illustration of EXAFS (c) Pt $L_3$ -edge XAS as an example . . . . .	57
4.3	Mechanisms by which the center of the local $d$ -band can change include (a) charge transfer from one element to another, (b) a change in the overlap between $d$ -states and the valence orbitals of neighboring atoms leading to a change in the $d$ -band width . . . . .	63
4.4	Measured and fitted EXAFS spectra for pure Pt and (a) Pt-Sn alloy, (b) Pt-Cu alloys. . . . .	64
4.5	Geometric structures of Pt alloys . . . . .	65
4.6	Electronic properties of Pt alloys. (a) Measured Pt $L_3$ -edge XANES spectra and calculated oscillator strengths for different Pt alloys. Insert shows calculated areas under the measured XANES spectra. These are plotted for different cutoff energies since it is not clear where the near edge ends. We find that independent of the cutoff energy the integrated spectra gives almost identical values for different alloys. (b) Density of states projected on different elements in the alloys: Pt $5d$ states are solid blue, and metal (Sn, Cu) $s$ and $p$ states are dash and dash-dot lines, respectively. Cu $3d$ states are solid green and purple for PtCu and PtCu <sub>3</sub> alloy, respectively. . . . .	66
4.7	(a) Binding energy of various adsorbates on $3d$ -M/Pt skin alloys as a function of characteristic orbital length ( $r_d^{3/2}$ ) of $3d$ metals. (b) Charge analysis of Pt on $3d$ -M/Pt skin alloys . . . . .	69

4.8	Binding energy of various adsorbates on Pt skin alloys as a function of characteristic orbital length ( $r_d^{3/2}$ ) of (a) $4d$ metals (b) $5d$ metals . . . . .	70
4.9	Hybridization energy between atomic orbital of O with Pt $3d$ skin alloys based on the Newns-Anderson model . . . . .	72
4.10	DFT-GGA adsorption energies of (a) O and (b) OH on Pd and Pt skin alloys are plotted as a function of the center of $d$ -band projected on surface atoms. (c, d) Surf-O and Surf-OH distance are plotted as a function of DFT-GGA adsorption energies of O and OH on Pd and Pt skin alloys. The model system is shown at the left bottom of the figure. The $d$ -band center ( $\epsilon_d$ ) projected on surface atoms of various skin alloys are shown in the Table. . . . .	76
4.11	(a) Density of states (DOS) of gas phase OH radical in vacuum. (b) DOS projected on the molecular orbitals of OH adsorbed on atop site of Al(111). (c) and (d) DOS projected on the O atom for OH adsorbed on atop site of Pd and Pt with $3d$ subsurface metal. . . . .	79
4.12	Comparison of DFT- and model-calculated OH adsorption energy on Pd (a) and Pt (b) skin alloys. The parameters obtained from the model are tabulated in insert. . . . .	81
4.13	(a) The covalent attraction and Pauli repulsion contributions to the OH binding energy on Pt skin alloys with $3d$ subsurface atom calculated using the model discussed in the text. (b) Surf-OH bond distance and the coupling matrix element ( $V^2$ ) are plotted as a function of the number of $sp$ -electrons on the surface substrate atoms. The number of $sp$ -electrons was calculated as total Bader charge minus the $d$ -band filling. . . . .	83
4.14	(a) F and Cl adsorption energies on Pt and Pd skin alloys as a function of $d$ -band center. (b) O and OH adsorption energies on Au and Ag skin alloys as a function of $d$ -band center. . . . .	85
4.15	Geometric structure of different model alloys . . . . .	87
4.16	(a) Schematic of electrode water interface where OH adsorbs (a) Objective for tuning the surface reactivity for ORR . . . . .	88
4.17	Schematic illustration of the chemical bonding between adsorbate states and metal $d$ -states, which leads to an upward shift in energies due to the Pauli repulsion, followed by the formation of bonding and anti-bonding states due to the orbital hybridization. . . . .	89
4.18	DFT calculated metal-OH bond distance on various Pt alloy surfaces correlated with the prediction of the model in Eq. 4.13. The sketch is an illustration of the effect of the change in the surface electron density on the adsorbate-substrate bond distance. . . . .	91
4.19	DFT calculated local $d$ -band center of various Pt alloy surfaces correlated with the model prediction using Eq. 4.14. . . . .	92
4.20	Model prediction of OH binding energies on Pt monolayer alloy surfaces with varying subsurface ligand (1 ML) and lattice strain (-10% to 5% expansion). Marked regions depict the alloy systems with desired catalytic properties ( $\sim 0.1$ eV weaker OH binding than pure Pt). Inserts show different mechanisms by which the OH adsorption energy changes. . . . .	94
4.21	Model screening of OH adsorption on core-shell alloy surfaces $Pt_{ML}/Au/Au_3X_{0.5}Y_{0.5}(111)$ . The parity plot in the bottom right insert shows a comparison of the OH binding energies on selected Pt monolayer alloys calculated using the model and self-consistent DFT. Top right figure shows the model system. . . . .	97
5.1	Dramatically enhanced reaction rate of ammonia synthesis over ruthenium (Ru) catalysts with the introduction of alkali promoters. Circle: Na, Square: K, Triangle: Cs. . . . .	101
5.2	Top and side view of Ag(111) model systems employed in our DFT calculations ( $3\times 3\times 4$ unit cell as an example) . . . . .	103
5.3	Schematic illustration of the gas-surface interface . . . . .	104
5.4	Schematic illustration of Metropolis Monte Carlo simulation algorithm . . . . .	107
5.5	The DFT-calculated potential energy surfaces for the $O_2$ dissociation reaction on clean and Cs-promoted Ag(111) surfaces. The barrier was calculated as the energy difference between the transition state and initial state. The surface structures with different oxygen species are shown in the $3\times 3$ unit cell. Cs adatom adsorbs on site $A$ or $B$ , where site $A$ is further away from the dissociation molecules than site $B$ . . . . .	108

5.6	(a) Cs induced work function change as a function of Cs coverage on Ag(111); Blue square is the experimental result adapted from literature, while red circles represent DFT-computed work function change. (b) The contour shows the Cs induced electron density difference on the plane cutting through Cs adatoms. Solid line represents the average electron density along $z$ -axis. The density is calculated as $\Delta n = n_{Cs/Ag(111)} - n_{Ag(111)} - n_{Cs}$ . Positive value corresponds to an $e^-$ charge increase. Zero on $z$ -axis corresponds to the top Ag layer. Cs atoms are adsorbed at $z=3.25$ above the top Ag layer. . . . .	109
5.7	Cs induced modification of the electronic properties of silver surfaces. (a) Cs induced electrostatic potential along different positions on the surface. The induced electric field $\epsilon_{Cs}^{max}$ is the maximum electric field out of surface as determined from the dashed line. (a) The projected density of states of surface silver atoms for clean Ag(111) and Cs modified Ag(111) surfaces. As illustrated in insert, Ag A is the one directly bonded to Cs, and Ag B is the one on the second near neighbor of Cs. . . . .	111
5.8	Two Level interaction model for oxygen species adsorption on clean transition metal surfaces. The parameters obtained from the Two-Level interaction model are tabulated in Table 5.1 (a) Initial and transition states of $O_2$ . (b) Atomic oxygen . . . . .	118
5.9	(a) Comparison between the self-consistent DFT calculated interaction energy and the model prediction between Cs and various oxygen adsorbates (initial, transition, and final state in the $O_2$ dissociation reaction). We can see that the model predicts very well the interaction energies for varying Cs-O separations and Cs coverages. Diagonal straight line is the line of perfect agreement. (b) Decoupling of various contributions including electronic (solid line), electrostatic (dashed line) and polarization (dash-dot line) contributions into the interaction energy for one Cs- $O_x$ configuration. . . . .	122
5.10	Surface free energy of various O/Ag(111) structures is plotted as a function of temperature and the pressure of $O_2$ . Structures with the lowest energy for a given set of conditions are considered thermodynamically the most stable. . . . .	127
5.11	Surface free energy of various Cs-O/Ag(111) structures is plotted as a function of temperature and the pressure of $O_2$ . . . . .	129
5.12	Enumeration of effective cluster interactions (65) on the metal surface. HCP and FCC sites are treated as different sites in the cluster expansion. . . . .	131
5.13	Surface free energies from Direct Enumeration (triangle) of Surface Configurations using Effective Interaction Coefficients and self-consistent DFT calculations (circle). This step took several iterations until no new structure is found. (a) clean Ag(111), (b) Ag(111) with 1/16 ML Cs . . . . .	133
5.14	Effective Interaction Coefficient for 65 characteristic clusters including monomer, pairs and trimers. The coefficients shown here have been updated using Direct Enumeration method. The cross-validation score is 0.05 eV based on the “taken-one-out” method . . . .	134
5.15	Grand Canonical Monte Carlo simulation of the effect of Cs promoters on the uptake of on-surface and subsurface oxygen. Blue: clean Ag(111), Red: Cs 0.04 ML, Cyan: 0.1 ML	135
5.16	Model calculated electrostatic and polarization contributions into the interaction of $CsO_x$ with different oxygen species on Ag(111) . . . . .	138
5.17	Correlation between oxygen adsorption and $d$ -band center of the surface silver atoms. The inserts model show the geometry of the oxygen adsorption on the Ag(111) surface with varying coverage of subsurface oxygen. The projected density of states of surface silver atoms on different geometries are shown to illustrate the effect of subsurface oxygen on the variation of surface $d$ -band center. . . . .	139
5.18	Cs promotion mechanism under different operating conditions . . . . .	141
6.1	Photo-thermal reaction on silver nanocubes. (a) Epoxidation rate as a function of light intensity at different temperature. (b) Calculated exponent of photo-thermal reaction as a function of light intensity at different temperature . . . . .	146
6.2	Schematic illustration of Newns-Anderson-Type Hamiltonian for the model . . . . .	149

6.3	(a) Molecular orbital of DOS for O <sub>2</sub> adsorption on Ag(100) Surface. Insert shows the adsorption configuration of O <sub>2</sub> /Ag(100) with 1/4 ML. (b) Potential energy surfaces of O <sub>2</sub> Dissociation on Ag(100) Surface. Insert shows the distribution of excited electrons at O <sub>2</sub> /Ag(100) complex, green is extra electron accumulation, and red is electron deficiency .	152
6.4	Schematic Illustration of the Two-Temperature Model . . . . .	154
6.5	Two-Temperature Model illumination. (a) Femto-second laser pulse, (b) Steady state under light illumination . . . . .	156
6.6	Schematic illustration of the initial phonon distribution at finite temperature . . . . .	159
6.7	General algorithm of the Finite-Temperature Electron Scattering model . . . . .	161
6.8	Theoretical results from electron scattering model. (a) Calculated reaction rate as a function of electron flux into adsorbate orbitals at different temperatures. (b) Exponent calculated from the rate showing the transition from linear to super-linear dependence on electron flux . . . . .	162
6.9	Cartoon illustration of regime transition mechanism . . . . .	163
6.10	Cartoon illustration of effect of emperature . . . . .	164
6.11	Kinetic isotope effect from Electron Scattering model . . . . .	165
6.12	(a) Measured vs calculated kinetic isotope effect. (b) Cartoon illustration of the mechanism of enhanced kinetic isotope effect . . . . .	167
6.13	Reduction of activation energies due to electron scattering . . . . .	168
6.14	Effect of electron energy and flux on the (a) rate and (b) exponent . . . . .	171
6.15	The rate enhancement due to the resonant electron distribution vs. thermalized hot electron distribution . . . . .	172
6.16	Trend of resonance energies of molecules adsorption on metal surfaces . . . . .	175

## LIST OF TABLES

### Table

4.1	Structural Parameters from EXAFS Fitting Results for Pt $L_3$ -edge EXAFS Spectra of Pt Alloys. (Coordination Numbers CN, Distances R). . . . .	66
5.1	Tabulated parameters of oxygen adsorption on transition metal surfaces for the two level interaction model . . . . .	119
6.1	Parameter of Two-Temperature Model for Silver . . . . .	157
6.2	Rate Sensitivity Analysis . . . . .	169
6.3	KIE Sensitivity Analysis . . . . .	170

## CHAPTER I

### General Introduction

A catalyst is any substance that accelerates a reaction without itself being consumed. Nowadays, catalysts have played an essential role in almost all major chemical processes, particularly for chemical conversion, energy production and pollution mitigation. For example, catalysts are of crucial importance to the chemical industry as these materials are responsible for the production of over 60% of all chemicals worldwide [1]. Most of the energy consumption by the modern society depends on the refining of fossil fuels with heterogeneous catalysts. Reducing emissions of greenhouse gases and hazardous chemicals from chemical industry or our cars can not be realized without catalysts. The impact of catalysis results not only from its capacity to accelerate chemical reactions, but also its propensity to improve the selectivity of desired products. Developing new technologies for converting alternative feedstocks, such as biomass, carbon dioxide, and water to transportation fuels and commodity chemicals relies on the discovery of catalytic materials facilitating and directing chemical transformations.

Increasing environmental concerns and energy demand require 21<sup>st</sup> century catalysts to perform desired chemical transformations with utmost energy efficiency and minimal environmental impact. Understanding the nature of interactions on catalyst surfaces is critical for unearthing underlying mechanisms of catalytic reactions, and for the rational

discovery of catalytic materials for chemical transformations.

## 1.1 Microscopic View of Heterogeneous Catalysis

Heterogeneous catalytic events commonly involve the adsorption of gas phase molecules onto solid surfaces, interactions with other adsorbed species or substrates forming products, and desorption of products into the gas phase. The catalytic sites are regenerated to their original form after a cyclic event.

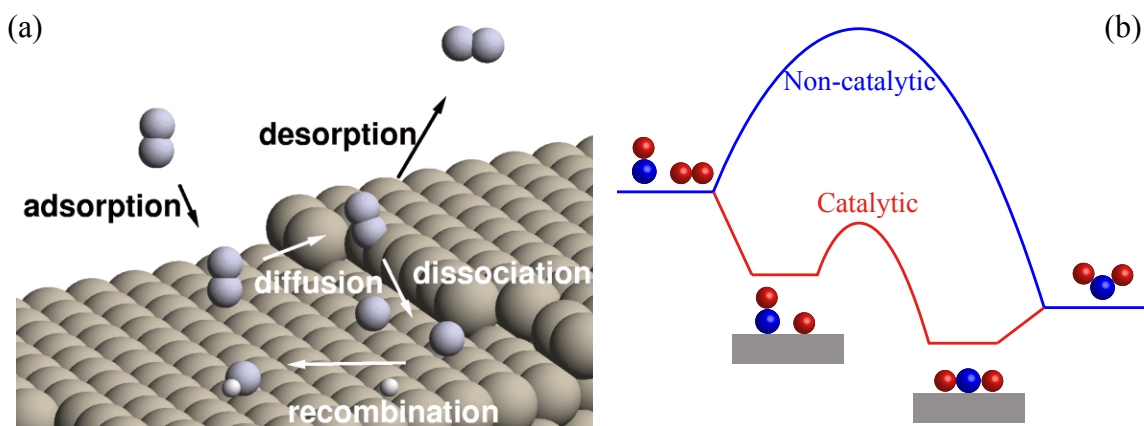


Figure 1.1: (a) The microscopic view of catalytic reactions on metal surfaces. (b) Potential energy diagram of a catalytic reaction vs. non-catalytic reaction

To illustrate the microscopic mechanism of the catalytic process, we have shown in Fig. 1.1(a) the elementary reaction steps involved in the CO oxidation on stepped metal surfaces, which has been taken as a simplest model reaction including all the essentials of catalytic processes. Even for this simple model reaction, the complexity of various adsorbate-adsorbate and adsorbate-substrate interactions makes the identification of reaction mechanisms difficult. The presence of catalyst surfaces enriches the interactions between adsorbates and also directs chemical transformations towards products. This can be illustrated in Fig. 1.1(b), where the energy landscape from the reactants to the products of a heterogeneous catalytic reaction involves different reaction pathways compared to gas phase non-catalytic reactions. The reaction energy remains the same, which indicates that

the catalyst could not change the thermodynamic driving force of the reaction, but only the kinetics.

The macroscopic properties measured in large scale chemical reactors, such as turn over frequency, selectivity and others, are mainly governed by the microscopic events happening on catalyst surfaces, i.e., the complex interplay of microscopic catalytic events governs the outcome of the chemical transformations and the catalytic performance of the surfaces. Understanding variations in the surface reactivity from one surface to another and physical factors governing the energetics for elementary reaction steps holds the keys to developing efficient catalytic materials.

## **1.2 Understanding the Kinetics of Catalytic Reactions**

### **1.2.1 Transition State Theory**

Collision theory was proposed previously to understand the kinetic rate of chemical reactions [2]. The activation energy for the reaction to occur was provided by effective collisions between reacting molecules. Even though the theory can qualitatively explain some experimental observed trends, the exclusion of the details about the molecular structures of molecules (partially taken into account by using steric factor) called for the development of rate theory built in the molecular level information of reacting species. Transition state theory [3], developed by Henry Eyring, Meredith Gwynne Evans and Michael Polanyi around 1935, remedied the limitation posed by Collision theory and was used to describe the kinetics of catalytic reactions ever since.

According to transition state theory, the reaction proceeds through an activated complex state located at the saddle point of the potential energy surface constructed by the degree of freedom of the reactant and product. The basic assumption is that there is equilibrium

between the reactant and the activated complex state as illustrated in Eq. 1.1 [1].



The rate can be written as

$$(1.2) \quad \begin{aligned} \frac{d[P]}{dt} &= \nu [R^\ddagger] = \nu K^\ddagger [R] \\ &= \nu \frac{q'^\ddagger}{q} [R], \end{aligned}$$

where  $q'^\ddagger$  is the partition function of the transition state  $R^\ddagger$  including reaction coordinate.  $q$  is the partition function of the reactant  $R$ .  $[R]$  is the concentration of the reactant.  $\nu$  is the vibrational frequency of transition state in the reaction coordinate.

According to Eq. 1.2, the rate constant of this elementary step ( $k$ ) can be written as follows

$$(1.3) \quad \begin{aligned} k &= \nu \frac{q'^\ddagger}{q} = \nu q_\nu \frac{q^\ddagger}{q} \\ &= \nu \frac{\exp^{-\frac{1}{2}h\nu/k_B T}}{1 - \exp^{-h\nu/k_B T}} \frac{q^\ddagger}{q}, \end{aligned}$$

where the vibrational partition function ( $q_\nu$ ) of transition state along the reaction coordinate can be approximated as  $h\nu/k_B T$  by the classical limit as  $h\nu \ll k_B T$ . Eq. 1.3 can be simplified as the following [1]

$$(1.4) \quad k = \frac{k_B T}{h} \frac{q^\ddagger}{q}.$$

It should be noted that the reaction coordinate is excluded in the partition function of transition state  $q^\ddagger$ . The same zero energy at the bottom of the potential well of the reactant is used for evaluation of the partition function of  $q^\ddagger$  and  $q$ .

Eq. 1.4 can be written in the form

$$(1.5) \quad k = \frac{k_B T}{h} K^\ddagger.$$

with the assumption that the transition state is fully equilibrated with the reactant except for the degree of freedom along the reaction coordinate. By replacing equilibrium constant with Gibbs free energy, Eq. 1.5 can be represented as the following

$$(1.6) \quad k = \frac{k_B T}{h} e^{-\Delta G^\ddagger} = \frac{k_B T}{h} e^{\Delta S_0^\ddagger/R} e^{-\Delta H_0^\ddagger/RT}.$$

The kinetic parameters defined in Arrhenius expression ( $k_{Arr} = v_{eff} e^{-E_a/RT}$ ) can be deduced directly from Eq. 1.6 by using

$$(1.7) \quad E_a = kT^2 \frac{\partial}{\partial T} \ln k = \Delta H_0^\ddagger + RT,$$

where the weak dependence of  $\Delta S_0^\ddagger$  on the temperature is neglected. By comparing Arrhenius form of rate constant with the Eq. 1.6, we can get the pre-factor  $v_{eff}$  is

$$(1.8) \quad v_{eff} = \frac{e k_B T}{h} e^{\Delta S_0^\ddagger/R}.$$

Alternatively, for Eq. 1.4, we can shift the reference energy of transition state to the energy at the saddle point, which is  $\Delta E$  higher than the energy of the reactant  $R$  at the bottom of potential well. So Eq. 1.4 can be written as

$$(1.9) \quad k = \frac{k_B T}{h} \frac{q_0^\ddagger}{q} e^{-\Delta E/k_B T},$$

where partition function  $q_0^\ddagger$  is referenced to energy at saddle point. For the calculation of vibrational partition function, the bottom of the potential well energy should be used as the reference, otherwise, the zero point energy should be taken into account in  $\Delta E$ . Exactly same expression of  $E_a$  and  $v_{eff}$  can be obtained. For simplicity, the detailed derivation is not shown here.

Nowadays, Density functional theory has been widely used to compute the kinetic parameters for elementary reaction processes. The derivation shown here aimed to provide the direct comparison to Arrhenius expression, which is often used as a standard kinetic analysis tool in experiment.

### 1.2.2 The Sabatier Principle

The catalytic performance of solid surfaces acting as catalysts for chemical transformations is determined by the complex interplay of different microscopic events. A good catalyst should be able to bring reactants down to the surface, cleave the required chemical bond, hold the surface species in close proximity for forming product and also allow the desorption of the product back into the gas phase, and finally release the active sites for next catalytic cycle. An active metal can probably dissociate the molecules easily, but might be limited by the desorption of products, which poison the catalytic sites. Less active metal adsorbs molecules weakly and may not have the capacity to cleave the bond initially resulting in negligible effect on the reaction. Intuitively, the optimum catalyst should be the compromise between those two capabilities. Sabatier [4] stated that there must be an optimum of the rate of a catalytic reaction as a function of the heat of adsorption. This is the Sabatier principle [4] developed in the beginning of last century.

Sabatier principle is illustrated in Fig. 1.2 where the schematic catalytic reactivity of various transition metals for oxygen reduction reaction (ORR in Eq. 1.10) shows a volcano-shaped relationship as a function of the binding energies of oxygen species. The observed catalytic trend of ORR on transition metals can be easily understood from Sabatier principle. The metal to the left of the periodic table can dissociate  $O_2$  easily, but the surface appears to be blocked by hydroxyl species. For the metal to the right side of the periodic table, such as Ag and Au, they are intrinsically less reactive than those metals on the left side. There is significant activation barrier to cleave the O-O for subsequent hydrogenation steps. Pt is the best pure-metal ORR electrocatalyst even though its catalytic performance is still limited by the strong binding of hydroxyl (OH) to surface Pt sites. The observed volcano relationship gives us indication that if we can slightly perturb the surface properties of Pt to weaken the OH binding on the Pt, the ORR could be performed on the

top of the volcano curve. Similar volcano-shaped relationships have been identified for many other catalytic reactions [5–7], which has been providing the fundamental insights into reaction mechanisms and guiding us designing better catalysts.

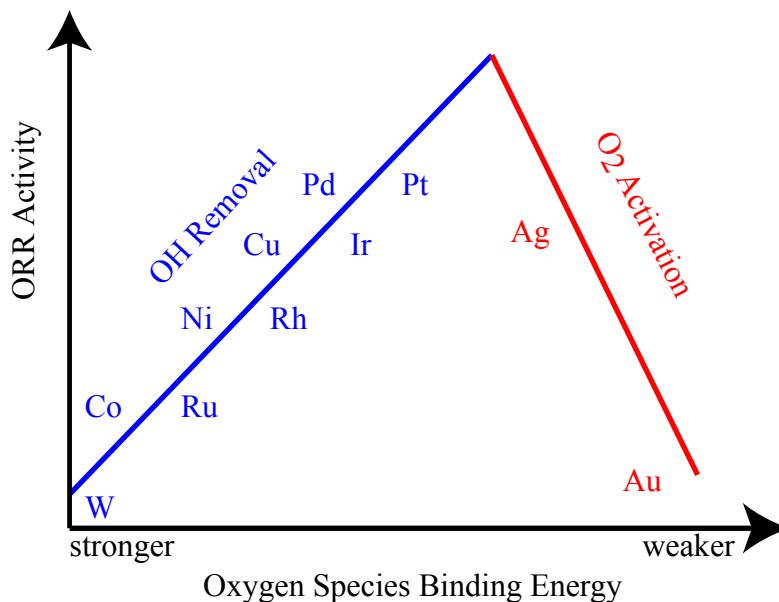


Figure 1.2: Schematic illustration of volcano relationship between catalytic activity of transition metals for oxygen reduction reactions as a function of oxygen species binding energies

### 1.3 Universal Relationships for Estimating Bond Energies

Understanding the nature of chemical bonding between adsorbate and catalyst surfaces is critical for unearthing underlying mechanisms of catalytic reactions, and for the rational manipulation of the catalyst surface to obtain the desired catalytic properties. According to Transition State Theory, the kinetic rate of the elementary chemical transformation is governed by the activation barrier resulting from its exponential dependence. At the optimum coverage of reacting species during the course of chemical reactions, the variation of pre-factor is less pronounced than the effect of energy barrier separating the re-

actants from the products. In principle, we could calculate the energetics of the chemical transformation steps on all the interesting catalyst surfaces to identify the better catalysts. However, considering that there are many elementary reaction steps and immense configuration space of catalytic materials, it is not practical to screen for optimum catalysts from first-principles calculations even though there are a few success [8–17]. To make the computational screening for optimum catalytic materials practical, it is necessary to have simple relationships for estimating the bond energies of reacting species or relating them to the simple descriptor which can be readily available. In this section, we will review several universal relationships related to the field of heterogeneous catalysis, which can be used to build the full potential energy surfaces of chemical reactions with the bond energies of simple adsorbates on catalyst surfaces. The potential energy surface can then be combined with kinetic modeling approaches to evaluate the rate and/or selectivity of the catalytic reactions. It should be noted that this step is usually used as rapid screening of potential interesting materials. The potential energy surfaces of chemical reactions on identified materials will be constructed from self-consistent electronic structure calculations for further studies and comparison with experiments.

### 1.3.1 The Brønsted-Evans-Polanyi Relationship

The adsorption energies of simple adsorbates are governed by electronic properties of the surface sites (see details in Chapter II). The similar argument can be applied to transition states of elementary chemical transformations on the same catalytic sites. Considering that the stability of different states of surface species are governed by the same underlying physics, there is no surprise that there is correlation between energetics of various surface intermediates including transition states. Actually, this linear relationship between the reaction energies and the activation barriers as shown in Eq. 1.11 has been widely used in homogeneous catalysis for a while, which is known as BEP relationship named after

Brønsted [18], Evans [19] and Polanyi [20].

$$(1.11) \quad \delta\Delta E_a = \alpha\delta\Delta E_R \quad (0 < \alpha < 1)$$

where  $\Delta E_a$  is the activation barrier and  $\Delta E_R$  is the reaction energy.  $\alpha$  is the BEP coefficient characterizing the transition state structure on the reaction coordinate [1].

The relationship is valid if the elementary reaction steps proceed through similar intermediate structures and reaction coordinates. The development of DFT allows us to validate the relationship for heterogeneous catalysis [21] and it has been shown that the BEP relationships are reasonably accurate for the prediction of the activation energies based on the adsorption energies. The principle has been used in kinetic analysis programs [22], such as micro-kinetic modeling and kinetic Monte Carlo simulations, and provides a fast way for evaluating the kinetic rate of catalytic reactions.

### 1.3.2 Linear Scaling Relationship

The BEP relationship has shown that there is a linear correlation between the reaction energy determined by the adsorption strength of surface species and the activation barrier separating those surface species. The CPU time to construct full potential energy surfaces of catalytic reactions can be significantly reduced since the transition state search calculation is very computationally rigorous. Some recent works have shown that the situation can be further simplified [23, 24]. The binding energies of hydrogen-containing adsorbates ( $\text{OH}_x$ ,  $\text{NH}_x$ ,  $\text{CH}_x$  and  $\text{SH}_x$ ) on metal surfaces can be related to the stability of small fragments (O, N, C and S) as shown in Eq. 1.12 since they are determined by the same underlying electronic structure.

$$(1.12) \quad \Delta E^{AH_x} = \gamma\Delta E^A + \xi \quad A = \text{C, N, O, S}$$

The same relationship can be extended to other types of catalytic materials, such as oxide, sulfide or nitride [24]. Based on the Linear Scaling relationship and the BEP rela-

tionship, it is possible to map out the full potential energy surfaces using only the binding energies of simple adatoms on varying catalytic surfaces. Those relationships have been used to understand the trend of the surface reactivity of transition metals for ethanol decomposition reaction [22], ammonia synthesis and methanation reactions [25]. The validation of the relationship from basic theory of surface chemisorption also provides a fundamental understanding of the nature of chemical bonding on metal surfaces [23].

### 1.3.3 Group Additivity

Based on the *d*-band model (details in Chapter II), BEP relationship and Linear Scaling relationship, the full potential energy surfaces of simple chemical transformations on various transition metal surfaces can be constructed based on the adsorption energies of simple adsorbates on one metal surface. This theoretical framework has greatly reduced the complexity and computational time of theoretical modeling of the surface reactions. However, for some chemical reactions involving large chain species an additional relationship needs to be introduced allowing us to theoretically understand those reaction mechanisms and predict the surface reactivity. Those chemical transformations are essentially for several industrial processes, such as hydrogenation of olefin with long chain hydrocarbons from oil refining and the biomass reforming involving polyol feedstock. Benson introduced group additivity for the kinetic modeling of gas phase reactions [26]. The same concept has been extended to surface chemisorption of hydrocarbon fragments on transition metal surfaces [27]. Combined with DFT calculations, the group additivity has been established for polyol adsorption on metal surfaces [28], which has potential application for developing active catalysts for biomass conversions. For those types of large molecules, group additivity provides a way to estimate the energetics based on the binding energy of simple fragments and the bond strength between those fragments, which are tabulated [26].

Together with well-established *d*-band model, BEP relationship, the Linear Scaling

relationship and Group Additivity, the kinetics of chemical transformations on catalyst surfaces can be related to adsorption energies of simple adsorbates on one metal surface. And there are several examples showing that a single descriptor exists for many chemical reactions [29]. To design better catalysts for any chemical transformations boils down to the question of how we can tune the surface reactivity or the binding energies of simple adsorbates on metal surfaces, so the chemical reactions can be performed at the peak of the volcano curve.

#### **1.4 Research Philosophy**

Since the thermodynamic stability of atoms or simple molecules can be used as the single descriptor of the catalytic reactivity, a good strategy for searching for better catalysts would be to design surfaces with the desired strength of chemical bonding of a specific adsorbate on the surface. Understanding the nature of chemical bonding between adsorbate and catalyst surfaces is the key component to rationally manipulate the catalyst surface to obtain the desired properties.

However, on the periodic table, there is significant difference in adsorption energies even for neighboring metals. According to Sabatier principle, the consequence of that is one metal is inert, but neighbouring metal will be too chemically active and equally inefficient. For example, Pt is the best elemental metal catalyst for oxygen reduction reaction (ORR) in acidic condition. And it has been illustrated that the binding energies of oxygen or oxygen containing species can be used as descriptors describing the catalytic performance of metal surfaces for ORR. The oxygen binding energy on the Pt(111) surface is about 1.0 eV ( $\sim 100$  KJ/mol), which places the Pt on the left of the volcano plot meaning that the removal of OH species is limiting the fuel cell performance as shown in Fig. 1.2. However, even the first near neighbor silver surface has binding energy way too low (0.5

eV) which makes adsorption of oxygen and O-O bond dissociation difficult.

To extend the phase space of periodic table, we need to figure out how we can slightly and rationally perturb the electronic properties of catalyst surfaces to have desired properties. Traditionally there are several ways to improve the catalytic performance in industrial catalysis, such as by alloying, doping or coupling with other stimuli (phonon, electron, photon, etc.). However, almost all commercial catalysts, typically composed of multiple ingredients, are selected through experimental trial and error approaches and far from optimized. The lack of predictive models for catalysts design is particularly problematic for multi-component or multi-stimuli systems since the number of potential candidates is too large to screen for optimal catalysts using time-consuming experimental measurements or quantum-chemical calculations. The central question we attempt to answer in this project is the following: *How does a perturbation of surface electronic properties affect the energetics for elementary reaction steps?* The ultimate objective is to develop simple predictive theories that can guide us in the discovery of novel, more efficient multi-component and multi-stimuli catalysts. While in our studies we focus on a number of case studies, every attempt is made to formulate universal knowledge-base that extends far beyond the concrete case studies.

## 1.5 Suggested Readings

To understand the fundamentals of DFT in the field of computational chemistry, please refer to the books [30, 31], which have been taken as standard DFT references with extensive mathematical derivations and chemistry insights. I would highly recommend the book by Philip Hofmann [32] and the [website](#) for the understanding of the general concepts in solid state physics. For details about the electronic structure of materials, two solid state physics books are highly recommended [33, 34]. To understand the concept of

chemical bonding on metal surfaces where the chemistry meets with physics, please refer to the review articles by Roald Hoffman [35, 36] or extended version in book form [37]. For the application of DFT in the field of heterogeneous catalysis, a few review articles by Nørskov et al. would be highly recommended [29, 38–40].

## 1.6 Scope of the Thesis

The objective of this thesis is to obtain a fundamental understanding of variations in the surface reactivity of transition metals with perturbed electronic properties. The critical question we attempt to answer is: *How does a perturbation of surface electronic properties affect the energetics for elementary reaction steps?* The perturbation of surface electronic properties can be accomplished by alloying with impurity elements, doping of surface promoters, or imposing stimuli for electronic excitations.

In Chapter I, we start from the microscopic view of heterogeneous catalysis to illustrate the length and time scales in our studies. After briefly introducing the transition state theory, we have talked about the well-known Sabatier principles for understanding the observed volcano-shaped trend of the surface reactivity of varying surfaces. Based on those analysis, we have highlighted the role of binding strength of important intermediates or adsorbates as the reactivity descriptor for catalytic reactions. We have briefly introduced the effort in theoretical catalysis community for relating the thermodynamic stability of molecules and the kinetics of elementary reaction steps to the adsorption energies of atoms or groups. The research philosophy is presented, where we emphasized that understanding of variations in the binding energies of simple adsorbates holds the keys to designing catalytic materials with utmost energy efficiency and minimal environmental impact.

In Chapter II, the fundamental principles of density functional theory are briefly introduced. For the development of physically transparent understanding of surface chemisorp-

tion, we have elaborated several approximated models which have helped us gain a tremendous amount of understanding of heterogeneous catalysis.

In Chapter III, we have developed a general theoretical framework for the analysis of variations in the surface reactivity due to perturbed electronic properties of transition metals. In this theoretical framework, the variations in surface reactivity can be attributed to one-electron energies, electrostatic and polarization contributions. The physical mechanism and numerical evaluations of each contribution has been illustrated.

In Chapter IV, we have elaborated underlying mechanisms that govern variations in the surface reactivity of host metal sites in response to the perturbation of electronic properties by forming alloys.

In Chapter V, we have developed a very general and physically transparent model, based on DFT calculations, which allows us to better understand adsorbate-adsorbate interactions on metal surfaces doped with chemical promoters.

In Chapter VI, we have developed a first-principles based Finite-Temperature Electron Scattering Model to investigate the energetic electron induced activation of adsorbed diatomic molecules over metal surfaces at finite temperature.

In Chapter VII, we have presented the general conclusions of our studies and the significance for the field of heterogeneous catalysis.

## CHAPTER II

### Density Functional Theory

In this introductory chapter we will review some of the fundamental aspects of density function theory (DFT) in order to lay the foundation for the model development and theoretical discussion in this thesis. The development of Density Functional Theory allows us to obtain the detailed electronic structure information about individual catalytic events by solving Schrödinger equation for collections of hundreds atoms at a high level of accuracy. To understand the underlying physical mechanism that governs the kinetics of surface reactions and develop simple models for rapid prediction without expensive quantum chemical calculations, a trade-off of simplicity and accuracy is necessary to describe the nature of interactions between the adsorbates and surfaces. In this chapter, I will introduce several models within the theoretical framework of Tight Binding Approximations for describing the surface chemisorption. Those theoretical models not only served as standard tools to understand the surface reactivity of transition metals, but also established the basis for further development in this thesis.

For deeper understanding of the electronic structure theory and its application for heterogeneous catalysis the reader is strongly encouraged to consult the textbooks listed in Recommended Readings in Chapter I.

## 2.1 Fundamental Principles

The Schrödinger equation [41] is the fundamental equation of physics for describing the behavior of electronic systems using quantum mechanics. The time-independent Schrödinger equation is given as

$$(2.1) \quad \hat{H}\Psi = E\Psi,$$

where the Hamiltonian of the system can be represented as

$$(2.2) \quad \hat{H} = -\sum_i \frac{1}{2} \nabla_i^2 - \sum_{i,I} \frac{Z_I e^2}{|r_i - R_I|} + \sum_{i>j} \frac{e^2}{|r_i - r_j|} + \hat{H}_{nucl}^{kin} + \hat{H}_{nucl}^{Hartree}.$$

The first three terms describe the kinetic energy of the electrons, and the interaction of electrons with nucleus and other electrons. The last two terms are the kinetic energy of nucleus and the nucleus-nucleus repulsion. Based on Born-Oppenheimer approximation [42], the

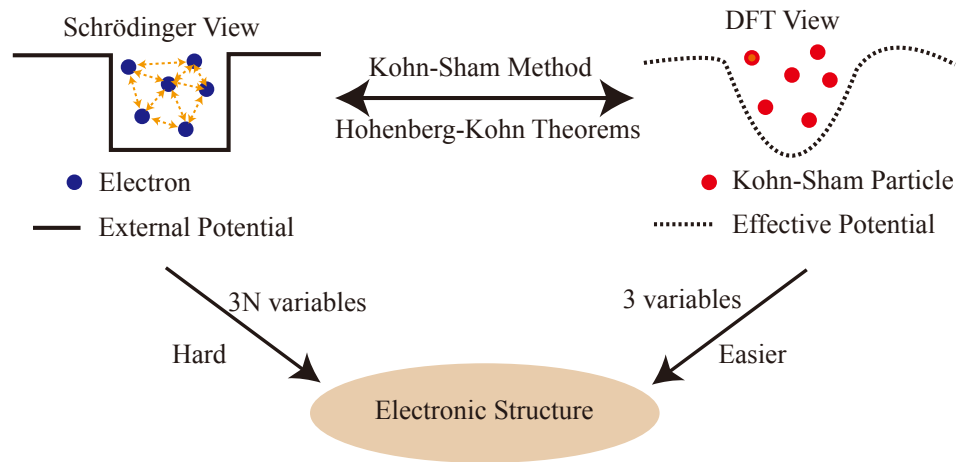


Figure 2.1: Schematic illustration of the comparison between Schrödinger and DFT views of many-body problems

kinetic energy of nucleus can be neglected. Even with that, solving the Schrödinger equation still seems a formidable task since many-particle wavefunction relies on all the spatial and spin coordinates of the particles ( $4N$ , where  $N$  is the number of particles in the system). At that time, electron density  $n(r)$  has been occasionally used as the fundamental

description of the system based on intuition instead of mathematical proof. The advantage of usage of electron density,  $n(r)$ , rather than many particle wave function is clear since electron density depends only on  $x$ ,  $y$  and  $z$  three variables. This comparison can be shown clearly on Fig. 2.1.

### 2.1.1 The Hohenberg-Kohn Theorems

In 1965, Hohenberg and Kohn [43] provided the solid proof that electron density alone determining the ground state electronic properties, and there exists the ground-state electron density minimizing the energy of the system. The proposed theorems have become the fundamental basis of modern density functional theory. Since we have used those fundamental formalisms in DFT for the derivation in Chapter 3, we will elaborate those fundamental theorems as follows.

**Theorem 2.1.1.** (The First Hohenberg-Kohn Theorem [43])

*For any system of electrons in an external potential  $v_{\text{ext}}(r)$ , that potential is determined uniquely, except for a constant, by the ground-state electron density  $n(r)$ .*

Simply speaking, if the electron density  $n(r)$  is available, then the external potential, defined by the position and types of nucleus, is determined with trivial constant, which will not change anything since the Hamiltonian with extra constant gives exactly the same eigenfunction as original Hamiltonian. So the ground-state electron density also determines all the electronic properties of the system. It contains all the information as the full many-body wavefunctions.

This theorem seems very trivial to proof, which can be found on any DFT textbook [31, 44]. The theorem tells that there is one-to-one mapping between electron density and the external potential and also all the other properties of the electronic system, however, it did not provide any indication of how the electron density looks like and how to construct

it.

**Theorem 2.1.2.** (The Second Hohenberg-Kohn Theorem [43])

For a trial density  $\tilde{n}(r)$ , such that  $\tilde{n}(r) \geq 0$  and  $\int \tilde{n}(r) dr = N$ , it satisfies

$$(2.3) \quad E_v[\tilde{n}(r)] \geq E_0.$$

In Eq. 2.3,  $E_v[\tilde{n}(r)]$  is the energy functional of trial electron density  $\tilde{n}(r)$ . Proof is straight forward as shown below,

$$(2.4) \quad \tilde{n}(r) \rightarrow v \rightarrow \tilde{H}_{el} \rightarrow \tilde{\Psi},$$

$$(2.5) \quad \langle \tilde{\Psi} | \hat{H} | \tilde{\Psi} \rangle = E_v[\tilde{n}(r)] \geq E[n_0(r)] \equiv E_0.$$

The second Hohenberg-Kohn theorem provides variational principle in electron density  $n(r)$  for ground states. In other words, if some density represents the correct number of electrons  $N$ , the total energy calculated from this density cannot be lower than the true energy of the ground state. The electron density  $n(r)$  minimizing the energy functional is the exactly ground state electron density. Even though the second theorem provides the path for obtaining the ground state density from variations principles, it did not have any practical implementation for doing that.

### 2.1.2 The Kohn-Sham Equations

Based on Hohenberg-Kohn theorems, density-functional theory reduces a many-body problem for the  $N$  particle wavefunction  $\Psi(r_1, s_1; \dots; r_N, s_N)$  ( $4N$  variables) to one in terms of the charge density  $n(r)$  (3 variables). The ground state energy of a many-electron system can be obtained as the minimum of the energy functional

$$(2.6) \quad E_0[n] = \min_{n \rightarrow N} (T[n] + V_{ee}[n] + \int n(r) v_{ext} dr),$$

where  $T$  is the kinetic energy of the electrons with density  $n(r)$ ,  $V_{ee}$  is the electron-electron interactions.  $v_{ext}$  is the external potential of the nucleus given by

$$(2.7) \quad v_{ext} = \sum_I \frac{-Z_I}{|R_I - r|}.$$

The straightforward application of this formula has one tremendous difficulty that there is no accurate density functional of the kinetic term. Kohn and Sham (1965) [45] have designed an ingenious way of working around this considering that the kinetic energy can be easily obtained if the wavefunction is known. By combining the idea of wavefunction and density approaches, they proposed a fictitious system with the same electron density as the real system. The energy of this system is written as

$$(2.8) \quad E = T_s[n] + \int n(r)v_{ext}dr + J_{ee}[n] + E_{xc}[n],$$

where  $T_s[n]$  is the kinetic energy of electrons in a system which shares the same electron density as the real system.  $J_{ee}[n]$  is the classical Coulomb interaction between electrons.  $E_{xc}[n]$  is the exchange-correlation functional.

Based on Kohn-Sham scheme, the problem in Eq. 2.6 was simplified to solving the Schrödinger equation with non-interacting electrons moving in an effective potential  $v_{eff}$  so that

$$(2.9) \quad -\frac{1}{2}\nabla^2\psi_i(r,s) + v_{eff}(r)\psi_i(r,s) = \epsilon_i\psi_i(r,s).$$

where the effective potential is defined as

$$(2.10) \quad v_{eff}(r) = v_{ext}(r) + \int \frac{n(r')}{r-r'}dr' + \frac{\delta E_{xc}[n]}{\delta n}.$$

$E_{xc}[n]$  is called exchange-correlation energy, which includes all the energy contributions which were not accounted for by the Hamiltonian [31], such as electron exchange and electron correlation since non-interacting electrons do not correlate their movements, the

kinetic energy correcting  $T_0[n]$  to obtain true kinetic energy of a real system  $T_e[n]$ , and the correction for self-interaction introduced by the classical coulomb potential.

Theoretically, if we know the exact functional  $E_{xc}[n]$ , we could solve the system exactly. The simplicity of the theory has the paid-off that there is no systematically way for improving this functional.

The corresponding charge density  $n(r)$  can be written as the sum of the squares of a set of orthonormal wave functions

$$(2.11) \quad n(r) = \sum_i^N \sum_s |\psi_i(r,s)|^2.$$

This system is then solved iteratively, until self-consistency of the electron density, eigenfunction and energy is reached. Density can be used to calculate the energy of the system according to

$$(2.12) \quad \begin{aligned} E[n] &= T_s[n] + J_{ee}[n] + \int v_{ext}n(r)dr + E_{xc}[n] \\ &= -\frac{1}{2} \sum_i^N \langle \psi_i | \nabla^2 | \psi_i \rangle + \frac{1}{2} \sum_i^N \sum_j^N \int \int |\psi_i(r_1)|^2 \frac{1}{r_{12}} |\psi_j(r_2)|^2 dr_1 dr_2 \\ &\quad - \sum_i^N \int \sum_A^M \frac{Z_A}{r_{1A}} |\psi_i(r_1)|^2 dr_1 + E_{xc}[n]. \end{aligned}$$

In practical implementation, the energy of the system can be more efficiently evaluated by combining Eq. 2.8 to 2.10 so that

$$(2.13) \quad E = \sum_i^N \varepsilon_i - \frac{1}{2} \int \frac{n(r)n(r')}{|r-r'|} dr dr' + E_{xc}[n] - \int \frac{\delta E_{xc}[n]}{\delta n(r)} n(r) dr.$$

The schematic illustration of the Kohn-Sham implementation of DFT is shown in Fig. 2.2 for simplicity.

This effective potential defined in Eq. 2.10 is a sum of the potentials due to electron/nuclei electrostatic interaction ( $v_{ext}(r)$ ), electron/electron electrostatic interaction, and the exchange-correlation potential,  $v_{xc}$  (which is unknown). Using this approach the prob-

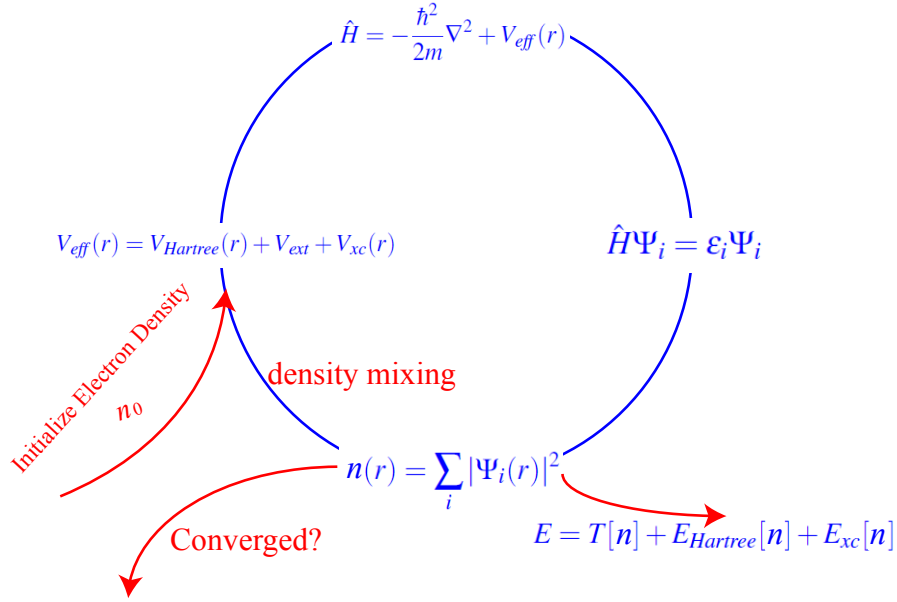


Figure 2.2: Schematic illustration of Kohn-Sham implementation of DFT

lem of strongly interacting electron gas is mapped rigorously onto a problem of single particles (electrons) moving in some effective, non-local potential  $v_{eff}$ .

In order to obtain ground-state  $n_0$  and  $E_0$  one needs to solve the Kohn-Sham equations self-consistently. For the practical application of the theory, an explicit expression for  $E_{xc}[n]$ , i.e.,  $v_{xc}$  is needed. The exact expression for  $E_{xc}[n]$  is not known. However, there are two commonly used approximations for  $E_{xc}[n]$ : the local density approximation (LDA) and generalized gradient approximation (GGA). In the LDA, the exact exchange and correlation energy per particle calculated for a homogeneous electron gas is used. In the GGA an extra term that depends on the gradient of electron density is added to the LDA exchange and correlation energy. There are certain conditions that this correction has to satisfy and for those Perdew et al. [46] can be consulted. It has been shown that these approximations, LDA and GGA, work surprisingly well and that DFT can reproduce various experimental results (the energies, bond lengths, ground state geometries of molecular structures, etc) with very high accuracies.

### 2.1.3 Relating Electronic Energies to Thermodynamic Properties

As stated in the Transition State Theory, the rate constant for an elementary reaction step depends on the free energy instead of just reaction enthalpy since the entropy will modify the pre-factor. It is critical to understand how the DFT-calculated energies related to thermochemistry.

The energy  $E(V, N)$  from standard DFT calculations represents the Helmholtz free energy  $A(T, V, N)$  at  $(T=0, p=0)$  with the neglect of the zero-point vibrational energies [47]. The Gibbs free energy of the system is

$$(2.14) \quad G(T, p, N) = A + PV = U - TS + pV.$$

In the following, I am going to talk about the contribution from various degree of freedom including vibration, rotation and translation into each terms.

#### 2.1.3.1 Vibration

By referencing energy to the zero-point energy state, the partition function of vibrational degree of freedom is

$$(2.15) \quad Q_{vib} = \sum_i \frac{1}{1 - e^{-h\nu_i/k_B T}}.$$

The contribution to the internal energy is expressed as

$$(2.16) \quad E_{vib} = \sum_i \left( \frac{h\nu_i}{2} + \frac{h\nu_i \cdot e^{-h\nu_i/k_B T}}{1 - e^{-h\nu_i/k_B T}} \right).$$

As we can see that the zero-point energy has been explicitly taken into account.

The entropy of the vibrational contribution can be calculated as

$$(2.17) \quad S_{vib} = R \sum_i \left( \frac{h\nu_i/k_B T e^{-h\nu_i/k_B T}}{1 - e^{-h\nu_i/k_B T}} - \ln(1 - e^{-h\nu_i/k_B T}) \right).$$

### 2.1.3.2 Rotation

For linear molecules, the partition function of rotation degree of freedom is

$$(2.18) \quad Q_{rot} = \frac{8\pi^2 I k T}{\sigma h^2},$$

where  $I$  is the initial of the molecule;  $\sigma$  is the symmetry number. For linear molecule  $\sigma$  is 2, but it is 1 for non-linear molecules. The energy contribution is  $RT$  for linear molecule and  $3/2RT$  for non-linear molecule.

The entropy of rotation contribution for linear molecules is

$$(2.19) \quad S_{rot} = R \ln \left[ \frac{8\pi^2 I k_B T}{\sigma h^2} \right] + R.$$

For non-linear molecules, it gives

$$(2.20) \quad S_{rot} = \frac{R}{2} \ln \left[ \frac{\pi}{\sqrt{\sigma}} \left( \frac{8\pi^2 c I_A}{h} \right) \left( \frac{8\pi^2 c I_B}{h} \right) \left( \frac{8\pi^2 c I_C}{h} \right) \left( \frac{k_B T}{hc} \right)^3 \right] + \frac{3}{2} R.$$

### 2.1.3.3 Translation

The partition function for translational degree of freedom is

$$(2.21) \quad Q_{tra} = \left( \frac{\sqrt{2\pi M k_B T / N_A}}{h} \right)^3.$$

The translational energy contribution is  $3/2RT$  for 3 degrees of freedom.

The entropy can be calculated as

$$(2.22) \quad S_{tra} = R \ln \left( \left( \frac{2\pi M k_B T}{h^2} \right)^{3/2} \frac{k_B T}{P} \right) + \frac{5}{2} R.$$

The internal energy is calculated as

$$(2.23) \quad U = E_{DFT} + [E_{zero} + E_{vib\ 0 \rightarrow T}] + E_{rot} + E_{tra}.$$

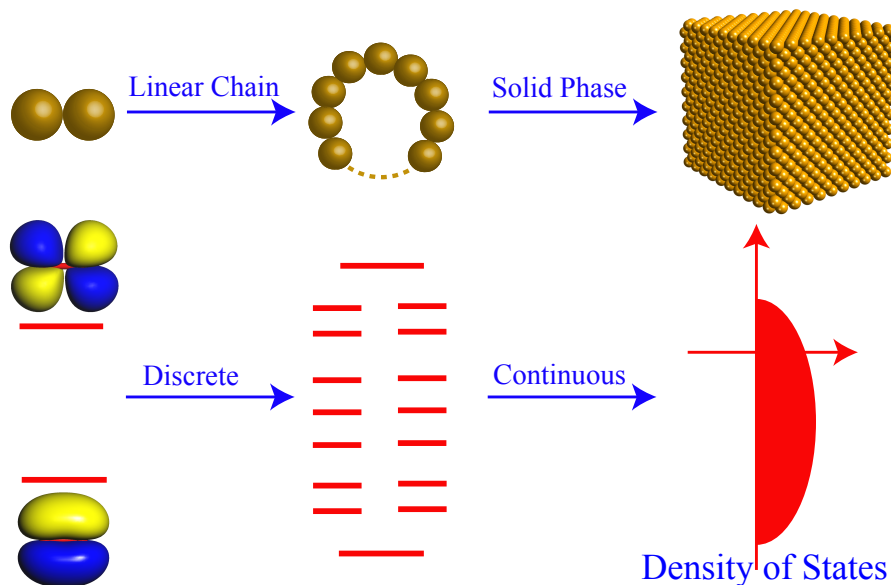


Figure 2.3: Schematic illustration of band formation

#### 2.1.4 Electronic Properties of Transition Metal Surfaces

To understand the electronic properties of transition metal surfaces, we first need to introduce the concept of band formation, which is illustrated in Fig. 2.3.

From the molecular orbital theory, widely used in chemistry, we can understand that the interaction between atomic orbitals forms two discrete states separated in energies, called bonding and anti-bonding states as shown on the left side of Fig. 2.3. As the number of interacting atomic orbitals increases by forming linear chains of atoms, the amount of resulting molecular orbitals increases, leaving small energy difference between energy levels. The solid materials contain Avogadro numbers of atoms and orbitals, the forming energy states are so close in energies that the distribution of energy states can be seen as continuous, i.e., the formation of band.

The electronic bands of transition metals include broad, featureless  $sp$ -band and localized  $d$ -band. The shape of different bands is governed by the symmetry of interaction orbitals and the coupling strength [35, 36]. In this section, we are also going to elaborate

the role of different bands for determining the binding energies of simple adsorbates. Understanding the basic interaction mechanism of a single adsorbate state with the transition metal electronic bands is the first step for tuning the electronic properties of metal surfaces for improved surface reactivity.

## 2.2 Tight-Binding Approximation for Understanding of Surface Chemisorption

### 2.2.1 Hammer-Morikawa-Nørskov Two-Level Interaction Model

Considering two arbitrary orbitals, denoted as  $\psi_A$  and  $\psi_B$ , which can be the orbital of any kind, such as atomic orbitals or molecular orbitals, the interaction between those two orbitals results in the new states with wavefunctions to be determined. From perturbation point of view, two non-interacting orbitals constitutes the unperturbed system and the interaction represents the perturbation as illustrated in Fig. 2.4 (adapted from [48]). We

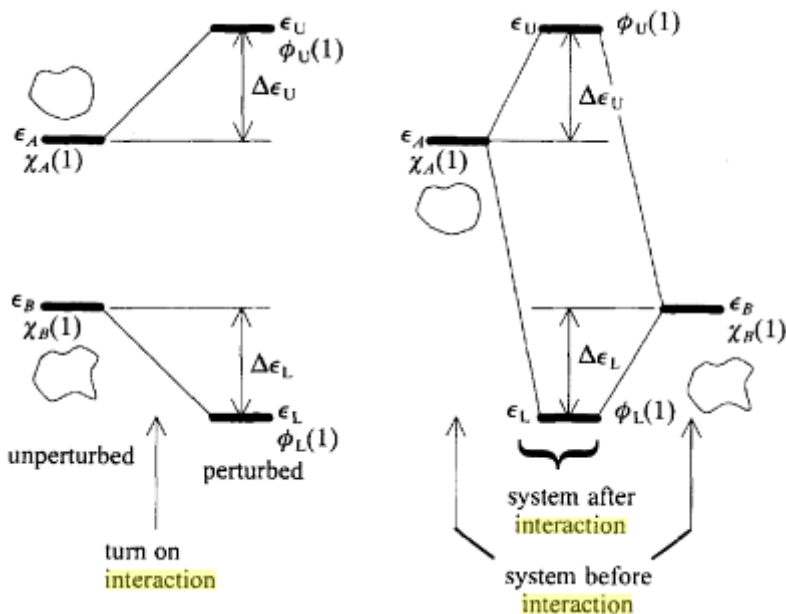


Figure 2.4: (a) Perturbation view of two orbital interactions (b) Standard interaction diagram of two orbital interactions

would like to determine the wavefunctions of whole system and energy of the forming new states. This basic problem has been solved using orbital interaction theory [48] and the so-

lution has been widely used in organic chemistry, known as molecular orbital theory. The similar approach has been extended for studying the interactions between adsorbate states with  $d$ -band of the surface [49]. Here, we will start from the same theoretical framework of interacting orbitals with emphasis on the *chemical insights* and *physical mechanisms*. This derivation will serve as standing alone section for understanding of basic interactions between orbitals.

According to molecular orbital theory, the molecular orbital wave function can be written as linear expansion of constituent atomic orbitals as

$$(2.24) \quad \Psi = c_A \psi_A + c_B \psi_B.$$

The Kohn-Sham equation for each orbitals is that

$$(2.25) \quad \left(-\frac{1}{2}\nabla^2 + v_A\right)\psi_A = \epsilon_A \psi_A,$$

where  $v_A$  is the effective potential for system A. For the combined system, assuming that  $v_{AB} = v_A + v_B$ , the Hamiltonian of the interacting system can be approximated as

$$(2.26) \quad H_{AB} = -\frac{1}{2}\nabla^2 + v_{AB} = H_A + v_B = H_B + v_A.$$

The Schrödinger equation we will solve is

$$(2.27) \quad H_{AB}\psi_{AB} = \epsilon \psi_{AB},$$

where

$$(2.28) \quad H_{AB} = \langle \psi_A | -\frac{1}{2}\nabla^2 + v_{AB} | \psi_B \rangle = V.$$

The overlap integral of two wavefunctions is

$$(2.29) \quad \langle \psi_A | \psi_B \rangle = S.$$

Solving Eq. 2.27, it yields

$$(2.30) \quad \epsilon_{\pm} = \frac{(\epsilon_A + \epsilon_B) \mp \sqrt{4V^2 + (1 - S^2)(\epsilon_A - \epsilon_B)^2}}{2(1 - S^2)}.$$

Typically  $S$  will be small, so Eq. 2.30 can be simplified as

$$(2.31) \quad \epsilon_{\pm} = \frac{\epsilon_A + \epsilon_B}{2} - VS \mp \frac{\sqrt{4V^2 + \Delta^2}}{2}.$$

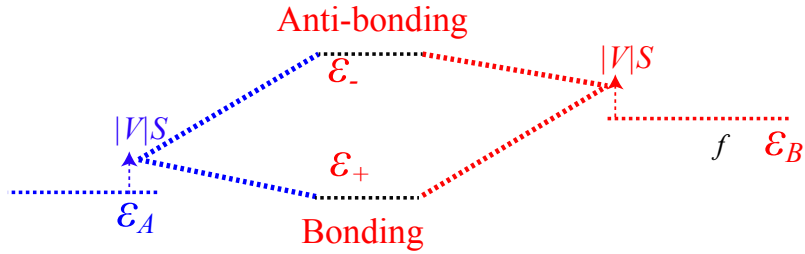


Figure 2.5: Simple case of interaction between adsorbate state  $\epsilon_A$  with metal  $d$ -state  $\epsilon_B$

For specific case of interaction of adsorbate state  $\psi_A$  with substrate  $d$ -state  $\psi_B$  with filling  $f$ , by summing the one-electron energies difference due to the interaction as shown Fig. 2.5, it yields

$$(2.32) \quad \Delta E = 2\epsilon_+ + 2f\epsilon_- - 2f\epsilon_B - 2\epsilon_A.$$

Based on the solution of two interacting orbitals in Eq. 2.31, we have

$$(2.33) \quad \begin{aligned} 2\epsilon_+ &= \epsilon_A + \epsilon_B - 2VS - \sqrt{4V^2 + \Delta^2} \\ 2\epsilon_- &= f(\epsilon_A + \epsilon_B - 2VS + \sqrt{4V^2 + \Delta^2}), \end{aligned}$$

where  $\Delta = |\epsilon_A - \epsilon_B|$ . As we define

$$(2.34) \quad W_{ad} = \sqrt{4V^2 + \Delta^2},$$

and  $S = -\alpha V$ , the energy change due to interaction can be written as

$$(2.35) \quad \Delta E = -(1 - f)(W_{ad} - \Delta) + 2(1 + f)\alpha V^2.$$

If  $\Delta^2 \gg 4V^2$ , using first-order Taylor expansion with  $x = 4V^2/\Delta^2$ , we have

$$(2.36) \quad W_{ad} \approx \Delta + \frac{2V^2}{\Delta}.$$

Take Eq. 2.36 into Eq. 2.35, we can obtain simplified expression for energy change as

$$(2.37) \quad \Delta = -2(1-f) \frac{V^2}{|\epsilon_A - \epsilon_B|} + 2(1+f)\alpha V^2,$$

where the coefficient 2 is accounting for 2 electrons in adsorbate orbital. If the adsorbate state is  $\pi$ -orbital, then the coefficient should be just 4.

Above, we have derived the energy change of fully occupied adsorbate orbital interacting with metallic  $d$ -band with filling  $f$ . For fully empty states interacting with metallic  $d$ -band of filling  $f$ , the energy change can be derived with same method. The final express we have derived is

$$(2.38) \quad \Delta = -2f \frac{V^2}{|\epsilon_A - \epsilon_B|} + 2\alpha f V^2,$$

where, for  $\pi$ -orbital, the coefficient is 4.

### 2.2.2 Newns-Anderson Model

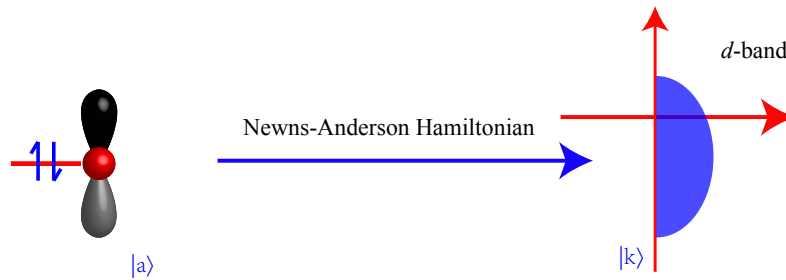


Figure 2.6: Schematic illustration of interaction between adsorbate orbital with the  $d$ -band of the substrate within Newns-Anderson model

The simple two level problem discussed above must be modified slightly at a surface. Here an adsorbate state will not just interact with a single surface state, but rather with a continuum of states as illustrated in Fig. 2.6.

Consider a metal surface with one-electron states  $|k\rangle$  with energy  $\varepsilon_k$ , and an adsorbate with a single valence state  $|a\rangle$  with energy  $\varepsilon_a$ . When the adsorbate is brought to a position just outside of the surface, the two sets of states are coupled by matrix elements  $V_{ak} = \langle a|\hat{H}|k\rangle$ , where  $\hat{H}$  is the Hamiltonian [50, 51] of the combined system defined as

$$(2.39) \quad \hat{H} = \varepsilon_a c_a^\dagger c_a + \sum_k \varepsilon_k c_k^\dagger c_k + \sum_k (V_{ak} c_k^\dagger c_a + V_{ak}^* c_a^\dagger c_k),$$

where the first term is the one electron energies of the adsorbate state before interaction, and the second term is the sum of one-electron energies of the substrate before switching the interaction with adsorbate state. The last term in Eq. 2.39 is the coupling between adsorbate state and metal  $d$ -states.

Following the derivation in literature [49, 51], we expand the solutions  $|i\rangle$  of  $\hat{H}$  in terms of the free adsorbate and surface solutions as

$$(2.40) \quad |i\rangle = c_{ai}|a\rangle + \sum_k c_{ki}|k\rangle.$$

The assumption is that the wavefunction of the whole system can be written as the linear combination of wavefunction of adsorbate  $|a\rangle$  and the surface  $|k\rangle$ , which essentially means that the Pauli repulsion is neglected. The the Schrödinger equation can be written

$$(2.41) \quad \hat{H}c_i = \varepsilon_i c_i.$$

Eq. 2.41 can be written in the vector representation as shown in the following,

$$(2.42) \quad \begin{pmatrix} \phi_a \\ \psi_1 \\ \vdots \\ \psi_k \\ \vdots \\ \psi_n \end{pmatrix} \hat{H}(\phi_a \psi_1 \cdots \psi_k \cdots \psi_n) \begin{pmatrix} c_{ai} \\ c_{1i} \\ \vdots \\ c_{ki} \\ \vdots \\ c_{ni} \end{pmatrix} = \varepsilon_i \begin{pmatrix} c_{ai} \\ c_{1i} \\ \vdots \\ c_{ki} \\ \vdots \\ c_{ni} \end{pmatrix},$$

where the matrix elements are

$$\begin{aligned}
 \langle a|\hat{H}|a\rangle &= \hat{H}_{aa} = \varepsilon_a \\
 \langle k|\hat{H}|k\rangle &= \hat{H}_{kk} = \varepsilon_k \\
 \langle a|\hat{H}|k\rangle &= \hat{H}_{ak} = V_{ak} = V_{ka}.
 \end{aligned}
 \tag{2.43}$$

This results in a determinant of the following form,

$$\begin{aligned}
 & \left| \begin{array}{cccccc}
 \hat{H}_{aa} - \varepsilon & V_{a1} & \cdots & V_{ak} & \cdots & V_{an} \\
 V_{1a} & \hat{H}_{11} - \varepsilon & \cdots & 0 & \cdots & 0 \\
 \vdots & \vdots & \ddots & \cdots & \cdots & \cdots \\
 V_{ka} & 0 & 0 & \hat{H}_{kk} - \varepsilon & \cdots & 0 \\
 \vdots & \vdots & \vdots & \vdots & \ddots & \vdots \\
 V_{na} & 0 & 0 & 0 & \cdots & \hat{H}_{nn} - \varepsilon
 \end{array} \right| = 0.
 \end{aligned}
 \tag{2.44}$$

There are infinitely many metal states and it is impossible to keep track of all of them when the coupling is switched on. It is therefore instructive to follow the projection of the density of states  $\Psi_i$  on the adsorbate state  $\phi_a$  as adsorbate approaches the surface and starts interaction with substrate states. We have

$$n_a(\varepsilon) = \sum_i |\langle i|a\rangle|^2 \delta(\varepsilon - \varepsilon_i),
 \tag{2.45}$$

where the sum is over the eigenstates of the full Hamiltonian. We can write this as the following.

$$n_a(\varepsilon) = -\frac{1}{\pi} \text{Im} \sum_i \frac{\langle a|i\rangle \langle i|a\rangle}{\varepsilon - \varepsilon_i + i\delta} = -\frac{1}{\pi} \text{Im} G_{aa}(\varepsilon),
 \tag{2.46}$$

with  $\delta = 0^+$ . The projection on the adsorbate state of the so-called single particle Green function [49] is

$$\mathbf{G}(\varepsilon) = \sum_i \frac{|i\rangle \langle i|}{\varepsilon - \varepsilon_i + i\delta},
 \tag{2.47}$$

which is defined by the function [49]

$$(2.48) \quad (\varepsilon - \mathbf{H} + i\delta)\mathbf{G}(\varepsilon) = 1.$$

The proof of Eq. 2.46 is the following. Lorentzian function

$$(2.49) \quad f(\varepsilon) = \frac{\delta}{\pi[(\varepsilon - \varepsilon_i)^2 + \delta^2]},$$

which will become a delta function for  $\delta \rightarrow 0^+$  since

$$(2.50) \quad \int_{-\infty}^{+\infty} f(\varepsilon)d\varepsilon = \int_{-\infty}^{+\infty} \frac{\delta}{\pi[(\varepsilon - \varepsilon_i)^2 + \delta^2]}d\varepsilon = 1.$$

The conversion from *delta* function to Green function is the following,

$$(2.51) \quad \begin{aligned} \lim_{\delta \rightarrow 0^+} \text{Im} \left( \frac{1}{\varepsilon - \varepsilon_i + i\delta} \right) &= \lim_{\delta \rightarrow 0^+} \text{Im} \left[ \frac{\varepsilon - \varepsilon_i}{(\varepsilon - \varepsilon_i)^2 + \delta^2} - \frac{i\delta}{(\varepsilon - \varepsilon_i)^2 + \delta^2} \right] \\ &= - \lim_{\delta \rightarrow 0^+} \frac{\pi\delta}{\pi[(\varepsilon - \varepsilon_i)^2 + \delta^2]} = -\pi\delta(\varepsilon - \varepsilon_i) \end{aligned}$$

Going back to the projected density of state on the adsorbate defined in Eq. 2.46 using one-particle green function  $G(\varepsilon)$ , we have

$$(2.52) \quad G_{aa}(\varepsilon) = \frac{1}{\varepsilon - \varepsilon_a - q(\varepsilon)},$$

where  $q(\varepsilon)$  can be written as

$$(2.53) \quad q(\varepsilon) = \Lambda(\varepsilon) - i\Delta(\varepsilon).$$

The expression for  $\Delta(\varepsilon)$  can be obtained as

$$(2.54) \quad \begin{aligned} \Delta(\varepsilon) &= - \lim_{\delta \rightarrow 0^+} \text{Im} \left( \sum_k \frac{V_{ak}^2}{(\varepsilon - \varepsilon_k + i\delta)} \right) \\ &= \pi \sum_k V_{ak}^2 \delta(\varepsilon - \varepsilon_k), \end{aligned}$$

which can be seen as the hopping matrix element between the adsorbate state and the metal state.

$\Lambda(\varepsilon)$  is basically the Kronig-Kramer transformation of  $\Delta(\varepsilon)$ , given by

$$(2.55) \quad \Lambda(\varepsilon) = \frac{1}{\pi} \int_{-\infty}^{+\infty} \frac{\Delta(x)}{x - \varepsilon} dx.$$

The projected adsorbate state is just the Imaginary part of  $G_{aa}$ , say

$$(2.56) \quad \begin{aligned} n_a(\varepsilon) &= -\frac{1}{\pi} \text{Im}(G_{aa}) = -\frac{1}{\pi} \text{Im} \left( \frac{1}{\varepsilon - \varepsilon_a - \Lambda(\varepsilon) + i\Delta(\varepsilon)} \right) \\ &= -\frac{1}{\pi} \text{Im} \left( \frac{\varepsilon - \varepsilon_a - \Lambda(\varepsilon - i\Delta(\varepsilon))}{[\varepsilon - \varepsilon_a - \Lambda(\varepsilon)]^2 + \Delta(\varepsilon)} \right) \\ &= \frac{1}{\pi} \frac{\Delta\varepsilon}{[\varepsilon - \varepsilon_a - \Lambda(\varepsilon)]^2 + \Delta(\varepsilon)^2}. \end{aligned}$$

Based on the calculated projected density of state on the adsorbate, the energy change due to the interaction between adsorbate state and metal  $d$ -states can be calculated. In next section, we are going to show some essential features of adsorbate interaction with electronic bands that could not be obtained with simple Two-Level interaction model. However, since the Pauli repulsion is not explicitly taken into account into the Hamiltonian, so the Newns-Anderson model can not be used for the system where the Pauli repulsion is dominant. We will elaborate this point further in Chapter IV.

### 2.2.3 Hammer-Nørskov $d$ -band Model

$d$ -band model can be seen as the simplification of Newns-Anderson model. The interaction of adsorbate states with metallic  $sp$  gives the resonance states. This normalized resonance state will further interact with localized  $d$ -band giving rise to bonding and anti-bonding states. The energy change due to  $sp$ -band interaction is similar for varying transition metal surfaces since they have similar broad and featureless  $sp$ -band. The further interaction with localized  $d$ -band leads to the variations in the surface reactivity.

The  $d$ -band model singles out three surface properties contributing to the ability of the surface to make and break adsorbate bonds: (i) the center of the  $d$ -bands, (ii) the degree of filling  $f_d$  of the  $d$ -bands, and (iii) the coupling matrix element  $V_{ad}$  between the adsorbate

states and the metal  $d$ -states. The effect of those physical variables is investigated thor-

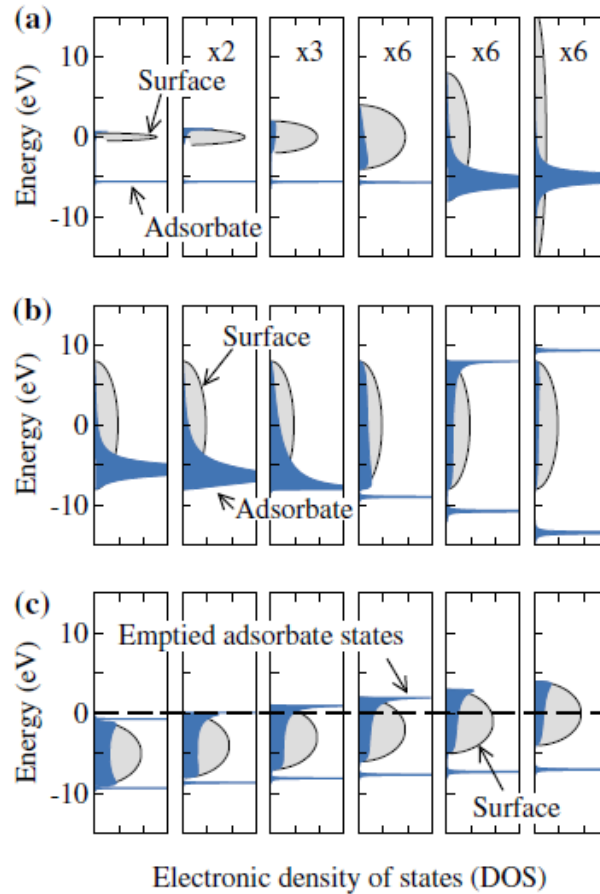


Figure 2.7: Interaction between adsorbate state with metal  $d$ -states based on the Newns-Anderson model with varying (a)  $d$ -band width (b) coupling strength (c)  $d$ -band center

oughly by using Newns-Anderson model [52] as shown in Fig. 2.7 (adapted from [52]).

From Fig. 2.7(a), we can clearly see that the adsorbate will form the resonance state by interaction with broad band, which is characteristic of the interaction with metal  $sp$ -band. In Fig. 2.7(b), the coupling strength between adsorbate state and metal band is increasing, and we can see the adsorbate state starts from single resonance to bonding and anti-bonding orbitals, which is characteristic of the interaction with metal  $d$ -band. In Fig. 2.7(c), as the  $d$ -band center is moving up, the forming anti-bonding orbital also moves up in energies and gets less occupied. That indicates that the adsorbate bonding strength to the surface would be stronger. All of the studies showing here are general conclusions from

*d*-band model, and it has significantly increased our general understanding of the surface interactions.

## CHAPTER III

# The General Theoretical Framework for Understanding Variations in the Surface Reactivity of Transition Metals

### 3.1 Introduction

Most heterogeneous catalysts of industrial importance are multicomponent materials that were discovered through experimental trial and error approaches [53]. Nowadays, electronic structure theory has been developed into the stage that it can be used to predict the energetics and reaction pathways of elementary chemical transformations on metal surfaces with reasonable accuracy. Density functional theory (DFT) calculations and kinetic modeling approaches, have shown that catalytic materials with atomically tailored structures and improved catalytic performance confirmed by experimental measurement can be designed from first-principles [8–17]. However, the immense phase space of possible formulations of catalytic materials precludes thorough screening [54], even with combinatorial high-throughput experiments or quantum-chemical calculations. The critical objective of fundamental research in heterogeneous catalysis is the development of predictive theories for rational design of efficient catalysts. The formulation of predictive theories will require the development of simple, physically transparent, yet sufficiently accurate models that would inform us about the underlying physical factors governing variations in the local chemical reactivity of catalytic sites.

Ever since the early development of density functional theory by Hohenberg-Kohn [43]

and later Kohn-Sham [45], there have been great efforts pursuing simple methods for predicting the energetics of elementary chemical transformations on solid surfaces, e.g., the adsorption of simple molecules. News [51, 55] first studied the surface chemisorption of simple molecules on metal surfaces using Anderson's [50] approach originally developed for understanding the occurrence of localized magnetic moments in metals with impurities. In this method, the phenomenon of surface chemisorption is described based on the coupling between adsorbate valence orbitals with the electronic band of the substrate within the Tight-Binding Approximation [56–58]. Varma and Wilson [59, 60] derived a simple model which can relate the binding energies of atoms (e.g., hydrogen and oxygen) on transition metal surfaces to the local electronic structure of catalytic sites, e.g., the average position of the  $d$ -states with respect to the adatom valence orbital energy and the overall width of the  $d$ -band. Almost simultaneously, Effective Medium Theory [61] has been developed to understand the chemisorption of simple molecules on metal surfaces by evaluating the embedding energy of simple adsorbates on a homogeneous electron gas. The covalent interaction between adsorbate valence states and metal  $d$ -states can be included as a perturbation to the embedding energy with a homogeneous electron gas [62]. This simple picture of surface chemisorption has been widely used for the general understanding of the surface reactivity of transition metals, and it has been guiding us to design better catalysts since then [63].

In this Chapter, we have employed the fundamental formalism of density functional theory (DFT) to develop a general theoretical framework allowing us to identify the underlying mechanisms that govern variations in the surface reactivity of transition metals upon the perturbation of electronic properties. This general and unifying theoretical framework has been the guiding principle for us to understand the fundamental mechanisms associated with variations in the surface reactivity of transition metals due to alloying with

impurity elements (Chapter IV), doping of substrates with chemical promoters (Chapter V), and imposing stimuli for electronic excitations (Chapter VI).

### 3.2 Detailed Derivation of the General Theoretical Framework

The intrinsic surface reactivity of catalytic materials is governed by their electronic properties [63]. Any perturbation of local electronic properties of the substrate would give rise to variations in the surface reactivity. Regardless of the underlying physics of perturbations introduced to the system, it is desirable to develop a general theoretical framework for describing variations in the surface reactivity due to the perturbation of surface electronic properties.

In this derivation, we have mainly employed the fundamental formalism of density-functional theory [43, 45, 64]. Similar methods have been used previously for energy-partitioning analysis of interacting atoms in molecules [44]. In this dissertation, we have extended this method for understanding of the stability of adsorbates on metal surfaces with arbitrary perturbation potential. The final expression we have derived in the following is very similar to the previous work by Nørskov et al. using Effective Medium Theory with frozen density and frozen potential approximations [65–67]. The mathematical expression obtained in this dissertation is very general since we did not restrict ourselves to the specific form of perturbation potential.

Starting from the basic DFT expression, the adsorption energy change of adsorbate A due to the perturbation ( $M \rightarrow \tilde{M}$ ) of electronic properties of the substrate can be illustrated in Fig. 3.1.  $\Delta\Delta E$  is defined as variations in the binding energy of adsorbate A due to the perturbation of the substrate from  $M$  to  $\tilde{M}$ .  $\rho$  (including electron and nucleus charge) and  $v$  are the charge density and electrostatic potential of the unperturbed electronic system, respectively. The variable with tilde represents the system with perturbations.

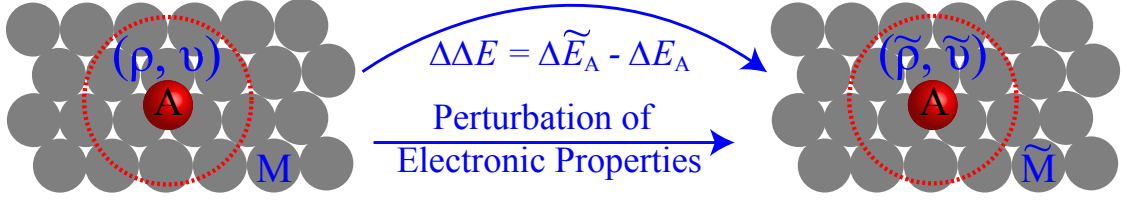


Figure 3.1: Variations in the binding energy of adsorbate A due to the perturbation of electronic properties of the substrate from  $M$  to  $\tilde{M}$

$$\begin{aligned}
 \Delta\Delta E &= \Delta\tilde{E}_A - \Delta E_A \\
 &= (E_{A/\tilde{M}} - E_{\tilde{M}} - E_A) - (E_{A/M} - E_M - E_A) \\
 (3.1) \quad &= (E_{A/\tilde{M}} - E_{A/M}) - (E_{\tilde{M}} - E_M)
 \end{aligned}$$

From Hohenberg-Kohn theorems [43, 64] and Kohn-Sham equations [45], the ground-state energy of the electronic system can be written as the functional of the ground-state electron density,  $n$ , as shown in

$$\begin{aligned}
 (3.2) \quad E &= \sum_i^{occ} \varepsilon_i[n] - \int n v_{eff} d\mathbf{r} + \int n v_{ext} d\mathbf{r} \\
 &+ \frac{1}{2} \iint \frac{n(\mathbf{r})n(\mathbf{r}')}{|\mathbf{r} - \mathbf{r}'|} d\mathbf{r}d\mathbf{r}' + E_{xc}[n] + E_{nn},
 \end{aligned}$$

where  $\varepsilon_i$  is the one-electron energies calculated for non-interacting electron gas moving in the effective potential  $v_{eff}$ . The only connection of this fictitious system with the real world counterpart is that they share the same electron density,  $n$ .  $v_{ext}$  is the external potential imposed by core electrons and nucleus (usually expressed as pseudopotentials [68]).  $E_{xc}$  is the exchange-correlation energy describing the dynamic interaction of moving electrons and everything else not taken into account by the Hamiltonian [44].  $E_{nn}$  is the energy associated with the repulsion between the ionic cores. The energy expression in Eq. 3.2 is also known as Harris functional [69]. If the ground-state electron density,  $n$ , for a given system is inserted in Eq. 3.2, the ground-state energy and all the electronic properties of the system can be determined. According to the variational principle, small variations in

the electron density (away from the ground-state density) lead to only a second order error in energies [49]. It has been demonstrated previously that an acceptable choice for the density is to assume that the region (in Fig. 3.1) close to A has a frozen density corresponding to only A adsorbed on the surface. This approach was utilized previously by Nørskov et al. [62] to obtain a meaningful and physically transparent expression for the adsorbate-adsorbate interaction energy in terms of electron densities and potentials calculated independently for each adsorbate on the surface.

Rather than assuming frozen density and potential, we have taken a slightly different approach. The adsorption energy change of adsorbate A in Eq. 3.1 due to the perturbation of electronic properties of the substrate ( $M \rightarrow \tilde{M}$ ) can be simplified as

$$(3.3) \quad \Delta\Delta E = \Delta E_{A/M}[N_{A/M}, \Delta v'] - \Delta E_M[N_M, \Delta v],$$

where we replace the perturbed surface by the clean surface with the corresponding perturbation of external potential,  $\Delta v'(\mathbf{r})$  and  $\Delta v(\mathbf{r})$ , denoted as dynamic perturbation potential (including the effect of coadsorbed adsorbate A) and static perturbation potential, respectively. This transformation is ground on the Hohenberg-Kohn theorem I [43].

In Eq. 3.3,  $N_{A/M}$  and  $N_M$  are the number of electrons of the system A/M and M, respectively.  $\Delta E_{A/M}[N_{A/M}, \Delta v']$  is the total energy change of the system A/M due to the dynamic perturbation potential,  $\Delta v'(\mathbf{r})$ , and  $\Delta E_M[N_M, \Delta v]$  is the total energy change of the system A/M due to the static perturbation potential,  $\Delta v(\mathbf{r})$ . Static perturbation potential,  $\Delta v$ , defined as

$$(3.4) \quad \Delta v(\mathbf{r}) = v_{\tilde{M}} - v_M,$$

is directly imposed by external perturbations in the absence of adsorbate A. Dynamic perturbation potential,  $\Delta v'$ , defined in

$$(3.5) \quad \Delta v'(\mathbf{r}) \approx \Delta v(\mathbf{r}) + \int \left[ \frac{\delta \Delta v_{\tilde{M}}}{\delta \Delta \rho_{\tilde{M}}(\mathbf{r}')} \right]_N \Delta \rho_A(\mathbf{r}') d\mathbf{r}',$$

has included the effect of adsorbate A on the external perturbation based on the linear response function.

In Eq. 3.5  $\Delta\rho_A$  is adsorbate A induced charge density difference which has included electrons and nucleus, is defined as

$$(3.6) \quad \Delta\rho_A = \rho_{A/M} - \rho_M.$$

The dynamic perturbation potential,  $\Delta v'(\mathbf{r})$ , can be replaced by the static perturbation potential,  $\Delta v(\mathbf{r})$ , with the ignorance of adsorbate A induced polarization energy on  $\tilde{M}$  system [44] temporarily as

$$(3.7) \quad \Delta\Delta E = \Delta E_{A/M}[N_{A/M}, \Delta v] - \Delta E_M[N_M, \Delta v].$$

For special cases where the adsorbate A induced polarization energy of external perturbation sources is not negligible, e.g., adsorbate-adsorbate interactions on metal surfaces, we can easily include it with second order perturbation theory.

The interaction energy  $\Delta\Delta E$  can be separated into electronic and nucleus-nucleus repulsion terms as

$$(3.8) \quad \begin{aligned} \Delta\Delta E = & \Delta E_{A/M}^e[N_{A/M}, \Delta v] - \Delta E_M^e[N_M, \Delta v] \\ & + \Delta V_{A/M}^n[Z_{A/M}, \Delta v] - \Delta V_M^n[Z_M, \Delta v], \end{aligned}$$

where  $Z$  is the nuclear charge distribution of the corresponding system,  $\Delta E^e$  and  $\Delta V^n$  are the change of the electronic energy and nucleus-nucleus repulsion energy due to the perturbation of external potential,  $\Delta v(\mathbf{r})$ , respectively. The interaction of the nucleus of substrates with the perturbation of external potential  $\Delta v(\mathbf{r})$  is cancelled in Eq. (3.8) resulting in

$$(3.9) \quad \begin{aligned} \Delta\Delta E = & \Delta E_{A/M}^e[N_{A/M}, \Delta v] - \Delta E_M^e[N_M, \Delta v] \\ & + \Delta V_A^n[Z_A, \Delta v]. \end{aligned}$$

The total energy change of free adsorbate  $A$  with the perturbation of external potential  $\Delta v(\mathbf{r})$ , for simplicity denoted as  $\Delta E_A[N_A, \Delta v]$ , can be expressed as [44]

$$\begin{aligned}
 \Delta E_A[N_A, \Delta v] &= \Delta V_A^n[Z_A, \Delta v] + \Delta E_A^e[N_A, \Delta v] \\
 &= \Delta \sum_i \varepsilon_A^i[\Delta v] + \int^A \rho_A \Delta v d\mathbf{r} \\
 &\quad + \iint \left[ \frac{\delta \rho_A(\mathbf{r})}{\delta \Delta v(\mathbf{r}')} \right]_N \Delta v(\mathbf{r}') \Delta v(\mathbf{r}) d\mathbf{r}' d\mathbf{r},
 \end{aligned}
 \tag{3.10}$$

which includes the energy change [44] of free adsorbate  $A$  due to the one electron energy change, the interaction of external potential  $\Delta v(\mathbf{r})$  with static dipole moment of  $A$ , and the relaxation of charge density  $\rho_A$ . Combining Eq. (3.9) and Eq. (3.10), it yields

$$\begin{aligned}
 \Delta \Delta E - \Delta E_A &= \Delta E_{A/M}^e[N_{A/M}, \Delta v] - \Delta E_M^e[N_M, \Delta v] \\
 &\quad - \Delta E_A^e[N_A, \Delta v].
 \end{aligned}
 \tag{3.11}$$

For simplicity, the terms on left can be denoted as  $\Delta \Delta E'$  temporarily as

$$\Delta \Delta E' = \Delta \Delta E - \Delta E_A.
 \tag{3.12}$$

The total differential interaction energy,  $\Delta \Delta E'$ , will be

$$d(\Delta \Delta E') = \sum_i \left[ \frac{\partial(\Delta \Delta E')}{\partial N_i} \right]_{N_j(j \neq i), \Delta v} dN + \int \left[ \frac{\delta(\Delta \Delta E')}{\delta \Delta v(\mathbf{r})} \right]_N d\Delta v(\mathbf{r}) d\mathbf{r},
 \tag{3.13}$$

where  $i$  represents  $A/M$ ,  $M$  and  $A$ .

From Janak Theorem [70], we can get

$$\left[ \frac{\partial(\Delta \Delta E')}{\partial N_i} \right]_{N_j(j \neq i), \Delta v} = \xi_i \left[ \frac{\partial \Delta E_i^e[N_i, \Delta v]}{\partial N_i} \right]_{\Delta v} = \xi_i \Delta \varepsilon_i^{N_i}[\Delta v],
 \tag{3.14}$$

where  $\Delta \varepsilon_i^{N_i}[\Delta v]$  is the energy change of Kohn-Sham orbital for system  $i$  under the perturbation of external potential  $\Delta v(\mathbf{r})$ .  $\xi_i$  is the coefficient for system  $i$ , which is  $+1$  for  $A/M$ ,  $-1$  for  $M$  and  $A$ .

Based on the standard first-order perturbation theory [44], we have

$$(3.15) \quad \begin{aligned} \left[ \frac{\delta(\Delta\Delta E')}{\delta\Delta v} \right]_N &= \left[ \frac{\delta\Delta E_{A/M}^e}{\delta\Delta v} \right]_N - \left[ \frac{\delta\Delta E_M^e}{\delta\Delta v} \right]_N - \left[ \frac{\delta\Delta E_A^e}{\delta\Delta v} \right]_N \\ &= \tilde{n}_{A/M} - \tilde{n}_M - \tilde{n}_A = \Delta n_A''[\Delta v], \end{aligned}$$

where  $\tilde{n}_i$  is the electron density distribution of system  $i$  under the perturbation of external potential  $\Delta v(\mathbf{r})$  and  $\Delta n_A''$  is adsorbate  $A$  induced total electron density difference for the perturbed system.

Eq. (3.13) can be simplified as

$$(3.16) \quad d(\Delta\Delta E') = \sum_i \xi_i \Delta \varepsilon_i^N[\Delta v] dN + \int \Delta n_A''[\Delta v] d\Delta v(\mathbf{r}) d\mathbf{r}.$$

Integrating Eq. (3.16) and combining with Eq. 3.12, it yields

$$(3.17) \quad \Delta\Delta E = \sum_i \xi_i \int_0^{N_i} \Delta \varepsilon_i^N[\Delta v] dN + \int \Delta n_A''[\Delta v] \Delta v(\mathbf{r}) d\mathbf{r} + \Delta E_A[N_A, \Delta v].$$

The integral  $\int_0^{N_i} \Delta \varepsilon_i^N[\Delta v] dN$  can be taken as the sum

$$(3.18) \quad \int_0^{N_i} \Delta \varepsilon_i^N[\Delta v] dN = \sum_{N=1}^{N_i} \Delta \varepsilon_i^N[\Delta v].$$

Using the first order Taylor expansions,  $\Delta n_A''[\Delta v]$  can be written as

$$(3.19) \quad \Delta n_A''[\Delta v] \approx \Delta n_A^t(\mathbf{r}) + \int \left[ \frac{\delta \Delta n_A^t(\mathbf{r})}{\delta \Delta v(\mathbf{r}') } \right]_N \Delta v(\mathbf{r}') d\mathbf{r}',$$

where the adsorbate  $A$  induced total electron density difference  $\Delta n_A^t(\mathbf{r})$  for unperturbed systems is defined as

$$(3.20) \quad \Delta n_A^t(\mathbf{r}) = n_{A/M} - n_M - n_A.$$

Insert the expression for  $\Delta n_A''[\Delta v]$  from Eq. 3.19 and  $\Delta v(\mathbf{r})$  from Eq. 3.5, into Eq. 3.17, we can get

$$(3.21) \quad \Delta\Delta E = \sum_i \xi_i \sum_{N=1}^{N_i} \Delta \varepsilon_i^N[\Delta v] + \int^A \Delta \rho_A^t(\mathbf{r}) \Delta v(\mathbf{r}) d\mathbf{r} + \Delta E_A[N_A, \Delta v].$$

Insert the expression of  $\Delta E_A[N_A, \Delta v]$  defined in Eq. 3.10 into Eq. 3.21, we can get the final expression of the model as

$$(3.22) \quad \begin{aligned} \Delta \Delta E = & \delta \sum_{N=1}^{N_i} \Delta \varepsilon_i^N[\Delta v] + \int^A \Delta \rho_A(\mathbf{r}) \Delta v(\mathbf{r}) d\mathbf{r} \\ & + \iint \left[ \frac{\delta \Delta \rho_A}{\delta \Delta v(\mathbf{r}')} \right]_N \Delta v(\mathbf{r}') \Delta v(\mathbf{r}) d\mathbf{r}' d\mathbf{r}, \end{aligned}$$

where  $\delta$  is due to the existence of adsorbate A. We note that the adsorbate A induced charge polarization effect on the external perturbation sources is ignored for simplicity and generality of the expression of Eq. 3.22. For special cases where the polarization energy due to the adsorbate A is not negligible, additional expression similar to the last term in Eq. 3.22 should be included.

### 3.3 Physical Interpretation and Computational Evaluation of Contributing Terms

The general theoretical framework (Eq. 3.22) we have developed based on the basic DFT formalism allows us to probe the fundamental mechanism of variations in the surface reactivity of transition metals with any perturbation. The advantage of this theoretical framework is that every term can be evaluated independently, so we can use it to identify the underlying physical factors governing the trend of surface reactivity.

#### 3.3.1 Electronic Orbital Interaction

The first term in Eq. 3.22 represents the electronic contribution related to the change in one-electron orbital energies of A/M and M due to change of surface electronic properties via surface-mediated or through-space electronic communication. This mechanism of interactions accounts for the covalent charge sharing due to the creation of bonding and anti-bonding states, or the Pauli repulsion due to the charge density overlap. The Newns-Anderson model [55] as illustrated in Fig. 3.2 provides a simple way for estimating the one-electron energy change due to the interaction between the adsorbate state and con-

tinuous band of substrate states. In this model, the interaction between adsorbate valence orbitals with the metal surfaces can be separated into two steps. We can imagine including interaction of valence orbitals of adsorbates with the broad  $sp$ -band of the substrate first, and then switching on the coupling to localized  $d$ -states as illustrated in Fig. 3.2.

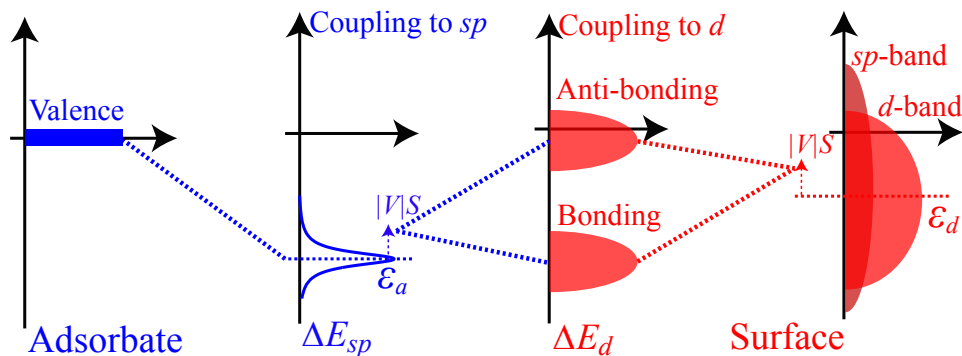


Figure 3.2: Schematic illustration of electronic orbital interaction

Within Newns-Anderson's theoretical framework, one electron energies change upon perturbation can be deduced from the density of states projected on adsorbate orbitals, which characterize the distribution of electron energies. I am going to show in this dissertation that the electronic contribution can be directly obtained and used to understand the fundamental mechanism of the surface reactivity of transition metals with varying perturbation potentials.

### 3.3.2 Dipole-dipole Interaction

The second term in Eq. 3.22 represents the electrostatic effect, which is basically the static dipole-dipole interaction as illustrated in Fig. 3.3. The electrostatic contribution can be calculated numerically from A induced charge density difference  $\Delta\rho_A$  and the perturbation potential  $\Delta v$  obtained from DFT calculations.

The adsorbate A induced charge density difference is defined in Eq. 3.6, which includes the electron density and nucleus point charge. Assuming that there is no dramatic geometric change of the substrate induced by surface adsorption of A, the nucleus point charge of

the substrate can be cancelled directly. So the  $\Delta\rho_A$  can be evaluated directly according to

$$(3.23) \quad \Delta\rho_A = n_{A/M} - n_M + Q_A,$$

where  $Q_A$  is the nucleus point charge distribution of adsorbate A.

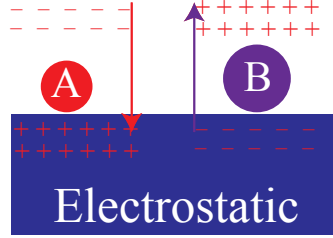


Figure 3.3: Schematic illustration of dipole-dipole interaction

The evaluation of electrostatic contribution has to be restricted to the local region of adsorbate A. However, there is no clear region boundaries of surface adsorbates. Ideally, the integral can be obtained by gradually increasing the integration volume around the adsorbate until approaching the local point with zero gradient. The concept is similar to the charge separation scheme employed in Bader charge analysis [71]. This difficulty associated with the region separation can be circumvented by the integration over the whole unit cell of DFT calculations. The direct integral can be divided by 2 to avoid the double count. Using this simplified method, it is critical to correct the potential in the core-region of adsorbates, i.e., replacing the pseudopotential within the cutoff radius with the ionic potential  $-Z/r$ . For example, if the perturbation potential is induced by the coadsorption of another adsorbate B, the electrostatic contribution defined in Eq. 3.22 should be equal as we switch the adsorbate A and B, so we have

$$(3.24) \quad \Delta\Delta E_{es} = \int^A \Delta\rho_A(\mathbf{r}) \Delta v_B(\mathbf{r}) = \int^B \Delta\rho_B(\mathbf{r}) \Delta v_A(\mathbf{r}).$$

### 3.3.3 Dipole-induced-dipole Interaction

The last term in Eq. 3.22 represents the polarization contribution, which is essentially the interaction between the induced dipole moment of adsorbate A on the surface and the electric field induced by the perturbation potential on the surface as illustrated in Fig. 3.4. For example, as a surface electric dipole of A/M experiences an electric field induced by a perturbation potential, its charge distribution will relax in response to the external electric field to reach the new ground-state. The energy associated with this relaxation is known as the polarization energy. Adsorbates with large polarizability are affected significantly via this mechanism.

The polarization contribution can be easily evaluated by imposing a homogeneous artificial electric field to the electronic system. The strength of the electric field can be obtained from the perturbation induced electrostatic potential on clean surfaces as

$$(3.25) \quad \varepsilon = \left. \frac{\partial(v_{\tilde{M}} - v_M)}{\partial z} \right|_{xy}.$$

Typically the electric field on the position where the adsorbate stays is used. With a small perturbation due to the external electric field, the one-electron energies do not change with respect to the Fermi level, so the electronic effect can be isolated from the electrostatic and polarization. The energy change due to an artificial homogeneous electric field consists of the first order electrostatic effect, and the polarization. The electrostatic effect can usually be estimated as the Stark effect based on

$$(3.26) \quad \Delta\Delta E_{es}^{\Delta v} = -\varepsilon \cdot \Delta\mu_A,$$

where  $\mu_A$  is the electric dipole moment of A/M, and  $\Delta v$  represents external perturbation potential.

So the polarization contribution can be obtained by subtracting the electrostatic contri-

bution from the adsorption energy change due to the perturbation electric field as

$$(3.27) \quad \Delta\Delta E_{pe}^{\Delta v} = \Delta\Delta E_A^{\Delta v} - \Delta\Delta E_{es}^{\Delta v}.$$

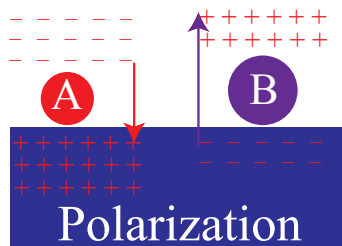


Figure 3.4: Schematic illustration of dipole-induced-dipole interaction

### 3.4 Various Forms of Perturbation

The electronic properties of metal surfaces can be tailored with various methods as shown in Fig. 3.5, such as alloying with impurity elements, doping of surface promoters or poisons, or imposing multiple stimuli for vibrational excitations. All of these methods have been employed previously to go beyond the intrinsic electronic structure of transition metals for desired catalytic properties. The general theoretical framework developed in this Chapter provides the fundamental basis for the understanding of variations in the surface reactivity of transition metals due to various forms of perturbations. To rationally tune the electronic properties of transition metals for enhancing the catalytic performance, we need to understand how those perturbations change the electronic properties of metal surfaces and how that affects the surface chemical reactivity in terms of adsorption and activation of atoms or simple molecules. In this Section, we are going to briefly introduce these three types of perturbations as illustrated in Fig. 3.5. Each of them will be the focal point of the following chapters.

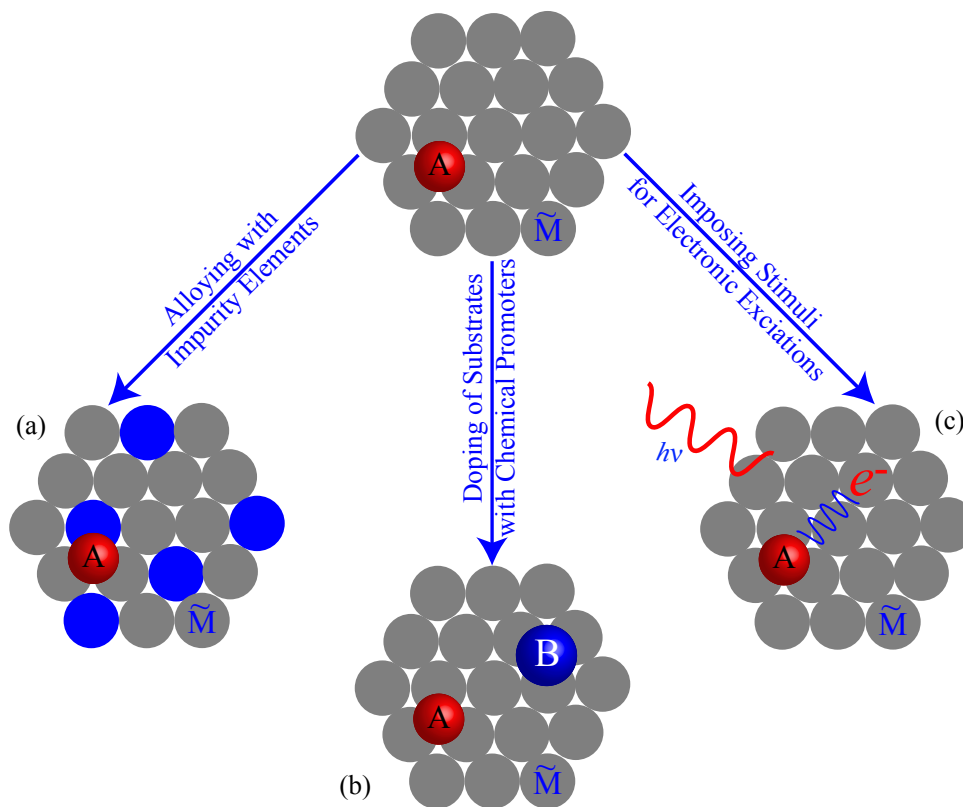


Figure 3.5: Perturbations of electronic properties of transition metal surfaces due to (a) alloying with impurity elements, (b) doping of substrates with chemical promoters, (c) imposing stimuli for electronic excitations

### 3.4.1 Alloying with Impurity Elements

Alloys, or generally intermetallics, are multicomponent materials with impurity elements embedded near the surface or in the bulk of the host metal as illustrated in Fig. 3.5(a).

The surface geometry and composition of forming alloys are governed by the segregation energy of constituent elements and the gas phase environment [72]. The electronic properties of host metal sites on alloy surfaces can be perturbed either due to the change of geometric structure, such as strain, stress or metal-metal coordination number, or due to the variation of metal ligands. Previously, both geometric and ligand effects have been studied experimentally and theoretically for the understanding of the fundamental mechanism governing the variations in the surface reactivity compared to host metals. It has been

realized that the arrangement of metal elements with atomic level precision in alloys has distinctive and decisive effect on the surface catalytic properties. Nowadays, the synthetic community has developed various types of advanced techniques in controlling the atomic arrangement of metal elements precisely, such as the solution-based polyol method, under-potential deposition method, atomic layer deposition and many others. Rational design of alloy catalysts to perform desired chemical transformation with utmost efficiency is really limited by our imagination of novel geometric structures and atomic compositions, and the capability to probe the phase space of alloy materials thoroughly with a highly-efficient modeling scheme.

In Chapter IV, we are going to develop a physically transparent model that allows us to relate easily accessible physical characteristics of the elements that form an alloy (mainly their electronegativity, atomic radius, and the spatial extent of valence orbitals) to the catalytic performance of alloy sites, and a rapid screening scheme allowing us to probe the phase space of alloy materials thoroughly without performing expensive DFT calculations.

### **3.4.2 Doping of Substrates with Chemical Promoters**

Doping of surface promoters or poisons on transition metals as illustrated in Fig. 3.5(b) provides a simple and elegant way of tuning the surface electronic properties. Additives that are often used in the design of heterogeneous catalysts are alkali metal elements, such as sodium (Na), potassium (K) and cesium (Cs). It has been demonstrated that alkali promoters can greatly increase the reactivity and/or selectivity for many reactions, such as ammonia synthesis [73], Fisher-Tropsch synthesis [74], alcohol synthesis [75], water-gas shift reactions [76], olefin epoxidation [77], and automotive three-way catalytic converters [78].

Despite the wide application of alkali promoters in heterogeneous catalysis, there is still no general agreement on the underlying mechanism of the promotion effect [79, 80].

Traditionally, adsorbate-adsorbate interactions have been grouped into two categories: direct and indirect interactions [79, 80]. Direct interactions can be further divided into the electrostatic interaction of charge distributions, the covalent bond formation due to orbital hybridization, and the Pauli repulsion resulting from orbital orthogonalization. Indirect interactions are characterized by adsorbate-induced electronic or structural modifications of metal surfaces. Complex interplay among different types of interactions makes the identification of the dominant mode of adsorbate-adsorbate interactions very difficult. As a result, all of the mechanisms mentioned above have been implied as crucial for the alkali promotion effect in heterogeneous catalysis [81–86].

In Chapter V, we are going to illustrate that the theoretical framework we have developed can shine light on the fundamental mechanism of alkali promotion in heterogeneous catalysis. Critical concerns about the so-called “pressure and material gap” have been investigated using various theoretical techniques to extend the insight from DFT calculations to catalytically relevant conditions.

### 3.4.3 Imposing Stimuli for Electronic Excitations

Chemical reactions on solid surfaces are typically driven by phonons, i.e., the coupling of adsorbates vibrational degree of freedom (the reaction coordinate) with the infinite heat bath of the substrate. The intrinsic thermal activation barrier separating reaction intermediates can only be surmounted if adsorbates gain enough energy from vibrational excitations. Identical chemical transformations with similar reaction pathways can proceed via the coupling of adsorbates with the other excitation source, such as photons as shown in Fig. 3.5(c).

The catalytic material I am going to focus in Chapter VI is plasmonic metal surfaces for oxidation reactions. By coupling to multiple excitation sources, e.g., thermal energy and photonic energy, we can perform desired chemical transformations more efficiently

than pure phonon-driven process. The hot electron induced surface chemistry can also be described within the general theoretical framework we have developed in this Chapter.

### **3.5 Summary**

Starting from the fundamental formalism of density functional theory (DFT), we have developed a general theoretical framework for the analysis of variations in the surface reactivity due to perturbed electronic properties of transition metals. In this theoretical framework, the variations in surface reactivity can be attributed to one-electron energies, electrostatic and polarization contributions. The physical mechanism and numerical evaluations of each contribution has been illustrated. The perturbation potential in this theoretical framework can be induced by alloying of impurity elements, doping of substrates with chemical promoters or imposing stimuli for electronic excitations. In this dissertation, we are going to elaborate all those three kinds of perturbation potential and understand the variations in surface reactivity due to the perturbation using the theoretical framework proposed in this Chapter.

## CHAPTER IV

### Alloying with Impurity Elements

#### 4.1 Introduction

Alloys, or in general intermetallic compounds, represent a rich family of materials that allows us to make a broad range of structures with interesting surface properties [87]. There are numerous examples showing that alloys can exhibit dramatically improved catalytic performance compared to the pure host metal [9, 14, 88–94]. Electronic communication between the constituent metal elements in alloys results in unique active sites that can perform desired chemical transformations efficiently. The improved catalytic performance of those alloy materials has been attributed to the modification of local electronic properties and so the thermodynamic stability of critical reaction intermediates on geometrically identical host metal sites [95–97]. While the potential for the utilization of alloys in heterogeneous catalysis is significant, predictive models relating the geometric structure of alloys to their chemical reactivity are lacking, and desirable alloy catalysts were typically identified through trial-and-error experimental approaches or high-throughput computational screening [6, 8, 9, 13, 14, 54, 90, 98].

In this Chapter we are going to elaborate underlying mechanisms that govern variations in the surface reactivity of host metal sites in response to the perturbation of electronic properties by forming alloys. The ultimate objective was to develop a physically transpar-

ent model that relates easily accessible physical characteristics of the constituent metal elements to the catalytic performance of alloy sites. Compared to previously developed computational searching methods based on electronic descriptors [6, 8, 9, 13, 14, 54, 90, 98], this model permits rapid screening through an enormous phase space of alloy structures and compositions using analytical expressions rather than expensive quantum-chemical calculations. The accuracy and applicability of the model was validated by using DFT calculations and experimental measurement reported in literature.

## 4.2 Relating the Geometric Structure of Alloys to Their Electronic Properties

The ultimate objective in heterogeneous catalysis is to develop predictive structure-performance relationships that would guide the discovery and design of catalytic materials for desired chemical transformations. To fulfil this goal, it is critical to identify the physical characteristics of a catalyst material that affect its chemical reactivity and catalytic performance. Hammer and Nørskov provided a simple model which predicts the trend of the chemical reactivity of metallic surfaces using one intrinsic property of the catalytic site, the  $d$ -band center (the average energy of the  $d$ -band) [63]. Many theoretical and experimental studies have supported the proposed  $d$ -band model [99]. The model is very useful since for pure monometallic catalysts it has a predictive capacity, i.e., the position of the center of  $d$ -band of pure metals can be easily predicted and therefore their chemical and catalytic behavior can be anticipated.

While simple relationships between the center of  $d$ -band and the chemical reactivity also apply for alloys, the application of these relationships for alloy systems is inherently limited since there are no available predictive theories informing us about the shifts in the position of  $d$ -band center in response to the formation of alloys.

In this Section, we propose a model, developed based on X-ray absorption spectroscopy

(XAS) measurements and density functional theory (DFT) calculations, allowing us to predict the impact of alloying on the electronic structure of different sites in alloys and on their local chemical reactivity. The advantage of the proposed model is that the chemical reactivity of various sites in complex alloy materials can be predicted based only on properties of the constituent metal elements. The proposed model has the great potential to assist in rapid screening and identification of optimum alloy materials for different catalytic reactions.

#### **4.2.1 Experimental Details**

##### **4.2.1.1 Synthesis of Alloy Materials**

The catalysts were synthesized using a dry impregnation technique.  $\gamma$ - $\text{Al}_2\text{O}_3$  powder from Alpha Aesar (3 micron, BET S.A.  $78 \text{ m}^2/\text{g}$ , 99.97% metal basis) was used as the support for small particles of pure Pt or Pt alloys. To remove impurities from the support, the powder was first stirred in deionized water. Ammonium hydroxide was then added to the solution until the pH reached 10. The powder was then rinsed several times with deionized water, dried under vacuum overnight, and calcined in air at 773 K for 3 hrs.

A 10% Pt/ $\text{Al}_2\text{O}_3$  sample was prepared by dissolving appropriate amount of  $\text{H}_2\text{PtCl}_6 \cdot 6\text{H}_2\text{O}$  (99.95% metals basis, Alpha Aesar) in just enough volume of water to fill the micro pore structure of the  $\text{Al}_2\text{O}_3$  support, as measured by BET analysis ( $0.366 \text{ mL/g}$ ). The solution was then added dropwise to the  $\text{Al}_2\text{O}_3$  support. To ensure even coverage of the solution on the support, the powder was shaken vigorously throughout the addition of the solution, and the powder was crushed with a mortar and pestle. To synthesize the alloy catalysts, an impregnation solution consisting of half the water and half the  $\text{H}_2\text{PtCl}_6 \cdot 6\text{H}_2\text{O}$  for the 10% Pt/ $\text{Al}_2\text{O}_3$  catalyst was prepared (this corresponds to a 5% Pt/ $\text{Al}_2\text{O}_3$  mixture). Another impregnation solution was made containing the same amount of water and enough of the appropriate alloy metal salt ( $\text{CuCl}_2$ ,  $\text{RuCl}_3$ , or  $\text{SnCl}_2$ ) for a Pt/M molar ratio of one.

The Pt and alloy metal solutions were then dispersed on the Al<sub>2</sub>O<sub>3</sub> support sequentially, as described above. All samples were then dried overnight under vacuum, and reduced in hydrogen (Cryogenic gases, pre-purified, 200 mL/min) at 573 K for 3 hrs.

The PtCu<sub>3</sub> alloy was synthesized using a colloidal, ion exchange method performed at room temperature. 0.1g of Cu(NO<sub>3</sub>)<sub>2</sub> was dissolved in ethylene glycol in a round bottom flask. The flask was sealed with a septum, vented, stirred with a stir bar, and purged with Ar gas. Ar gas was used to purge the vessel throughout the entire synthesis process. Next, just enough aqueous solution of 1.8 M NaOH/ 0.5 M NaBH<sub>4</sub> was added to the Cu solution until the solution turned a deep red/brown. This step forms a Cu colloid. After resting for an hour, an ethylene glycol solution of H<sub>2</sub>PtCl<sub>6</sub> was added to the copper colloid solution (enough Pt precursor for a 3:1 Cu:Pt molar ratio). In this step, the metallic copper in solution reduces the Pt precursor solution, depositing Pt on the Cu colloid particles, turning the solution black. After letting the solution stir for 1 hr, the final colloid solution was then centrifuged and washed several times with isopropyl alcohol to remove residual sodium. The pure colloid solutions were then mixed with the Al<sub>2</sub>O<sub>3</sub> powder and dried in a heated sonicator ( 60 °C) until all the solvent had evaporated.

#### **4.2.1.2 X-ray Absorption Spectroscopy Measurement**

X-ray absorption spectroscopy (XAS) studies were performed at Argonne National Laboratory Advanced Photo Source (APS) beamline MR-CAT 10-ID-B. Scans of the Pt L<sub>3</sub>-edge (~11564 eV) were collected in transmission mode using Ar ion chambers for detection. Data was simultaneously recorded for Pt foil as the reference for energy calibration. The pure Pt and Pt alloy samples were packed into wafers supported in a steel sample tube, which could accommodate six separate samples. The steel sample holder was then placed in a glass in-situ reactor. The samples were re-reduced in 4% H<sub>2</sub>/N<sub>2</sub> at 573 K for 1 hrs. The samples were then flushed in N<sub>2</sub> at 573 K to remove any residual

hydrogen. Scans were performed at room temperature in nitrogen.

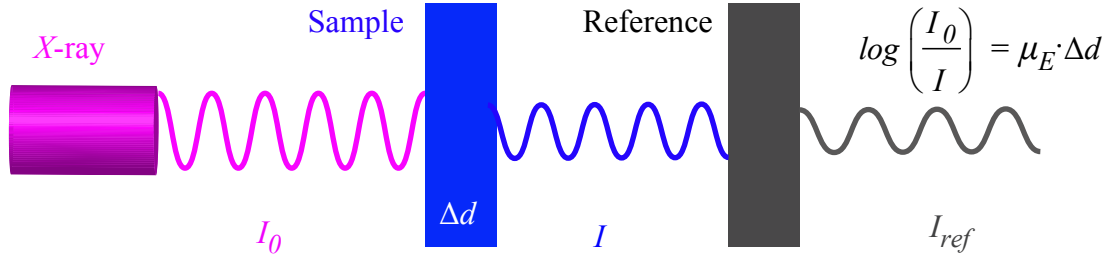


Figure 4.1: Schematic illustration of x-ray absorption spectroscopy technique

Fig. 4.1 shows the general scheme of the XAS setup. When a monochromatic beam of X-rays with energy  $E$  and intensity  $I_0$  passes through a sample of thickness  $\Delta d$ , the transmitted intensity is given by Lamber-Beer Law

$$(4.1) \quad I = I_0 e^{-\mu_E \cdot \Delta d},$$

where  $\mu_E$  is the absorption coefficient of the material at incident X-ray energy  $E$ . The absorption of photons occurs by giving specific amount of energy to the core-electron, which is excited from an occupied core-state  $E_i$  with wavefunction  $\psi_i$  to an unoccupied level (bound or unbound)  $E_f$  with wavefunction  $\psi_f$ . The absorption coefficient is proportional to the dipole transition probability given by the Fermi's golden

$$(4.2) \quad \mu_E \propto \sum_f |\langle \psi_f | r | \psi_i \rangle|^2 \delta(E - E_f + E_i),$$

where the difference in energies of initial and final state is the X-ray photon energy, so  $E_f - E_i = E$ .  $\psi_i$  and  $\psi_f$  are the initial and final state wavefunctions. When an electron is excited from core-state (similar to the atomic orbital of the atom) of the targeted atom, its wavefunction can be represented by a spherical harmonic wave scattering into neighboring atoms as shown in Fig. 4.2(b). The backscattered wave will have interference with the ongoing wave. As the kinetic energy of outgoing electron varies with the X-ray energy  $E$ , the interference creates constructive or destructive oscillations. The only non-vanishing

contribution to the absorption matrix element in Eq. 4.2 comes from the region (Energy scale) where the final state (linear combination of ongoing electron wave and backscattered wave) wavefunction is non-zero. The variation of final state wavefunction results in the

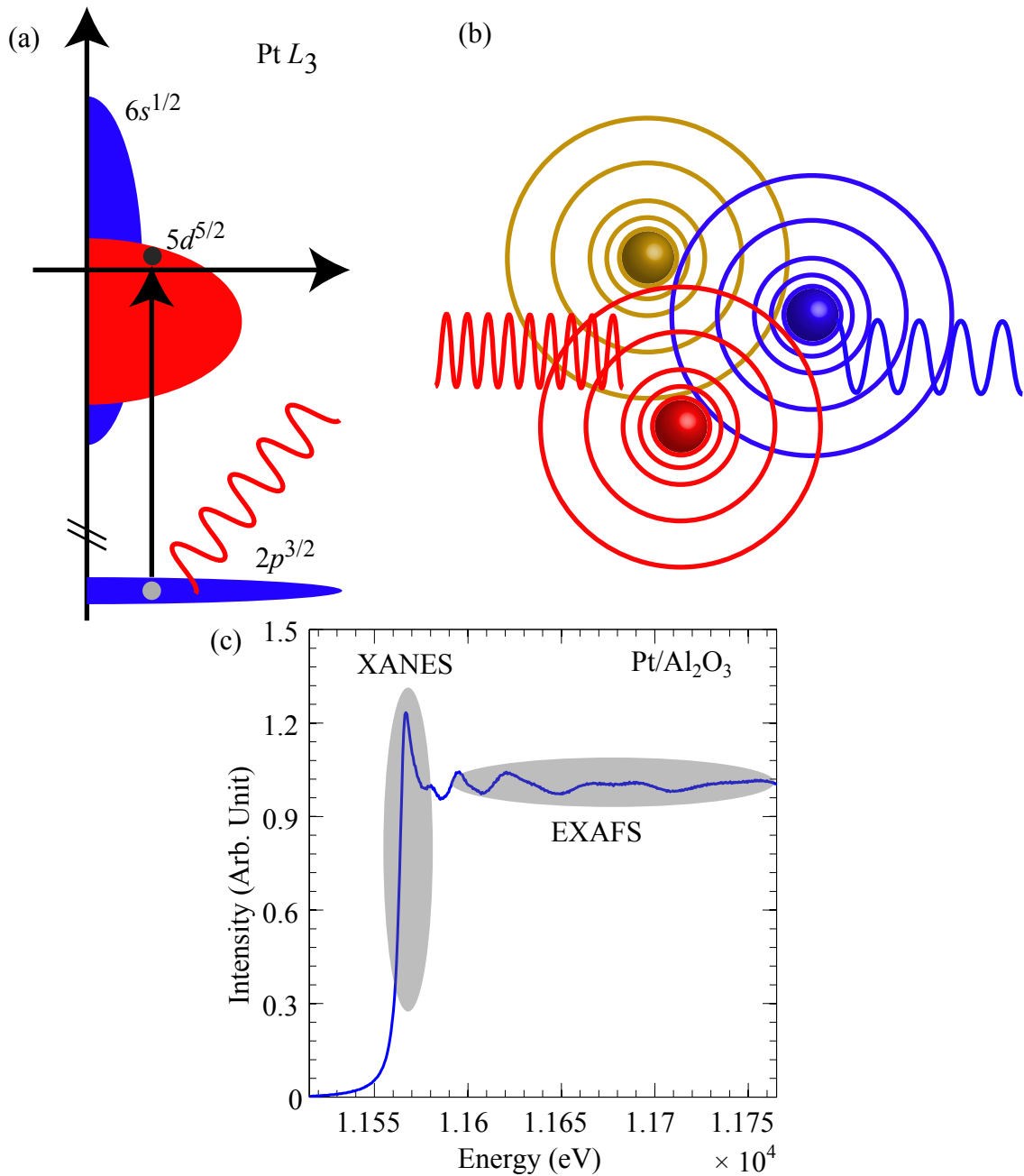


Figure 4.2: (a) Schematic illustration of XANES (b) Schematic illustration of EXAFS (c) Pt  $L_3$ -edge XAS as an example

oscillation in absorption coefficient  $\mu$ . Since this oscillation is due to the existence of

scattering with neighboring atoms, so the geometric structure such as the bond length and coordination number can be directly deduced from the spectra. The spectra in this region is called extended X-ray absorption fine-structure (EXAFS). For the electron excitation into the bound state right above the Fermi level as shown in Fig. 4.2(a), the variation of X-ray energy will map out the electronic structure of local atoms directly. The spectra in this region is called X-ray absorption near-edge structure (XANES).

XAS results were analyzed using publicly available software Athena and Artemis following standard analysis procedures. First, the curves were calibrated by setting the point of the Pt foil data with the maximum slope to the theoretical Pt  $L_3$ -edge onset, 11564 eV. The background data of each curve was removed by fitting the pre-edge data to a linear function and subtracting out the result. The curves were normalized by fitting the post-edge data to a third degree polynomial and dividing the data by the extrapolated value at  $E_0$  (the edge onset). Phase and amplitude for each first nearest neighbor scattering path (Pt-Pt and Pt-M where M is Cu, Ru, or Sn) were calculated using FEFF.

The general mechanism along with the typical spectra of Pt  $L_3$ -edge of XAS is shown in Fig. 4.2. The excitation of core electron into conduction band right above the Fermi level allows us to probe the electronic structure of metal sites, especially the  $d$ -band. The information we obtained from measurement is significant since the occupation and shape of the  $d$ -band has been shown to correlate with the surface reactivity. In the XANES spectra region, the spectra essentially gives the information about the electronic structure of local sites. For  $L_3$ -edge, it is the transition from  $p$ -state to  $s$  and  $d$ -states above the Fermi level. Since the dipole transition probability to  $s$ -states is very low compared to transition to  $d$ -state, so the measurement is governed by the electronic fingerprint of the  $d$ -band. In the EXAFS region, the excited electron scatters with the incoming wave of X-ray, creating ripples on the outgoing wave which can be measured on the spectra. The

geometric structure information, such as the bond distance and coordination number, can be elucidated from the spectra in this region by fitting spectra to standard EXAFS equation.

## 4.2.2 Computational Details

### 4.2.2.1 Adsorption Energies

First-principles density functional theory (DFT) calculations were performed using the ultrasoft pseudopotential [100] plane-wave method with the generalized gradient approximation (GGA-PW91) coded in Dacapo [ref]. The wave-functions were expanded in plane-waves with an energy cutoff of 350 eV. The Pt skin alloys were modeled by a four-layer slab separated by 10 Å of vacuum space with subsurface  $3d$ ,  $4d$  or  $5d$  metals. An adsorbate was placed at 1/4 ML coverage on one side of the slab. A dipole correction was applied in z-direction to minimize interactions among neighboring cells. The adsorbates and top two layers were fully relaxed until the force on the atoms was less than 0.05 eV/Å. We used 32 Monkhorst-Pack irreducible  $k$ -points in the irreducible Brillouin-zone (IBZ) of the  $p(1 \times 1)$  Pt surface unit cell. A finite temperature Fermi function ( $k_B T_{el} = 0.1$  eV) was utilized to facilitate the SCF convergence, and the total energy was extrapolated to  $k_B T_{el} = 0$  eV. Our calculations have shown that this setup yields converged adsorption energy differences between an adsorbate on different surfaces. The adsorption energies of different adsorbates on Pt skin alloys ( $3d$ ,  $4d$  and  $5d$  metals) were calculated and referenced to the corresponding gas phase CO, H<sub>2</sub>O, N<sub>2</sub> and H<sub>2</sub>. The Bader [71] and Mulliken charge distribution of  $3d$ -M/Pt skin alloys has been determined to investigate the effect of alloying on the number of electronic charge localized on surface Pt atoms. Bader charge analysis provides an intuitive way of partitioning the electron density of atoms based on 2D zero-flux surfaces. As another mean of separating electron density within atoms, Mulliken charge analysis is mostly often used in computational chemistry, based on linear combination of atomic orbitals method. In order to evaluate the number of localized  $d$ -states on

surface Pt atoms, we have calculated the projected density of states (PDOS) by projection of the one-electron states onto spherical harmonic atomic  $d$ -orbitals centered on surface Pt atoms.

#### 4.2.2.2 Oscillator Strength Calculations (X-ray Absorption Near Edge Structure Calculations)

X-ray absorption near edge structure (XANES) of the Pt  $L_3$ -edge (oscillator strength) was calculated from first-principles using plane-wave pseudopotential method as incorporated in CASTEP code [101]. The exchange-correlation was described using PW91 functional of the generalized gradient approximation (GGA). The wave-functions were expanded in plane-waves with an energy cutoff of 400 eV and the bulk system was modeled by a supercell with the lattice constant from experimental measurement.  $12 \times 12 \times 12$  MonkhorstPack set of  $k$ -points was used for Brillouin-zone sampling of  $1 \times 1 \times 1$  unit cell. The  $k$ -points density in  $k$ -space was held constant for calculations with larger unit cells. An ultrasoft pseudopotential was generated on the fly while performing the calculations of the oscillator strength with partial occupancy of core states [102]. To test the significance of core-hole effect in the calculations of the oscillator strength, we calculated Pt  $L_3$ -edge XANES spectra of the same system using different populations of the core hole states. We found that the spectrum calculated with ground state approximation matches the experimental measurement very well, which indicates that the core-hole interaction has only negligible effect for the Pt alloy system. So in our study, we use ground state approximation. All oscillator strength calculations with partial core holes were carried out using unit cells sufficiently large to eliminate the core-hole interactions between periodic images. The calculated spectra for all alloys were adjusted (shifted in energy by a constant value) so that the calculated edge onset energy for pure Pt corresponds to the experimentally measured edge onset energy of pure Pt  $L_3$ -edge. Gaussian broadening with 3.0 eV, which encompasses instrumental broadening and the lifetime of excited states, was

applied in order to compare calculated spectra to experimental measurements.

The oscillator strength is the computationally equivalent to the XAS measured absorption coefficient,  $\mu$ . Based on Fermi's golden rule, the oscillator strength gives the dipole transition probability between initial core-states to final state with a hole and the extra electron above the Fermi level [103]. It is the product of transmission function and the density of states at each energy level as shown in Eq. 4.4:

$$(4.3) \quad F(E) = T(E)\rho(E)$$

where  $T(E)$  is the transmission function defined in Eq. 4.4 and  $\rho(E)$  is the density of state at the transition frequency.

$$(4.4) \quad T = \frac{1}{3} \frac{2mE}{\hbar^2} |\langle \psi_{i,c} | r | \psi_{i,f} \rangle|^2$$

where  $\psi_{i,c}$  is the core state and  $\psi_{i,f}$  is the final state. The key step of calculating the oscillator strength is the evaluation of the transition matrix elements between the core state on the site of interest and the unoccupied final state.

#### 4.2.3 Challenges for Predicting Variations in Surface Reactivity of Alloys

The chemical reactivity of metal surfaces (including alloys) can be understood in terms of the Hammer-Nørskov  $d$ -band model [52, 63, 104–107] which relates the electronic structure of a site on a metal, more specifically the center of the  $d$ -band (i.e., the average energy of  $d$ -states), to the local chemical reactivity. Metals with a higher  $d$ -band center, with respect to the Fermi level, bind most adsorbates more strongly than metals with a lower  $d$ -band center [52, 63, 106]. We note that we have found some exceptions to this model, and these exceptions will be one focal point of the Section 3 of this chapter.

The  $d$ -band model of chemical bonding on metal surfaces emerges naturally based on the analysis of the one electron contribution in Eq. 3.22 within the tight-binding approximation or Newns-Anderson model, see details in Chapter 2. The change in the adsorption

energy of an adsorbate on a given surface site on metals are dominated by the difference in one-electron energies upon adsorption. The electrostatic and polarization component of the adsorbate-substrate interaction is very similar for a given adsorbate on different metals. Since all transition and noble metals have half-filled  $s$ -band, the main difference in the adsorption energy of an adsorbate comes from the metal-specific interaction of the adsorbate orbitals with substrate  $d$ -electron ( $d$ -band). One parameter that can capture the difference in the  $d$ -band between different metals is the center of  $d$ -band (average energy of  $d$ -states with respect to the Fermi level). For metal surfaces with higher  $d$ -band, the adsorbate-metal anti-bonding orbital will also be higher in energy and so less occupied. The one electron energies difference by integrating to Fermi level will result in lower energy corresponding to stronger chemical bonding. One assumption of  $d$ -band model is that the effect of  $sp$ -electron on the bonding geometry and strength is similar for different surfaces since it is broad and featureless, which might not be true for small metal particles or alloys [49]. We are going to elaborate this assumption and its consequence on the nature of chemical bonding on alloy surfaces on Section 3 of this Chapter.

For pure monatomic metals, the relative positions of the  $d$ -band center can be easily estimated and thus their relative chemical reactivity can be predicted [104]. The only parameter in the model is the  $d$ -band center which is governed by the filling and the shape (mainly width) of the  $d$ -band. The  $d$ -band filling is related to the number of occupied  $d$ -orbitals. The width of the  $d$ -band (i.e., the width of the projected density of states) is a function of the geometry (the distance between atoms,  $d$  in Fig. 4.3(b)) and the spatial extent of the  $d$ -orbitals, ( $r_d$  in Fig. 4.3(b)) [58]. For any pure metal the  $d$ -band filling, the distance between atoms, and the spatial extent of  $d$ -orbitals are known and therefore the relative positions of the center of  $d$ -band and the relative chemical reactivity can be easily estimated [58].

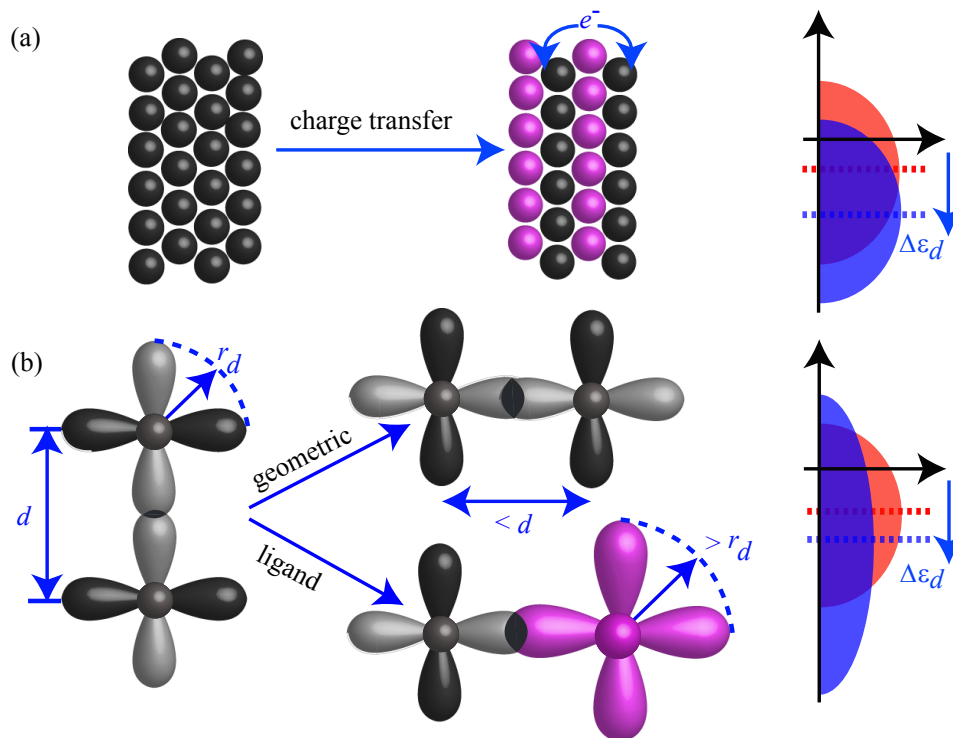


Figure 4.3: Mechanisms by which the center of the local  $d$ -band can change include (a) charge transfer from one element to another, (b) a change in the overlap between  $d$ -states and the valence orbitals of neighboring atoms leading to a change in the  $d$ -band width

Predicting the position of the  $d$ -band center for various sites in alloys and therefore the chemical reactivity of the sites is more challenging. When two different elements interact with each other in an alloy, the center of the  $d$ -band localized on an atom can be affected by: (i) Transfer of electronic charge from or to the  $d$ -states localized on the atom without a change in the width or shape of  $d$ -band (i.e., change in local  $d$ -band filling) as shown in Fig. 4.3(a). This is basically a rigid band model [108]. Charge transfer to  $sp$ -states also can induce  $d$ -band center shift on the host metal sites, and we are going to elaborate this in Section 4 of this Chapter. (ii) Change in the width of  $d$ -band due to hybridization between local  $d$ -orbital and the valence orbitals of neighboring atoms without significant charge transfer as shown in Fig. 4.3(b). This mechanism is consistent with the rectangular band model [58], and it has been proposed to play the critical role by Kitchin et al.[109]. (iii) Combination of charge transfer and the change in the width of  $d$ -band. The mechanisms

(i)-(iii) are dominant as long as the shape of the  $d$ -band defined in terms of skewness and kurtosis is not significantly affected by alloying.

#### 4.2.4 Measurement of Geometric Structure

To develop reliable models that would allow us to predict how the chemical reactivity of a metal site changes as another element is introduced to form an alloy, it is imperative to unearth which mechanism (i-iii above) is responsible for the change in the  $d$ -band center of local sites in alloys. To address this question a number of Pt (Pt/Cu, Pt/Ru, and Pt/Sn) and Ni (Ni/Sn, Ni/Au, Ni/Ag) alloy catalysts were synthesized, and their electronic structure in the neighborhood of Fermi level was measured using XANES and ELNES. The alloys were selected to sample a broad range of electronically different elements with  $3d$  (Ni, Cu) metals interacting with  $4d$  (Ag, Ru),  $5d$  (Au, Pt), and  $sp$  (Sn) metals. Since we arrived at identical conclusions for both families of alloys, we discuss in detail the results for the Pt alloys.

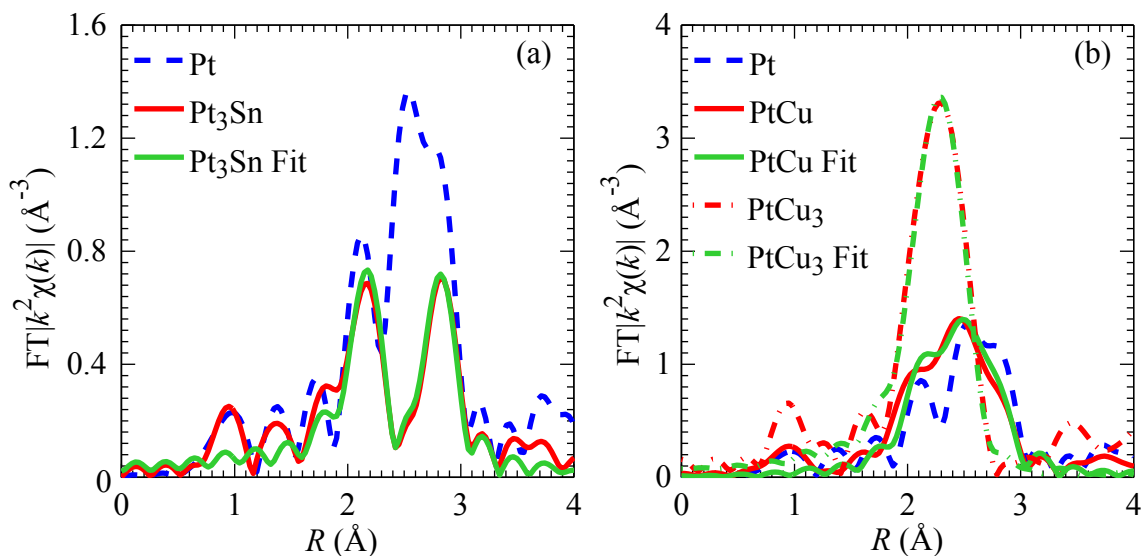


Figure 4.4: Measured and fitted EXAFS spectra for pure Pt and (a) Pt-Sn alloy, (b) Pt-Cu alloys.

To establish that our synthesis resulted in the formation of alloys, we used Extended X-ray Absorption Fine Structure (EXAFS) spectroscopy, which probes the average, local

geometric environment of an element in a material. In Fig. 4.4 we show the measured Pt  $L_3$ -edge EXAFS spectra for Pt, Pt/Cu, and Pt/Sn. Fig. 4.4 shows that there is a significant difference in the spectra of pure Pt and the Pt alloys which is indicative of the formation of the alloy materials. The measured alloy spectra were also compared to the best-fit, simulated EXAFS spectra [102]. The fitting parameters for the best-fit spectra are shown in the Table 4.1. Since the best-fit spectra required nearest neighbor Pt-Pt and Pt-M (where M is either Cu or Sn) scattering paths, it was concluded that alloys, defined as partial or complete Pt-M solutions, were formed. The measured bond distances for different alloys agreed very well with previously identified crystal structures of  $\text{Pt}_3\text{Sn}$  ( $Pm\bar{3}m$ ),  $\text{PtCu}$  ( $R\bar{3}m$ ) and  $\text{PtCu}_3$  ( $Pm\bar{3}m$ ) [110, 111]. The structure can be shown in Fig. 4.5.

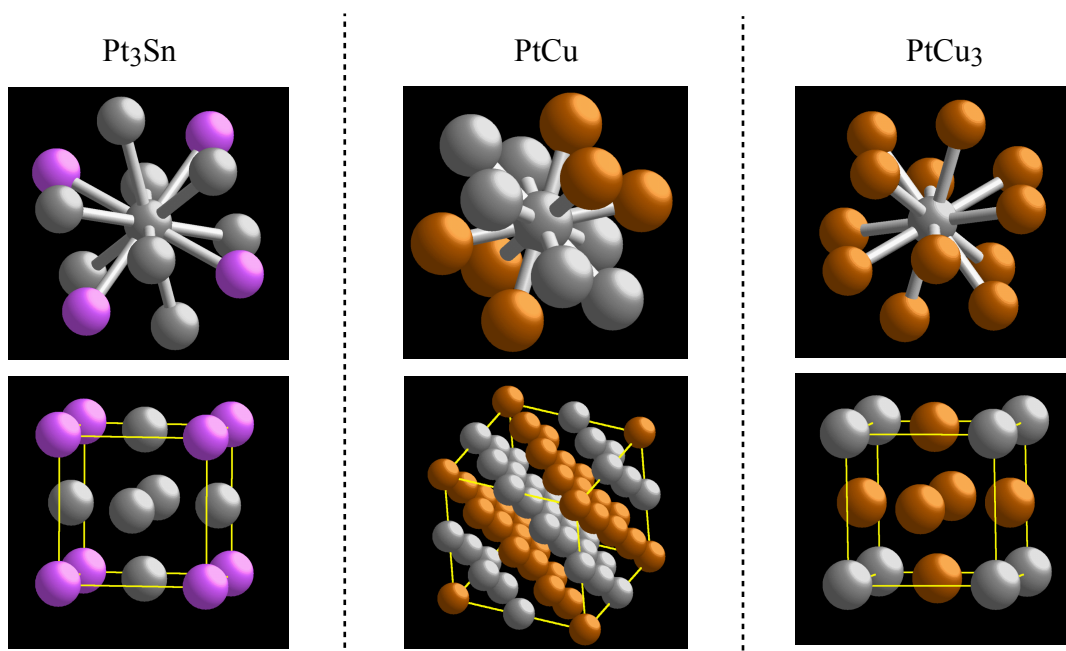


Figure 4.5: Geometric structures of Pt alloys

#### 4.2.5 Measurement of Electronic Structure

To measure the electronic structure of the alloy catalyst, we used X-ray Absorption Near Edge Structure (XANES) spectroscopy. This technique allows us to measure electronic states above the Fermi level localized on a particular element in the material. For

Sample	Scatter Path	CN	R Exp. (Å)	R Model (Å)	$E_0$ (eV)
Pt <sub>3</sub> Sn	Pt - Pt	$4.8 \pm 0.3$	$2.78 \pm 0.01$	2.83	$4.4 \pm 1.0$
	Pt - Sn	$3.1 \pm 0.2$	$2.74 \pm 0.01$	2.83	$4.9 \pm 0.9$
PtCu	Pt - Pt	$7.6 \pm 0.8$	$2.73 \pm 0.01$	2.71	$7.6 \pm 1.5$
	Pt - Cu	$2.5 \pm 0.5$	$2.64 \pm 0.02$	2.66	$7.3 \pm 5.1$
PtCu <sub>3</sub>	Pt - Pt	-	-	-	-
	Pt - Cu	$12.8 \pm 1.3$	$2.59 \pm 0.01$	2.6	$5.1 \pm 1.1$

Table 4.1: Structural Parameters from EXAFS Fitting Results for Pt  $L_3$ -edge EXAFS Spectra of Pt Alloys. (Coordination Numbers CN, Distances R).

example, the Pt  $L_3$ -edge XANES spectra probes the unoccupied  $s$  and  $d$  density of states (DOS) localized on Pt atoms in the alloy materials by measuring the photoabsorption cross-section associated with the excitation of Pt  $2p_{3/2}$  core electrons to the unoccupied Pt  $6s$  and  $5d$  states. Since the dipole transition probability to the  $d$ -states is much larger than that to the  $s$ -states due to the intrinsic shape of atomic orbitals [112], the spectra are essentially dominated by the  $d$ -states [112].

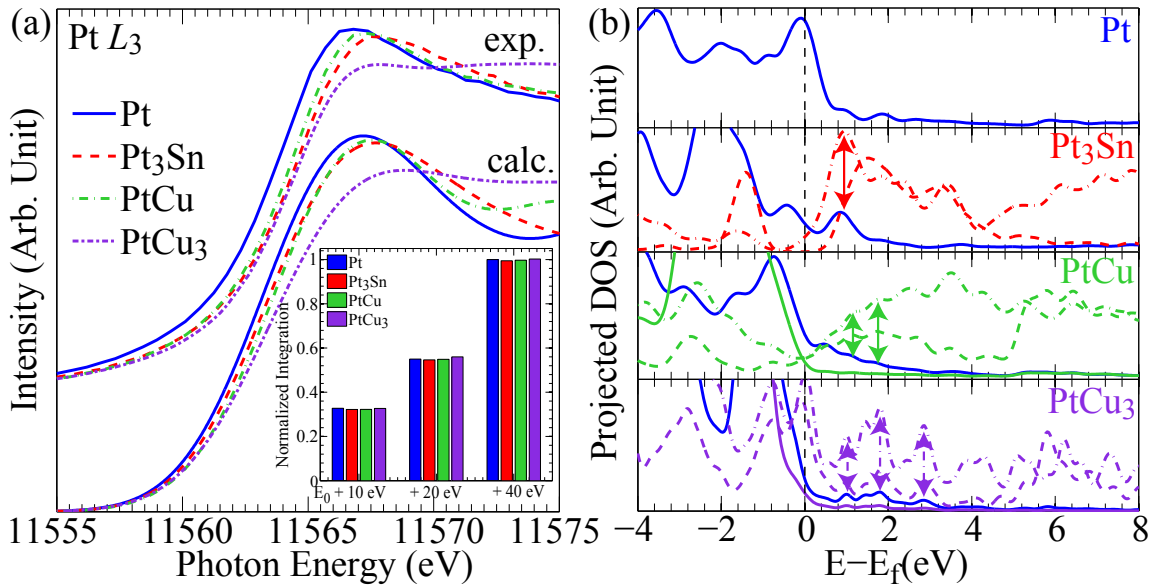


Figure 4.6: Electronic properties of Pt alloys. (a) Measured Pt  $L_3$ -edge XANES spectra and calculated oscillator strengths for different Pt alloys. Insert shows calculated areas under the measured XANES spectra. These are plotted for different cutoff energies since it is not clear where the near edge ends. We find that independent of the cutoff energy the integrated spectra gives almost identical values for different alloys. (b) Density of states projected on different elements in the alloys: Pt  $5d$  states are solid blue, and metal (Sn, Cu)  $s$  and  $p$  states are dash and dash-dot lines, respectively. Cu  $3d$  states are solid green and purple for PtCu and PtCu<sub>3</sub> alloy, respectively.

The Pt  $L_3$ -edge XANES spectra for pure Pt and the Pt alloys are shown in Fig. 4.6(a).

The figure shows that the formation of the alloys affects the Pt  $L_3$ -edge: there are shifts in the positions of the edge onsets and changes in the width and height of the post-edge peak. To identify the origin of the observed changes in the Pt  $L_3$ -edge, we used DFT to calculate oscillator strengths (see previous Section for the discussion of calculations), the computational equivalent of XANES spectra, for the electron transition from the Pt  $2p_{3/2}$  core states to the Pt  $5d$  and  $6s$  states above the Fermi level for pure Pt and the Pt alloys. The calculated oscillator strengths for the alloy crystal structures identified in our EXAFS measurements are shown in Fig. 4.6(a). The figure shows that there is an excellent agreement between calculated oscillator strengths and measured XANES spectra, i.e., the main features of the spectra for different alloys, including the edge onset and the peak width are reproduced in our calculations. We found that the initial (ground) state electronic structures, used to calculate the oscillator strengths in Fig. 4.6(a), reproduced the measured spectra better than the electronic structures calculated for a partially filled Pt  $2p$  core hole. This has been observed before and it is attributed to the electron shielding effect in Pt, which greatly reduces the interaction between the core hole and the promoted electron in the excited state [113, 114]. The agreement between the measured spectra and the spectra calculated using the ground state electronic structure indicates that the measured Pt  $L_3$ -edge XANES spectra maps well on the ground state Pt DOS of  $d$ -symmetry, therefore allowing us to experimentally measure the ground state electronic structure. Further analysis of the calculated changes in the local  $d$ -DOS in response to alloying showed that the changes in XANES spectra due to alloying were the result of the formation of new electronic states (orbitals), through the hybridization of the Pt  $d$ -states and the valence orbitals of the neighboring atoms in the alloys, as shown in Fig. 4.6(b) [99].

In addition to providing information about the shape of  $d$ -band, the XANES  $L_3$ -edge also allows for a quantification of the relative number of electronic states above the Fermi

level localized on the atom in different environments. The number of localized  $d$ -states is proportional to the integrated area under the measured normalized spectra [103, 112, 115, 116]. In the insert in Fig. 4.6 (a) we show measured integrated areas, i.e., the relative numbers of  $d$ -states above the Fermi level localized on Pt atoms for pure Pt and the Pt alloys. The figure shows that the number of  $d$ -states localized on Pt atoms does not change significantly in response to alloying. This indicates that the transfer of  $d$ -holes (or  $d$ -electrons) between Pt atoms and the atoms of the other elements in the alloys is very small, i.e., the local potential of elements in the alloys is sufficient to preserve the local charge (local  $d$ -band filling) on the atoms.

#### 4.2.6 Fundamental Mechanisms of the $d$ -band Center Shift

Fig. 4.6 (a) provides experimental evidence that for all studied Pt alloys, irrespective of their composition: (i) the formation of the alloys results in a change in the width of the  $d$ -band localized on Pt due to hybridization between valence orbitals, and (ii) there is no significant charge transfer to or from the Pt  $d$ -states.

There are a number of important consequences of these observations. Upon the formation of alloys the local  $d$ -charge on an atom in the alloys is preserved, the local  $d$ -band center and therefore the local chemical reactivity are functions of only the local  $d$ -band width (measured with respect to the Fermi level). The width is governed by the spatial extent of the hybridizing valence orbitals ( $r_d$ ) and the geometry (bond distance between atoms in the alloy,  $d$ ) [58]. This means that for different alloys with similar geometries, the width of the  $d$ -band and therefore the  $d$ -band center is a unique function of only the spatial extent of the  $d$ -orbitals of constituent metal elements.

For example, since the distance between Pt atoms and  $3d$ -metal atoms in different  $3d$ -M/Pt alloys is approximately equal for a given crystal structure [117] —the geometry is to a large degree governed by the  $sp$ -states, which are in the case of  $3d$  metals very similar

to each other—the width of the  $d$ -band projected on geometrically similar Pt sites (and therefore the center of  $d$ -band and the chemical reactivity of the Pt sites), should be only a function of the spatial extent of the  $d$ -orbitals of the  $3d$  metals directly interacting with the Pt atom.

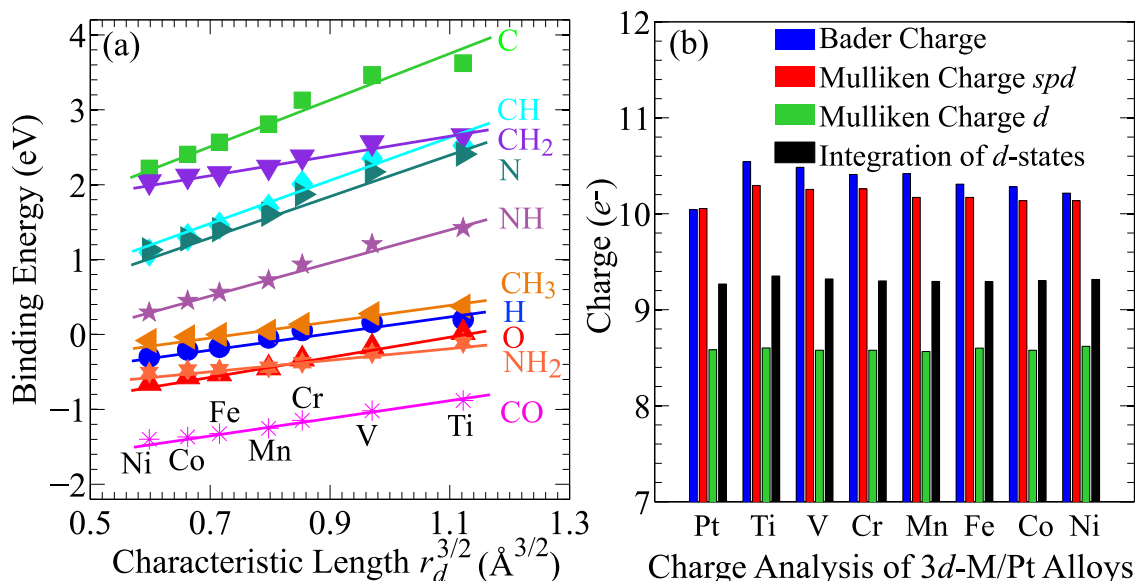


Figure 4.7: (a) Binding energy of various adsorbates on  $3d$ -M/Pt skin alloys as a function of characteristic orbital length ( $r_d^{3/2}$ ) of  $3d$  metals. (b) Charge analysis of Pt on  $3d$ -M/Pt skin alloys

We have tested the predicted relationships using DFT to calculate adsorption energies of various adsorbates on geometrically identical Pt sites on a number of model  $3d$ -M/Pt skin alloys. The skin alloys were modelled as a Pt fcc slab terminated with the Pt(111) surface, with  $3d$ -metals replacing Pt in the subsurface layer of the slab. Identical models were used previously [118]. We note that the  $3d$ -M/Pt skin alloys exhibit higher tolerance to CO and lower over-potential losses associated with the oxygen reduction reaction (ORR) compared to the pure Pt when used as electrodes for low temperature proton exchange membrane (PEM) fuel cells [95]. Fig. 4.7(a) shows that as predicted by the analysis above, the adsorption energies for various adsorbates on the Pt surface sites scale linearly not only with the center of  $d$ -band, as shown previously, but also with  $r_d^{3/2}$ , where  $r_d$  is the

spatial extent of the  $d$ -orbitals of the  $3d$  metals which form the  $3d$ -M/Pt skin alloys. The values for the spatial extent of  $d$ -orbitals were obtained from ref [58]. Similar relationships have been found for adsorption on geometrically identical sites on  $4d$ -M/Pt and  $5d$ -M/Pt alloys as shown in Fig. 4.8. The scaling of the adsorption energies with  $r_d^{3/2}$  is not accidental. Muffin-Tin Orbital theory (Atomic Sphere Approximation [58]) predicts that, for a fixed geometry, the  $d$ -band width projected on a given atom in an alloy is proportional to  $r_d^{3/2}$ .

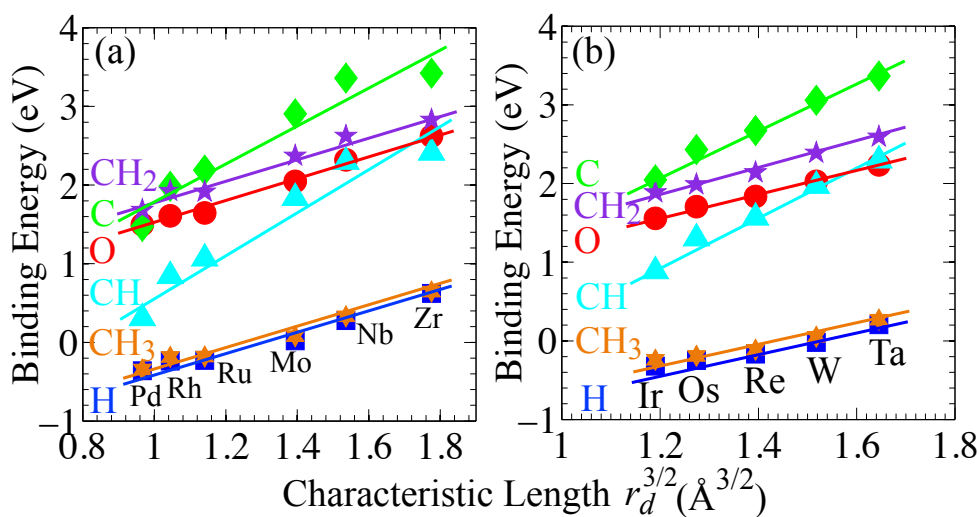


Figure 4.8: Binding energy of various adsorbates on Pt skin alloys as a function of characteristic orbital length ( $r_d^{3/2}$ ) of (a)  $4d$  metals (b)  $5d$  metals

The relationships presented in Fig. 4.7 were obtained for geometrically identical Pt sites on various Pt skin alloys. However, it is important to stress that our experiments show that the preserved local  $d$ -charge concept is also valid even if there is a change in the local geometry. For example, while the bond distances between Pt and Cu or Sn in the respective Pt alloys are different, the measured local charge on Pt is preserved, see Fig. 4.6. The impact of the local geometry on the width of the  $d$ -band can also be estimated based on tight binding approximation, showing that the width of the  $d$ -band is proportional to  $1/d^{7/2}$  for  $sd$  and  $pd$  hybridization and  $1/d^5$  for  $dd$  hybridization, where  $d$  is the length

of the bond between the atoms in the alloy [58]. The effect of geometry on the  $d$ -band center has been studied before and these relationships have been supported by extensive DFT calculations [109, 118].

#### 4.2.7 $sp$ -band Contribution to the Chemical Bonding

As shown in Fig. 4.7(b) we can see that there is a slight charge transfer from the  $3d$ -M to the surface Pt atoms based on the Bader charge analysis. However, orbital-resolved integrated projected density of states and Mulliken charge distribution indicate that the charge transfer stems from the  $3d$ -M to the delocalized  $sp$ -states of Pt atoms. The Newns-Anderson (N-A) model of chemisorption as introduced in Chapter 2 was used to investigate the effect of the  $sp$ -band occupancy on the adsorption energies of various adsorbates (atomic oxygen as an example) on Pt and Pt skin alloys. Simply speaking, N-A model is used to describe the coupling between an adsorbate state and a large number of electronic states of a surface within the tight-binding approximation. For details about the algorithm, see Chapter 2 or the original contributions and the following publications.

To approximate the  $sp$ -band of the Pt and Pt alloy substrates, we used a semi-elliptic function fitted to the DFT-calculated  $sp$  projected density of states on the surface Pt atoms without cutoff radius. The band occupancy, depending on the constituent metal elements in alloys, was consistent with the band filling obtained from DFT calculations.

The weighted  $sp$  density of states of a substrate can be written as Eq. (4.5).

$$(4.5) \quad \Delta(\varepsilon) = \pi V_{sp}^2 \rho(\varepsilon)$$

where  $\rho(\varepsilon)$  is the semi-elliptic function representing the  $sp$  projected density of state on surface Pt atoms and  $V_{sp}$  is the coupling matrix element between the adsorbate valence state with the electronic band of substrates. In the wide-band limit,  $V_{sp}$  is assumed to be constant with respect to energies. As the adsorbate is brought close to the surface, the

two sets of states will be coupled by the matrix element,  $V_{sp}$ . The projected density of states on the adsorbate in Fig. 4.9 (a) and therefore the hybridization (adsorption) energy in Fig. 4.9 (b) due to the interaction can be calculated from the N-A model. In Fig. 4.9 (b), we show the hybridization energy of the atomic oxygen interacting with the  $sp$  electronic bands of different  $3d$ -M/Pt skin alloys (the different alloys are characterized by different occupancies of the  $sp$  band) as a function of the coupling matrix element. Assuming that the coupling matrix element between the adsorbate state and the  $sp$ -band is similar for the different  $3d$ -M/Pt skin alloys (this should be the case since it is Pt surface atoms that are interacting with the adsorbate for all skin alloys), we can see in Fig. 4.9 that the hybridization energy is not sensitive to the change in the occupancy of the  $sp$ -band. This leads us to conclude that the difference of the binding energy of adsorbates on Pt skin alloys is mainly due to the change of the  $d$ -band.

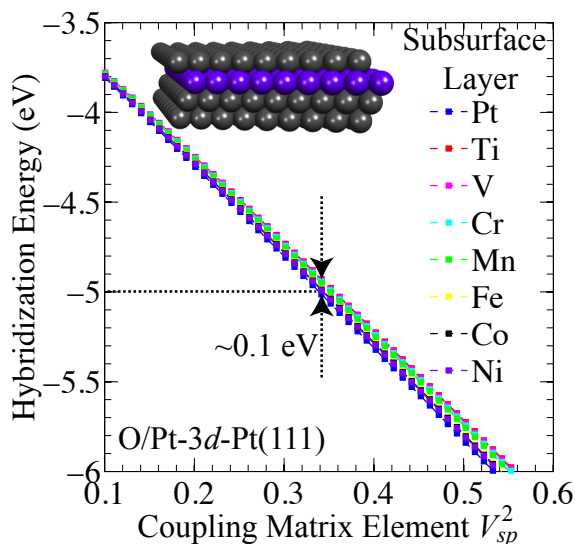


Figure 4.9: Hybridization energy between atomic orbital of O with Pt  $3d$  skin alloys based on the Newns-Anderson model

The above analysis is focusing on the effect of  $sp$ -electron density on the hybridization of adsorbate states and metal substrate states. We can conclude that the energy change due to interaction with  $sp$ -band is not sensitive to the  $sp$ -band electron density. We noticed

that there is variations in the adsorbate bond distance to the surfaces which gives different coupling matrix elements for different surfaces. It has been indicated previously that the *sp*-electron density has a determined effect on the adsorbate distance to the surface. In this Chapter, we are going to elaborate the consequence of varying bond distance, and how that can govern the trend of chemical bonding in some adsorbate/substrate systems.

Finally, it is important to address the ambiguity of the concept of charge transfer from one element in an alloy to another. In the analysis above, we have referred to the transfer of *d*-electrons from one element to another in terms of a uniquely defined area under the measured or calculated oscillator strength. We established that there is no significant transfer of *d*-electrons between constituent metal elements. This information was sufficient to design a model which allows us to predict the impact of alloying on the local electronic structure and chemical reactivity of a catalytic site based on the ground states electronic structures. On the other hand, it is also possible to define the localized charge in terms of the partitioning of the ground state electron density among the atoms in the alloy. For example, Bader and Mulliken charge analysis [71, 119] of the DFT-calculated electron density of the model alloys shows that there are shifts in the electron density from the *3d* metal atoms to the Pt atoms as shown in Fig. 4.7(b). However, projections of the local *d*-orbitals on the partitioned volumes show that the only contributions to the charge transfer are to the *sp*-states of Pt. It can be shown, using the Newns-Anderson model [50–52], that small changes in the filling of the *sp*-bands have only a negligible effect on the chemical reactivity of the surfaces.

In summary, the picture that emerges from these studies is that when two transition metals are brought together to form an alloy there is no significant shifts in the filling of local *d*-states (no charge transfer to or from the *d*-states), and therefore the change in the position of the *d*-band center and the local chemical reactivity of alloy sites is to a large

degree governed only by the width of the local  $d$ -band. The width of local  $d$ -band is a function of the local geometry (more specifically the bond distance between the elements that form the alloy) and the spatial extent of valence orbitals of the atoms. Since the bond distance between constituent metal elements in alloys can be predicted, for example by applying Vegard's law [120], and since the spatial extent of the orbitals of elements in alloys is known, the position of the center of  $d$ -band for various sites in alloys and therefore the chemical reactivity of these sites can also be predicted easily. It is also important to note that relaxations at surfaces could affect the bond distance; however, for a given family of alloys ( $3d$ ,  $4d$  or  $5d$ ) with similar crystal structures these changes are approximately the same. The fundamental advantage of this model is that the chemical reactivity is predicted based only on physical properties of elements that form the alloy in their unalloyed form. This means that the model can be used to screen very rapidly through large alloy space seeking optimal alloy catalysts for a particular chemical transformation.

### 4.3 Exceptions to the General Trend Predicted by the $d$ -band Model

Developing predictive models of chemisorption on metal surfaces is critical for the understanding of surface chemical reactions [23, 62, 63, 106]. It has been shown that the  $d$ -band model [39, 63] of chemisorption, developed by Hammer and Nørskov, can predict the trend in chemisorption energies of various adsorbates on metal surfaces. The model correlates the central moment of the  $d$ -band projected on surface atoms ( $d$ -band center referenced to the Fermi level) with the surface reactivity since the chemisorption strength is largely governed by the population of adsorbate-metal anti-bonding orbitals. As the  $d$ -band center of the metal substrate atom moves up in energies, the anti-bonding orbital will move up away from the Fermi level and result in less occupation and so stronger bond. It has been used successfully to design novel metal surfaces for various catalytic reactions

[8, 93, 121]. In general, for a given adsorption geometry adsorbates bind to the surface of transition or noble metals more strongly if the  $d$ -band center of the surface atom is higher in energies [39, 63]. The model is very robust and most adsorbates follow the trends predicted by the model [39, 63, 104].

In this Section, we show that there is a family of adsorbate-substrate systems that does not follow the general trend in adsorption energies predicted by the  $d$ -band model. We discuss this exception to the  $d$ -band model by analyzing hydroxyl (OH) adsorption on a series of Pt and Pd skin alloys. This exception is important since OH adsorption on metals is crucial for the understanding of various catalytic, electro-catalytic and photo-catalytic reactions including oxygen reduction [122] and water splitting reactions [123]. It has been shown previously that Pt and Pd skin alloys are promising alternatives to conventional Pt catalysts in these chemical transformations [6].

#### 4.3.1 Computational Details

The DFT calculations were performed using the ultra-soft pseudopotential plane-wave method with the generalized gradient approximation (GGA-PW91) coded in Dacapo. The wave-functions were expanded in plane-waves with an energy cutoff of 350 eV. The Pt or Pd alloy surfaces were modeled by a  $2 \times 2 \times 4$  slab separated by 10 Å of vacuum space. The adsorbates and top two layers were allowed to relax until the total force on the atoms was less than 0.05 eV/Å. In the  $p(2 \times 2)$  Pt surface unit cell,  $4 \times 4 \times 1$  Monkhorst-Pack  $k$ -points were used for the Brillouin-zone integration. Convergence of the results with respect to various calculation parameters was verified in all cases.

#### 4.3.2 Surface Phenomenon in Contradiction to the General Understanding of the $d$ -band Model

Fig. 4.10 (a, b) shows adsorption energies, calculated using Density Functional Theory (DFT) of O (fcc site) and OH (we found that the top site binds OH the strongest) at 1/4

ML coverage on a number of Pt and Pd skin alloys as a function of the  $d$ -band center projected on the surface atoms. In the model system, the subsurface layer of the host

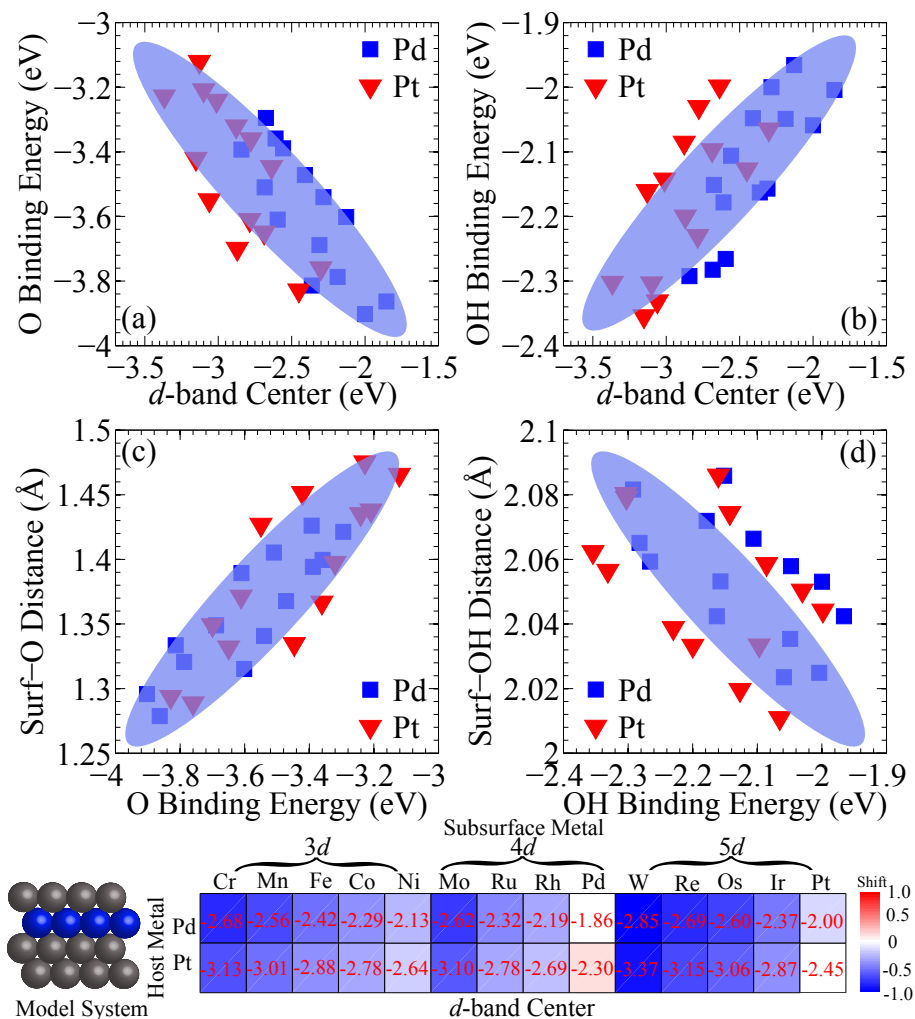


Figure 4.10: DFT-GGA adsorption energies of (a) O and (b) OH on Pd and Pt skin alloys are plotted as a function of the center of  $d$ -band projected on surface atoms. (c, d) Surf-O and Surf-OH distance are plotted as a function of DFT-GGA adsorption energies of O and OH on Pd and Pt skin alloys. The model system is shown at the left bottom of the figure. The  $d$ -band center ( $\epsilon_d$ ) projected on surface atoms of various skin alloys are shown in the Table.

metal slab (Pt or Pd) is substituted by a guest metal ( $3d$ ,  $4d$  or  $5d$  with more than half filled  $d$ -band). Similar models have been used previously to model skin alloys [118]. The calculated  $d$ -band center, showing that for the subsurface elements to the left of a given row of the periodic table, the center of  $d$ -band projected on surface Pt or Pd atoms moves down in energies, are tabulated at the bottom of Fig. 4.10 (a). Fig. 4.10 (a) shows that

the adsorption of O follows the  $d$ -band model. On the other hand, the OH adsorption energies are reversely correlated with the  $d$ -band center as shown in Fig. 4.10 (b), i.e., those substrates with the higher  $d$ -band center adsorb OH less strongly than the substrates with the lower  $d$ -band center. Fig. 4.10 (c, d) also shows that the stronger chemisorption of OH on an alloy surface is accompanied with longer adsorbate-substrate bonds, which is counterintuitive. In addition, the stronger bonding of OH occurs on the Pt and Pd sites interacting with more chemically active subsurface atoms in the alloy (i.e., Cr is more chemically active than Ni), which is in contradiction to the bond order conservation [124].

### 4.3.3 Two-Level Interaction Model

To understand this exception to the  $d$ -band model, we first discuss a physically transparent framework allowing us to analyze chemisorption of adsorbates on transition or noble metal substrates as shown in Chapter 3. Almost identical framework has been used previously to analyze the adsorption of CO and O on metal surfaces [39, 106]. The model assumes that there are two main substrate-specific components contributing to the difference in the adsorption energies: electronic ( $\Delta E_{el}$ ), electrostatic ( $\Delta E_{es}$ ) and polarization ( $\Delta E_{pe}$ ) interactions [62]. It is generally assumed that the electrostatic and polarization contributions are similar for a given adsorbate on different transition or noble metal surfaces [83]. Our DFT calculations supported this point and showed that the electrostatic component of the adsorbate-substrate interaction calculated by multiplying the self-consistent subsurface atoms induced electric field (reference to induced electric field on pure metal surface) with the dipole moment of adsorbate on the surface is very similar for different skin alloys. The electronic contribution is due to the change of one-electron energies, and it is insightful to further divide this contribution into the  $sp$ -band and  $d$ -band contributions [52] as shown in Eq. (4.6). We will treat the interaction of the adsorbate with the substrate

$sp$ -band as an adjustable parameter in the model.

$$(4.6) \quad \Delta E_{el} = \Delta E_{sp} + \Delta E_d$$

The interaction of the molecular orbitals of OH with the substrate  $d$ -band can be treated as an interaction between two localized molecular orbitals approaching each other and forming a chemical bond. It can be described by two terms: covalent attraction due to the orbital hybridization and repulsion due to the energy cost associated with the orbital orthogonalization (this term is sometimes referred to as Pauli repulsion) [104]. Since in the case of OH there are two molecular orbitals interacting with the  $d$ -band ( $d$ -orbitals of the substrate), populated  $1\pi$  and empty  $4\sigma^*$  orbitals, we need to account for the interaction of both orbitals with the substrate  $d$ -band as shown in Eq. (4.7) [106].

$$(4.7) \quad \Delta E_d \approx -4 \left[ (1-f) \frac{V_\pi^2}{|\epsilon_d - \epsilon_{1\pi}|} + (1+f) S_\pi V_\pi \right] \\ - 2 \left[ f \frac{V_\sigma^2}{|\epsilon_d - \epsilon_{4\sigma^*}|} + f S_\sigma V_\sigma \right]$$

Here,  $f$  and  $\epsilon_d$  are the respective filling and center of  $d$ -band projected on the surface metal atoms.  $\epsilon_{1\pi}$  and  $\epsilon_{4\sigma^*}$  are the energy levels of the renormalized adsorbate orbitals formed after the interaction with broad, free-electron-like substrate  $sp$ -band.  $S$  and  $V$  are the overlap integral and coupling matrix element describing the interaction between renormalized adsorbate orbitals and metal  $d$ -band, respectively. The first term in each bracket describes the covalent attraction, while the second term describes the Pauli repulsion. The coefficient in front of the bracket is the degeneracy of the adsorbate states.

To use the model in Eq. (4.6) and Eq. (4.7) to analyze the adsorption of OH on the skin alloys, we need to evaluate the energy levels of the renormalized  $\epsilon_{1\pi}$  and  $\epsilon_{4\sigma^*}$  orbitals with respect to the substrate Fermi level. To accomplish this objective, we have investigated the evolution of these molecular states on the Al(111) surface. Since Al has no  $d$ -electrons,

this system can mimic the interaction of OH with the  $sp$ -band of skin alloy surfaces [106].

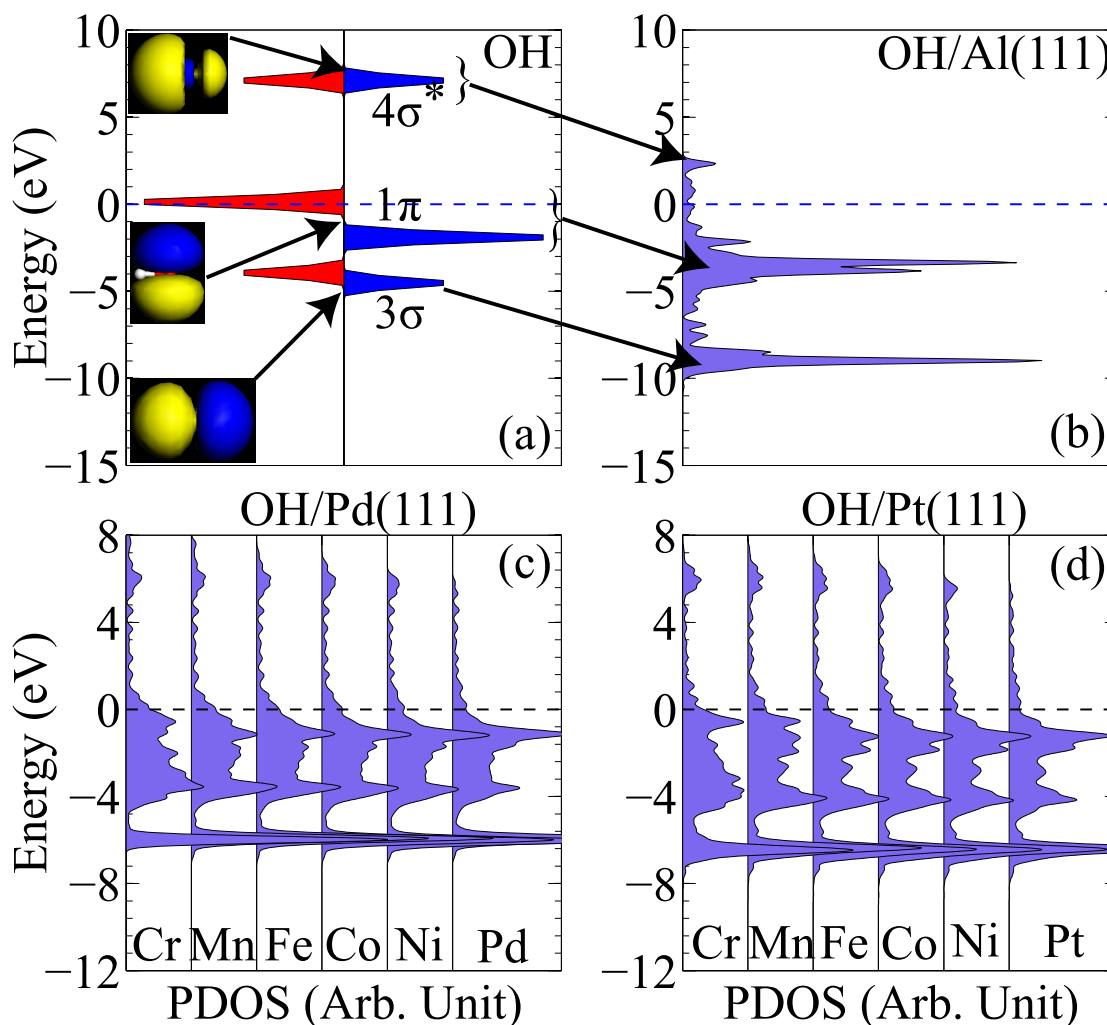


Figure 4.11: (a) Density of states (DOS) of gas phase OH radical in vacuum. (b) DOS projected on the molecular orbitals of OH adsorbed on atop site of Al(111). (c) and (d) DOS projected on the O atom for OH adsorbed on atop site of Pd and Pt with  $3d$  subsurface metal.

In Fig. 4.11 (b), we show the density of states projected on the molecular orbitals of the OH adsorbate on the Al(111) surface. The positions of molecular orbitals of OH ( $3\sigma$ ,  $1\pi$  and  $4\sigma^*$ ) in vacuum are shown in Fig. 4.11 (a). Comparison of Fig. 4.11 (a) and (b) shows that the molecular orbitals of OH adsorbed on the Al(111) surface are broadened and shifted down in energies with respect to the molecular states of the gas phase OH.

Due to the difference in the  $sp$ -electron density of the Al(111) surface compared to Pt and Pd skin alloy surfaces, the calculated positions of the renormalized adsorbate states on the Al(111) surface need to be recalibrated. This can be done straightforwardly since the low lying  $3\sigma$  adsorbate state interacts mainly with  $sp$ -states on the Al(111) and skin alloy surfaces, and therefore provides a reasonable reference. It is shown in Fig. 4.11 (c, d) that  $3\sigma$  orbital is shifted slightly upward on Pt and Pd skin alloys compared to the Al(111). We assume that renormalized states ( $1\pi$  and  $4\sigma^*$ ) have shifted upward by the same energy relative to the  $3\sigma$  orbital of OH adsorption on Pd and Pt skin alloys, respectively. This assumption is reasonable since the level shift of renormalized adsorbate states will be mainly a function of the substrate  $sp$  density of states [125]. This analysis shows that the renormalized  $1\pi$  and  $4\sigma^*$  states of OH on the Pd alloys are at -0.6 and 5.0 eV with respect to the Fermi level. The corresponding energy levels on the Pt alloy surfaces are at -1.0 and 4.6 eV.

We can now evaluate various parameters in Eq. (4.11). It has been shown previously based on Muffin-Tin Orbital theory that the interatomic matrix element  $V_\pi$  can be calculated from Eq. (4.8) [58].

$$(4.8) \quad V_\pi = \eta_{pd\pi} \frac{\hbar^2 r_d^{3/2}}{m d^{7/2}}$$

where  $\eta_{pd\pi} = 1.36$  and  $\hbar^2/m = 7.62 \text{ eV}\text{\AA}^2$  are constant.  $r_d$  is the characteristic length of the  $d$ -orbitals of a surface atom. It is constant for a given surface atom. We use the value for  $r_d$  tabulated in the Solid State Table [58].  $d$  is the adsorbate-metal bond length. We use the bond lengths calculated in the DFT-GGA geometry optimization calculations. Eq. (4.8) shows that the interatomic matrix element for a given adsorbate interacting with metal  $d$ -bands on a family of skin alloys (Pt or Pd), is only a function of  $d$  (metal-adsorbate bond length). To calculate the overlap integral  $S$ , we use a simple relationship  $S_\pi \approx -\alpha V_\pi$ , where  $\alpha$  is an adjustable parameter [39, 106]. We also assume that the  $d$ -band filling

of Pt and Pd surface atoms is 0.9, and it is equal for different alloys. This assumption is consistent with previous experimental measurements showing that the formation of alloys is not accompanied by charge transfer between  $d$ -states of constituent metal elements [99, 126, 127]. Due to different geometric arrangements of  $\pi$  and  $\sigma$  orbitals, the overlap integral ratio of  $S_\sigma/S_\pi$  is approximated to be 1.3, calculated previously for the adsorption of CO on transition metal surfaces [106].

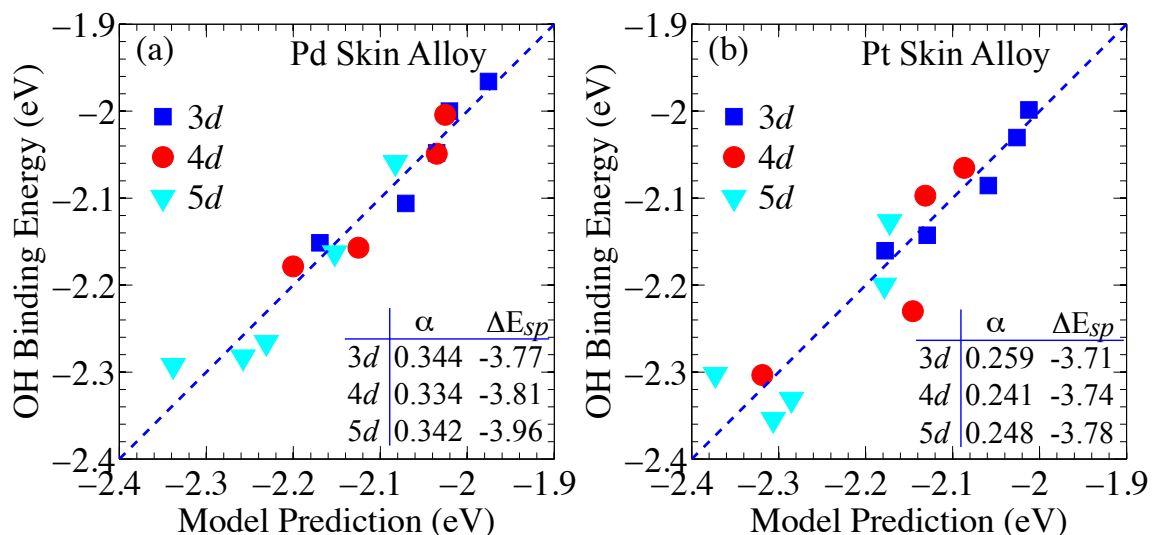


Figure 4.12: Comparison of DFT- and model-calculated OH adsorption energy on Pd (a) and Pt (b) skin alloys. The parameters obtained from the model are tabulated in insert.

Fig. 4.12 shows a comparison between the OH adsorption energies obtained from DFT calculations and the prediction of the model with two adjustable parameters,  $\alpha$  and  $\Delta E_{sp}$ . The adjustable parameters were obtained by minimizing the residual between DFT-calculated adsorption energies and the energies obtained from the model in Eq. (4.6). Fig. 4.12 shows that for a series of Pd and Pt skin alloys with different subsurface atoms (3d, 4d, or 5d) the model captures the chemisorption of OH very well.

#### 4.3.4 Fundamental Mechanisms Associated with this Surface Phenomenon

Further inspection of the tabulated parameters in Fig. 4.12 shows that the interaction of the  $sp$ -band of the alloy substrates ( $\Delta E_{sp}$ ) with the OH adsorbate is attractive. Fur-

thermore, excellent agreement between DFT adsorption energies and the model-predicted energies can be obtained with a constant value of  $\alpha$  and  $\Delta E_{sp}$  for skin alloys with subsurface elements in the same row of periodic table ( $3d$ ,  $4d$ , or  $5d$ ). Comparison between the contribution of  $sp$ -band and the total adsorption energies shows that the interaction with the substrate  $d$ -band is repulsive, and it differs significantly for different alloys as shown in Fig. 4.12(a). It is this repulsion term that drives the unusual behavior of OH on the Pt and Pd skin alloys.

As discussed above, the repulsion is the consequence of orbital orthogonalization between the renormalized adsorbate state and the metal  $d$ -states, which is proportional to  $-SV \approx \alpha V^2$ . This suggests that the adsorption energies of OH on Pt or Pd skin alloys are different due to different interatomic matrix elements ( $V$ ). We showed above that the difference in the interatomic matrix element on Pt or Pd skin alloys arises from different metal-adsorbate bond lengths. The Pt or Pd alloys with larger metal-adsorbate bond lengths (skin alloys containing subsurface atoms to the left in periodic table) have smaller interatomic matrix element and therefore the repulsion between the metal  $d$ -band and the renormalized adsorbate states is weaker. This explains the stronger chemisorption of OH on those alloy surfaces characterized with longer adsorbate-substrate bonds.

It is important to discuss why the Pt or Pd alloys with subsurface atoms to the left in a row of the periodic table have larger metal-adsorbate bond lengths compared to the alloys containing metals to the right in the periodic table. Adsorbate-substrate bond length is to a large degree governed by the substrate  $sp$ -electron density, i.e., the bond length is determined by the distance outside of the surface where the electron density around the adsorbate is optimal for adsorption [23, 39]. This is consistent with the model that shows that a large fraction of the absolute bond strength, and therefore the length of the bond, is due to the interaction of the OH adsorbate with the  $sp$ -band. Due to the difference in

the electronegativity of the different metals in the skin alloys, there is an electron transfer between subsurface and surface metal atoms. It was shown previously, experimentally and theoretically, that mainly free-electron-like  $sp$ -states participate in this electron transfer [126, 127]. This transfer of  $sp$ -charge between subsurface and surface atoms of the substrate affects the adsorbate-substrate bond length. For example, for skin alloys with  $3d$  subsurface metals to the left in the periodic table (e.g., Cr), there is larger driving force to have more electron transfer to the surface due to the increased difference in electronegativity between guest and host metal atoms compared to the subsurface atoms to the right in periodic table (e.g., Ni). In response to this increased electron transfer, the OH adsorbate will move away from the surface to maintain the optimal electron density, as shown in Fig. 4.13 (b).

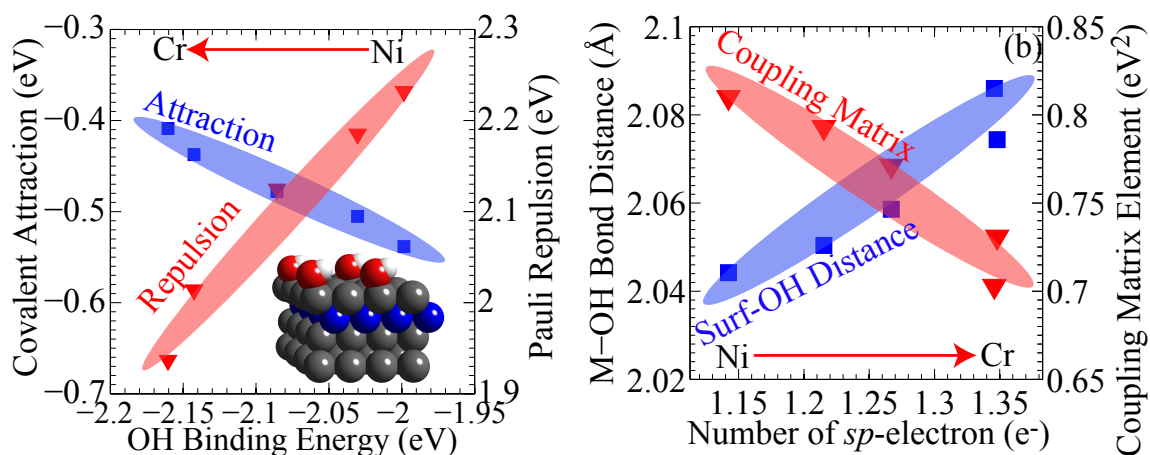


Figure 4.13: (a) The covalent attraction and Pauli repulsion contributions to the OH binding energy on Pt skin alloys with  $3d$  subsurface atom calculated using the model discussed in the text. (b) Surf-OH bond distance and the coupling matrix element ( $V^2$ ) are plotted as a function of the number of  $sp$ -electrons on the surface substrate atoms. The number of  $sp$ -electrons was calculated as total Bader charge minus the  $d$ -band filling.

It is also important to understand why OH and O exhibit fundamentally different chemisorption behavior on the skin alloys as shown in Fig. 4.3. The main difference between OH and O is that the O atom in OH is more electron rich, i.e., there is a transfer of electron density from H to O in OH. This shift in electron density causes the OH adsorbate to require lower

optimal electron density when adsorbed on a metal surface than the O adsorbate. Since the lower electron density is encountered further away from the surface atoms, the bond distance between the OH adsorbate and the substrate surface is larger than that for the O adsorbate. This larger bond distance results in smaller coupling matrix element for the adsorption of OH, ultimately yielding smaller spread between bonding and anti-bonding metal-OH states and causing the anti-bonding states (formed due to the hybridization of OH  $1\pi$  molecular orbital with surface  $d$ -states) to be below the Fermi level. The populated anti-bonding state effectively means that the interaction between substrate  $d$ -states and the adsorbate states is repulsive [104]. Unlike the OH adsorbate, atomic O binds closer to a metal surface, and the coupling matrix element is much larger. This large coupling matrix element pushes the anti-bonding metal-O states to be partially above the Fermi level, resulting in the trend dominated by the covalent attraction between the  $d$ -band and renormalized adsorbates states. The position of the partially occupied anti-bonding state with respect to the Fermi level is dependent on the position of the substrate  $d$ -band center; higher  $d$ -band center leads to higher energy of the anti-bonding state and so results in less occupied anti-bonding states and stronger chemical bonding.

#### 4.3.5 Generality of this Surface Phenomenon

OH adsorption on the Pt and Pd skin alloys is not the only exception to the  $d$ -band model of chemisorption. In fact any adsorbate characterized by the repulsive interaction between substrate  $d$ -states and renormalized adsorbate states will behave similarly, i.e., stronger bonding will be accompanied by larger bond length and lower energy of the center of  $d$ -band projected on surface atoms. These systems are always associated with substrates that have nearly fully occupied  $d$ -band (mainly  $d^9$  and  $d^{10}$  metals) and adsorbates with almost completely filled valence shell (OH, F, Cl,  $\dots$ ). In Fig. 4.13 (a, b) we show that F and Cl show similar dependence on the center of  $d$ -band projected on surface atoms of

the Pt and Pd skin alloy compared with the OH adsorbate. The same trend follows the chemisorption of O and OH on Ag and Au skin alloys.

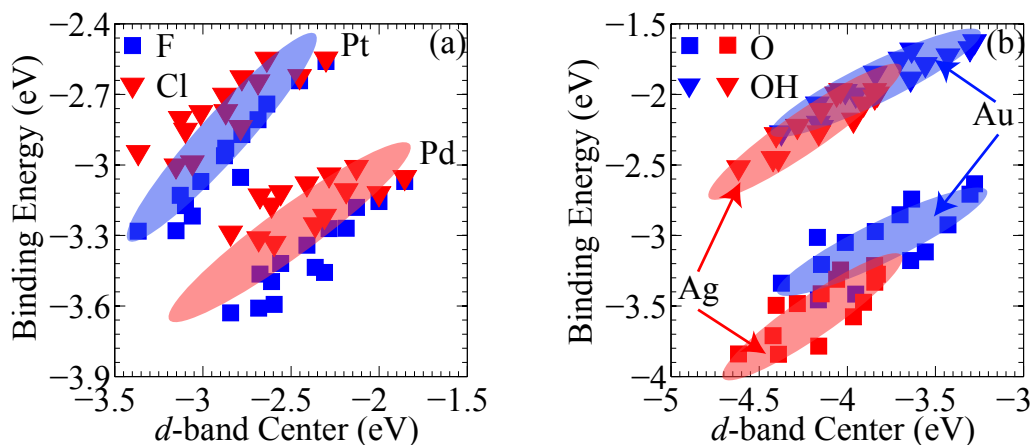


Figure 4.14: (a) F and Cl adsorption energies on Pt and Pd skin alloys as a function of  $d$ -band center. (b) O and OH adsorption energies on Au and Ag skin alloys as a function of  $d$ -band center.

#### 4.4 Potential Application of the Model for Alloy Catalyst Design

Alloy materials represent a virtually infinite phase space of potential heterogeneous catalysts. While many alloys have been found to exhibit excellent performance for various catalytic reactions, the vast phase space of possible formulations precludes thorough screening, even with combinatorial high-throughput experiments or quantum-chemical calculations. A long-term goal of fundamental catalysis using alloy materials is to develop simple models for predicting variations in chemisorptions energies of important reaction intermediates based on physical characteristics of the constituent metal elements and feasible schemes for rapid screening of optimal alloy compositions.

In this Section, we have developed such a physically transparent model that allows us to relate easily accessible physical characteristics of the elements that form an alloy (mainly their electronegativity, atomic radius, and the spatial extent of valence orbitals) to the catalytic performance of alloy sites. Compared to previously developed computational searching methods based on electronic descriptors, this model permits rapid screening

through an enormous phase space of alloy structures and compositions using analytical expressions instead of expensive quantum-chemical calculations. We have specifically focused on Pt-based multimetallic catalysts for the electrochemical oxygen reduction reaction (ORR). We demonstrate that: (1) the simple model allows for rapid screening through large libraries of Pt-alloys, (2) the model identifies almost all Pt alloys that have thus far been shown to exhibit enhanced ORR activity compared to pure Pt and suggests many new promising alloy compositions, and (3) since the model is grounded on validated theories of chemisorption on metal surfaces, it allows us to identify the critical physical features that characterize optimal alloy electrocatalyst for ORR and propose how these features can be engineered.

#### 4.4.1 Computational Details

The DFT calculations were performed using the ultra-soft pseudopotential plane-wave method with the generalized gradient approximation (GGA-PW91) coded in Dacapo. The wave-functions were expanded in plane-waves with an energy cutoff of 450 eV. The Pt alloy surfaces were modeled by a  $2 \times 2 \times 4$  slab for Pt/X/Pt(111) and Pt/X(111) alloy structures and  $2 \times 2 \times 6$  slab for Pt/PtX(111) and Pt/Au/AuXY(111) alloy structures separated by 10 Å of vacuum space. The adsorbates and top two layers were allowed to relax until the total force on the atoms was less than 0.05 eV/Å. In the  $p(2 \times 2)$  Pt surface unit cell,  $4 \times 4 \times 1$  Monkhorst-Pack  $k$ -points were used for the Brillouin-zone integration. Convergence of the results with respect to various calculation parameters was verified in all cases. Various types of model system were used in this study, such as Pt monolayer skin alloy, 1<sup>st</sup>-generation core-shell and 2<sup>n</sup> $d$ -generation core-shell as shown in Figure below.

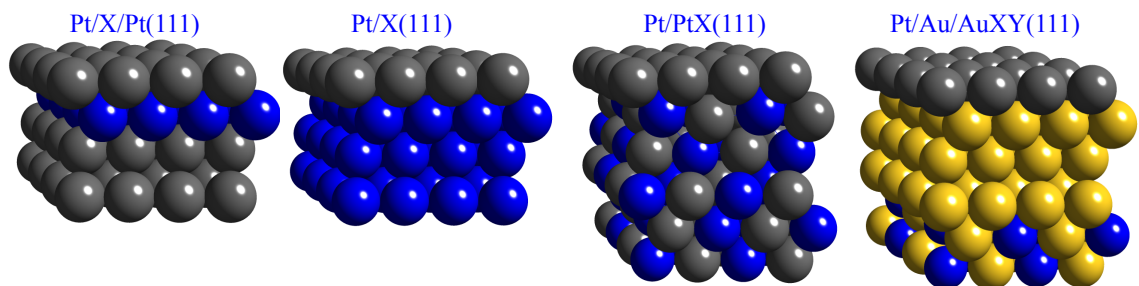


Figure 4.15: Geometric structure of different model alloys

#### 4.4.2 Pt-Containing Electrocatalysts Design for Fuel Cell Applications

The primary cause of efficiency loss in low temperature proton exchange membrane (PEM) fuel cells is the sluggish kinetics of the ORR,  $4(\text{H}^+ + e^-) + \text{O}_2 \rightarrow 2\text{H}_2\text{O}$ , at the cathode as illustrated in Fig. 4.16 (a) [128–130]. Though Pt is the best pure-metal ORR electrocatalyst, it still exhibits an appreciable overpotential due to the strong binding of surface hydroxyl (OH) to surface Pt sites, which poisons Pt at high operating potentials [23, 128, 131]. The key objective in formulating optimal Pt alloys for ORR is to identify elements that would, when alloyed with Pt, electronically perturb the surface Pt sites so that they bind OH with slightly lower adsorption energy ( $\sim 0.1$  eV less exothermic) than pure Pt without changing the rate limiting step to be  $\text{O}_2$  activation as illustrated in Fig. 4.16 (b) [23, 80, 130]. In this Section we propose a model that accomplishes this objective, allowing us to rapidly screen through the immense phase space of Pt alloys. In our analysis, we assume that under relevant electrochemical conditions the surface of Pt alloys is occupied by Pt atoms, which is consistent with experimental and computational findings [8, 95, 132–134].

We have previously shown that the change in the OH adsorption energy on a Pt site as a function of the local chemical environment of the site can be described by focusing on the interactions of the local  $d$ -states of the site with the OH adsorbate states [127]. More

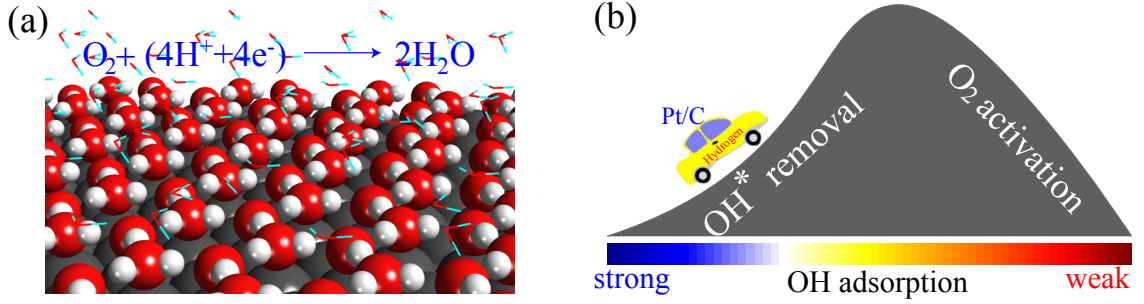


Figure 4.16: (a) Schematic of electrode water interface where OH adsorbs (a) Objective for tuning the surface reactivity for ORR

specifically, we showed that the change in the OH adsorption energy ( $\Delta\Delta E$ ), in response to the change in the local chemical environment of the Pt surface site, is governed by two physical characteristics of the site: the average energy of electronic  $d$ -states projected on the adsorption Pt site (i.e., the center of  $d$ -band,  $\varepsilon_d$ ), and the interatomic matrix element ( $V_{ad}^2$ ) [58] describing the coupling strength of OH valence states with the substrate  $d$ -band. For small perturbations in the local chemical environment of the Pt site, for example induced by alloying, the change of adsorption energy ( $\Delta\Delta E$ ) can be written as a linear function of  $\Delta\varepsilon_d$  and  $\Delta V_{ad}^2$  as shown in Eq. 4.9.

$$(4.9) \quad \Delta\Delta E = k_1\Delta\varepsilon_d + k_2\Delta V_{ad}^2$$

Eq. (4.9) can be easily derived based on the first-order Tylor expansion of  $\Delta\Delta E$  with respect to  $\varepsilon_d$  and  $V_{ad}^2$  as shown in Eq. 4.10.

$$(4.10) \quad \Delta\Delta E = \left(\frac{\partial\Delta E}{\partial\varepsilon_d}\right)_{V_{ad}} \Delta\varepsilon_d + \left(\frac{\partial\Delta E}{\partial V_{ad}^2}\right)_{\varepsilon_d} \Delta V_{ad}^2$$

where,

$$(4.11) \quad \left(\frac{\partial\Delta E}{\partial\varepsilon_d}\right)_{V_{ad}} = -4(1-f)\frac{V_{\pi}^2}{(\varepsilon_d - \varepsilon_{1\pi})^2} - 2f\frac{V_{\sigma}^2}{(\varepsilon_d - \varepsilon_{4\sigma^*})^2}$$

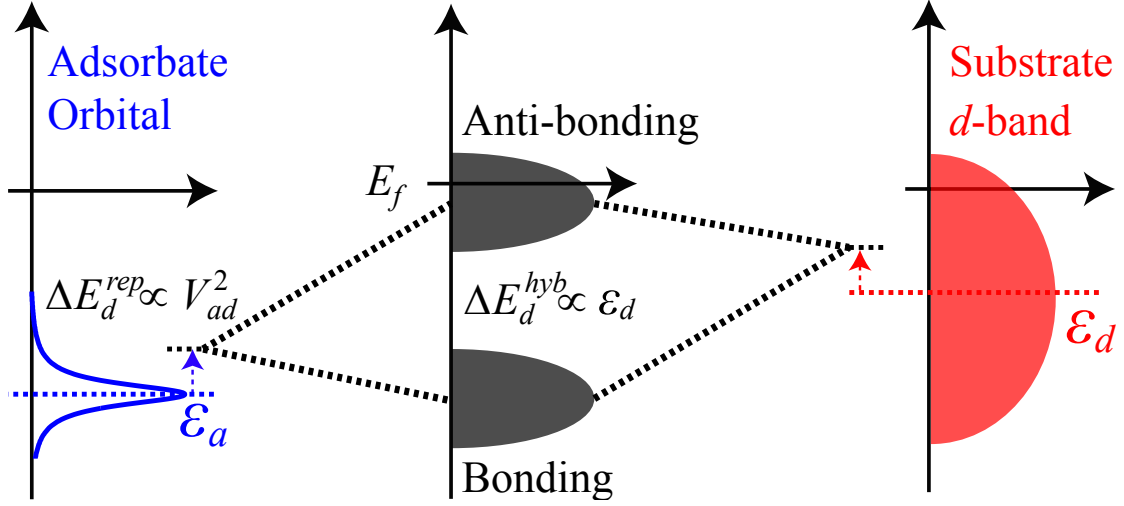


Figure 4.17: Schematic illustration of the chemical bonding between adsorbate states and metal  $d$ -states, which leads to an upward shift in energies due to the Pauli repulsion, followed by the formation of bonding and anti-bonding states due to the orbital hybridization.

and,

$$(4.12) \quad \left( \frac{\partial \Delta E}{\partial V_{ad}^2} \right)_{\epsilon_d} = -4 \left[ (1-f) \frac{1}{|\epsilon_d - \epsilon_{1\pi}|} - \alpha(1+f) \right] - 2 \left[ f \frac{1.3^2}{|\epsilon_d - \epsilon_{4\sigma^*}|} - 1.3^2 \alpha f \right]$$

where the constant 1.3 comes from the approximation  $V_{4\sigma^*} \approx 1.3V_{1\pi}$  [106]. Based on the tabulated parameters [135] we can easily get the linear coefficient  $k_1 \approx -0.20$  and  $k_2 \approx 1.95$  eV<sup>-1</sup>.

On a conceptual level, the first term in Eq. 4.9 describes the covalent attraction due to the hybridization between an adsorbate state (orbital) and substrate  $d$ -states, while the second term describes the Pauli repulsion due to the energy cost associated with the orbital orthogonalization as illustrated in Fig. 4.17 [63, 136]. We have previously demonstrated that when  $\Delta\epsilon_d$  and  $\Delta V_{ad}^2$  are calculated using self-consistent Density Functional Theory (DFT) [127, 135], the model gives excellent agreement with the DFT-calculated OH adsorption energies on Pt-based alloys [127].

We now make Eq. 4.9 useful for rapid screening of optimal ORR alloy catalysts by

developing simple expressions, which do not require computationally expensive quantum-chemical calculations, to evaluate the change in the  $d$ -band center ( $\Delta\varepsilon_d$ ) of the Pt adsorption site and the change in OH-Pt coupling matrix element ( $\Delta V_{ad}^2$ ), in response to the perturbation of the local chemical environment of Pt due to alloying.

#### 4.4.3 Prediction of Adsorbate Bond Distance to the Surface

It has been shown based on Muffin-Tin Orbital Theory within the tight binding approximation that, for an adsorbate on metal sites, the coupling matrix element,  $V_{ad}$ , is a function of the adsorbate-metal bond distance,  $d$ , and the spatial extent of the metal  $d$ -orbital ( $r_d$ ) ( $V_{ad} \propto r_d^{3/2}/d^{7/2}$ ) [58]. For OH adsorption on Pt sites,  $r_d$  is identical, irrespective of the chemical environment of the site (i.e., it is an inherent property of the Pt atom). Therefore the change in OH-Pt coupling matrix,  $\Delta V_{ad}^2$ , in response to the formation of an alloy (more specifically the change of the local chemical environment) is only a function of the change in the metal-OH bond distance. To determine the relative OH-Pt bond distance for different Pt alloys, we have employed extensive DFT studies which established that, on geometrically similar Pt sites of alloys, the bond distance is linearly correlated with the difference in the geometric mean [137] of the Mulliken electronegativity of the local Pt atom and its neighboring atoms, as shown in Eq. 4.13. The proportionality coefficient,  $\gamma=0.094$ , was obtained by linearly fitting the metal-OH bond distance calculated using DFT for a subset of Pt alloy surfaces. Comparison of bond distances predicted by the model to DFT calculations shows good agreement (RMSE $\approx 0.01$  Å) for many different families of Pt monolayer alloys as shown in Fig. 4.18.

$$(4.13) \quad \Delta d = \gamma \left( \left[ \prod_i^N \chi_i^{nm} \right]^{1/N} - \chi_{Pt} \right) = \gamma \Delta \chi$$

The observed relationship between the change in electronegativity and the metal-OH bond distance can be rationalized by the fact that the main fraction of OH adsorption en-

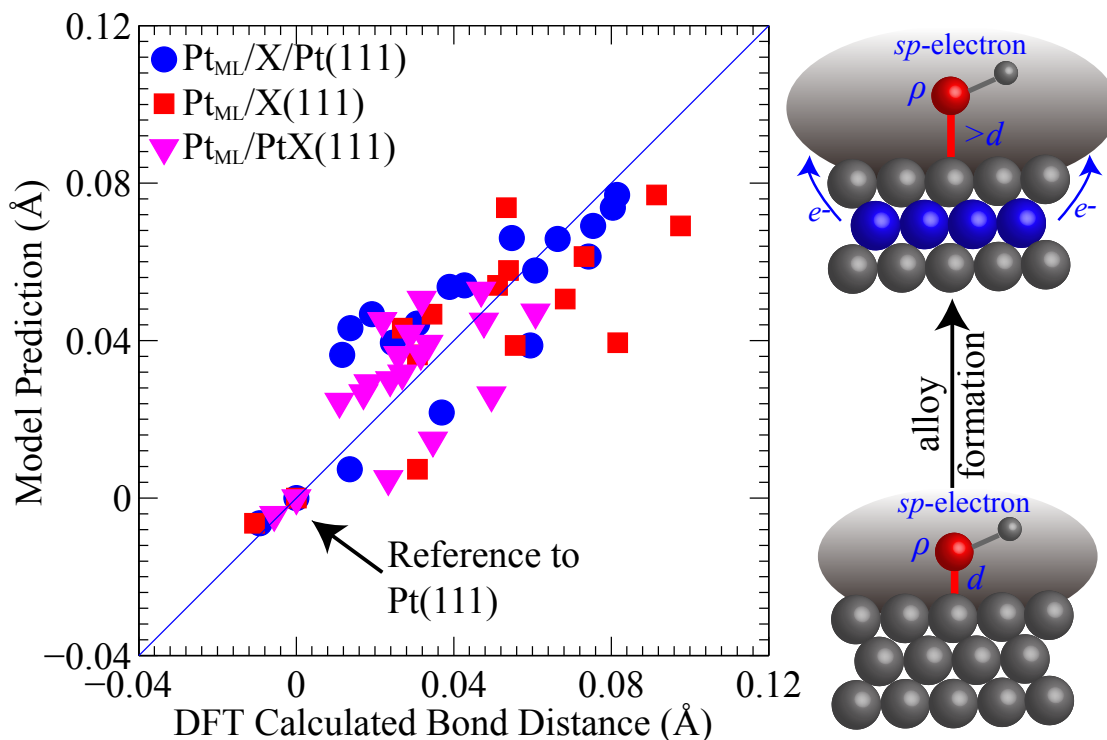


Figure 4.18: DFT calculated metal-OH bond distance on various Pt alloy surfaces correlated with the prediction of the model in Eq. 4.13. The sketch is an illustration of the effect of the change in the surface electron density on the adsorbate-substrate bond distance.

energy on Pt sites comes from the interaction of the OH valence states with the free-electron-like  $sp$ -band of the substrate. Thus, the interaction between the  $sp$ -band and the OH states, to a large degree, governs the metal-OH bond distance [23]. Due to the difference in the electronegativity of Pt atoms and the neighboring atoms in an alloy, there is a transfer of electron density, changing the filling of the  $sp$ -band of Pt (i.e., the free-electron density is perturbed). This change in the local electron density affects the adsorbate-substrate bond length at the local site as illustrated in Fig. 4.18 [138]. The process can be understood in terms of the adsorbate seeking the regions of optimal electron density on a metal surface. The electron density around local adsorption sites changes in response to the formation of an alloy, and the adsorbate responds by changing the bond distance and finding a new geometry with optimal electron density. In practice, this means that if a Pt surface site is surrounded by less electronegative atoms, charge will be transferred to the Pt site, and the

OH adsorbate will move further away, lengthening the bond. We have noted that the same relationship exists for many other adsorbates on Pt alloy surfaces based on the electronegativity defined in Eq. 4.13. The parameters are shown in Table below along with the Parity plot.

#### 4.4.4 Simple Models for the Prediction of $d$ -band Center of Alloys

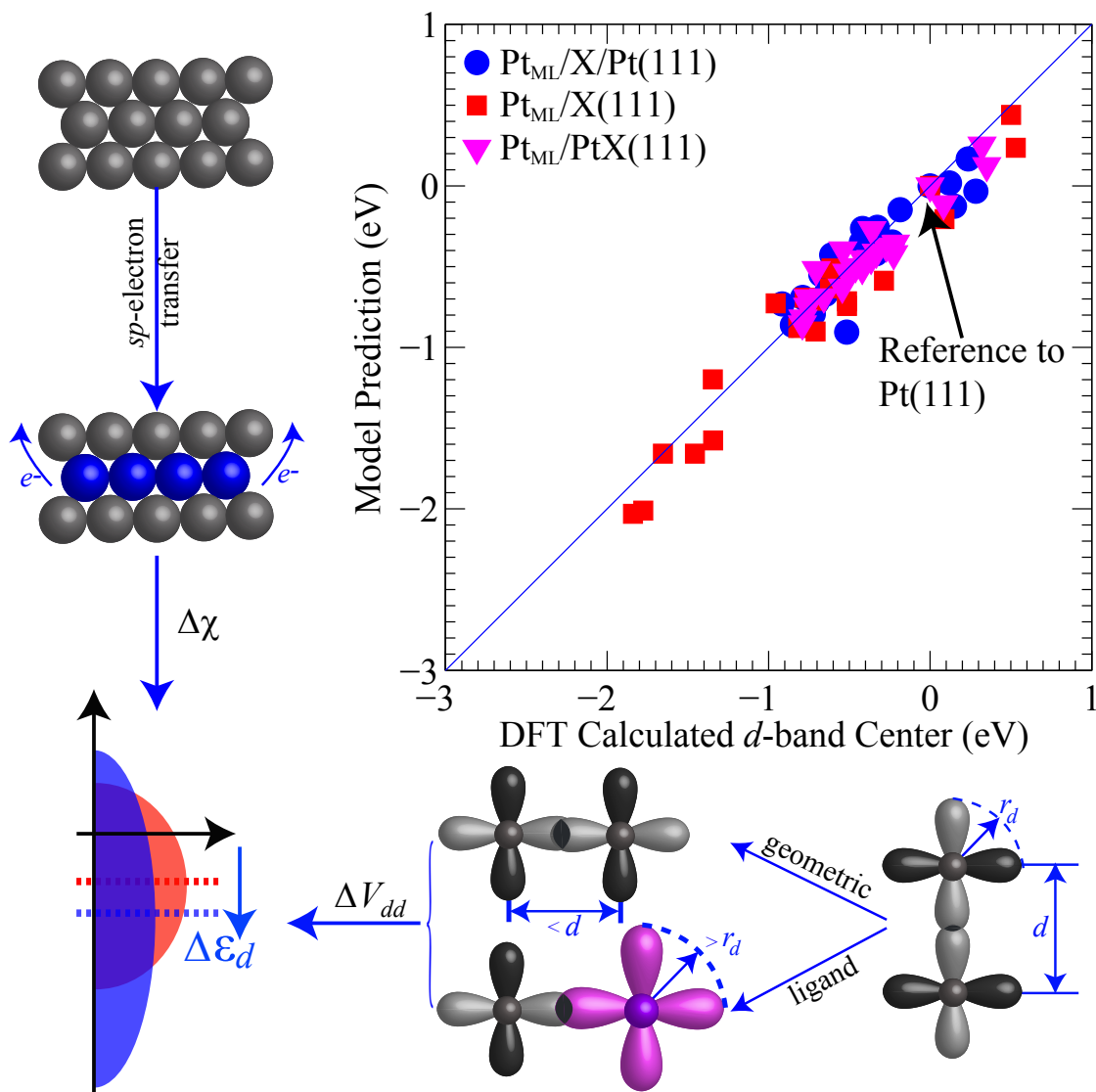


Figure 4.19: DFT calculated local  $d$ -band center of various Pt alloy surfaces correlated with the model prediction using Eq. 4.14.

As shown in Eq. 4.9, the other major quantity governing the relative OH adsorption

energy on Pt sites is the center of the electronic  $d$ -band ( $\epsilon_d$ ) projected on the site. It has been shown previously that for many alloys, the shift in the center of the  $d$ -band ( $\Delta\epsilon_d$ ) projected on individual atoms, induced by the change in the local chemical environment of the site, is uniquely determined by the change in the  $d$ -band width (the spread of  $d$ -states around the center of the  $d$ -band) as shown in Eq. 4.14 and described in more detail below [99, 126, 135].

$$(4.14) \quad \Delta W_d^i \propto \Delta\epsilon_d^i = \alpha\Delta \sum_j V_{dd}^{ij} + \beta\Delta\chi$$

The change in the  $d$ -band width for a given substrate atom is governed by the interaction of the  $d$ -orbitals of that atom with the valence orbitals of neighboring atoms (both  $d$ -states and the delocalized  $sp$ -states) [58]. The interaction with neighboring  $d$ -orbitals is captured by the  $d$ - $d$  interatomic matrix element ( $V_{dd}$ ) describing the  $d$ -coupling strength [58, 139, 140]. This is a function of the bond distance between neighboring atoms and the spatial extent of the  $d$ -orbitals:  $V_{dd}^{ij} \propto r_{d_i}^{3/2} r_{d_j}^{3/2} / d_{ij}^5$  [58, 118, 135, 139, 140]. The bond distance between neighboring atoms ( $d$ ) in an alloy can, in turn, be estimated by generalizing Vegard's law, while the spatial extent of  $d$ -orbital ( $r_d$ ) is an intrinsic property of the pure metal atom [58]. In our analysis we used  $r_d$  values calculated using Muffin-Tin Orbital Theory within the tight binding approximation [58]. Finally, the change in the  $d$ -band width due to interaction with the free-electron-like  $sp$ -band can be described in terms of the difference in electronegativity (governing  $sp$ -electron density),  $\Delta\chi$  (defined in Eq. 4.13) [58, 141]. The parameters  $\alpha=-6.21$  and  $\beta=0.55$  eV in Eq. (3) were obtained by linearly fitting DFT-calculated  $d$ -band centers for strained surfaces of pure Pt and a subset of alloy surfaces, respectively [139, 140]. Comparison of the  $d$ -band center predicted by the model to the DFT calculations for different families of Pt alloys shows that the model predicts the change of  $d$ -band center very well with RMSE $\approx 0.1$  eV (as shown in Fig. 4.19).

#### 4.4.5 Rapid Screening of Pt-Containing Multimetallic Electrocatalysts

The practical value of Eq. 4.9-Eq. 4.14 is that the relative adsorption energy of OH (with respect to pure Pt) and therefore the relative ORR activity of Pt sites on various Pt alloys can be calculated using only physical characteristics of the constituent metal elements. This allows for a rapid screening through a large phase space of Pt alloy compositions and geometries to identify those with desired catalytic properties (in this case binding OH with  $\sim 0.1$  eV lower adsorption energy than pure Pt [23, 80, 130]).

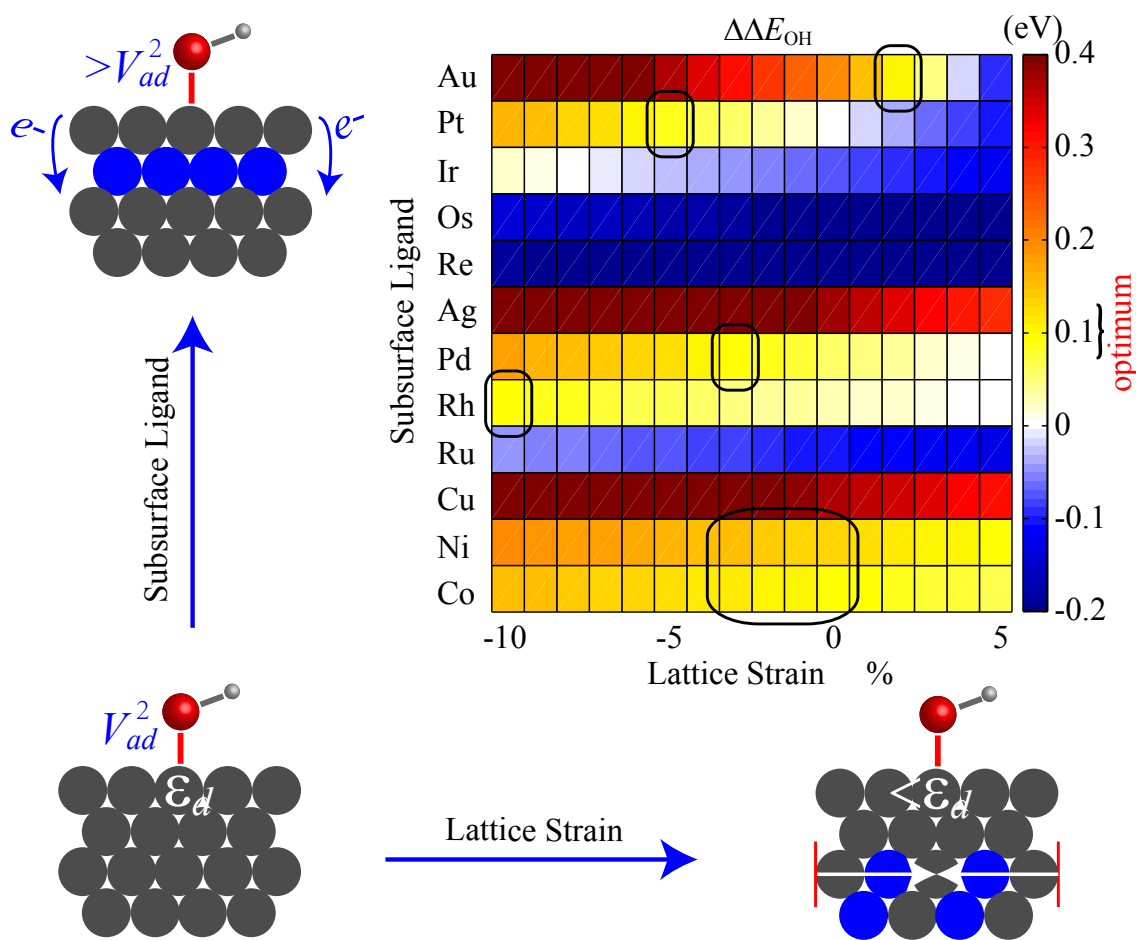


Figure 4.20: Model prediction of OH binding energies on Pt monolayer alloy surfaces with varying subsurface ligand (1 ML) and lattice strain (-10% to 5% expansion). Marked regions depict the alloy systems with desired catalytic properties ( $\sim 0.1$  eV weaker OH binding than pure Pt). Inserts show different mechanisms by which the OH adsorption energy changes.

To illustrate the value of the model in Eq. 4.9-Eq. 4.14, we first use it to investigate

the effect of a simultaneous change in the substrate lattice constant and the nature of sub-surface metal on the OH adsorption energy on Pt surface sites. Here, the model system is a pure Pt slab, with variable lattice constant and Pt atoms in the second layer are substituted by another element. Fig. 4.20 shows that compression of the Pt-Pt bond in the surface layer lowers the OH adsorption energy. In this case, the compressed lattice yields an increased overlap among neighboring  $d$ -orbitals and therefore larger coupling matrix element,  $V_{dd}$  [109]. This results in a wider substrate  $d$ -band, lower  $d$ -band center, and therefore weaker OH-metal bond according to Eq. 4.9. Alloys exhibiting these structural features have been synthesized by depositing Pt monolayers pseudomorphically on a substrate with compressed lattice compared to Pt [79, 142]. Fig. 4.20 also shows that a similar outcome is accomplished in Pt alloys with the second layer rich in  $3d$  metals. These inter-metallic compounds (e.g., Pt<sub>3</sub>Ni and Pt<sub>3</sub>Co), often called 1<sup>st</sup> generation core-shell alloys, have been identified previously experimentally, showing 2~3 times increased specific activity over pure Pt [95–97]. Fig. 4.20 also shows that Pt alloys in which the Pt surface sites are coordinated with more electronegative metal atoms (e.g., Au) bind OH less strongly than pure Pt. The model in Eq. 4.9-Eq. 4.14 suggests that the reason for this is that the withdrawal of  $sp$ -electron density from the Pt adsorption site by Au results in a shorter OH-metal bond which in turn increases the repulsive interaction between adsorbate states and metal  $d$ -states [127]. Similar structures have also been shown previously to exhibit enhanced ORR activity [143, 144]. For example, a Pt monolayer deposited on an Au interlayer, which is supported on Au-Ni-Fe ternary alloy, has been shown to exhibit 5- to 7-fold improved specific activity compared to pure Pt [143, 144]. These multi-layer alloys are often referred to as 2<sup>nd</sup> generation core-shell alloys.

In general, Fig. 4.20 gives us critical insights about the nature of the optimal Pt site for the ORR. The optimal Pt sites are characterized by a lower center of the  $d$ -band projected

on the surface Pt atoms and/or shorter Pt-OH bond distance compared to pure Pt. In practice there are three ways to accomplish these objectives: (1) creating alloys where surface Pt-Pt bonds are contracted, (2) coordinating Pt surface sites with  $3d$  metals, (3) coordinating Pt surface sites with more electronegative metals (Au).

Among identified geometries, particularly appealing are the  $2^{nd}$  generation core-shell alloys characterized by a Pt monolayer on top of an Au-interlayer, which is then supported on an alloy core. These structures are desirable since the Au interlayer gives enhanced protection to elements in the core that are otherwise thermodynamically unstable under relevant electrochemical conditions [143]. Additionally, these materials are characterized by relatively low Pt content moderating the cost of raw materials. To further probe the  $2^{nd}$  generation core-shell alloys, we have applied the model in Eq. 4.9-Eq. 4.14 to screen through a large library of Pt monolayer alloys that belong to this family of materials. In this model, the core contained Au (75%) with two other (X and Y) metal elements (25% total). The lattice constant of the core structure was estimated from Vegard's law, i.e., the composition weighted lattice constant of constituent metal elements. The interlayer between the core and the Pt surface layer contained 3 layers of Au. The model-predicted adsorption energies of OH on those alloy surfaces, relative to pure Pt, are shown in Fig. 4.21 as a function of the X and Y elements.

Fig. 4.21 demonstrates that the rapid screening procedure identified a large number of promising  $2^{nd}$  generation Pt monolayer core-shell alloys, characterized with weaker OH binding energies ( $\sim 0.1 \pm 0.02$  eV) than pure Pt. It is encouraging to note that some of these alloys, such as the above mentioned  $Pt_{ML}/Au/Au-Ni-Fe$ , have been synthesized and tested previously, showing an improved performance compared to pure Pt [143]. Fig. 4.21 shows that in the family of  $2^{nd}$  generation core-shell alloys, in addition to the previously tested  $Pt_{ML}/Au/Au-Ni-Fe$  alloy, there are many additional Pt alternatives. In all of these

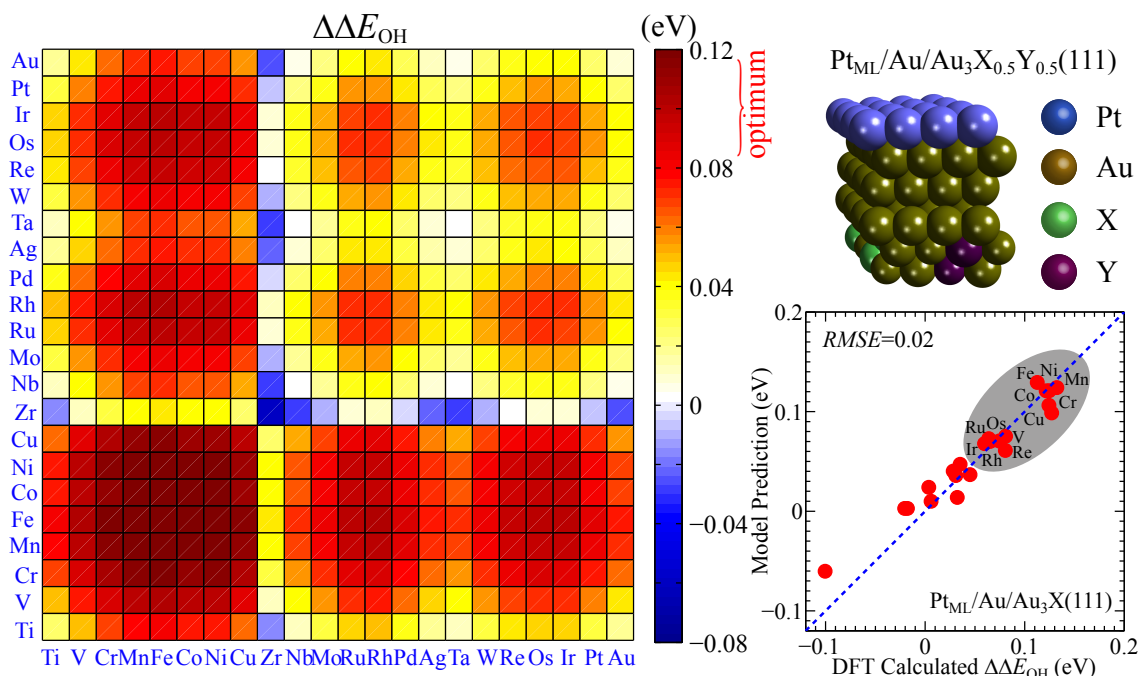


Figure 4.21: Model screening of OH adsorption on core-shell alloy surfaces  $\text{Pt}_{ML}/\text{Au}/\text{Au}_3\text{X}_{0.5}\text{Y}_{0.5}(111)$ . The parity plot in the bottom right insert shows a comparison of the OH binding energies on selected Pt monolayer alloys calculated using the model and self-consistent DFT. Top right figure shows the model system.

cases a combination of Au-induced shortening in Pt-OH bond length and the change in substrate lattice constant due to alloy formation pushes the OH adsorption energy towards the desired values ( $\sim 0.1$  eV lower bond strengths compared to pure Pt).

We have compared the adsorption energy calculated using the simple model in Eq. 4.9- Eq. 4.14 with the self-consistent DFT calculations for a few selected  $2^{nd}$  generation core-shell alloys ( $\text{Pt}_{ML}/\text{Au}/\text{Au}_3\text{X}(111)$ ). These calculations showed that the model can adequately predict even small changes in the OH adsorption energy with  $\text{RMSE} \approx 0.02$  eV. Thorough testing of the model showed that it performs the best for alloy structures characterized by small perturbations compared to pure Pt, manifested in small alloy-induced changes in the substrate lattice constant and the Pt alloying with metals of similar electronegativity. It is important to note that alloys with these characteristics are of particular interest since they should be the easiest to synthesize [145].

## 4.5 Summary

We have used X-ray absorption spectroscopy (XAS) and quantum chemical density functional theory (DFT) calculations to identify critical features in the electronic structure of different sites in alloys that govern the local chemical reactivity. The measurements led to a simple model relating local geometric features of a site in an alloy to its electronic structure and chemical reactivity. The central feature of the model is that the formation of alloys does not lead to significant  $d$ -charge transfer between the constituent metal elements in the alloys, and that the local electronic structure and chemical reactivity can be predicted based on physical characteristics of constituent metal elements in their unalloyed form.

We show that there is a family of adsorbate-substrate systems that does not follow the trends in adsorption energies predicted by the  $d$ -band model. A simple, physically transparent model is used to analyze this phenomenon. We found that these adsorbate-substrate pairs are characterized by the fact that Pauli repulsion dominates the interaction of the substrate  $d$ -band with the adsorbate. The exceptions to the  $d$ -band model are mainly associated with the adsorbates having almost completely filled valence shell, and the substrates with nearly fully occupied  $d$ -band, i.e., OH, F, Cl adsorbing on metals and alloys characterized by  $d^9$  or  $d^{10}$  substrate surface atoms. We have established the key underlying factors governing variations in the surface electronic structure upon alloy formation. A physically transparent framework allowing us to relate these factors to the change in OH chemisorption energies on Pt alloy surfaces was developed. This framework was used to search through libraries of Pt alloys allowing us to identify the key features of optimal catalytic sites and suggest alloy compositions that meet the criteria for promising ORR catalysts.

We have established the key underlying factors governing variations in the surface elec-

tronic structure upon alloy formation. A physically transparent framework allowing us to relate these factors to the change in OH chemisorption energies on Pt alloy surfaces was developed. This framework was used to search through libraries of Pt alloys allowing us to identify the key features of optimal catalytic sites and suggest alloy compositions that meet the criteria for promising ORR catalysts.

## CHAPTER V

### Doping of Substrates with Chemical Promoters

#### 5.1 Introduction

Interactions among adsorbates on metal surfaces play a critical role in heterogeneous catalysis [82, 146, 147], electro-catalysis [79], self-assembly [148], nucleation and growth [149, 150], and almost every other phenomenon governed by chemical or physical surface processes. Traditionally, adsorbate-adsorbate interactions have been grouped into two categories: direct and indirect interactions [151–154]. Direct interactions [151, 152] can be further divided into the electrostatic interaction of charge distributions, the covalent bond formation due to orbital hybridization, and the Pauli repulsion resulting from orbital orthogonalization. Indirect interactions [153, 154] are characterized by adsorbate-induced electronic or structural modifications of metal surfaces. Understanding of adsorbate-adsorbate interactions on metal surfaces is critical to unearth the underlying mechanism of promotion and poisoning effect in heterogeneous catalysis [83]. Additives that are often used in the design of heterogeneous catalysts are alkali metal elements, such as sodium (Na), potassium (K) and cesium (Cs), which have been shown to significantly alter the outcome of catalytic reactions by selectively promoting or inhibiting targeted elementary steps [82, 83, 147]. To illustrate the effect of alkali promoters on the catalytic reactions, in Fig. 5.1 (adapted from [155]) we show dramatically enhanced reaction rate of ammonia

synthesis over ruthenium (Ru) catalysts with the introduction of alkali promoters [155]. Recent work of Davis et al. using steady-state isotopic transient kinetic analysis have yielded similar conclusions, mainly that the intrinsic rate of ammonia synthesis increases by two orders of magnitude for the Cs-promoted Ru catalyst as compared to un-promoted Ru at identical reaction conditions [156]. Many others have made similar observations [157–162]. In addition to ammonia synthesis it has been shown that alkali promoters enhance reactivity and/or selectivity in many other critical commercial processes including Fisher-Tropsch synthesis [163, 164], alcohol synthesis [155, 165], water-gas shift reactions [155], olefin epoxidation [77, 166], automotive three way converters [167].

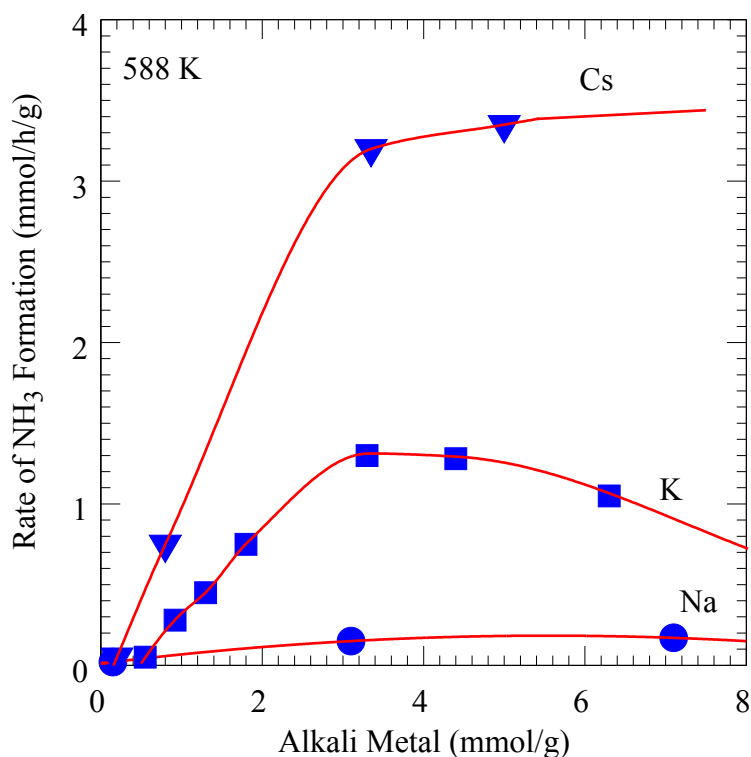


Figure 5.1: Dramatically enhanced reaction rate of ammonia synthesis over ruthenium (Ru) catalysts with the introduction of alkali promoters. Circle: Na, Square: K, Triangle: Cs.

Although the alkali promotion effect in heterogeneous catalysis has been recognized for decades [155, 168–172], there still lacks cohesive insights regarding the role of alkali

metals in catalytic reactions. Multiple investigators have argued that alkali adsorbates act through an electrostatic mechanism [9, 173]. Specifically, alkalis induce strong electric fields that interfere with relevant surface intermediates and transition states via the long-range, static dipole-dipole interaction [9, 173]. Others have suggested that alkalis influence the surface chemistry by modifying the electronic structure of metal catalysts [146]. There is also the postulation that alkali metals act as geometric promoters by increasing the dispersion of active metal catalysts [174] or simply by blocking the un-selective site [175].

In this Chapter, the issue of alkali promotion is addressed in a case study of the role of Cs adatoms on silver (Ag) catalysts for oxidation reactions. We choose the Cs/Ag system since it is well-established that alkali promoters enhance the reactivity and/or selectivity in various olefin epoxidation reactions on Ag catalysts [176–179]. For example, Campbell [77] and Grant et al. [166] have demonstrated experimentally that Cs promoters enhance the reactivity of Ag catalyst as well as the selectivity towards ethylene oxide in ethylene epoxidation over well-defined Ag surfaces.

Density Functional Theory (DFT) calculations, ab-initio atomistic thermodynamics, and Monte Carlo simulations were employed in this study. We emphasize that those computational methods allow us to go beyond the zero Kelvin temperature and zero pressure, i.e., beyond the conditions that are usually associated with DFT calculations [180–184]. We believe that pressure and temperature have a significant impact on the mechanisms of alkali promotion. While in this studies we focus on the case of Cs promotion in oxidation reactions over silver catalysts, every attempt is made to formulate universal knowledge-base that extends far beyond the concrete case studies. In addition to unearthing the underlying mechanisms associated with alkali promotion, the acquired knowledge-base will allow us to shed light on the general problem of adsorbate-adsorbate interactions on metal surfaces.

## 5.2 Computational Methods

### 5.2.1 DFT Calculations

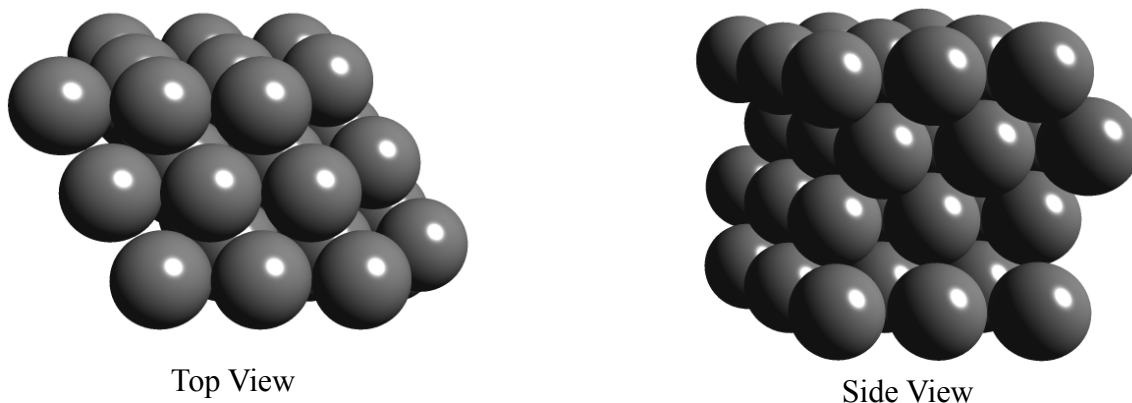


Figure 5.2: Top and side view of Ag(111) model systems employed in our DFT calculations ( $3 \times 3 \times 4$  unit cell as an example)

First-principles density functional theory (DFT) calculations are performed using the ultrasoft pseudopotential [100] plane wave method with the generalized gradient approximation (GGA-PW91) coded in Dacapo [185]. In our calculations we employ a close packed Ag(111) substrate as a model system as shown in Fig. 5.2 (top and side view of  $3 \times 3 \times 4$  unit cell). The wave-functions are expanded in plane waves with an energy cutoff of 350 eV and the Ag(111) surface is modelled by a four-layer slab separated by  $10 \text{ \AA}$  of vacuum space. Adsorbates are placed on one side of slab where the induced dipole moment is taken into account by applying a dipole correction. The adsorbates and top two silver layers are totally relaxed until the force on the atoms is less than  $0.05 \text{ eV/\AA}$ .  $4 \times 4 \times 1$  Monkhorst-pack [186]  $k$ -points is used for the Brillouin zone integration. The equivalent  $k$ -points sampling is used for all of the surface structures studied in order to maximize the accuracy when comparing the energies of different structures as calculated in different size of unit cells. Finite temperature Fermi smearing function ( $k_B T = 0.1 \text{ eV}$ ) is utilized to facilitate the SCF convergence, and the total energy is extrapolated to  $k_B T = 0 \text{ eV}$ . A climbing-image nudged elastic band method [187] was used to find saddle points

and minimum energy pathways for elementary reaction steps on the clean and Cs-doped Ag(111) surfaces. The frequency analysis for obtaining vibrational contribution to free energies of surface reactions was performed using standard finite difference methods.

### 5.2.2 Ab-Initio Atomistic Thermodynamics

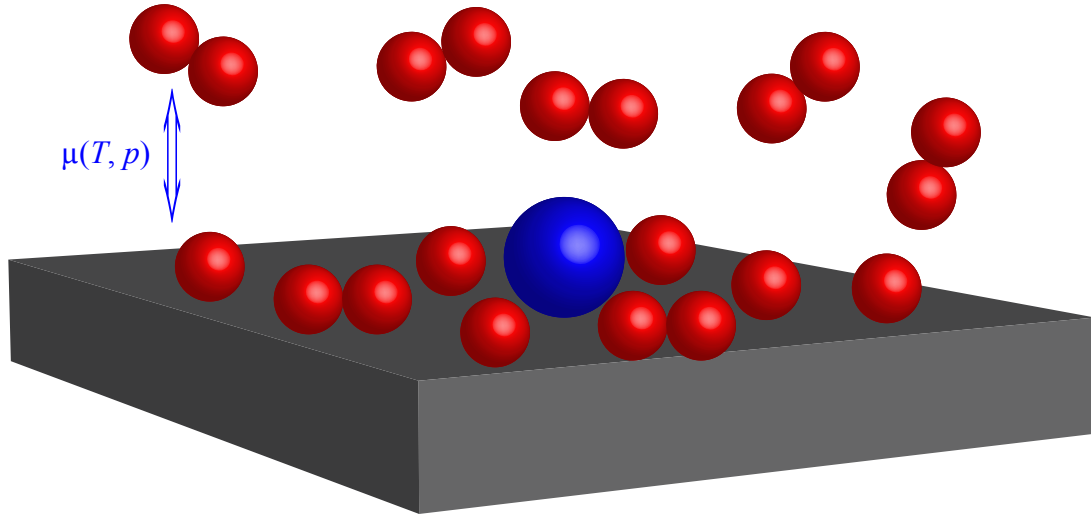


Figure 5.3: Schematic illustration of the gas-surface interface

As the metal substrate, e.g., Cs/Ag(111), is in contact with  $O_2$  gas at a given chemical potential  $\mu(T, p)$ , surface or even subsurface sites of the substrate will be continuously occupied by the gas phase molecules or fragments until the equilibrium condition is established as shown in Fig. 5.3. At specific surface configuration, the Gibbs surface free energy  $\gamma(T, p)$  of the adsorption system can be calculated as

$$(5.1) \quad \gamma(T, p) = \frac{1}{A} [G_{Cs/O/Ag(111)} - G_{Cs/Ag(111)} - N_O \mu_O],$$

where  $N_O$  is the number of adsorbed O atoms in the unit cell, which has the surface area,  $A$ .  $G_{Cs/Ag(111)}$  and  $G_{Cs/O/Ag(111)}$  are the Gibbs free energy of the Cs/Ag(111) slab, and the slab with adsorbed oxygen species, respectively.  $\mu_O$  is the chemical potential of the gas-phase oxygen. Gibbs free energies, ( $G_{Cs/O/Ag(111)}$  and  $G_{Cs/Ag(111)}$ ), can be obtained from first-principles by calculating DFT electronic energies,  $E_{Cs/O/Ag(111)}$  and  $E_{Cs/Ag(111)}$ ,

and correcting these for the effect of vibrational degrees of freedom since translational and rotational effect are negligible for surfaces. The vibrational properties of the system can be calculated within the quasi-harmonic approximation using first-principles phonon density of states [188–193] The chemical potential of gas phase  $O_2$ ,  $\mu_O(T, p)$ , can also be computed easily from electronic, vibrational, rotational, and translational partition functions as we introduced in Chapter 2.  $\mu_O(T, p)$  can be written as

$$\begin{aligned} \mu_O(T, p) &= 1/2E_{O_2} + \Delta\mu_O(T, p) \\ (5.2) \quad &= 1/2 \left[ E_{O_2} + \mu_{O_2}(T, p^o) + k_B T \ln \left( \frac{p_{O_2}}{p^o} \right) \right], \end{aligned}$$

where  $E_{O_2}$  is the electronic energy of  $O_2$  molecule calculated using DFT.  $\mu_{O_2}(T, p^o)$  accounts for the change in free energy of  $O_2$  as a function of  $T$ . The expression for  $\mu_{O_2}(T, p^o)$  is readily available from thermodynamic tables, or it can even be calculated from vibrational, rotational, and translational partition functions which can be estimated from DFT calculations. The NIST thermodynamic table gives the expression of  $\mu_{O_2}(T, p^o)$  for standard pressure  $p^o$ , which is usually 1 bar. In order to account for the deviation of  $\mu_O$  from the standard pressure an additional pressure dependent term,  $k_B T \ln \left( \frac{p_{O_2}}{p^o} \right)$ , is added. The scheme introduced here can be used to relate the DFT calculated energies to the catalytic relevant conditions.

### 5.2.3 Metropolis Monte Carlo Simulation

The Ag(111) surface in the Monte Carlo simulations has been modeled as  $(50 \times 50)$  Ag(111) lattice with periodic boundary conditions. Atomic oxygen can adsorb on the surface hollow sites and subsurface octa (beneath surface fcc) and tetra-1 (beneath surface hcp) sites, and Cs is only restricted to be on the surface hollow site since the penetration into subsurface is energetic unfavorable. The interatomic interaction potentials have been obtained using cluster expansion method with coarse-graining of DFT energies. The

selection rule for a Monte Carlo move from state  $m$  to  $n$  is governed by the transition probability

$$(5.3) \quad \rho_{mn} = \min\left\{1, \frac{\rho_n}{\rho_m}\right\},$$

where the  $\rho_m$  and  $\rho_n$  is the probability for each state determined from Boltzmann distribution. Three different Monte Carlo moves within grand canonical ensemble scheme have been incorporated as below with the transition probability calculated from Eq. 5.3.

### 1. Particle Displacement

$$(5.4) \quad \rho_{mn} = \min\{1, \exp(-\Delta E/k_B T)\}$$

### 2. Particle Insertion

$$(5.5) \quad \rho_{mn} = \min\{1, \exp\{-(\Delta E - \Delta\mu_O)/k_B T\}\}$$

### 3. Particle Removal

$$(5.6) \quad \rho_{mn} = \min\{1, \exp\{-(\Delta E + \Delta\mu_O)/k_B T\}\}$$

where  $\Delta E = E_{new} - E_{old}$ .

Metropolis Monte Carlo is an efficient tool to investigate the thermodynamic stability of the surface structure under various conditions. We have performed the Monte Carlo simulations in the Grand Canonical ensemble with an applied oxygen chemical potential determined by the gas phase partial pressure with fixed temperature. Many Monte Carlo cycles ( $10^8$ ) are performed until the surface and subsurface oxygen coverage, and system energy is converged with some statistical fluctuation. The general scheme of Monte Carlo simulation in our studies can be illustrated in Fig. 5.4.

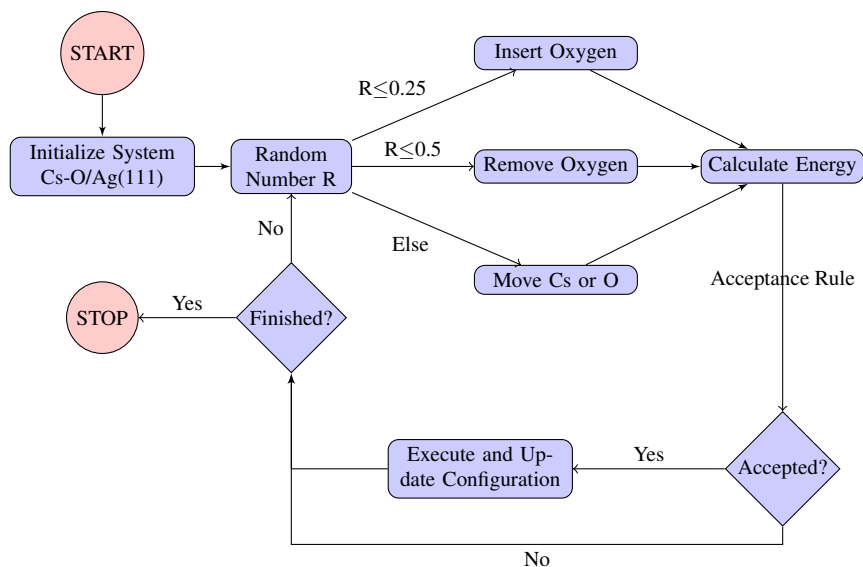


Figure 5.4: Schematic illustration of Metropolis Monte Carlo simulation algorithm

## 5.3 Fundamental Mechanisms that Govern Alkali Promotion

### 5.3.1 Cs Promotion on O<sub>2</sub> Dissociation

The dissociation of O<sub>2</sub> is an important elementary step in many oxidation reactions on metal surfaces [194]. We have performed DFT calculations to study the effect of Cs adatoms on the energetics of O<sub>2</sub> dissociation reaction on the Ag(111) surface. The results of these calculations are shown in Fig. 5.5. Geometries of relevant transition states were obtained in DFT calculations using a climbing nudged elastic band (cNEB) algorithm [187] and shown along with the potential energy surfaces in Fig. 5.5. Site *B* is the surface hollow site close to dissociating O<sub>2</sub> molecule, and site *A* is the furthest on the 3×3 unit cell we have employed in this study. The same final state energy is used since CsO<sub>2</sub> is the most thermodynamically favourable structure at this coverage of Cs and O. Fig. 5.5 shows that the activation barrier for O<sub>2</sub> dissociation is lower on Cs/Ag(111) (1.04 eV for far site *A*, 0.87 eV for near site *B*) than that on the un-promoted Ag(111) surface (1.26 eV). Furthermore, the adsorption energy of atomic oxygen (final state in O<sub>2</sub> dissociation) is significantly more exothermic for the Cs-promoted Ag(111) compared to un-promoted

Ag(111). We also observe that the extent of Cs promotion is larger for those Ag sites that are close to the Cs adsorbates (site *B* in Fig. 5.5). These results clearly demonstrate that there is a significant interaction between oxygen adsorbates and Cs on the Ag(111) surface and are consistent with various experimental observations which showed that the O<sub>2</sub> adsorption and desorption processes on Ag(111) can be significantly altered when Cs is adsorbed on the surface [195–197].

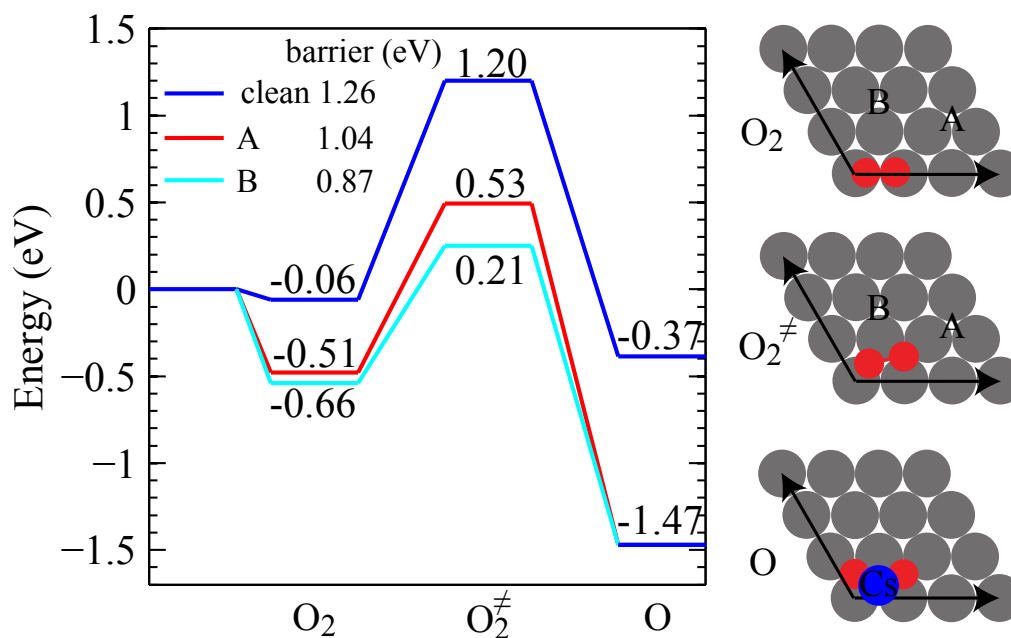


Figure 5.5: The DFT-calculated potential energy surfaces for the O<sub>2</sub> dissociation reaction on clean and Cs-promoted Ag(111) surfaces. The barrier was calculated as the energy difference between the transition state and initial state. The surface structures with different oxygen species are shown in the 3×3 unit cell. Cs adatom adsorbs on site *A* or *B*, where site *A* is further away from the dissociation molecules than site *B*

To understand the mechanism of alkali promotion it is critical to identify the underlying physical factors that induce such a substantial Cs-induced change in the energetics of the O<sub>2</sub> dissociation reaction.

### 5.3.2 Alkali-Modified Electronic Properties of Metal Surfaces

To be able to unearth the mechanism (for example, via Eq. 3.22 in Chapter III) by which promoters affect chemical reactions on metal surfaces, it is critical to understand

how an alkali adsorbate modifies electronic properties of metal substrates. To address this question, we have performed electronic structure DFT calculations where we studied Cs adsorption on the Ag(111) surface. These calculations were performed to provide important insights regarding the alkali-induced modifications of various physical characteristics of metal substrates and to establish a level of confidence that DFT can obtain accurate and experimentally verifiable results.

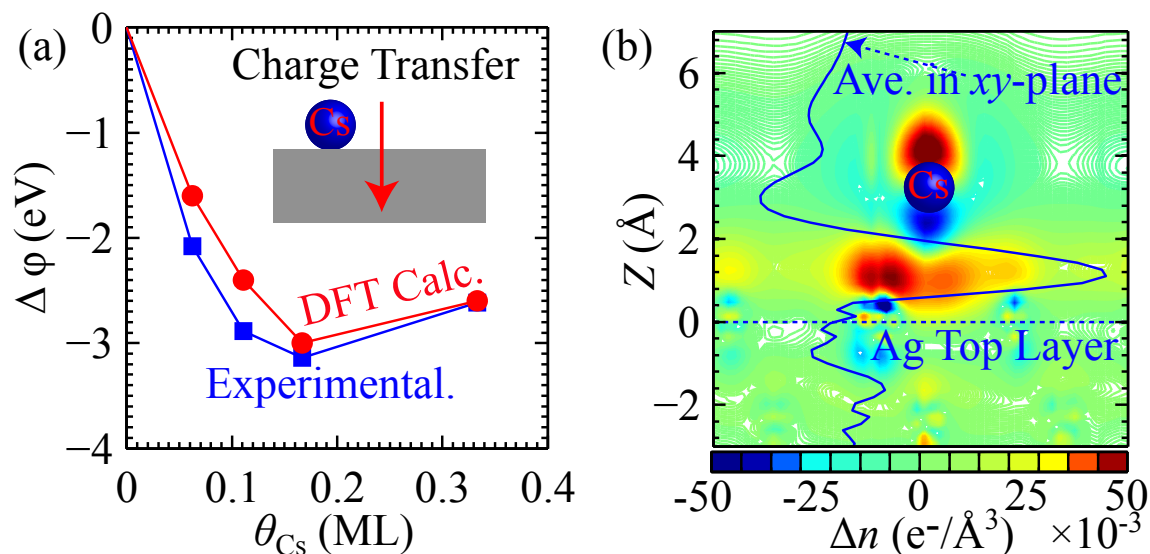


Figure 5.6: (a) Cs induced work function change as a function of Cs coverage on Ag(111); Blue square is the experimental result adapted from literature, while red circles represent DFT-computed work function change. (b) The contour shows the Cs induced electron density difference on the plane cutting through Cs adatoms. Solid line represents the average electron density along  $z$ -axis. The density is calculated as  $\Delta n = n_{Cs/Ag(111)} - n_{Ag(111)} - n_{Cs}$ . Positive value corresponds to an  $e^-$  charge increase. Zero on  $z$ -axis corresponds to the top Ag layer. Cs atoms are adsorbed at  $z=3.25$  above the top Ag layer.

Our DFT calculations show that Cs preferentially adsorbs on the hcp three-fold hollow site at a height of  $\approx 3.25$   $\text{\AA}$  above the top layer of Ag atoms. We observed that there is a strong repulsive interaction among Cs adsorbates on the surfaces, which is consistent with experimental observations [155, 168]. It has also been observed experimentally that adsorption of alkalis on metal surfaces decreases the electronic work function (energies required to remove electron from the system to vacuum) of these substrates [198]. In order to establish a level of confidence regarding the accuracy of DFT and its ability to

capture the Cs-induced modifications of the Ag(111) surface, we compared the experimentally measured work function [198] to the theoretical predictions of our DFT studies, see Fig. 5.6(a).

Fig. 5.6(a) shows that for a broad range of Cs coverage, the Cs-induced change in the work function is very well captured by the DFT calculations. The change in the work function is a consequence of charge donation from the Cs adsorbate to Ag substrate. This is corroborated by Fig. 5.6(b), where we plot the average Cs-induced electronic charge density along  $z$ -direction (normal to the surface) cutting through the Cs atom. The charge density was calculated as the difference between the charge of Cs/Ag system minus the charge of un-promoted Ag and minus the charge associated with the Cs atom without the substrate. It is observed that upon the Cs adsorption the electron density shifts away from the Cs adsorbates towards the Ag substrate, resulting in a large induced dipole moment which opposes the clean substrate charge spill-over dipole. This induced dipole moment ultimately results in the work function decrease, as corroborated by Fig. 5.6(a) [199, 200]. In Fig. 5.6(b), we also show the contour of electron density induced by Cs adsorption on the plane perpendicular to the surface. As we can see, alkali-induced change in the charge density is essentially localized to the first near neighbor Ag atoms of alkalis. There is also a free-electron like layer just above the Ag top layer in the interface, which is assigned to be the delocalized  $sp$ -electrons. Cs also induced a strong polarization due to the lateral repulsion, which will decrease the charge transfer from alkali atoms to the Ag(111) surface.

Along with the change in the electronic work function, which is a global property of the substrate, we observe that Cs adsorbates also modify various local properties of Ag. We are particularly interested in the Cs-induced modifications of those local properties that might impact the adsorption energies of various co-adsorbates on specific Ag sites.

For example, an important consequence of Cs adsorption is that it induces an electrostatic potential along  $z$ -direction. The Cs-induced electrostatic potential varies as a function of the position in  $xy$  plane, i.e., it is a function of the distance from the Cs adsorption site. Fig. 5.7(a) shows the Cs-induced electrostatic potential along the  $z$ -direction through the sites labeled A, B, C, and D in the  $3 \times 3$  unit cell shown in the Fig. 5.7(a). The Cs-induced electrostatic potential is calculated by subtracting the electrostatic potential of Ag(111) substrate from the electrostatic potential of Cs/Ag(111) system. It is observed that Cs induces a significant change in electrostatic potential even for the sites that are relatively far from the Cs adsorption site, such as site D.

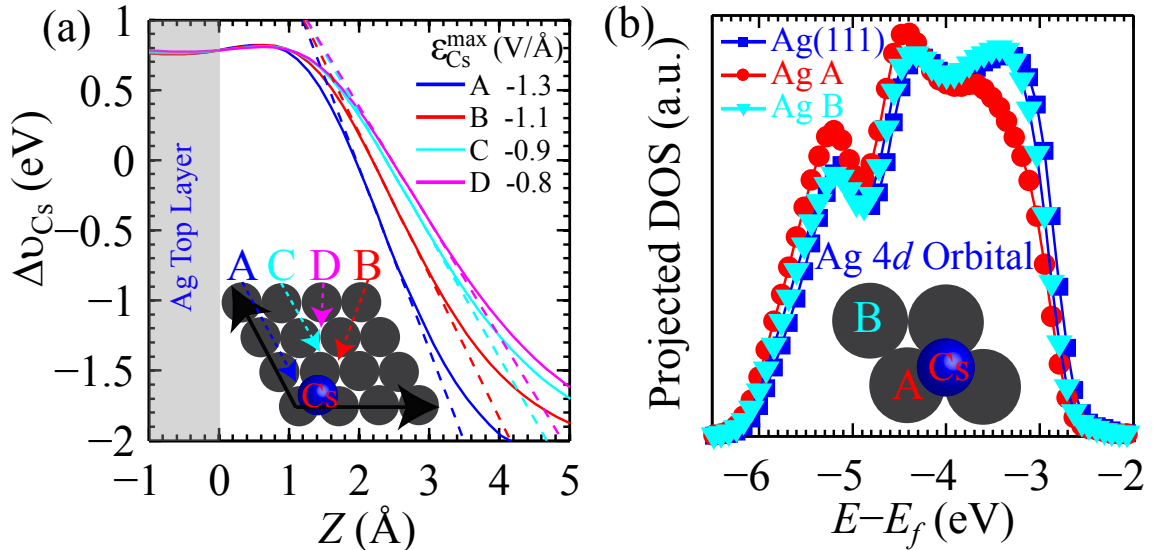


Figure 5.7: Cs induced modification of the electronic properties of silver surfaces. (a) Cs induced electrostatic potential along different positions on the surface. The induced electric field  $\epsilon_{Cs}^{max}$  is the maximum electric field out of surface as determined from the dashed line. (a) The projected density of states of surface silver atoms for clean Ag(111) and Cs modified Ag(111) surfaces. As illustrated in insert, Ag A is the one directly bonded to Cs, and Ag B is the one on the second near neighbor of Cs.

It is important to emphasize that the Cs-induced electrostatic potential will change the adsorption energy of various adsorbates, particularly those with significant molecular dipole moments or those that are easily polarized in an electric field. This is a consequence of the fact that the Cs-induced potential varies in the  $z$ -dir., as shown in Fig. 5.7(a) which

results in significant electric fields. For example, we calculate the maximum electric field defined in Eq. 5.7 through site A at a height  $\sim 2 \text{ \AA}$  above the top Ag layer (which is a typical adsorption height for simple adsorbates on metal substrates) to be  $-1.3 \text{ V/\AA}$  through the site A and to be  $-0.8 \text{ V/\AA}$  through the site D. These electric fields interact with the dipole moment of various adsorbates impacting their adsorption energy and their chemistry on the alkali-promoted metal substrates.

$$(5.7) \quad \varepsilon_{Cs}^{max} = -\max \left| \frac{d\Delta v_{Cs}}{dz} \right|_{x,y}$$

Another local physical property of a metal substrate that is modified by an alkali adsorbate is the surface electronic structure. The physical quantity that describes the local electronic structure associated with various discrete surface sites is the local density of states (LDOS) [201], which is defined as

$$(5.8) \quad \rho_i(\varepsilon) = \sum_p |\langle \psi_p | \phi_i \rangle|^2 \delta(\varepsilon - \varepsilon_p),$$

where  $i$  represents local site;  $\psi_p$  is the wave-function of  $p^{th}$  orbital of the system;  $\phi_i$  is the basis function on the local site  $i$ . The density of state  $\rho_i(\varepsilon)$  of local site  $i$  is obtained by the summation of projection of all the state  $p$ .

The promoter-induced change in the LDOS has a direct impact on the adsorption energy of surface reactants and transition states and can lead to significant alkali-induced modifications in the activation barriers for certain elementary steps, therefore altering the reactivity and selectivity of the catalyst [202].

The electronic structure of metal  $d$ -band has been well established to be the governing parameters for the surface chemical bonding with simple adsorbates [202]. In Fig. 5.7(b) we plot the LDOS ( $d$ -symmetry) projected onto an Ag atom which is directly bonded to Cs (atom labeled A), and the LDOS projected onto a nearest neighbor to this Ag atom (atom B), as well as the LDOS projected onto an Ag atom of an un-promoted Ag(111)

surface. Fig. 5.7(b) demonstrates that the adsorption of Cs on Ag(111) has a fairly short range electronic effect. For example, it is observed that the LDOS has shifted downward in energy for those Ag atoms that are directly bonded to the adsorbed Cs, i.e., the atom labeled A. However, for the second nearest neighbor (atom B) the LDOS is not modified compared to the LDOS of Ag atoms of un-promoted Ag surfaces. We conclude that the impact of Cs adsorption on the  $d$ -states of the metallic substrate is localized to those Ag atoms that directly bind to Cs. This is not surprising considering that electrons in metal will respond to the Cs adsorption, shielding the effect of Cs and limiting it to very short range. The impact of Cs on the  $sp$ -states of metal is slightly more spread since  $sp$ -electrons are nearly free and delocalized, which could affect the coupling of adsorbate states with metal  $d$ -states by adjusting the optimum adsorbate bond distance to the surface.

The main conclusions of our studies of the Cs adsorption on Ag(111) are:

- Cs decreases the electronic work function of Ag(111) surface. The decrease in the work function is a consequence of the Cs-induced dipole moment which opposes the clean substrate charge spill-over dipole. DFT methodology can predict very accurately the experimentally observed decrease in the work function.
- Cs changes substantially electrostatic potential above the Ag substrate. The induced electrostatic potential is significant even for those surface sites that are relatively far, a few Å, from the Cs adsorption sites. The gradient in the electrostatic potential along the  $z$ -direction leads to significant electric field.
- The adsorption of Cs on Ag(111) modifies only slightly the substrate electronic structures. For  $d$ -electrons of the substrates these changes are localized, and only Ag atoms directly bonded to Cs feel the presence of Cs. For  $sp$ -electrons, the effect of Cs is felt further away from the Cs adsorption site since  $sp$ -electrons are delocalized

on the surface.

We have performed similar calculations for Na adsorption on a close packed Ru(0001) substrate as well as for Na and Cs on the Pd(111) surfaces. These calculations yielded the conclusions that are consistent with the observations for the Cs/Ag(111) system. These similarities suggest that alkali adsorption on metal surfaces results in fairly universal changes in the physical characteristics of those substrates. The fundamental reason for these similarities is that alkalis are electropositive and upon adsorption on metal substrates they donate electronic charge to these substrates. This universal shift in electron charge distribution results in universal alkali-induced modifications of various physical characteristics of metal substrates. The important question that needs to be addressed is whether and how the alkali-induced modifications of the physical characteristics of metal surfaces impact the chemical reactivity of these surfaces.

### 5.3.3 Fundamental Understanding of Alkali Promotion Mechanism

To explore the fundamental mechanism of alkali promotion, we have employed the general theoretical framework that we have introduced in Chapter 3 based on the underlying machinery of DFT. The model allows us to obtain a transparent and physically intuitive description of the interaction energy between two adsorbates on metal surfaces. We note that this expression is very similar to the one obtained by Nørskov and Hammer using the frozen density and potential approximation [202]. All of the contributing terms in Eq. 3.22 can be evaluated independently of each other providing us with a very clear view of the dominant mechanism of adsorbate-adsorbate interactions.

As stated above in the beginning, there are many mutually contradicting mechanisms that have been proposed as important for alkali-induced modification of the catalytic reactivity of metal surfaces. The ultimate challenge was to identify those physical factors

that affect chemical transformations on metal surfaces. Our strategy was to design an approach, guided by Eq. 3.22, which will allow us to completely decouple from each other different modes of adsorbate-adsorbate interaction (electronic, electrostatic and polarization) and to quantify their respective relevance. The aim of current studies was to identify the mechanism that govern the interactions of atomic Cs, adsorbed on the Ag(111) surface, with the initial, transition and final states involved in the O<sub>2</sub> dissociation reaction.

Eq. 3.22 provides a natural and physically transparent description for the interaction energy between two adsorbates on a surface. Basically, Eq. 3.22 states that Cs adsorbates can affect the stability of these adsorbates by changing the electronic structure of the substrate, by inducing an electrostatic dipole on the surface, or by polarizing the adsorbate in the electric field. So in the following we are going to talk about the details of each contribution.

### 5.3.3.1 Electronic Contribution due to the One-Electron Energies

The electronic contribution in Eq. 3.22 is shown below for reference only.

$$(5.9) \quad \Delta\Delta E_{el} = \sum_i \xi_i \sum_{N=1}^{N_i} \Delta\varepsilon_i^N[\Delta v]$$

$\Delta\varepsilon_i^N[\Delta v]$  is the change of the one-electron energy of  $N^{th}$  Kohn-Sham orbital of the system  $i$  with the perturbation potential  $\Delta v$ .

To evaluate the impact of Cs adsorption on the one-electron energies of various oxygen adsorbates (initial, transition, and final states in the O<sub>2</sub> dissociation) as shown in Eq. 5.9, we have utilized Two-Level interaction model [106], which is basically an application of the tight binding approximation to the adsorption on metal surfaces. In this approximation adsorbate states (orbitals) represented by discretized energy level interact with the  $d$ -state centered at average energy of the  $d$ -band of the substrate [106]. Based on the general framework proposed by Nørskov et al., the binding energy of adsorbate on metal surfaces

is given by

$$(5.10) \quad \Delta E = \Delta E_0 + g\Delta E_d,$$

where  $\Delta E_0$  is the energy contribution from the coupling of adsorbate states with  $sp$ -electrons, and  $\Delta E_d$  is the interaction energy between adsorbate resonance state (after interaction with  $sp$ -states) with  $d$ -band of the surface, and the factor  $g$  accounts for the degeneracy of the adsorbate valence states. The interaction energy of adsorbate states with the “free-electron-like”  $sp$  substrate states is assumed to be similar for different surface sites according to Newns-Anderson model and our analysis in Chapter 4. This is not a rigorous assumption considering that  $sp$ -band of extended metal surfaces is very broad and featureless for transition metal surfaces and alloys. It will certainly fail if  $sp$ -states become discretized as in small metal clusters [49]. It should be noted that the  $sp$ -interaction is governing the adsorbate bond distance to surface atoms since this interaction has the most contribution to the binding energy, and the interaction with  $d$ -band can be taken as a perturbation [49, 203]. We have shown in Chapter 4 that  $sp$ -electron density of local metal sites in alloys dictated by the electronegativity of constituent metal elements is the governing factor for determining the adsorbate bond distance to metal surfaces, and the coupling matrix of adsorbate states to localized metallic  $d$ -states is a function of interatomic bond length,  $V_{pd} \propto 1/d^{7/2}$  [58]. In the following we are going to talk about the specific form of Two-Level interaction model for different states of oxygen and elaborate the details of evaluation.

For molecular oxygen adsorption on the Ag(111) surface, the occupied  $2\pi_o^*$  and unoccupied  $2\pi_u^*$  orbitals are closely around the Fermi level, which can interact with the metallic  $d$ -states. The occupied  $2\pi_o^*$  state centers at around -2.14 eV below the Fermi level as calculated from the molecular oxygen adsorption on the  $sp$ -electron metal Al(111) surface. The unoccupied  $2\pi_u^*$  state is around 1.32 eV above the Fermi level calculated in the same

way. So the interaction of  $2\pi^*$  orbitals with Ag(111)  $d$ -band can be seen as these two states both interacting with the  $d$ -orbitals of Ag(111) surface atoms, without specifying the proper symmetries of interacting  $d$ -orbitals. From the tight binding approximation [49, 138], we can easily write down the energy associated with these two interactions as

$$(5.11) \quad \Delta E_d \approx -2 \left[ f \frac{V_{2\pi_u}^2}{|\epsilon_{2\pi_u^*} - \epsilon_d|} + f S_{2\pi^*} V_{2\pi^*} \right] - 2 \left[ (1-f) \frac{V_{2\pi_o}^2}{|\epsilon_{2\pi_o^*} - \epsilon_d|} + (1+f) S_{2\pi^*} V_{2\pi^*} \right].$$

The coupling matrix element ( $V$ ) and also the overlap integral ( $S$ ) of  $2\pi_o^*$  and  $2\pi_u^*$  orbitals are assumed to be similar as an approximation. The coupling matrix element  $V$  is linearly related to the overlap integral  $S$ , e.g.  $S = \alpha V$ , where  $\alpha$  is an adsorbate dependent parameter related to the repulsive interaction between coupling orbitals. To evaluate the coupling matrix we have used the simple relationship,  $V \propto 1/d^{7/2}$ , where  $d$  is from DFT fully optimised bond distance. To obtain the absolute value of  $V$ , we also used the relationship  $V^2 = \beta V_{ad}^2$ , where  $V_{ad}^2$  for pure metals has been tabulated [138].  $\beta$  is the adsorbate and adsorption geometry dependent parameter. We have used the oxygen adsorption on clean metal surfaces to numerically calculate those two adsorbates dependent parameters. For Cs doped Ag(111) surface, the adsorbate bond distance to the surface is changing due to the variations of  $sp$  electron density donated by Cs to the surface. So the relative coupling matrix  $V_{ad}^2$  according to the relationship  $V \propto 1/d^{7/2}$  is different for varying Cs-O configurations since  $sp$ -electron density is not homogeneous over the surface. For transition state oxygen we have used the same relationship to evaluate of the energy contribution due to interaction with  $d$ -band. The adsorbate energy level of transition state oxygen is calculated in the same way as molecular oxygen, resulting  $2\pi_o^*$  at -1.75 eV and  $2\pi_u^*$  at 0.26 eV.

For atomic oxygen adsorption on the surface, the adsorbate valence state and substrate  $d$ -band are represented as two atomic states at  $\epsilon_a$  and  $\epsilon_d$ , respectively. The energy change

in this two level interaction is given by [204]

$$(5.12) \quad \Delta E_d = -2(1-f)\beta \frac{V_{ad}^2}{|\epsilon_a - \epsilon_d|} + 2\alpha\beta(1+f)V_{ad}^2,$$

where  $f$  is the filling factor of  $d$ -band of surface atoms; For the Ag(111) surface, the filling factor of  $d$ -band  $f$  is 1.  $\beta$  is defined as the ratio of the actual coupling matrix elements to the relative matrix elements  $V^2/V_{ad}^2$ , which is adsorbate and adsorption geometry dependent, but metal independent;  $V_{ad}^2$ , which is only metal dependent, has been tabulated [204].  $\alpha$ , which is independent of metal surfaces, is the parameter related to Pauli repulsion [204].  $V_{ad}^2$  for clean Ag(111) surface is 2.29 relative to Cu(111) (defined as 1)

The energy contribution to the interaction energy between Cs adatom with the oxygen species including initial, transition and final state can be evaluated based on Eq. 5.11 and Eq. 5.12. The  $\alpha$  and  $\beta$  in those equations can be obtained by the fitting the model into oxygen species adsorption on clean transition metal surfaces as shown in Fig. 5.8. The obtained parameters are tabulated in Table 5.1.

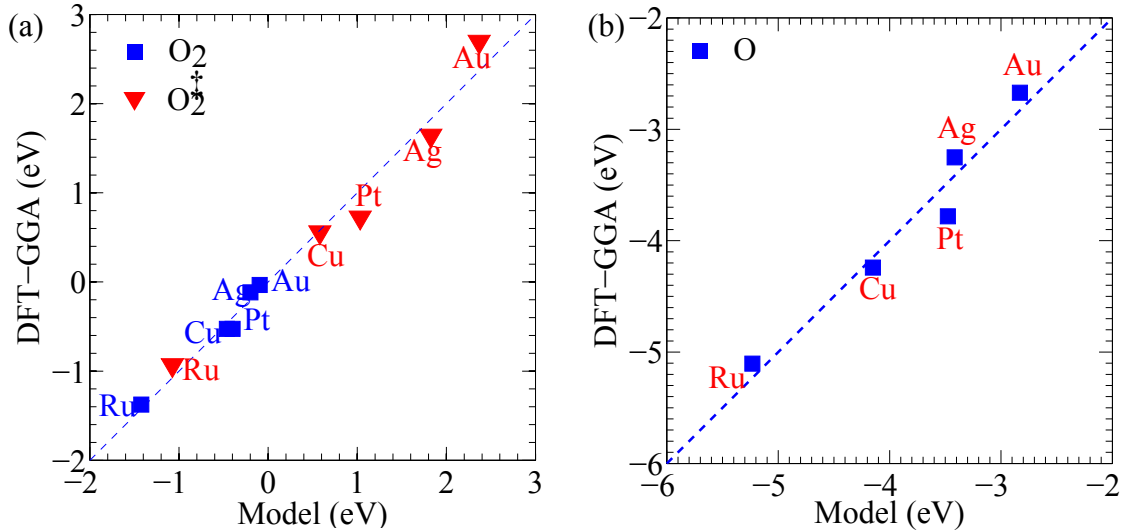


Figure 5.8: Two Level interaction model for oxygen species adsorption on clean transition metal surfaces. The parameters obtained from the Two-Level interaction model are tabulated in Table 5.1 (a) Initial and transition states of O<sub>2</sub>. (b) Atomic oxygen

Species	$\alpha$	$\beta$	$E_{sp}$
O <sub>2</sub>	0.47	0.07	-0.56
O <sub>2</sub> <sup>‡</sup>	0.21	0.95	0.00
O	0.04	1.11	-4.71

Table 5.1: Tabulated parameters of oxygen adsorption on transition metal surfaces for the two level interaction model

### 5.3.3.2 Electrostatic Contribution due to the Dipole-dipole Interaction

The electrostatic contribution in Eq. 3.22 is shown below for reference only.

$$(5.13) \quad \Delta\Delta E_{es} = \int^A \Delta\rho_A(\mathbf{r}) \Delta v(\mathbf{r}) d\mathbf{r}$$

$\Delta\rho_A$  is adsorbate  $A$  induced charge density difference upon adsorption on the substrate including nucleus point charge and electrons.  $\Delta\rho_A$  can be obtained by subtracting the charge density of the substrate from the charge density of  $A$  adsorbed on the substrate ( $\Delta\rho_A = \rho_{A/M} - \rho_M$ ). Nucleus charge can be seen as a point charge at the ground state geometric positions.  $\Delta v(r)$  is the perturbation of external potential which can be induced by coadsorbates, alloying and many others. In this Chapter, the perturbation potential is due to the alkali promoters, so  $\Delta v(r)$  is the alkali ( $B$ ) induced change in the potential ( $\Delta v = v_{B/slab} - v_{slab}$ ). To avoid double counting, the integration should be performed in the region of adsorbate  $A$ . In our study, we have evaluated the Eq. 5.13 within the whole unit cell and divided the integral by 2 to avoid the double counting.

The interaction between the static dipole of an oxygen adsorbate on the surface and the Cs-induced electric field was evaluated by calculating the integral in Eq. 5.13. The induced charge density difference on adsorbed oxygen was obtained by subtracting the calculated charge density of Ag(111) from the charge density of oxygen adsorbed on Ag(111) with the inclusion of electrons and nucleus. The Cs-induced electrostatic potential ( $\Delta v$ ) was calculated by subtracting the DFT-calculated electrostatic potential of Ag(111) from the electrostatic potential of the atomic Cs adsorbed on Ag(111). The ionic potential in the

ionic core region of pseudopotential should be properly corrected, or simply speaking replaced by true ionic potential  $-Z/r$ , so the integral will be equal irrespective of the view of adsorbates (switching  $A$  with  $B$ ).

### 5.3.3.3 Polarization Contribution due to the Dipole-induced-dipole Interaction

The polarization contribution in Eq. 3.22 is shown as

$$(5.14) \quad \Delta\Delta E_{pe} = \iint \left[ \frac{\delta\Delta\rho_A}{\delta\Delta v(\mathbf{r}')} \right]_N \Delta v(\mathbf{r}') \Delta v(\mathbf{r}) d\mathbf{r}' d\mathbf{r},$$

where  $\Delta\rho_A$  is the adsorbate  $A$  induced charge density, and  $\Delta v(r)$  is the perturbation potential. In the context of adsorbate-adsorbate interactions where the perturbation potential is introduced by coadsorbate  $B$ , Eq. 5.14 should also include the polarization energy contribution of adsorbate  $B$  due to the coexistence of adsorbate  $A$ .

The polarization contribution is slightly more challenging to evaluate. We have calculated this interaction by introducing an artificial homogeneous electric field across the surface in our simulation cell and evaluating how the adsorption energy of an adsorbate changes. This artificial electric field can be manipulated so that the electrostatic potential drop or local electric field around the adsorbate matches the Cs-induced electrostatic potential or local electric field. The stability of the adsorbate in this artificial electric field will change due to the interaction of static- and induced-dipole moment with the electric field. To isolate the change due to the polarization only, we simply subtract the interaction energy of the static-dipole interacting with the artificial field based on Stark effect from the DFT-calculated overall adsorption energy change in the artificial field as shown in Eq. 5.15.

$$(5.15) \quad \Delta\Delta E_{pe}^{\Delta v} = \Delta\Delta E^{\Delta v} - (-\mu_{A/M} \cdot \mathbf{\epsilon}^{\Delta v})$$

The polarization energy of  $B/M$  due to the existence of adsorbate  $A$  can be obtained using the same method, simply imposing the external electric field due to adsorbate  $A$

on the system  $B/M$ . This method provides a reasonable way to decouple the different contributions and identify the most dominant mechanism.

#### 5.3.3.4 Comparison of DFT-Calculated Interaction Energies with the Model-Prediction

Using the approach discussed here, we have assessed the relative influence of different modes of interactions governing the  $O_2$  dissociation on the Cs-promoted Ag(111). Fig. 5.9(a) shows that the overall agreement between the self-consistent DFT calculations and the prediction of our simple model, which combined independent calculations of electronic, electrostatic and polarization effects, is excellent for different Cs surface coverage (1/16 ML and 1/9 ML) and varying Cs-O separations. That indicates that our model can be used to understand the sophisticated adsorbate-adsorbate interactions on metal surfaces. To illustrate the dominant mode of interactions for oxygen adsorbates with alkali promoters, we have shown the calculated different contributions by selecting one specific surface configuration. It is clear from Fig. 5.9(b) that all the contributions stabilize the oxygen species on the surface, and that electrostatic and polarization interactions are the dominant modes of Cs promotion. These modes of the interaction are characterized by the interaction of the Cs-induced electric field with the static- and induced-dipole moments of adsorbates (initial, transition, and final state) involved in the  $O_2$  dissociation. The adsorbates that are stabilized the most by Cs have largest dipole moments (i.e., these adsorbates withdraw electron density from the substrate) and the bonds that these adsorbates form with Ag are highly polarizable in the Cs-induced electric field. These effects are more pronounced for the transition and final states involved in  $O_2$  dissociation than for the initial state, which ultimately leads to the lowering of the activation barrier.

The analysis above stipulates a simple theoretical argument that might explain the general effect of alkali promoters for chemical reactions on metal surfaces. It is clear that alkali-induced electric fields play a critical role in stabilizing electronegative adsorbates on

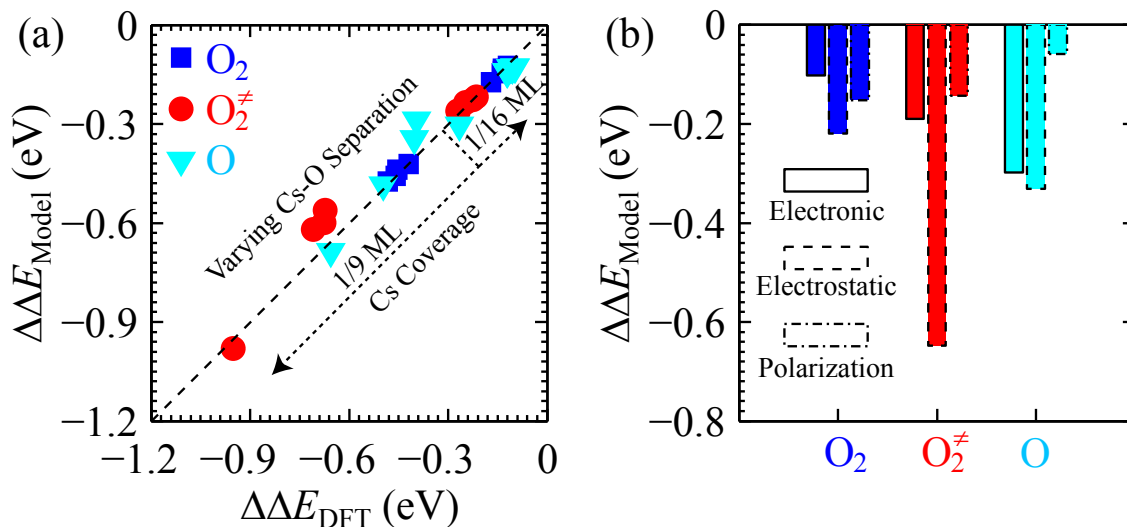


Figure 5.9: (a) Comparison between the self-consistent DFT calculated interaction energy and the model prediction between Cs and various oxygen adsorbates (initial, transition, and final state in the  $\text{O}_2$  dissociation reaction). We can see that the model predicts very well the interaction energies for varying Cs-O separations and Cs coverages. Diagonal straight line is the line of perfect agreement. (b) Decoupling of various contributions including electronic (solid line), electrostatic (dashed line) and polarization (dash-dot line) contributions into the interaction energy for one Cs- $\text{O}_x$  configuration.

metal surfaces. The main reason for this is the favorable interaction of the alkali-induced field with the dipole moment of the adsorbate. If a transition state in an elementary reaction is characterized by a large dipole moment (due to the electronic charge donation to the transition state) then alkali adsorbates will stabilize this transition state and decrease the activation barrier associated with the elementary step that proceeds through this transition state. This suggests that in order to be able to predict if an alkali adsorbate should lower the activation barrier for an elementary step, the only information that is needed is whether the transition state for this step accepts the electronic charge from the surface or donates the charge. A transition state that accepts electronic charge will be stabilized in alkali-induced fields and a transition state that donates charge will be destabilized. The information regarding the charge distribution can be obtained easily either from DFT calculations or even from simple electronegativity arguments regarding the charge donation or withdrawal.

This theoretical argument is likely to be important for the dissociation of many diatomic molecules (CO, NO, N<sub>2</sub>, etc.) over alkali-promoted metal substrates. Dissociation of these diatomic molecules is important in many commercial heterogeneous catalytic processes. Commercial metal catalysts for many catalytic processes are promoted by alkali promoters. The underlying mechanisms that govern alkali promotion in the dissociation of these diatomic molecules might be similar to the mechanisms discussed above for the dissociation of O<sub>2</sub> on Cs/Ag(111). The reason for this is that the dissociation of these diatomic molecules on metal substrates proceeds via a similar mechanism known as the donation/back-donation mechanism, where the stretching of the molecular atom-atom bond in the transition state is characterized by the donation of the electronic charge from the metal to the anti-bonding states of the diatomic molecule. This charge transfer from the metal to the transition state results in a dipole moment, which is stabilized in the alkali-induced electric field, and so decreases the activation barrier associated with the dissociation of these diatomic molecules.

#### **5.4 Extend Insight from DFT to Catalytic Relevant Conditions**

Alkali metals have been widely used as chemical promoters in many technological applications, such as the pretreatment of semiconductor materials for the formation of the oxide/substrate interface [205–207] and the chemical transformations of the molecules on catalyst surfaces for the production of valuable products [77, 146, 208] or for the mitigation of environmentally unfriendly wastes [209, 210]. Fundamental understanding of the promotion mechanism of alkali metals under relevant conditions requires the knowledge base of the structural and electronic properties of alkali-modified substrates, which might be sensitively influenced by the chemical potential ( $T, p$ ) of the gas phase in the surrounding environment.

In this study, we are focusing again on alkali promotion mechanism in the oxidation reactions over silver surfaces. Even though alkali metals have been widely used as promoters in many catalytic oxidation reactions, the mechanistic understanding of the alkali promotion effect remains rather limited. One of the reasons comes from that there are many possible oxygen species in the system under relevant conditions, such as the surface atomic oxygen [211], subsurface oxygen [211–213] or bulk-dissolved oxygen [212], and various associative oxygen species, such as peroxides [214], superoxide [215, 215], and ozonides [216], which makes the interpretation of experimental and theoretical observations rather convoluted. The nature, e.g., electrophilic vs. nucleophilic [217, 218], and functionality of different oxygen species remained highly debated before the early 1980s; however, just recently there is a general agreement that the atomic oxygen is the reactive species for many oxidation reactions [166, 219]. Interestingly, the subsurface oxygen has been shown to be necessary for the activation of the catalysts and the abundance of the subsurface oxygen can be directly correlated with the surface reactivity for ethylene epoxidation reaction over silver catalysts [219]. Another possible reason for the lack of understanding is from the well-known material and pressure gap between UHV surface science experiments and traditional reactor studies operated under relevant catalytic conditions.

We have described above an approach used to identify underlying physical mechanisms that govern alkali-induced modifications in the chemical reactivity of metal substrates. We have described this effort in the context of the Cs-induced lowering of the activation barrier for O<sub>2</sub> dissociation over the Ag(111) surface. In these studies we have mainly focused on a simple model system where an O<sub>2</sub> molecule is dissociating in a unit cell that contains one Cs adatom. Even though this model system can qualitatively explain various experimental observations, our studies also show that it is too simple to capture all relevant aspects of the alkali promotion. Catalytic processes take place at elevated  $T$  and

$p$ . For example, oxidation reactions, such as olefin epoxidation over Ag, take place at O<sub>2</sub> pressure ranging from 1 to 15 atm and temperature of 500-600 K [220]. It is important to analyze how these external conditions impact the working form of the alkali promoter [156]. In order to answer these questions, we have utilized a number of computational techniques including Metropolis Monte Carlo (MC) simulations and ab-initio atomistic thermodynamics that can extend DFT calculations, which are generally considered as zero-temperature and zero-pressure, to catalytic relevant conditions [47, 221, 222].

Previously, we have shown that the adsorbate-adsorbate interaction model combined with the first-principles DFT calculations allows us to distinguish between different mechanisms of adsorbate-adsorbate interactions on metal surfaces. In this Section, ab-initio atomistic thermodynamics has also been used to identify the stable species under different region ( $T$ ,  $p$ ). The Grand Canonical Monte Carlo (GCMC) simulation, which employs systematic coarse-graining of DFT calculated energies for the Cluster Expansion and Direct Enumeration, has been used to extend the insight from DFT calculations to relevant catalytic conditions. We found that depending on the external conditions different oxygen species and Cs-O complexes can be formed on the Ag(111) surface, and the mechanism that governs the interaction of Cs or Cs complexes with different atomic oxygen species (onsurface or subsurface) changes significantly. We will focus on the atomic oxygen adsorption in this study because it has been generally agreed that the atomic oxygen species are responsible for several oxidation reactions, such as ethylene epoxidation, methanol oxidation, CO oxidation and many others. Another complex issue that has been overlooked in previous studies of alkali promotion is the alkali-induced modification of the working state of a catalytic material. For example, it is quite conceivable that in an oxidation process, introduction of an alkali would affect the extent of oxidation of a metal catalyst due to attractive interactions between the electropositive alkali element and electronegative O

atoms [222, 223]. It is important to be able to predict how alkali promoters affect the working state of catalytic materials. To our knowledge, no work has been done in exploring these crucial questions [224].

#### 5.4.1 Oxidation States of the Substrate under Relevant Catalytic Conditions

We have performed DFT calculations and ab-initio atomistic thermodynamics studies to investigate the stability of various O adsorption configurations on clean and Cs-promoted Ag(111) substrates. The objective of this study was to identify those structures characterized by the lowest surface free energy for a given set of external conditions ( $T$  and  $p$  of gas phase  $O_2$ ).

The surface free energy of O adsorption on un-promoted Ag(111) was calculated as

$$(5.16) \quad \gamma(T, p) = \frac{1}{A} [G_{O/Ag(111)} - G_{Ag(111)} - N_O \mu_O].$$

And for O adsorption on promoted Ag(111) the surface energy was calculated as

$$(5.17) \quad \gamma(T, p) = \frac{1}{A} [G_{Cs/O/Ag(111)} - G_{Cs/Ag(111)} - N_O \mu_O],$$

where  $A$  is the surface area of the unit-cell,  $G_{Cs/O/Ag(111)}$  and  $G_{O/Ag(111)}$  are the Gibbs free energies of O adsorption on Cs-promoted and clean Ag(111) surfaces, respectively.  $N_O$  corresponds to the number of O atoms in the unit cell, while  $\mu_O$  is the chemical potential of O, which is in equilibrium with the gas phase oxygen, i.e.,  $\mu_O = \frac{1}{2}\mu_{O_2}$ . The chemical potential of O was calculated by counting for the effect of  $T$  and  $p$  using the following expressions

$$(5.18) \quad \begin{aligned} \mu_O(T, p) &= 1/2 E_{O_2} + \Delta\mu_O(T, p) \\ &= 1/2 \left[ E_{O_2} + \mu_{O_2}(T, p^o) + k_B T \ln \left( \frac{p_{O_2}}{p^o} \right) \right]. \end{aligned}$$

In Fig. 5.10, we show the calculated surface free energies for various O/Ag(111) structures as a function of oxygen chemical potential  $\Delta\mu_O$ , which is reference to DFT-calculated

internal energy,  $1/2E_{O_2}$ . Two temperature scales have been shown below the chemical potential of oxygen at two distinct pressure (1 vs.  $10^{-12}$  atm). The shaded area is marked to show the region of chemical potential under which the different oxygen species are stable. We can see that there is clear transition from the clean surface at low chemical potential of oxygen to the surface oxygen species, and then to the oxide-like surface structure before total bulk oxide occurs.

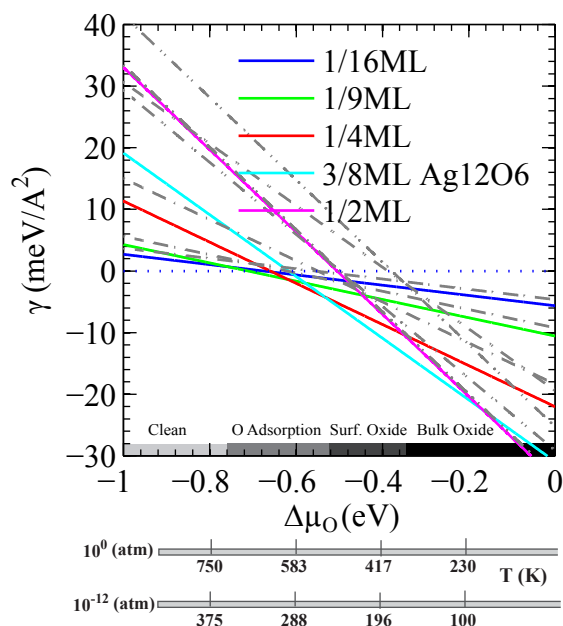


Figure 5.10: Surface free energy of various O/Ag(111) structures is plotted as a function of temperature and the pressure of  $O_2$ . Structures with the lowest energy for a given set of conditions are considered thermodynamically the most stable.

Fig. 5.10 shows that under typical epoxidation conditions ( $T \approx 500$  K,  $p(O_2) = 1$  atm) the most stable O/Ag structure could be the oxide-like surface structure with the coexistence of on-surface and subsurface oxygen species. This finding is consistent with numerous experimental observations which showed that under commercial olefin epoxidation conditions, subsurface O is present [211–213]. Furthermore, our ab-initio thermodynamic studies indicate that thermodynamically the most stable structure under these conditions, is a Ag(111)- $p(4 \times 4)$ -O structure with stoichiometry  $Ag_{12}O_6$ , which has been identified to

be the most stable structure under relevant conditions [225, 226]. However, several DFT studies have shown that  $\text{Ag}_9\text{O}_6$  and  $\text{Ag}_{11}\text{O}_6$  surface oxides have lower surface free energies than experimentally identified structure  $\text{Ag}_{12}\text{O}_6$  [226]. This discrepancy has been attributed to the van der Waals-like interactions, which is not captured by standard DFT functional. For the purpose of this project, the exact stoichiometry of the most stable  $\text{Ag}(111)$ - $p(4\times 4)$ -O structure is not critical. It is much more relevant that at fairly modest  $\text{O}_2$  pressure, consistent with ethylene epoxidation on Ag, there is a thermodynamic driving force to form subsurface O atoms.

The main reason for the formation of subsurface oxygen is the repulsive interaction among O atoms on the surface of  $\text{Ag}(111)$ . This repulsive interaction increases with the on-surface coverage of O. The critical on-surface O coverage, at which any additional O atom is pushed subsurface, is  $1/4$  ML, which is consistent with previous thermodynamic analysis for the oxidation of transition metals [227].

To probe the effect of Cs on the oxidation state of the substrate, we show in Fig. 5.11 the surface free energies, calculated for various O/Cs/ $\text{Ag}(111)$  systems for the  $1/16$  ML coverage of Cs on  $\text{Ag}(111)$ , as a function of oxygen chemical potential,  $\Delta\mu_{\text{O}}$ . We observe that for a wide range of oxygen chemical potential the most stable structures are those with the O atoms adsorbed on surface of the Cs-promoted  $\text{Ag}(111)$ , forming  $\text{CsO}_x$  surface complexes. We have tried to approach the ground state free energy surfaces using DFT calculations, however, the immense phase space of adsorption configurations with Cs adsorbates at this coverage ( $1/16$  ML) precludes the thorough screening with expensive DFT calculations. So here we could not comment on the stability of subsurface oxygen with Cs on the surface due to the limited sampling of configuration space. We only conclude that at relevant conditions,  $\text{CsO}_x$  would be the stable structure of Cs promoters. In the next Section, we are going beyond this limitation, and utilize Cluster Expansion method

to evaluate the energy of the system rapidly, and investigate the structure of silver surface under relevant conditions using Grand Canonical Ensemble Monte Carlo simulations.

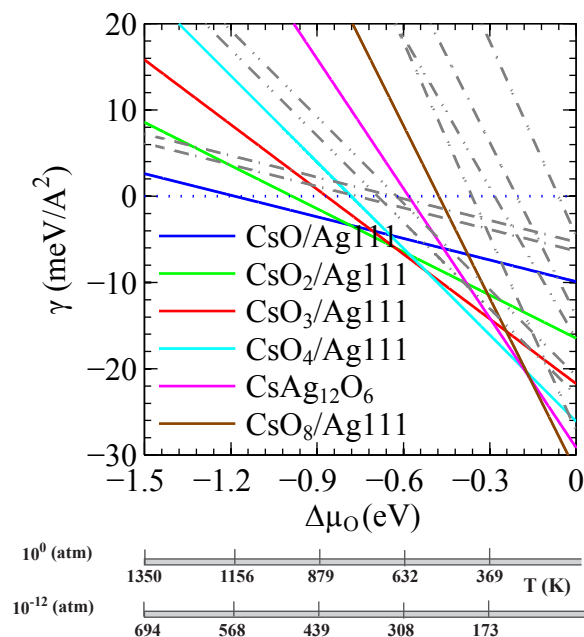


Figure 5.11: Surface free energy of various Cs-O/Ag(111) structures is plotted as a function of temperature and the pressure of O<sub>2</sub>

#### 5.4.2 Stabilization of Oxygen Species by Alkali Promoters

Ab-initio atomistic thermodynamics is a great tool to examine the stability of surface structures under relevant conditions if the phase space of the surface configuration is small and can be easily probed with regular DFT calculations [228, 229]. However, in most cases, we are facing the difficulty of sampling phase space thoroughly to search for lowest energy structures. That indicates that more efficient sampling scheme is necessary for this study.

##### 5.4.2.1 Cluster Expansion Formalism with Coarse-Graining of DFT Energies

To investigate the effect of alkali metals on the stability of oxygen species adsorbed on the silver surface, we need to sample all the surface configurations with varying oxygen coverage. It is important to recognize that there is a large number of possible Cs<sub>x</sub>O<sub>y</sub>

configurations that need to be examined to determine the equilibrium structures for given external conditions and given Cs coverage. This phase space requires a very large number of computationally expensive DFT calculations. The need for expensive DFT calculations can be circumvented by a cluster expansion of the DFT calculated energies [230]. Essentially, effective cluster interaction potentials of pairs and multibodies corresponding to geometrically different clusters are computed from a limited number of DFT calculations, and these potentials are then utilized to calculate the energy of any configuration as an appropriate sum of the interaction potentials [231, 232]. For example, in this procedure, the energy of a system with O and Cs adsorbed on the Ag(111) surface is expressed as

$$(5.19) \quad E(\vec{\sigma}, \vec{\delta}) = V_0 + \sum_j V_j \delta_j + \sum_i V_i \sigma_i + \sum_{i,j} V_{ij} \sigma_i \sigma_j + \sum_{i,j} V_{ij} \delta_i \delta_j + \sum_{i,j} V_{ij} \sigma_i \delta_j + \dots, \quad ,$$

where the indices  $i, j, \dots$  correspond to a collection of sites that form a cluster of atoms such as a pair cluster, a triplet cluster, etc. Coefficients  $V_0, V_i, V_{ij}$ , and  $V_{ijk}$  are called effective cluster interactions (ECI) and are constants, while  $\sigma$  and  $\delta$  corresponds to occupation variables of different species (this is either 1 or 0), in this case either Cs or O, in the cluster. The ECI obtained using this scheme instead of spin variable 1 and -1 notation of site occupation has the advantage of physical intuition. While the expansion, in the exact limit, includes terms corresponding to all possible clusters of sites, from a practical point of view, the equation must be truncated after some maximal sized cluster.

The ECIs ( $V_0, V_i$  and  $V_{ij} \dots$ ) of a cluster expansion need to be determined from first-principles. Several techniques have been used to determine ECIs, and most are based on a linear regression of a truncated cluster expansion to the first-principles energies of different configurations with least-squares method [233–236]. It has been our experience that this approach can give energies that are very close (within 0.01 eV) to the exact DFT-calculated energies with up to 3-body interactions.

In this algorithm, we have explicitly taken into account the subsurface oxygen because

it has been shown that the abundance of the subsurface oxygen can be directly correlated with the catalytic reactivity of Ag catalysts for many oxidation reactions.

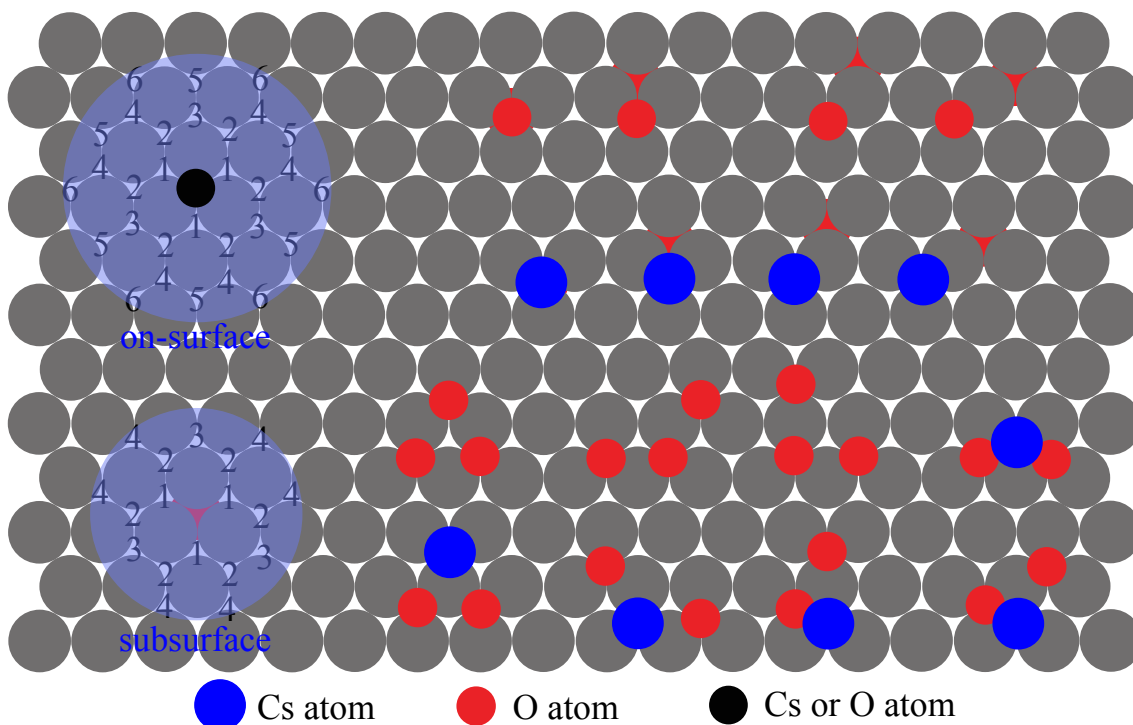


Figure 5.12: Enumeration of effective cluster interactions (65) on the metal surface. HCP and FCC sites are treated as different sites in the cluster expansion.

As shown in Fig. 5.12, we have enumerated all the effective interaction clusters in our cluster expansion method. The on-surface adsorbate-adsorbate interaction up to 6<sup>th</sup> near neighbor has been included and the less long-ranged subsurface oxygen-oxygen interaction up to 4<sup>th</sup> near neighbor is included because of the shielding effect on the subsurface oxygen due to the substrate. The onsurface species (Cs, O) interaction with the subsurface oxygen has been taken into account within 3<sup>rd</sup> near neighbor as shown in Fig. 5.12. The different configurations with fcc and hcp non-degeneracy have been taken into account in the ECIs. Cs is only allowed to adsorb and diffuse on the surface since it is observed experimentally that Cs did not penetrate into subsurface layer under 600 K and it will not desorb until 800 K at low pressure. It must be mentioned that only the Octa and Tetra1

subsurface sites are available for the subsurface oxygen for simplicity, which is not a dramatic approximation since the Tetra2 site has been shown to be highly unfavorable below 1 ML coverage of oxygen. Eight three-body interactions have been included as shown in Fig. 5.12. In this study, the total number of effective interaction clusters is 65. 150 independent DFT calculations with different oxygen and Cs coverage were used for the cluster expansion with a linear least square fit method. The cross-validation score, which is used as the measurement of the predictability of the expansion, is calculated to be less than 0.05 eV.

#### 5.4.2.2 Direct Enumeration for Updating Effective Interaction Coefficients

To obtain reliable ECI parameters for predicting the energies of the electronic system, we need to systematically check the interaction parameters to see if we can approach the ground states using Direct Enumeration method [237]. Basically, if the new ground state at specific coverage of oxygen is found using the current ECI parameters, the DFT calculated energy and structure will be built into the database of DFT calculations for cluster expansion and the interaction parameters will be updated until the ground state free energy profile is converged and there is no new structure with lower free energies.

The results of Direct Enumeration after several iterations are shown in Fig. 5.13 for Ag(111) and Cs/Ag(111) surfaces with oxygen coverage up to 0.375 ML employed in  $4 \times 4$  unit cell, respectively. The surface configuration with higher O coverage than 0.375 ML is difficult to probe due to the enormous amount of possible combinations. Since we are investigating the initial stage of the oxidation of the substrate, the system with higher oxygen coverage than 0.375 ML is less relevant. So we have not taken further steps to probe this phase space completely. In this system, we can make sure that the energetics of all the possible structures with oxygen coverage up to 0.375 ML can be evaluated effectively using calculated interaction parameters with Lattice Gas Hamiltonian. The solid triangle

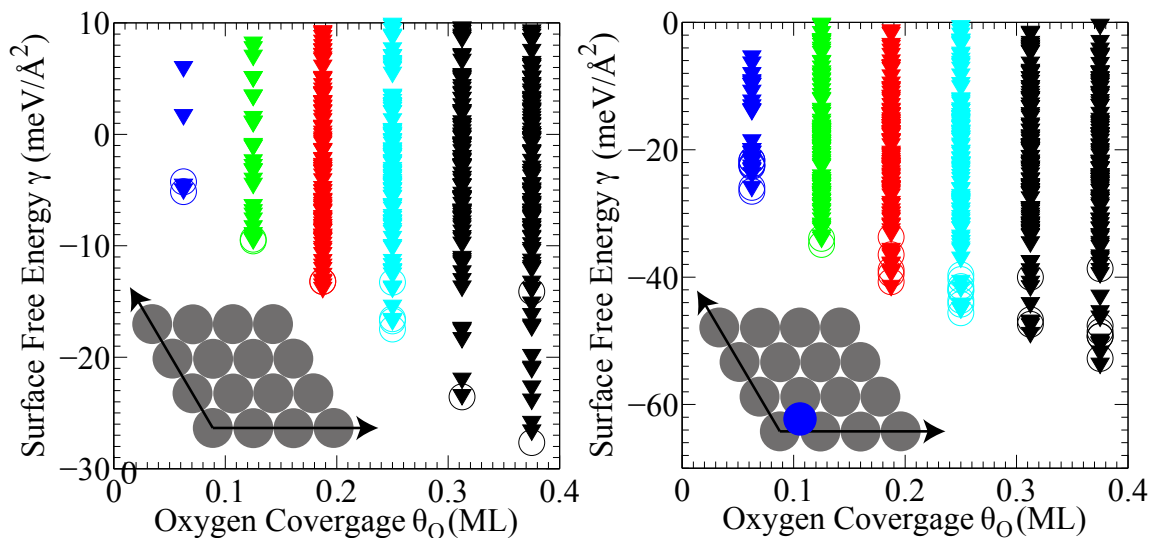


Figure 5.13: Surface free energies from Direct Enumeration (triangle) of Surface Configurations using Effective Interaction Coefficients and self-consistent DFT calculations (circle). This step took several iterations until no new structure is found. (a) clean Ag(111), (b) Ag(111) with 1/16 ML Cs

is the surface free energy obtained from cluster expansion and the open circle is from the DFT calculations. The colored ones ( $\leq 1/4$  ML) are for the calculations without subsurface oxygen in the ground state structure and the black ones are for the systems with subsurface oxygen stable on the ground state structures. We can see that the cluster expansion method can predict the ground state energy under the oxygen coverage up to 0.375 ML very well compared with DFT calculations. The transition from on-surface oxygen to the coexistence with subsurface oxygen around 1/4 ML is consistent with previous thermodynamic analysis [227]. The 65 interaction parameter is plotted in Fig. 5.14 with different near neighbor interaction. The physical meaning of the interaction parameter can be deduced from the trend of the each set of interaction parameters.

As shown in Fig. 5.13 we have observed there is a discrepancy between the cluster expansion and DFT calculations with high coverage of oxygen, which involves significant amount of subsurface oxygen, resulting in the reconstruction and roughing of the silver substrate. So the conclusion drawn from this paper can only be limited to the region of the initial oxidation of the Ag substrate with limited amount of surface reconstruction.

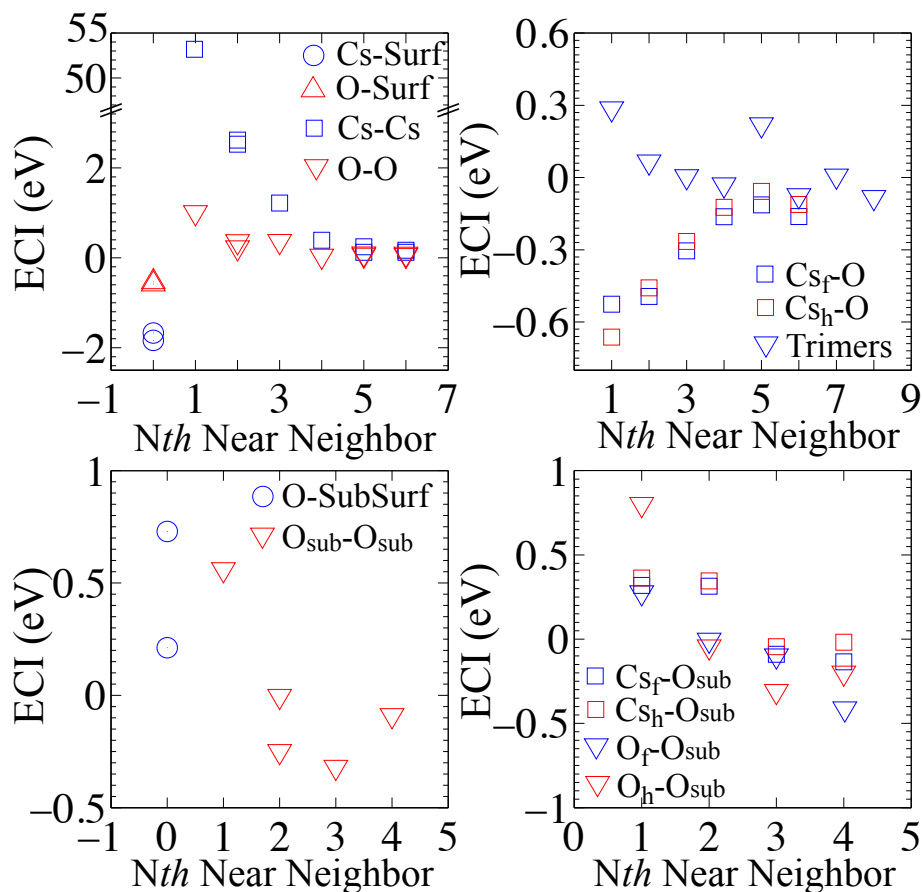


Figure 5.14: Effective Interaction Coefficient for 65 characteristic clusters including monomer, pairs and trimers. The coefficients shown here have been updated using Direct Enumeration method. The cross-validation score is 0.05 eV based on the “taken-one-out” method

It is important to note that again the oxygen coverage in the Direct Enumeration is only up to  $3/8$  ML. The current computational algorithm cannot assure the extensive searching in the higher coverage. So the method will not be valid for higher coverage. But the high repulsion between oxygen atoms will exclude the formation of local high coverage of adsorbed oxygens in the attempted move of the Monte Carlo simulation.

#### 5.4.2.3 Grand Canonical Monte Carlo Simulation

We have utilized cluster expansion method, combined with the ground state Direct Enumeration search on the Ag(111) surface, to calculate the effective cluster interaction parameters. After updating the parameter for several iterations, we have been successfully

approaching the ground states free energy profiles up to 3/8 ML oxygen coverage with reasonable accuracy compared with DFT calculations.

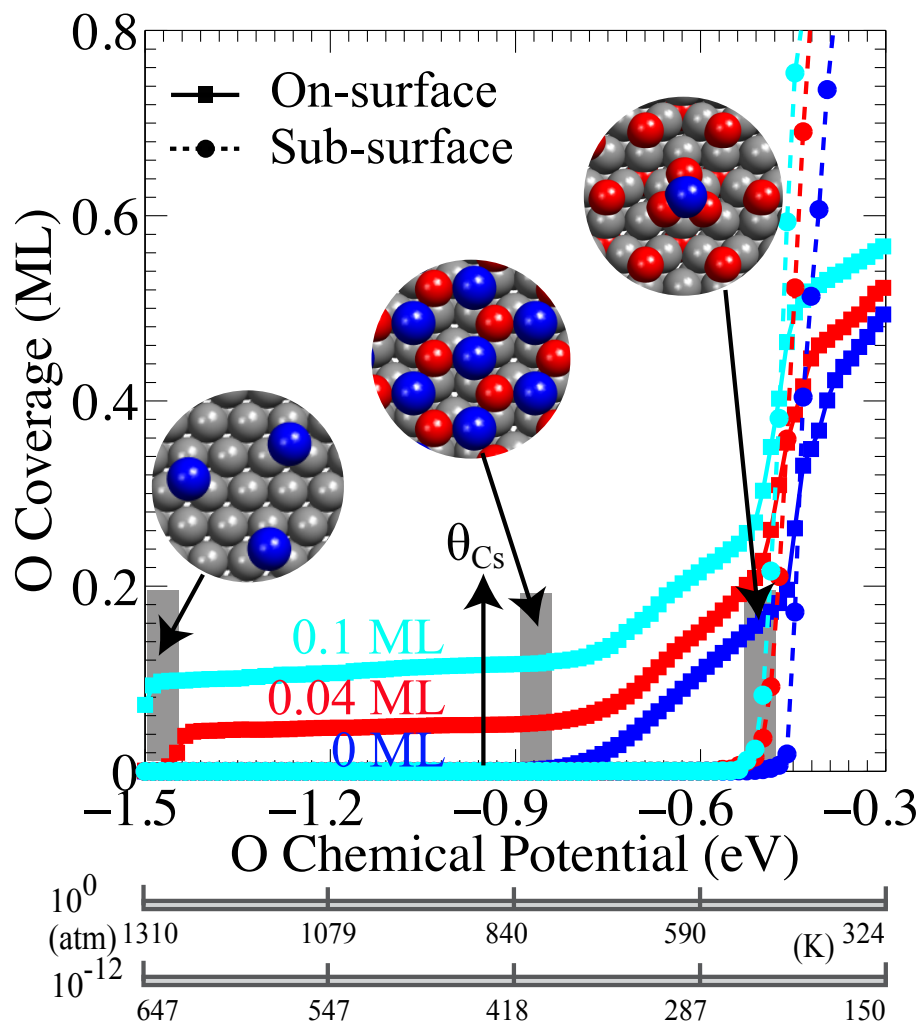


Figure 5.15: Grand Canonical Monte Carlo simulation of the effect of Cs promoters on the uptake of on-surface and subsurface oxygen. Blue: clean Ag(111), Red: Cs 0.04 ML, Cyan: 0.1 ML

Using Grand Canonical Monte Carlo simulations, we can investigate the effect of Cs on the thermodynamic stability of the ground state structures and on the partition of on-surface and sub-surface oxygen uptake under different oxidation conditions. The energy difference associated with each Monte Carlo move is calculated using ECI parameters on-the-fly. The details of the simulation is elaborated on the method section. As the simulation approaches the thermodynamic equilibrium, the coverage of on-surface and

sub-surface oxygen is counted. The results of the simulation are shown in Fig. 5.15.

In a wide range of oxygen chemical potential ( $T, p$ ), we can see that the surface oxygen adsorption have been greatly promoted by Cs. Higher Cs coverage results in the greater on-surface oxygen uptake, which makes sense because there is a strong attraction between Cs and O on the Ag(111) surface. Because of the attraction between on-surface and sub-surface oxygen in the far region as shown in Fig. 5.14(d), the sub-surface oxygen adsorption has also been promoted due to the increased coverage of on-surface oxygen. For the Cs coverage at 0.1 ML, the different surface configurations were observed under different chemical potentials of oxygen gas phase. In the region with low oxygen chemical potential, typical of UHV surface science experiments, there is the Cs adatom on the Ag(111) surface as shown in Fig. 5.15. The forming ordered Hexagonal superlattice has been observed previously using STM at similar coverage [238], and can be attributed to the strong dipole-dipole interactions between Cs adatoms on the Ag(111) surface. In the region with medium oxygen chemical potential, there is the formation of Cs superoxide patches  $(2\sqrt{3}\times 2\sqrt{3})R30^\circ$  on the surface, which is very stable and appears to block the surface. The similar structure and Cs/O stoichiometry has been experimentally measured previously using LEED and TDS [77]. In the region with higher oxygen chemical potential, there is the coexistence of Cs oxides ( $\text{CsO}_x$ ) and subsurface oxygen as shown in Fig. 5.15. This is the direct consequence of the strong O-O repulsion of on-surface oxygen and the slight attraction of subsurface oxygen with on-surface oxygen at third and forth near neighbor as shown in Fig. 5.14. We can also observe that Cs lowers the critical oxygen chemical potential for the formation of the subsurface oxygen, i.e., the stabilization of subsurface oxygen by Cs promoters via the promotion of onsurface oxygen adsorption. The on-surface oxygen coverage is around 0.25 ML as the onset formation of subsurface oxygen, which is fully consistent with Scheffler's thermodynamic analysis of initial oxi-

dation of transition metal substrates.

### 5.4.3 Consequence and Mechanism of Subsurface Oxygen Formation on the Surface Reactivity

The observations that there are different stable Cs complexes and oxygen species on the Ag(111) surface under different oxidation conditions from the Monte Carlo simulation stimulate us to understand their effects on the kinetics and thermodynamics of the dissociative adsorption of O<sub>2</sub> on the Ag(111) surface. We have utilized DFT calculations and the adsorbate-adsorbate interaction model developed previously in Chapter 3 to investigate the underlying mechanism of interaction between relevant surface structures with different oxygen species, i.e., molecular oxygen, transition state oxygen and the atomic oxygen.

Under very low oxidation condition, or reducing environment, it has been shown that there are Cs adatoms adsorbed strongly on the Ag(111) surface. Previously, we have shown that there is the formation of a strong induced dipole moment as Cs adatoms adsorb on the Ag(111) surface. The induced electric field from the surface dipole moment can stabilize the electronegative species, especially for species with significant polarizability. For Cs promoted adsorption and activation of O<sub>2</sub> species, the electrostatic and polarization contribution dominates the interactions between Cs and adsorbates. Cs induced electronic effect through the substrate *sp*- and *d*-electrons is small compared to electrostatic and polarization.

Cs superoxides (CsO, CsO<sub>2</sub> and CsO<sub>3</sub>) have been observed and identified from Monte Carlo simulations starting from medium O<sub>2</sub> chemical potential as shown in Fig. 5.15. However, the fundamental understanding of the effect of Cs superoxides on the different oxygen species is still lacking. Here, we have investigated the interaction of different Cs superoxides with atomic oxygen, molecular oxygen and transition state oxygen. From Fig. 5.16, we can see that the electrostatic and polarization can predict the trend of the interaction energies from DFT calculations, which indicates that electrostatic and polar-

ization components have a great contribution to the interaction. However, the electronic effect also plays an important role here as we can see from Fig. 5.16. So we can conclude that the combined mechanism of electronic together with electrostatic and polarization mechanism dominates the effect of Cs superoxides on the kinetics and thermodynamics of the dissociative adsorption of oxygen. CsO species will promote the oxygen dissociation just like pure Cs adatoms due to induced electric field, but CsO<sub>3</sub> structure will poison the oxygen dissociation from Fig. 5.16 because of the shielded induced electric field and the electronic Pauli repulsion from surface oxygen.

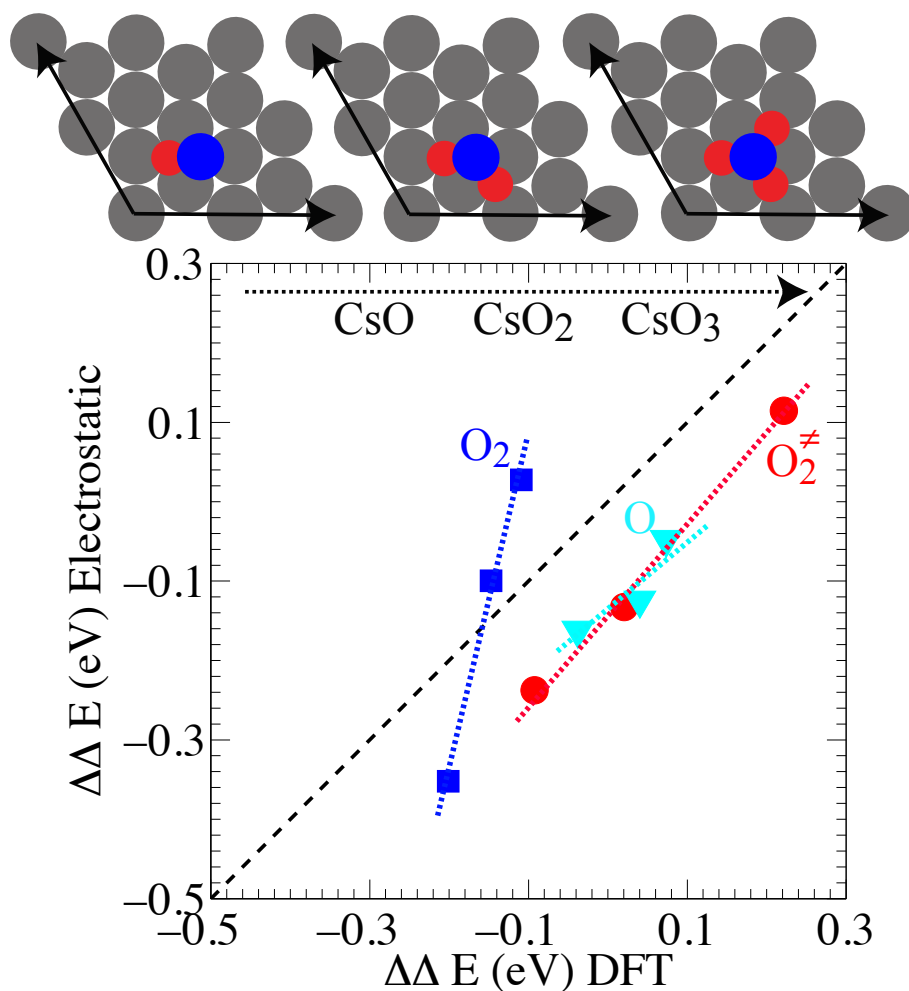


Figure 5.16: Model calculated electrostatic and polarization contributions into the interaction of CsO<sub>x</sub> with different oxygen species on Ag(111)

The role of subsurface oxygen on the adsorption of several simple molecules has been

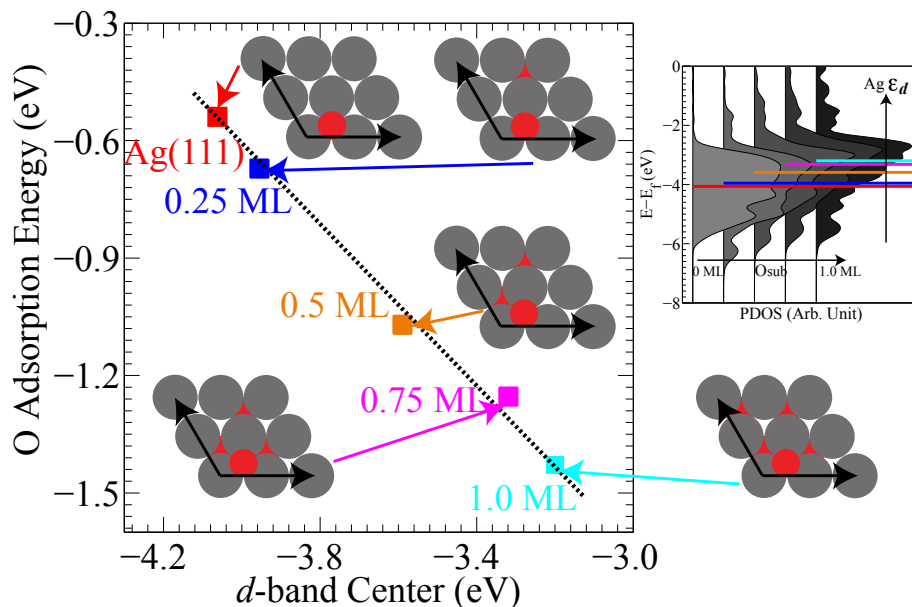


Figure 5.17: Correlation between oxygen adsorption and  $d$ -band center of the surface silver atoms. The inserts model show the geometry of the oxygen adsorption on the Ag(111) surface with varying coverage of subsurface oxygen. The projected density of states of surface silver atoms on different geometries are shown to illustrate the effect of subsurface oxygen on the variation of surface  $d$ -band center.

addressed by previous researchers [239]. In order to further understand the working mode of subsurface oxygen on the thermodynamics and kinetics, we have calculated the atomic oxygen adsorption on the Ag(111) surface with subsurface oxygen coverage up to 1 ML. From Fig. 5.17, we can see that there is a direct correlation between the surface  $d$ -band center and the atomic oxygen binding energy for the different subsurface oxygen coverage. The subsurface oxygen induced change in the electrostatic potential above the surface is negligible since the screening effect of the free  $sp$ -electrons of the substrate. So the mechanism of the promotion of subsurface oxygen on the surface oxygen adsorption is mainly due to the electronic effect, where the  $d$ -band center can be used as the single parameter to determine the binding energy of simple adsorbates on metal surfaces. The  $d$ -band center change of the surface Ag atoms as the formation of subsurface oxygen is due to the decrease of the coupling strength of Ag-Ag from the significant surface roughing [58] and the electronic depletion of  $d$ -band due to the electronegative nature of subsurface

oxygen as we can see from the density of states plot of surface metal  $d$ -bands in Fig. 5.17.

## 5.5 Summary

We have developed a very general and physically transparent model, based on DFT calculations, which allows us to better understand adsorbate-adsorbate interactions on surfaces. This model was utilized to examine the effect of Cs adsorbates on the  $O_2$  dissociation reaction on the Ag(111) surface. These studies revealed that the main mode by which Cs affects the dissociation of  $O_2$  on Ag(111) is long-range electrostatic and polarization interactions between Cs and relevant reaction intermediates. These electrostatic and polarization interactions stabilize the transition state involved in the dissociation of  $O_2$ , lowering the activation barrier. The developed model was further utilized to address a number of other phenomena (alkali promoted NO adsorption on Pd surfaces) where adsorbate-adsorbate interactions play an important role. These studies demonstrated that the proposed approach is fairly universal, and that it can be used to address multiple issues related to chemical reactions on metal surfaces.

Cluster Expansion and Direct Enumeration methods were used to parameterize the adsorbate-substrate and the adsorbate-adsorbate interactions involving cesium (Cs) and oxygen (O) on the Ag(111) surface. The subsurface oxygen species has for the first time been directly taken into account in the Lattice Gas Hamiltonian to evaluate the energetics of the system under different oxidation conditions. The surface structures with lowest surface free energies under different chemical potentials of the gas phase oxygen have been identified using Grand Canonical Monte Carlo simulations. The physical mechanism of the interactions between the observed surface structures and relevant oxygen species has been investigated in details by using previously proposed the adsorbate-adsorbate interaction model on metal surfaces. And we have illustrated that there is the transition of the

promotion mechanism of oxygen adsorption on the Ag(111) surface from the mode of electrostatic/polarization into electronic as going from the reducing environment or UHV conditions to the highly oxidizing environment or relevant catalytic oxidation conditions as shown in Fig. 5.18. The insights obtained from the multi-scale modeling can shed light on the understanding of alkali promotion mechanism for various oxidation reactions taking place on the Ag(111) surface and facilitate the rational design of better and efficient catalysts.

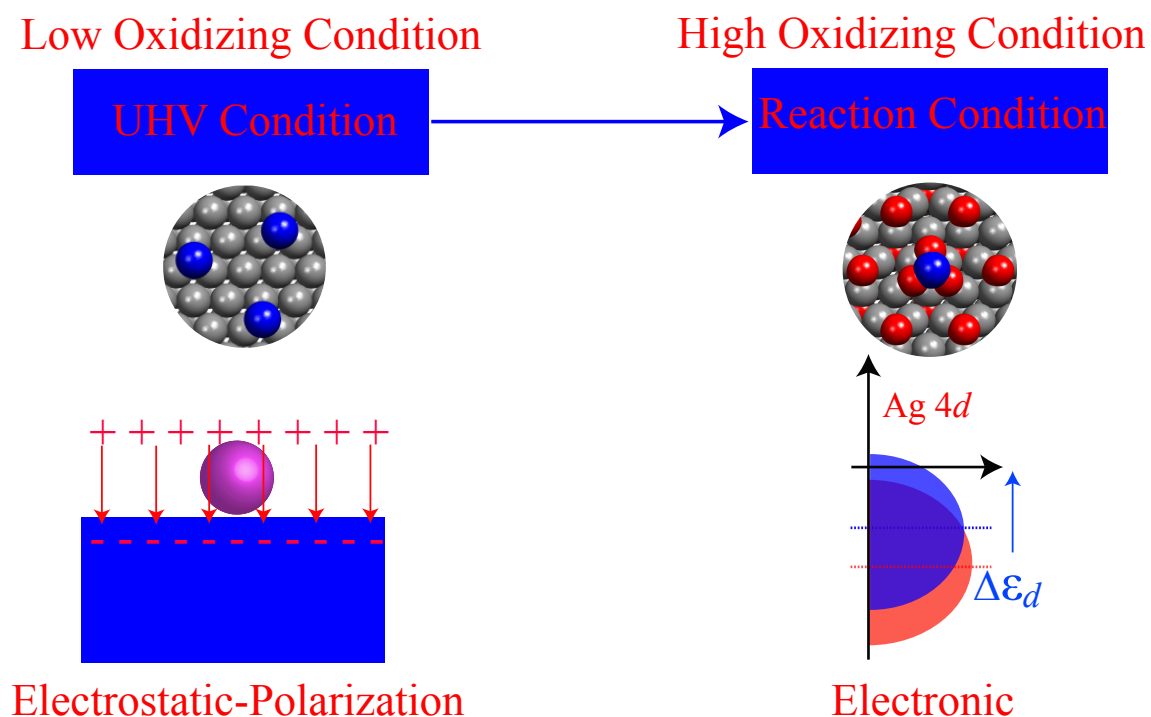


Figure 5.18: Cs promotion mechanism under different operating conditions

## CHAPTER VI

### Imposing Stimuli for Electronic Excitations

#### 6.1 Introduction

Chemical reactions on metal surfaces are typically driven by phonons, i. e., the coupling of adsorbates vibrational degree of freedom (the reaction coordinate) with the infinite heat bath of the substrate [240]. The intrinsic activation barrier separating reaction intermediates can only be surmounted if adsorbates gain enough energy from vibrational excitations. Identical chemical transformations on metal surfaces can proceed via the coupling of adsorbates with the other excitation sources, such as electrons. Hot electron induced surface chemistry has been recognized for decades and attracted much more attention recently due to its great significance in fundamental surface science and practical applications, such as hot electron based photovoltaic system [241].

Energetic electrons can be generated from many physical processes [241], such as photoelectrons from the absorption of photons in materials, tunnelling electrons from the tip of Scanning Tunnelling Microscope (STM) and emitting electrons from metal-insulator-metal (MIM) devices with bias potential [242]. For example, as a high intensity ultra-fast laser pulse strikes the solid surface, it can produce hot electrons with high temporal resolutions [243]. The generated electrons quickly ( $\sim 10$  fs) scatter around resulting in thermalized electron gas described by the Fermi-Dirac distribution [244]. Two-temperature model

has been employed previously to describe the energy transfer and evolution of the system upon the illumination of laser pulses [243]. The time-dependent phonon and electron temperature of the substrate obtained from Two-Temperature Model can then be coupled to the vibrational degree of freedom of the adsorbate based on the empirical Friction model [245]. The time evolution of vibrational states of the adsorbate can be used to calculate the reaction probability statistically. Even though those models have enjoyed some success in explaining the desorption dynamics of the molecules with ultra-fast laser pulses, however, wavelength dependence [246] of surface chemistry and adsorbate-substrate system-dependent [247] power law exponent ( $R \propto I^n$ ) can not be directly understood using this theoretical framework due to their statistical nature.

Instead of purely statistical descriptions of the system, the fundamental mechanism of the hot electron induced surface reactions has also been elaborated using inelastic resonance electron scattering model [248, 249]. In this model, hot electrons scattering into adsorbate-metal anti-bonding orbitals form transient negative ions, which accelerate on excited-state potential energy surfaces due to the force exerted on the nucleus. During this process energy can be directly deposited into adsorbates vibrational degree of freedom upon decaying back to the ground state. If enough energy is gained or accumulated due to electron scattering events, surface reactions can occur. Based on this model, the desorption induced by electronic transition (DIET) [250] and desorption induced by multiple electronic transition (DIMET) [251] have been proposed to understand phenomenon observed in femto-second laser experiments. The wave-length dependent surface chemistry and system-dependent power law exponent of reaction rates with respect to incident light intensity can be physically interpreted. Usually those experiments have to be performed under the UHV condition with extremely low temperature to exclude any thermal disturbance for surface characterization. The effect of the temperature on the electron scattering

events has been briefly introduced previously [252], but there is no model explicitly taking into account of the effect the temperature. To further understand this surface phenomenon with the coupling of thermal energy and photon energies (e.g., solar energy), it is beneficial to have one unified model which can effectively describe the coupling of various energy forms and provide physical insight into the surface chemistry with multiple stimuli.

In this Chapter, we start from the experimental observation of highly efficient photo-thermal ethylene epoxidation reaction on silver plasmonic (collective oscillation of free electron gas density) nanoparticles. By using low-intensity visible light the operating temperature can be decreased by as much as 100 K with similar viable reaction rate as pure thermal process [253], which has great potential for suppressing the side combustion reactions and lengthening the catalyst lifetime. To understand the dramatic effect of light intensity and operating temperature on the kinetics of the reaction, we have developed and employed a Finite-Temperature Electron Scattering Model based on first-principles DFT calculations. The main feature of the model compared to existing ones, e.g. empirical Friction model and Electron Scattering Model, is that it can describe the kinetics of the surface reactions which are coupled to the bath of multiple excitation sources (phonons and electrons) with the consideration of microscopic events occurring on the surface. So current model can provide more physically-transparent understanding of the surface reactions at molecule level. To tackle the problem theoretically, we have focused on the oxygen dissociation reaction on Ag(100) surface since it has been shown that oxygen dissociation is rate limiting step for various olefin epoxidation at low temperature regime. By focusing on the dynamics of oxygen activation on the surface with the inclusion of multiple excitation sources, we can understand the experimentally observed phenomenon and provide a rational way to improve the efficiency of current technology. Targeted electron attachment of resonance states can potentially induce selective surface chemistry which

can not be obtained using homogeneous heating. In this Chapter, we have shown some preliminary studies elaborating the underlying electronic properties governing the variations in resonance energies of simple adsorbates on metal and alloy surface, which can be used as guideline for tuning the surface chemistry using MIM device with tunable resonant electron energies.[242]

## 6.2 Experimental Phenomenon

In this collaborated project, we have performed extensive experiments on the ethylene epoxidation reaction over plasmonic silver nanocubes (75 nm) with low intensity visible light illumination (0~1000 mW/cm<sup>2</sup>). For details of the experiments, please see following publications [253]. Energetic electrons resulting from the photo-absorption of low-intensity visible light in silver nanocubes are confined within the nano-meter scale. The excitation of surface plasmon resonance of silver nanocubes significantly enhances the local field in hot spots of close-packed particles and localizes the hot electrons on surfaces, which plays an important role for the enhancement of efficiency of photochemistry on metal surfaces [253]. or metal/semiconductor interface [254]. The main finding of our experimental studies are shown in Fig. 6.1. First, as shown in Fig. 6.1(a) we observed that there is regime transition from linear to super-linear of the reaction rate ( $R \propto I^n$ ) on the incident light intensity, which can only be obtained previously utilizing high-intensity ultra-fast laser pulses. The exponent  $n$  calculated from the relationship  $R \propto I^n$  is shown along with the measured photo-rate at varying intensity. As we can see the exponent can be as high as 3.5 at higher intensity regime as shown in Fig. 6.1(b). At varying temperatures, we have observed similar behavior. Second, we found that there is an exponential increase of photo-rate with respect to the operating temperature as shown in Fig. 6.1(a), which is in sharp contrast to the general feature of semi-conductor photochemistry where the

temperature only has minimal or detrimental effect on the photo-rate due to the phonon-assisted electron-hole pair recombination. To understand these experimental observations, we have extended the previous electron scattering model to investigate the dynamics of the hot-electron induced surface reactions at the finite temperature and developed a theoretical framework providing guidance for selective photo-chemistry on metal surface with tailored electronic properties.

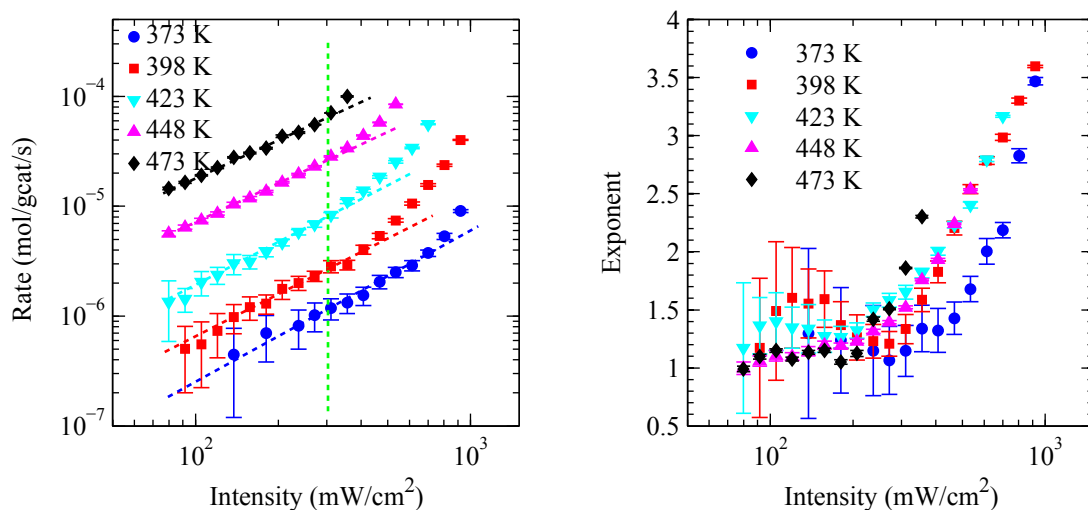


Figure 6.1: Photo-thermal reaction on silver nanocubes. (a) Epoxidation rate as a function of light intensity at different temperature. (b) Calculated exponent of photo-thermal reaction as a function of light intensity at different temperature

### 6.3 Theoretical Approaches

Understanding of the fundamental mechanism of surface reactions with multiple excitation sources is critical for the rational design of energy efficient and environmentally-friendly chemical processes. From theoretical point of view, it is desirable to develop a physically-transparent unified reaction rate theory which can describe the dynamics of surface reactions coupled to the bath of multiple excitation sources. Here we are going to elaborate the theoretical approaches we employed to study the surface reactions with transient multiple excitations coupled to the reaction coordinates.

### 6.3.1 Non-adiabatic Newns-Anderson Model

In the Born-Oppenheimer approximation the molecular wavefunction of extended systems can be separated into the nucleus and electronic part, and the electronic wavefunction is only parametrically dependent on the coordinate of the nucleus. The underlying principle for this approximation is that the motion of nucleus is relatively slow compared to electrons, which is a reasonable approximation considering the mass difference between electron and proton. So the electronic state can be seen adiabatically varying with respect to the nucleus motion. This approximation has been widely used currently for the general understanding of catalytic process and the electronic and vibrational properties of catalytic materials.

However, Born-Oppenheimer approximation breaks down if electronic transitions occur. For laser-induced surface chemistry or photochemistry, the eigenstate of the system is not adiabatic with respect to applied electro-magnetic field. Whenever the non-adiabatic transition occurs, the system should be dealt with non-adiabatic surface chemistry.

The non-adiabatic surface chemistry can also be described based on the theoretical framework of Newns-Anderson model (shown in Chapter 2) with additional coupling of electronic states with vibrational states of the adsorbate [248]. The Hamiltonian describing the Non-adiabatic system including electronic, phonon and the coupling between those two systems upon electronic transition can be represented on Eq. 6.1 as

$$(6.1) \quad \hat{H} = \hat{H}_{el} + \hat{H}_{ph} + \hat{H}_{int},$$

where the Hamiltonian for the electronic system is described as in Eq. 6.2. It includes the energy of adsorbate electronic resonance states, the substrate states and the coupling between those two via coupling matrix  $V_{ka}$ .  $c_{\dagger}$  and  $c$  are the creation and annihilation

operators for electronic transition, respectively [248].

$$(6.2) \quad \hat{H}_{el} = \varepsilon_a c^\dagger c + \sum_k \varepsilon_k c_k^\dagger c_k + \sum_k V_{ka} (c_k^\dagger c + c^\dagger c_{ka}^\dagger)$$

The Hamiltonian of the phonon contribution basically consists of all the phonon energies of different modes including the zero-point energy based on simple Harmonic oscillator approximation. We have

$$(6.3) \quad \hat{H}_{ph} = \hbar \sum_i \omega_i (b_i^\dagger b_i + \frac{1}{2}),$$

where  $b^\dagger$  and  $b$  are creation and annihilation operators of Harmonic Oscillator. The product of those operator essentially gives the number of the vibrational quanta for each vibrational mode.

The coupling between the electronic system and the vibrational states is linearly represented as

$$(6.4) \quad \hat{H}_{int} = \sum_i \lambda_i c^\dagger c (b_i + b_i^\dagger),$$

where  $\lambda_i$  is the coupling constant between the electronic resonance states and the vibrational mode  $i$ . Classically, for each vibrational mode, the energy change due to the occupation of excited electronic state ( $c^\dagger c = 1$ ) can be written as

$$(6.5) \quad \lambda_i (b_i^\dagger + b_i) = -f_i |(x_i - x_i^1)|,$$

where  $f_i$  is the nuclear force on the reaction coordinate upon the occupation of excited electronic state.  $x_i - x_i^1$  is the distance off the equilibrium position of excited state potential energy surface for vibrational mode  $i$ , where  $x_i^1$  is the reaction coordinate of excited state potential energy surface with minimum energy and  $x_i$  is the instant reaction coordinate of adsorbate/surface complex upon excitation. According to the basic definition of the operator in Harmonic Oscillator [255], we can get

$$(6.6) \quad b_i^\dagger + b_i = \sqrt{2}(x_i - x_i^1) / \sqrt{\frac{\hbar}{m\omega_i}}.$$

Based on Eq. 6.5 and Eq. 6.6, we can easily relate the lambda to the driving force for nucleus motion,  $f_i$ , which can be directly deduced from the excited state potential energy surface as

$$(6.7) \quad f_i = -\frac{dV_i}{dx_i}.$$

The coupling constant can be calculated as

$$(6.8) \quad \lambda_i = \frac{l}{\sqrt{2}} \frac{dV_i}{dx_i} \Big|_{x_i=x_i^0}, \quad l = \sqrt{\frac{\hbar}{m\omega_i}},$$

where  $x^0$  is the ground state minimum position.

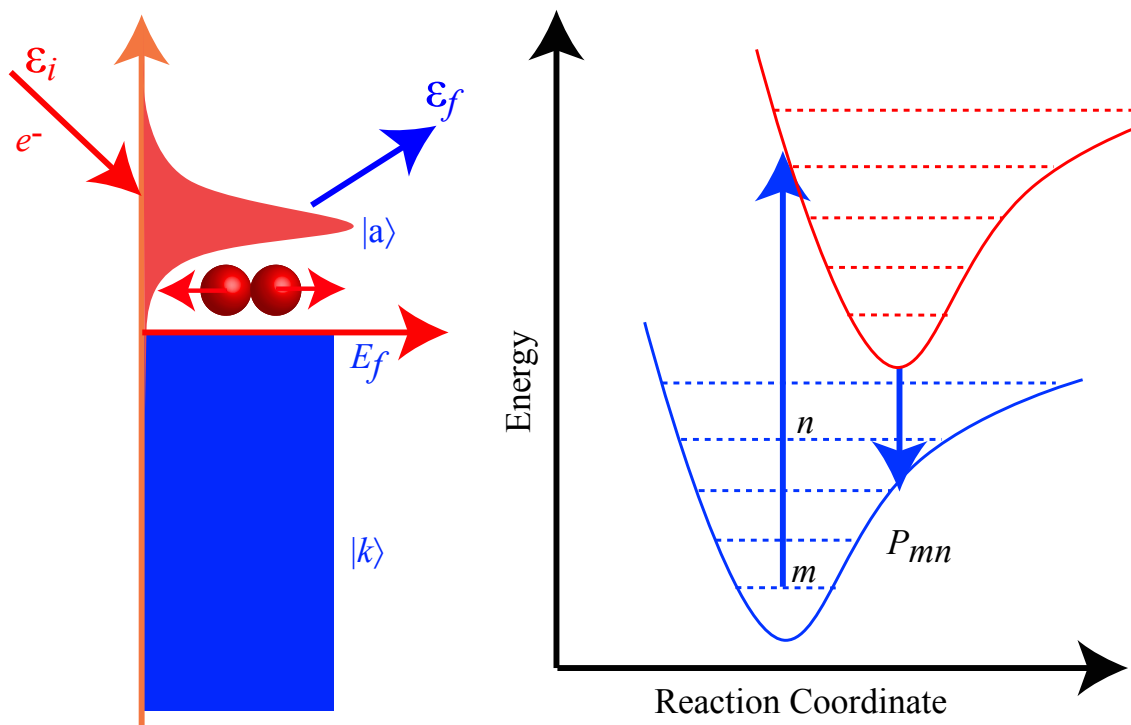


Figure 6.2: Schematic illustration of Newns-Anderson-Type Hamiltonian for the model

To calculate the coupling constant we need the vibrational frequency of adsorbates which can be easily obtained from ground state DFT calculations or standard frequency analysis, and also the details information about the potential energy surfaces excited state which can be obtained using Linear-Expansion  $\Delta$ SCF-DFT. The physical process of this

phenomenon can be illustrated in Fig. 6.2. The transition probability  $P_{mn}$  from one vibrational state  $m$  to another vibrational state  $n$  if the incident electron energy is  $\varepsilon_i$  can be calculated based on the non-adiabatic Newns-Anderson Model. For details of the derivation, please see the following publications [248, 252].

### 6.3.2 Linear-Expansion $\Delta$ SCF-DFT for Excited States

The ground state PES can be calculated easily using any quantum-chemical calculations, mostly DFT for extended systems. For example, for single vibrational mode of the adsorbate-surface complex, we can obtain the energy topology by varying the inter-nucleus distance to map out the potential energy surfaces associated with this specific vibrational mode. Excited-state arises upon the transient electron attachment of initially unoccupied resonance state due to electronic excitations. For finite system, such as molecules in gas phase, the excited state energies can be calculated based on HF or DFT method, but it is usually approximated as the Morse potential [256] for adsorbates on extended surfaces. Other methods, such as Time-dependent DFT (see recent review [257]), GW approximation, Cluster Configuration, *et al.*, are available for obtaining excitation energies but usually computationally expensive and only applicable to small systems. Just recently a Linear-Expansion  $\Delta$ SCF-DFT method, which is an implementation in GPAW, has been employed to study the excited state. In this method, electrons can be taken from the Fermi level and populated on specific molecular orbitals, which are not any of the Kohn-Sham orbitals of the ground state calculation, but the superposition or linear expansion of many orbitals obtained from each SCF cycle to resemble the initial resonance state of gas phase adsorbate/surface complexes or just the gas phase molecule. The electron density and energy of the system is calculated self-consistently by using this new set of orbitals. The calculation usually needs careful convergence with respect to the number of unoccupied bands. The results can be directly compared to the experimental measured spectra using

inverse emission spectroscopy [258]. And it has been shown previously that this method can give reasonable agreement with experimental measurement with minimal computational cost comparable to ground state calculations [258].

In this method, electron density of the system with occupation of the excited state can be written as the sum of electron densities of all orbitals including  $N-1$  low lying orbitals and the high-lying orbital where excited electron stays based on

$$(6.9) \quad n(r) = \sum_{i=1}^{N-1} f_{N-1}(\epsilon_i) \psi_i^*(\mathbf{r}) \psi_i(\mathbf{r}) + \psi_a^*(\mathbf{r}) \psi_a(\mathbf{r}),$$

where  $f_{N-1}$  is the Fermi smearing function for  $N-1$  electronic states,  $\psi_i$ , with orbital energy  $\epsilon_i$ ;  $\psi_a$  is a linear expansion of a set of empty Kohn-Sham orbitals ( $\phi_n$ ) of self-consistent calculations as shown in Eq. 6.10. The Kohn-Sham states from  $\Delta$ SCF method are different from the Kohn-Sham states from ordinary ground-state calculations due to the difference of Hamilton through the change in the density when different orbitals are occupied. For initially unoccupied state, the Kohn-Sham orbitals above the Fermi level are used to expand the new resonance orbital as shown in Eq. 6.10 and the coefficients  $c_{na}$  are obtained by the overlap between ground state Kohn-Sham orbital ( $\phi_n$ ) and the molecular wavefunction of gas phase or adsorbate/surface resonance state ( $\phi_a$ ). The number of unoccupied orbitals needs to be significantly large to ensure better expansion and convergence.

$$(6.10) \quad |\psi_a\rangle = \sum_{i=N}^M c_{ia} |\psi_i\rangle$$

In Eq. 6.10, resonance orbital is written as linear expansion of empty Kohn-Sham orbitals self-consistently obtained from the calculations. The expansion coefficient is determined by maximizing the resemblance of this resonance with specific molecular orbital of the gas phase molecule as

$$(6.11) \quad c_{ia} = \frac{\langle \psi_i | \psi_a \rangle}{(\sum_i |\langle \psi_i | \psi_a \rangle|^2)^{1/2}}.$$

In Fig. 6.3, we show the DFT calculated ground state and excited state ( $2\pi^*$ ) potential energy surfaces for  $O_2$  adsorption on the Ag(100) surface. The bridge site adsorption configuration has been shown to be the most stable geometry at this coverage (1/4 ML) [259]. For the ground state, the  $O_2$   $2\pi^*$  anti-bonding orbital is only partially occupied as shown in Fig. 6.3(a), which keeps  $O_2$  molecule intact and not dissociated until there is sufficient amount of vibrational energies provided by heat to surmount the energy barrier. The activation barrier for  $O_2$  dissociation on Ag(100) surface bridge site is about 1.17 eV from GPAW NEB calculations. In Fig. 6.3(b), the ground-state and excited-state potential energy surfaces are obtained by perturbing the O-O bond distance around the ground state minimum equilibrium position.

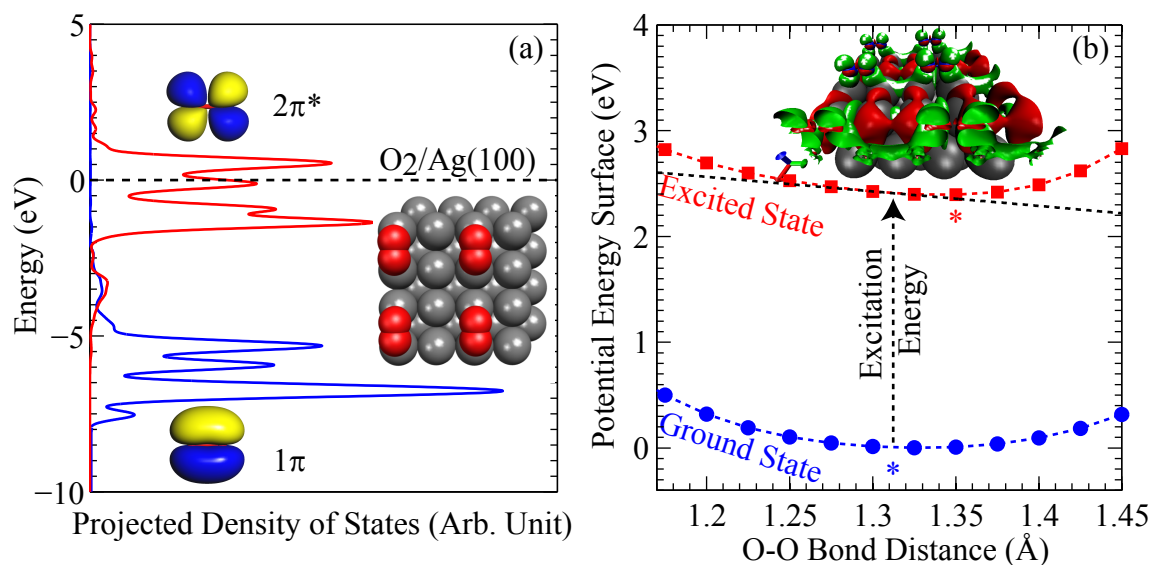


Figure 6.3: (a) Molecular orbital of DOS for  $O_2$  adsorption on Ag(100) Surface. Insert shows the adsorption configuration of  $O_2/Ag(100)$  with 1/4 ML. (b) Potential energy surfaces of  $O_2$  Dissociation on Ag(100) Surface. Insert shows the distribution of excited electrons at  $O_2/Ag(100)$  complex, green is extra electron accumulation, and red is electron deficiency

The resonance energy of  $O_2$   $2\pi^*$  anti-bonding orbital in the excited state is about 2.4 eV at the ground state minimal bond distance based on the linear-expansion  $\Delta$ SCF-DFT method. This energy characterizes the required hot electron energies to excite the  $O_2$  molecule to form transient negative ion evolving on excited state potential energy surfaces.

Due to the finite lifetime of electronic resonance state ( $\tau = \hbar/\Gamma$ , where width  $\Gamma \sim 1$  eV), the energy range of hot electrons accessible to  $O_2$   $2\pi^*$  anti-bonding state is much wider. The vibrational frequency deduced from ground state potential energy surface using Harmonic oscillator approximation is 101.9 meV. This is used as we calculate the coupling constant between electronic state with vibrational state in Eq. 6.8 and the dissociation probability due to electronic and phonon excitation. The force imposed on the adsorbate nucleus due to the formation of transient negative ion in the excited state potential energy surface -  $dV/dx$  can be directly evaluated from excited state potential energy surface (-0.95 eV/Å). The O-O internal vibrational mode coupling constant  $\lambda$  from Eq. 6.8 is -47.9 meV. Those parameters obtained from DFT-calculated potential energy surfaces are used to evaluate the energy transfer process associated with substrate electron mediated  $O_2$  dissociation on Ag(100) surface. The potential energy surface is assumed to be harmonic at the local area of the equilibrium for ground state and excited state. As we can see for  $O_2$  molecule dissociation reaction, this is the fair approximation.

## 6.4 Local Heating of Metal Surfaces due to Photon Absorption

### 6.4.1 Two-Temperature Model

Impinging photons into the substrate can be absorbed or scattered giving the extinction spectra in UV-vis measurement. Absorption of photons in the metallic substrate gives rise to a non-equilibrium distribution of electron-hole pairs. Due to electron-electron scattering in metals the energetic electrons quickly thermalize resulting in a Fermi-Dirac distribution with characteristic electronic temperature. Previously Two-Temperature model has been developed and extensively used to describe energy relaxation of hot electron gas via electron-phonon coupling to lattice phonons and via heat diffusion into the bulk [243]. The energy flow of the system upon photon impinging on the substrate is illustrated in

Fig. 6.4. From the model, the time dependent electron and phonon temperature can be obtained. The calculated phonon and electron temperature can further couple with adsorbates on the surface and induce surface chemistry. We will talk about the Empirical Friction model later as we introduce the electron scattering model. Here we are going to review the Two-Temperature model generally used in femto-chemistry. We use the same model for the silver surface with ultra-short laser pulses and the steady-state system with continuous light input. The main objective of this study is to evaluate the possible thermal effect due to light illumination.

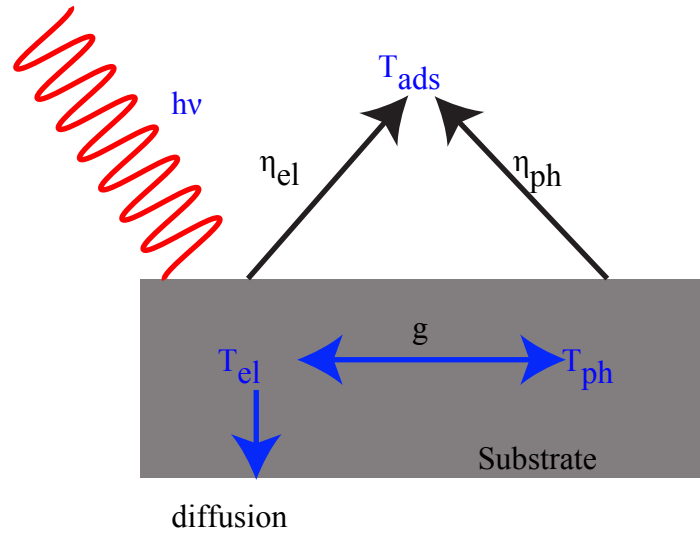


Figure 6.4: Schematic Illustration of the Two-Temperature Model

The two-temperature model [243] uses two coupled PDE as shown in Eq. 6.12 to describe the energy transfer among electron, phonon, the bulk as well as the energy source, such as laser pulse or continuous wave light.

$$(6.12) \quad \begin{aligned} C_{el} \frac{\partial}{\partial t} T_{el} &= \nabla_z k \nabla_z T_{el} - g(T_{el} - T_{ph}) + S(z, t) \\ C_{ph} \frac{\partial}{\partial t} T_{ph} &= g(T_{el} - T_{ph}) \end{aligned}$$

$T_{el}$  and  $T_{ph}$  are the electron and phonon temperature, respectively; the origin of each term in the model is physically transparent. The photo-absorption of photons in the sub-

strate generates a collection of hot electrons. The electron-electron collision quickly results in the thermalized hot electrons with Fermi-Dirac distribution. The hot electron gas dissipates the energy by electron-phonon coupling term and the heat conduction into the bulk. The phonon temperature is linearly coupled to electron temperature with the electron-phonon coupling coefficient, many of which for transition and noble metals have been measured and tabulated previously [260].  $C_{el} = \gamma T_{el}$  ( $\gamma$  is the electron specific heat) is the electron heat capacity and phonon heat capacity  $C_{ph}$  can be calculated based on Debye model as

$$(6.13) \quad C_{ph} = 9nk_B \left( \frac{T_{ph}}{\Theta_D} \right)^3 \int_0^{\Theta_D/T_{ph}} dx \frac{x^4 e^x}{(e^x - 1)^2},$$

where  $n$  is the atom density;  $\Theta_D$  is the Debye temperature of metals.

In Eq. 6.12,  $k$  is the thermal conductivity governing the energy dissipation into the bulk. The time evolution of the phonon and electron temperature can be directly solved by imposing the time dependent source profile  $S(z, t)$  which can be written as Eq. 6.14. Intensity  $I(t)$  can have different forms depending on the profile of source energy as

$$(6.14) \quad S(z, t) = (1 - R)I(t)\lambda^{-1}e^{-z/\lambda},$$

where  $R$  is the reflectivity of the materials, characterizing the scattering versus the absorption properties of the bulk material.  $\lambda$  is the penetration length of light source.

#### 6.4.2 Ultra-short Laser Pulses vs. Continuous Light Wave

For laser pulse, the intensity of the source is usually written as Gaussian distribution with specific pulse duration as

$$(6.15) \quad I(t) = F \exp\left(\frac{-t^2}{2\sigma^2}\right) / \sqrt{2\pi\sigma^2},$$

where  $F$  is the fluence of the energy source in  $J/m^2$ , and  $\sigma$  is related to the Pulse duration by  $\sigma = \tau/2.355$ ,  $\tau$  is the half width of the Gaussian distribution. For continuous light

wave we are going to focus in this chapter,  $I(t)$  is simply the constant over time.

To understand the optical response of the silver surfaces with respect to laser pulses and continuous light wave, first we have performed the Two-Temperature model for silver with laser pulse of similar intensity as done previously on Ru in the literature [261]. In this study, we use laser fluence  $120 \text{ J/m}^2$ , pulse duration  $110 \text{ ps}$ , initial temperature  $200 \text{ K}$ , and all the other properties of silver are tabulated in Table 6.1. The temperature profile after the laser shot is shown in Fig. 6.5(a). As we can see the electron temperature rises up very quickly, but the phonon temperature barely change because the electron-phonon coupling is small compared to Ru. Heat dissipation is fast since silver has larger heat conductivity than Ru. That indicates that the electron driven reaction could be case for silver since the phonon temperature is only weakly coupled to the electrons.

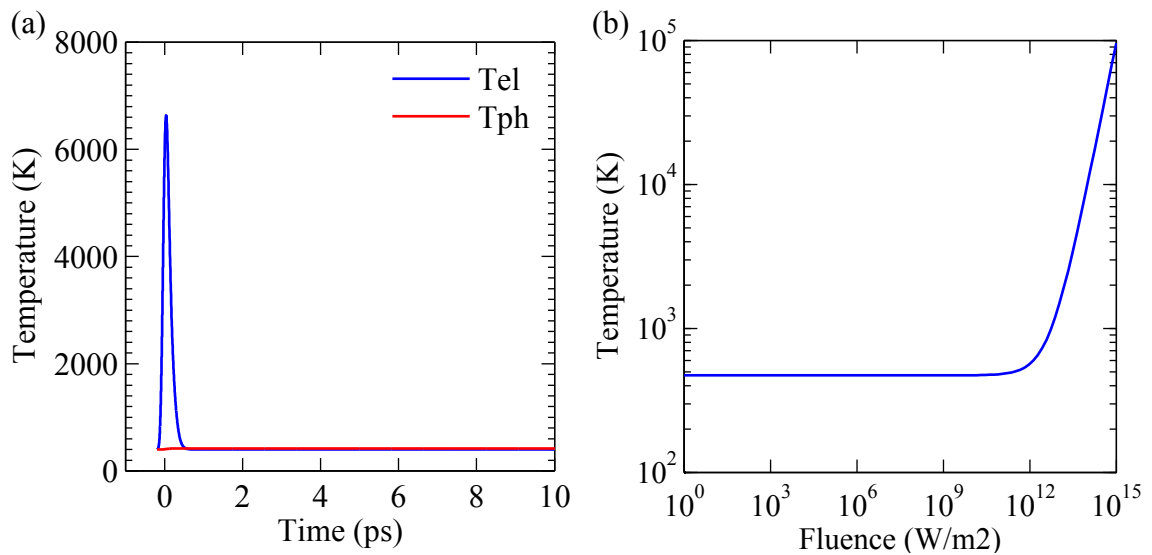


Figure 6.5: Two-Temperature Model illumination. (a) Femto-second laser pulse, (b) Steady state under light illumination

We also looked at the evolution of energies of the silver system with low-intensity continuous wave under steady state. In this condition, it is reasonable to assume that the phonon and electron temperature are equal. The equation essentially turns out to be single second order ODE and can be easily solved using standard Matlab function. As we can see

in Fig. 6.5 (b) the electron and phonon temperature remain unchanged until the intensity approaches very high value which can only be obtained using ultra-fast laser pulse. The intensity in the experiment I quoted here is about  $1000\sim 10000$  mW/cm<sup>2</sup>, so it is far off the region the local heat should occur. This is also another support for the electron driven surface chemistry instead of local heating due to light illumination.

Table 6.1: Parameter of Two-Temperature Model for Silver

Electron Specific Heat $\gamma$	58.24	J m <sup>-3</sup> K <sup>-2</sup>
Electron heat conductivity $k_0$ (300 K)	429	Wm <sup>-1</sup> K <sup>-1</sup>
Electron-Phonon coupling constant $g$	3.55E+16	Wm <sup>-3</sup> K <sup>-1</sup>
Debye temperature $\theta_D$	215	K
Atom density $n$	5.86E+28	m <sup>-3</sup>
Optical penetration depth $\lambda$ (800 nm)	1.62E-08	m

## 6.5 Development of Finite-Temperature Electron Scattering Model

The phenomenon of hot electron induced surface chemistry has been discussed previously in terms of non-adiabatic Newns-Anderson Hamiltonian. The essential function of this Model Hamiltonian is to determine the probability for single electron scattering event that an incident electron with energy  $\epsilon_i$  scatters into final state energy  $\epsilon_f$ , depositing energy difference  $(\epsilon_i - \epsilon_f)$  into the oscillator system. The source of electrons can be photo-electrons due to absorption of photons in the substrate or the tunnelling electrons from STM tip or other electrons emitting from metal junction devices. Regardless of the source of electrons, the common feature of electron induced surface reactions is the temporary trapping of incident electrons within the adsorbate-surface complex region, forming transient negative ions. The force imposed on the nucleus of adsorbate due to the non-equilibrium geometric structure for the lifetime of the electronic resonance results in a non-equilibrium distribution of vibrationally excited states as the system returns to the initial electronic ground state. If the energy gain is sufficient to surmount the thermal activation barrier, the adsorbate will react immediately. If not, the adsorbate staying at

higher vibrational state will decay towards the initial thermal distribution of vibrational states before consecutive electron scattering. The pure thermal effect in the model has not been explicitly taken into account, limiting its application for well-defined surface science experiments, which are usually performed under extremely low temperature to preclude thermal disturbance for the formation of ordered adsorbate adlayer. There is increasing interest to combine different stimuli, such as phonon and electron, to facilitate the chemical reaction at viable rate [253]. In this section, we are going to extend previous inelastic resonance electron scattering model to include the finite system temperature. The theoretical framework is fully consistent with previous presented Model Hamiltonian. At finite temperature, the initial thermal distribution of vibrational states of adsorbates before electron scattering can be written by the following Eq. 6.16 based on Bose-Einstein statistics assuming that the adsorbate is in thermodynamic equilibrium with the substrate. As also illustrated in Cartoon Fig. 6.6 the number of vibrationally excited oscillators is larger for the system with higher temperature. Here the substrate represents an enormous heat bath with phonon temperature predefined.

$$(6.16) \quad p_0(m) = \frac{1}{e^{(m+1/2)\hbar\omega/k_B T} - 1}$$

In Eq. 6.16,  $T$  is the substrate temperature,  $\omega$  is the angular vibrational frequency of the targeted normal mode. The distribution in Eq. 6.16 will become Boltzmann distribution at significantly high temperature.

Assuming the phonon distribution  $p(m), m = 0, 1, 2 \dots$ , the probability of the adsorbate (oscillator) being in the  $n^{\text{th}}$  vibrational state after electron scattering is

$$(6.17) \quad Q(n) = \sum_{m=0}^{\infty} p(m) P_{mn}(\epsilon_i, m),$$

where the summation has to be truncated. The vibrational matrix element  $P_{mn}$  is calculated based on the non-adiabatic Newns-Anderson-type Hamiltonian [252], which describes the

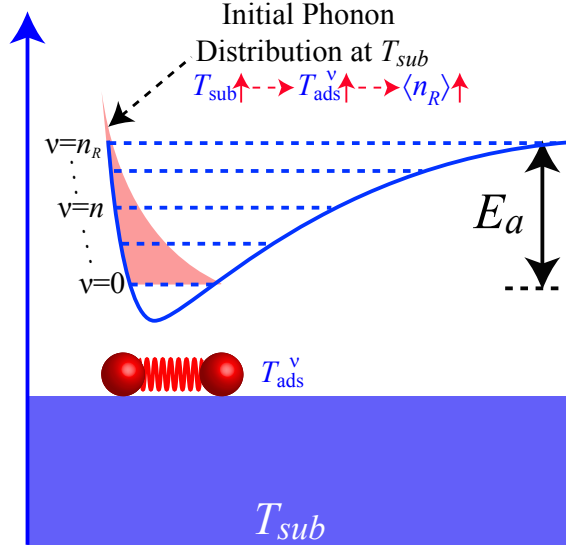


Figure 6.6: Schematic illustration of the initial phonon distribution at finite temperature

linear coupling between substrate states and adsorbate resonant state, and the coupling between adsorbate resonant state with the vibrational modes of adsorbates. One thing to note that as  $n$  is smaller than  $m$ , it is corresponding to stimulated emission, where the incident electron gains energy after scattering into adsorbates. The probability  $P_{mn}$  can also be obtained using the same equation with the index switch. The reaction rate is obtained as the following based on the assumption that the adsorbate oscillator with higher vibrational energy than thermal barrier will react

$$(6.18) \quad P^R = \sum_{n=n_R}^{\infty} Q(n) \cdot F,$$

where  $F$  is the flux of incident electrons on the per site and per second basis. Initially,  $p(m)$  is equal to  $p_0(m)$ , which corresponds to the thermal equilibrium distribution of vibrational states. Before the consecutive electron scattering event, the vibrational damping of adsorbate by transferring energy back to the substrate via emission of photon or creating electron-hole pairs, can be described using Empirical Friction model as

$$(6.19) \quad \frac{dT_{ads}}{dt} = -\eta(T_{ads} - T_{sub}),$$

and

$$(6.20) \quad T_{ads} = (T_0 - T_{sub}) \cdot e^{-\eta t} + T_{sub},$$

where  $T_{ads}$  is the adsorbate temperature, which can be converted to the distribution of vibrational states using Bose-Einstein statistics.  $T_{sub}$  is the temperature of the substrate.  $\eta$  is the Friction coefficient.  $T_0$  is the initial temperature before decaying.

$p(m)$  is the probability of the adsorbate is in  $m^{th}$  vibrational state after  $\Delta t$ , the time interval between two consecutive scattering electrons. It should be noted that after the electron scattering, the distribution of vibrational states of adsorbate can not be represented by pure thermal Bose-Einstein distribution with one specific temperature. To circumvent this difficulty, we have calculated the adsorbate temperature associated each vibrational energies based on the statistical distribution of vibrational states as a function of temperature in Bose-Einstein distribution. The statistical occupation of vibrational state  $m$  is calculated based on this adsorbate temperature using Bose-Einstein distribution. Simply speaking, the non-equilibrium distribution of vibrational states is transformed to adsorbate temperature associated with each vibrational energy level and then converted back into the phonon distribution after the relaxation time, i.e., the time interval between two consecutive scattering electrons. The final distribution should be normalized under the steady state condition. The general algorithm of the electron scattering model can be represented in Cartoon Fig. 6.14.

For many adsorbate/substrate system,  $\eta^{-1}$  is  $1 \sim 10$  ps, which can be deduced from the line-width of IR spectra. In our study, we did not try to experimentally measure or identify the adsorbate vibrational state lifetime. We simply assume that the Empirical Friction coefficient  $\eta$  is constant for different vibrational states, we wrote the Flux and so  $\Delta t$  with

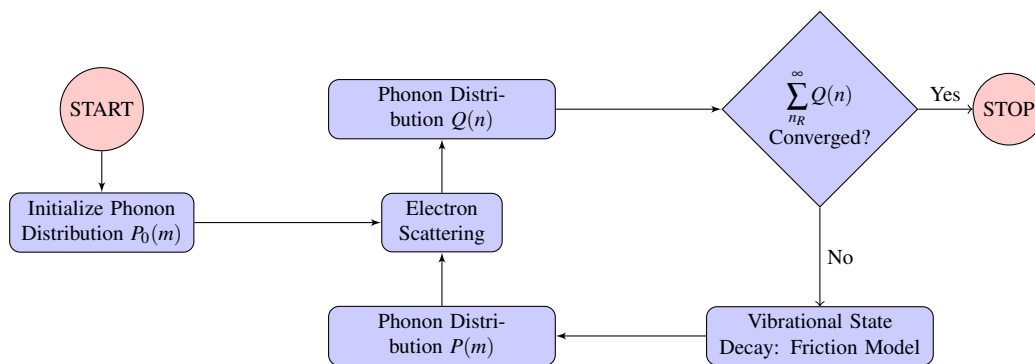


Figure 6.7: General algorithm of the Finite-Temperature Electron Scattering model

unit of the friction coefficient as

$$(6.21) \quad \Delta t = 1/F[\eta].$$

To compare with experiment, we have calibrated the flux by aligning up the region transition from linear to super-linear dependence of reaction rate on flux.

## 6.6 Fundamental Understanding of Oxygen Dissociation Induced by Multiple Stimuli

In previous section, we have introduced the Finite-Temperature inelastic resonance electron scattering model which can describe the dynamics of surface reactions driven by various excitation modes (electron and phonon). Experimentally, it has been shown in Section 2 that silver nanoparticles can effectively couple thermal energy and solar energy to drive catalytic reactions. We have observed the linear to super-linear regime transition of photo-rate with respect to light intensity, and we also show that the system temperature has significant effect on the efficiency of the process. To understand those phenomenon, we have employed the electron scattering model just introduced to probe the underlying mechanism, and first-principles Density Functional Theory calculations for all the parameters involved in the non-adiabatic model Hamiltonian describing the hot-electron-induced vibrational transition process. In this model, the electronic system consisting of the adsorbate and the substrate is described by a Newns-Anderson-type Hamiltonian with the

linear coupling of unoccupied resonant electronic state with the vibrational states of the adsorbate.

### 6.6.1 Power Law Dependence of O<sub>2</sub> Dissociation Rate on Light Intensity

For the ethylene epoxidation reaction on silver catalysts, oxygen dissociation step has been shown to be the rate-limiting step in the temperature regime of our study. This is consistent with our kinetic isotope labelling experiments [253]. This technique has been widely used previously to identify the rate-limiting step and reaction mechanism. To understand the experimentally observed power law dependence of reaction rate on light intensity, we have used the model to investigate the energy transfer from hot electrons into the reaction coordinate of oxygen dissociation. The assumption is that the frequency of electron scattering event is linearly proportional to the incident light intensity. This is the first case showing the crossover of linear to superlinear using low intensity light with nanoparticles. For experimental details and results, please refer to the paper [253].

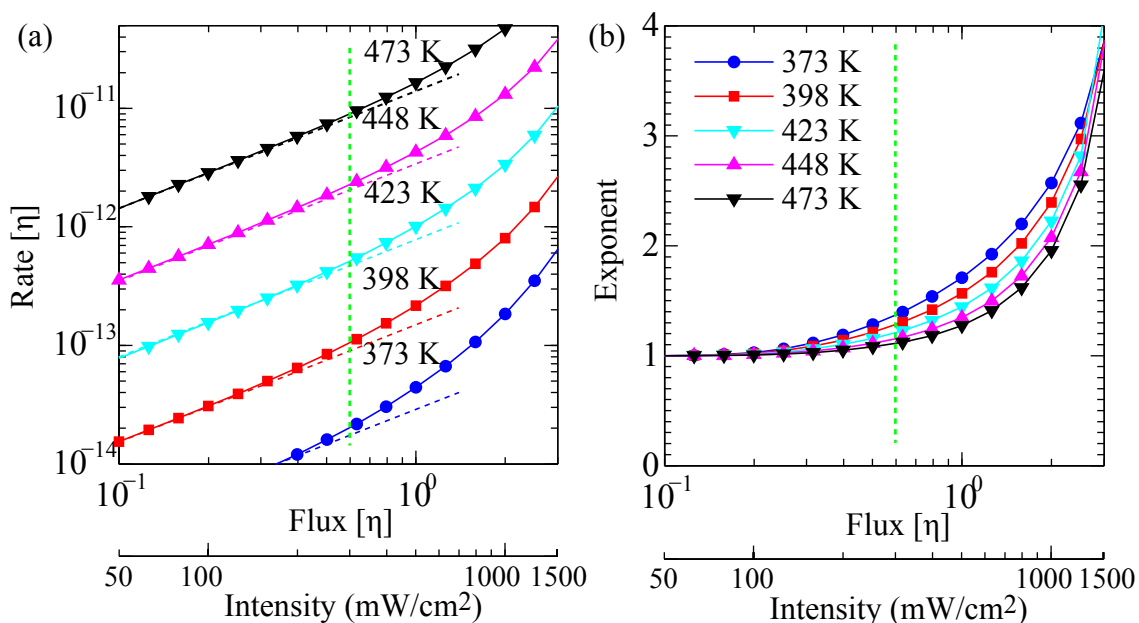


Figure 6.8: Theoretical results from electron scattering model. (a) Calculated reaction rate as a function of electron flux into adsorbate orbitals at different temperatures. (b) Exponent calculated from the rate showing the transition from linear to super-linear dependence on electron flux

In Fig. 6.8, I have shown the simulation results, which agree with experimental measurement very well, in term of the general trend of reaction rates vs electron flux and system temperature. The parameters are as follows: Width of Resonance: 1.3 eV, Incident Electron Energy: 2.2 eV, Resonance Energy: 2.4 eV, Vibration Frequency of  $^{16}\text{O}_2$  0.102 eV from DFT calculated ground state PES, lambda: -47.863 meV from DFT calculated excited state PES. For kinetic isotope effect, parameters for  $^{18}\text{O}_2$  are scaled by mass accordingly.

We can see that the model can capture the region transition of oxygen dissociation reaction with hot electron excitation. Also, the exponent observed here is very close to experimental measurement,  $\sim 3.5$  at the highest flux in the experiment. The agreement of model prediction with experimental measurement allows us to probe the underlying mechanism of the enhancement due to visible light illumination.

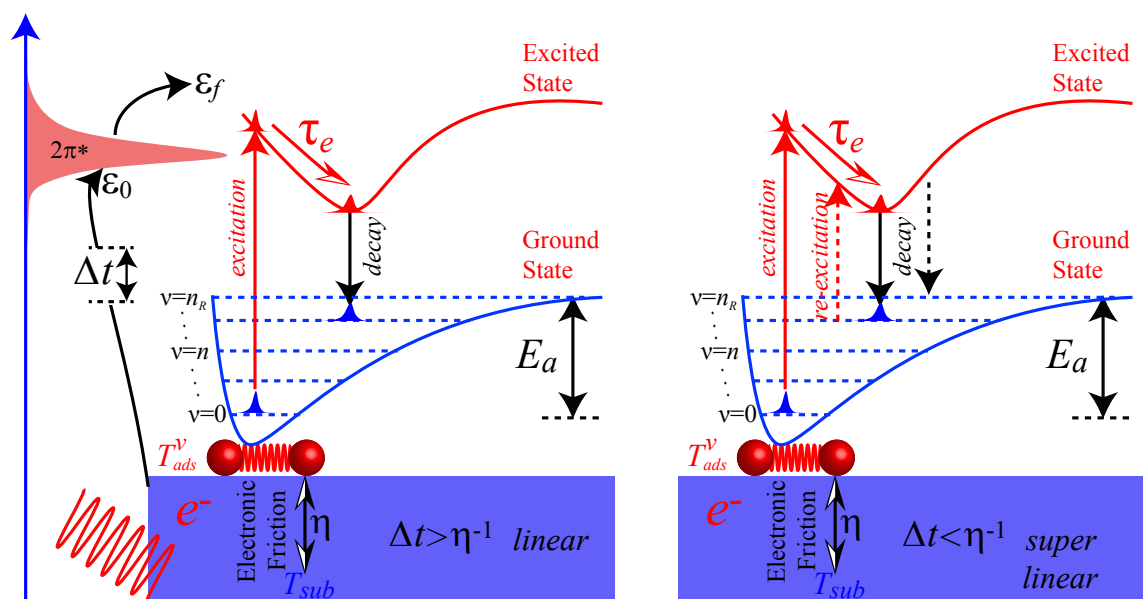


Figure 6.9: Cartoon illustration of regime transition mechanism

The mechanism for regime transition can be illustrated on Fig. 6.9. Under low light intensity, the frequency of electron scattering events into the adsorbate is low. The vibrational excited adsorbates have enough time to decay back down or close to the initial

thermal distribution as shown in Fig. 6.9(a). So all the scattering events have similar effect on the rate, and so the same cross section or quantum efficiency. At high flux regime, the adsorbate got hit by hot electrons before its completely decaying into the initial thermal distribution of phonon states, accumulating part of the energy gain from the electron scattering. The energy gain keeps accumulating until there is balance between the re-excitation and decay. So there are different multiple electronic excitation steps as shown in Fig. 6.9(b). So the governing factor of the regime transition is  $\eta^{-1}$ , which can be seen as the average lifetime of excited vibrational states. If the  $\Delta t$  is larger than the  $\eta^{-1}$ , the rate will be linear with respect to light intensity, which is linearly proportional to the frequency of the electron scattering events. If the  $\Delta t$  is smaller than the  $\eta^{-1}$ , the electron scattering events are so frequent that the excited adsorbate does not have enough time to fully decay back to to thermal distribution until the equilibrium is reached.

### 6.6.2 Enhanced Quantum Efficiency due to Phonon Excitation

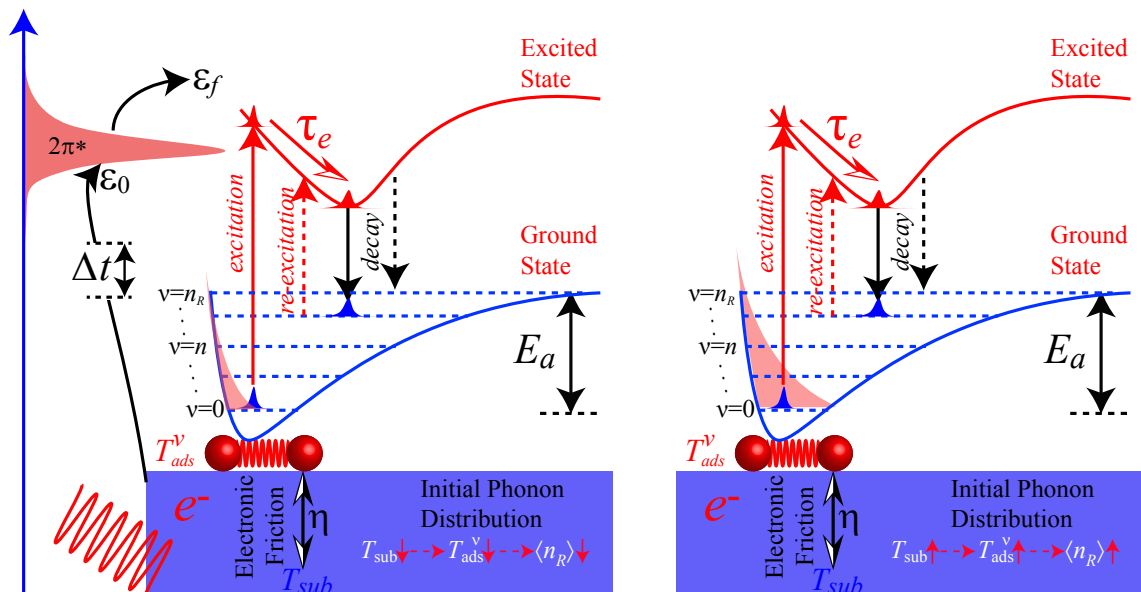


Figure 6.10: Cartoon illustration of effect of emperature

Another thing we see in the experimental measurement is that the quantum efficiency

is exponentially increasing with respect to the temperature. This phenomenon can be explained by the initial thermal occupation of vibrational states at system temperature [252]. At low temperature, there are only limited number of excited vibrational state with higher energies than thermal activation barrier populated as shown in Fig. 6.10. The electron scattering needs to provide large amount of energy to have significant amount of excited vibrational state population, i.e., the photo-rate. At higher temperature, the thermal distribution of vibrational states at the energy level of activation barrier is significantly higher. It has two consequences. First, the pure thermal rate will be higher since the pure phonon excitation has provided enough population of excited vibrational state to surmount the activation barrier. Second, the electron scattering event has much higher probability to promote phonons from the excited vibrational state up to the activation barrier. Those two scenario can be well illustrated on Fig. 6.10.

### 6.6.3 Characteristic Features for Electron-driven Surface Reactions

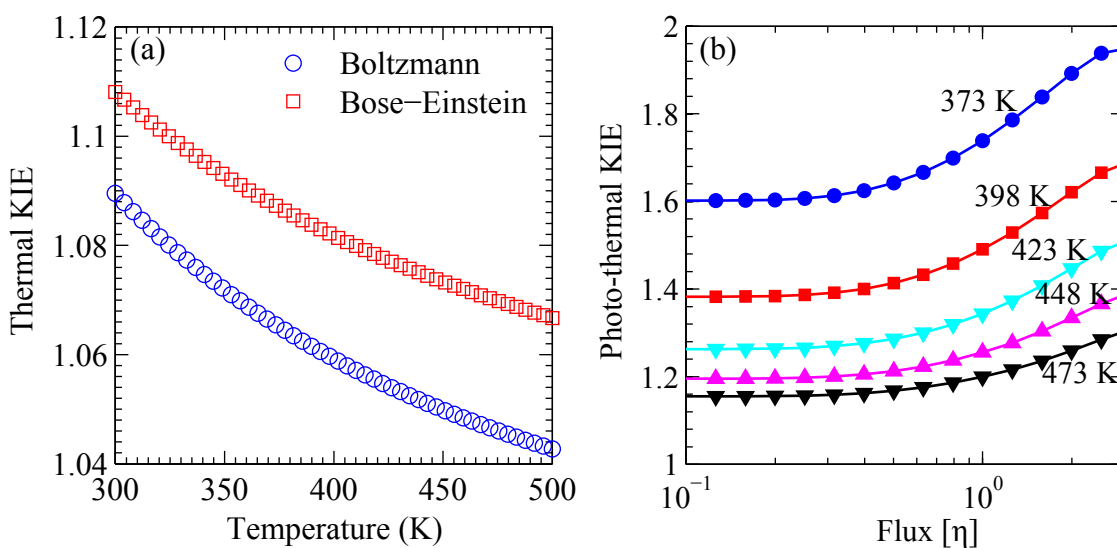


Figure 6.11: Kinetic isotope effect from Electron Scattering model

Enhanced KIE effect has been shown previously to be the characteristic feature of the electron driven process [262]. To illustrate the electron-driven nature of our experimental

observed phenomenon, in Fig. 6.11 we are showing the model calculated pure thermal KIE using Bose-Einstein and Boltzmann distributions (for comparison purpose only), and also the KIE obtained from the model based on electron scattering model we have introduced. The pure thermal KIE is calculated as the ratio of thermal reaction probability for  $^{16}\text{O}_2/^{18}\text{O}_2$ . The reaction probability is evaluated the same way as photo-rate, e.g., the summation of phonon distributions of vibrational states with higher energies than pure thermal activation barrier. The zero-point vibrational energy difference of two isotopes has been taken into account for pure thermal activation barrier. The calculated pure-thermal KIE using Bose-Einstein distribution is fully consistent with previous experimental measurement [253]. On Fig. 6.11(b), we show that the calculated photo-thermal KIE is much higher than pure thermal KIE, which agrees with the experimental measurement very well as shown in Fig. 6.12(a). This indicates us that (1) The resonance electron scattering model can capture the main effect of the photo-thermal chemistry on metal surfaces. (2) The dissociation of  $\text{O}_2$  molecule on silver surface is the rate-limiting step under the temperature region we investigated. (3) The photo-thermal process is electron-driven in nature with the aid of phonon coupling to the substrate.

Since the model can really describe the dynamics of the system very well as shown in our KIE measurement and simulations, it allows us to talk about the details of the fundamental mechanism based on the model in terms of the kinetic isotope effect. Upon the incident electron scattering into the anti-bonding orbital, the adsorbed  $\text{O}_2$  suddenly finds itself as a non-equilibrium state on the excited potential energy surface, and so the harmonic oscillator of adsorbates will be displaced and accelerated for the elongation of the bond. The force on different isotope is similar since it is governed by the valence electronic structure. For isotope  $^{18}\text{O}_2$ , the acceleration is smaller compared to  $^{16}\text{O}_2$ , so in the same interval,  $^{16}\text{O}_2$  can travel further on the potential energy surface before decaying

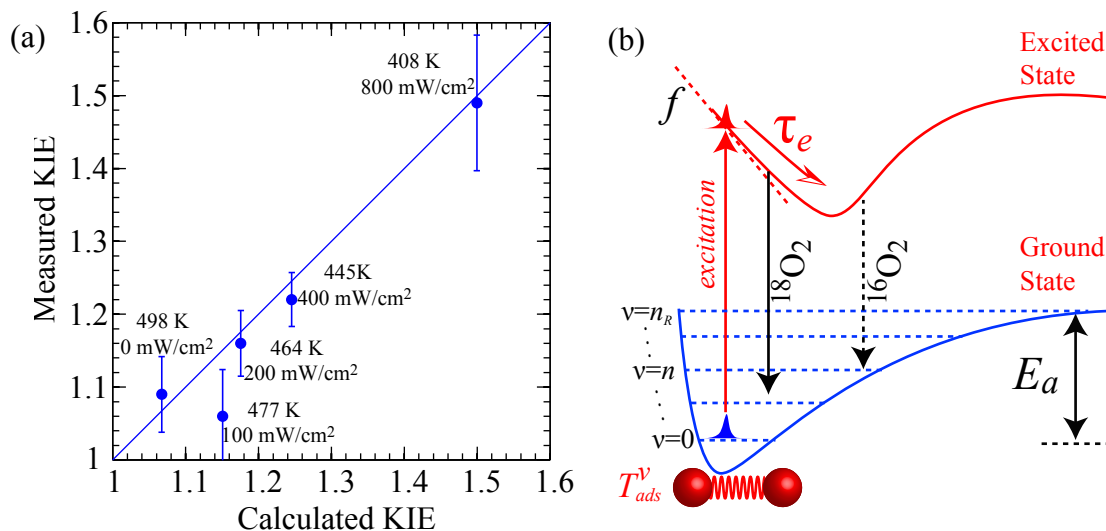


Figure 6.12: (a) Measured vs calculated kinetic isotope effect. (b) Cartoon illustration of the mechanism of enhanced kinetic isotope effect

back down to the ground state. The energy gain due to the acceleration will be different for two isotopes. The mechanism of kinetic isotope effect is illustrated on Fig. 6.12(b).

#### 6.6.4 Interpretation of Power Law Exponent $n$

As we can see in Fig. 6.1 and Fig. 6.8, there is linear to superlinear transition of reaction rates to the incident light intensity from experiments and also the simulation. The corresponding exponent we observed is between  $1 \sim 3.5$  depending on the light intensity or the frequency of electron scattering events. Exploring the physical origin of the exponent is critical for us to understand the fundamental mechanism of electron driven reactions and validate the developed Finite Temperature electron scattering model. Previously, based on electron scattering model it has been shown that the power exponents results from the summing up the combinatorics of all possible ways of rising through the vibrational state in potential energy well. In the high flux limit, the exponent is approaching the  $n_R$ , which is required vibrational quanta to across the activation barrier, defined as  $E_a/\hbar\omega$ . This simple interpretation of power exponent as contributing vibrational quanta has found to be consistent with several experimental measurement [247]. It should be noted that in all those

systems the energy needed to across the activation is solely provided by electron scattering event by operating the experiment under extremely low temperature to isolate the thermal effect.

In our system, the reaction is carried out under elevated temperature coupled with low intensity visible light. Part of the energy required to across the activation barrier is provided by phonon excitation, or thermal energy. Based on the reaction rate measured in the experiment and the simulated from the model, we can calculate the average energy gain due to electron scattering events by subtracting the photo-thermal activation barrier from the pure thermal activation barrier. The results are shown in Fig. 6.13. The intensity scale of experimental is overlaying with simulation scale. As we can see the energy gain from electron scattering events can be approximately represented as  $n \cdot \hbar\omega$  considering that the exponent is from 1 to 3.5 in our experimental measurement, and the  $\hbar\omega$  is around 0.1 eV for  $O - O$  bond vibration. So the exponent can be seen as contributing vibrational quanta to the activation of rate-limiting step. The conclusion here is fully consistent with previous surface science experiments with  $fs$  laser excitations.

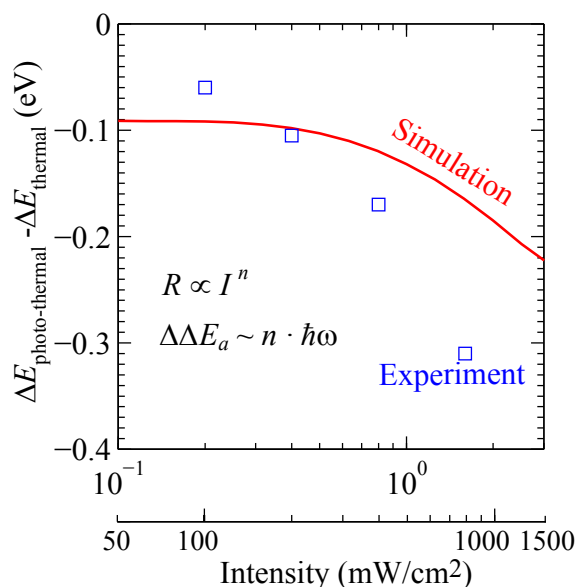


Figure 6.13: Reduction of activation energies due to electron scattering

### 6.6.5 Sensitivity Analysis of the Model

The inelastic electron scattering on metal surfaces is a very complex surface phenomenon governed by several physical factors, and there is no simple linear relationship between those physical parameters with the electron induced reaction rate or kinetic isotope effect. A sensitivity analysis can be used to interpret the dependency of those parameters on a target quantity in the simulation. It is also seen as a standard procedure to validate the model. Here we have focused on two target function (Reaction Rate of O<sub>2</sub> dissociation and Oxygen Kinetic Isotope Effect on the reaction rate). We are going to perturb all the independent physical quantities by 2% (relative to DFT calculated value) in the model to see how the target function change. The consistency of physical relationship between all the parameters is still ensured in this analysis. The definition of target function follows in Eq. 6.22. Y can be Rate or KIE. X can be physical parameters. As we can see, the reaction rate and KIE are quite sensitive to  $\epsilon_i$ ,  $\epsilon_a$ ,  $\Delta E_a$  and  $\lambda$  as shown in Table 6.2 and 6.3. The variation of rate with respect to those changes is fully consistent with the analysis in this Chapter.

$$(6.22) \quad C_i = \frac{\Delta Y/Y}{\Delta X/X}$$

I	Temp	tau	mass	g	epsilon_i	epsilon_a	dV/dx	barrier	omega	lambda
100	100	-3.30	-3.94	2.49	6.11	-5.68	5.19	-24.47	-1.87	5.19
100	125	-2.25	-2.70	1.63	3.84	-3.71	3.37	-23.70	-1.01	3.37
100	150	-1.54	-1.87	1.07	2.45	-2.45	2.21	-22.87	-0.53	2.21
100	175	-1.09	-1.35	0.74	1.64	-1.69	1.51	-22.02	-0.27	1.51
100	200	-0.80	-1.01	0.53	1.16	-1.22	1.09	-21.18	-0.12	1.09
800	100	-4.36	-4.80	3.18	7.57	-7.10	6.64	-23.98	-2.36	6.64
800	125	-3.33	-3.55	2.35	5.42	-5.27	4.88	-23.20	-1.50	4.88
800	150	-2.51	-2.60	1.73	3.87	-3.88	3.56	-22.41	-0.94	3.56
800	175	-1.91	-1.92	1.28	2.82	-2.89	2.64	-21.62	-0.58	2.64
800	200	-1.48	-1.44	0.97	2.11	-2.20	1.99	-20.83	-0.35	1.99

Table 6.2: Rate Sensitivity Analysis

Intensity	Temperature	tau	mass	g	epsilon_i	epsilon_o	dV/dx	barrier	omega	lambda
100	100	-0.80	-2.06	0.62	1.64	-1.69	1.26	-3.54	-4.12	1.26
100	125	-0.60	-1.34	0.45	1.15	-1.16	0.92	-2.32	-2.82	0.92
100	150	-0.41	-0.86	0.30	0.74	-0.75	0.61	-1.66	-2.05	0.61
100	175	-0.27	-0.55	0.20	0.48	-0.48	0.40	-1.28	-1.59	0.40
100	200	-0.19	-0.34	0.13	0.32	-0.33	0.27	-1.02	-1.31	0.27
800	100	-0.74	-2.28	0.55	1.46	-1.56	1.11	-4.68	-5.11	1.11
800	125	-0.66	-1.58	0.48	1.21	-1.27	0.96	-3.19	-3.77	0.96
800	150	-0.53	-1.06	0.37	0.92	-0.97	0.76	-2.25	-2.83	0.76
800	175	-0.40	-0.69	0.28	0.68	-0.71	0.57	-1.66	-2.19	0.57
800	200	-0.31	-0.42	0.21	0.50	-0.53	0.43	-1.26	-1.76	0.43

Table 6.3: KIE Sensitivity Analysis

## 6.7 Insight into the Efficiency and Selectivity of Electron-Mediated Surface Reactions

First, we are going to extract the governing physical factor for the selectivity of photochemistry on metal surfaces with electron mediation. Previously, MIM device has been used to show that selective surface chemistry can be obtained by tuning the electron to be specifically into the electronic resonance [242]. Since the rate is largely governed by the overlapping of resonance to electron distribution window. By using MIM device, the electron energy can be tuned to be within 0.1 eV width in energy distribution. The selective tuning into or detuning out of particular electron attachment resonance provides an elegant way of selective surface photochemistry on metal surfaces. Suppose we can adjust the electron energy to specific range within very narrow distribution, the question is if we can know easily the electron attachment resonance critical to the surface chemistry selectivity. In the following, we are going to show two simple examples where we can use calculated excitation energy obtained from DFT to understand the surface selectivity and point to the rational path to manipulate the selectivity. Another question is if we can manipulate or predict the resonance state energy of adsorbate on metal surfaces or alloys to rationally design the devices with maximum selectivity.

The thermodynamic stability of various critical intermediates on catalyst surfaces is

intrinsically linked together. So there is no easy way to tune the stability independently as we desired. This is the most often scenario for heterogeneous catalysis, where two or more surface intermediates determines the rate. In conventional chemical reaction using heat stimuli, there is not much room to improve the rate. Usually there is a volcano relationship to the temperature, which is essentially the coverage effect. If we can selectively tune the stability of intermediates to the direction we need, we could be able to further improve the catalytic performance. We should note that by changing the electronic properties, there is little success since the chemical bonding is still intrinsically linked.

### 6.7.1 Critical Role of Electronic Resonance Energy

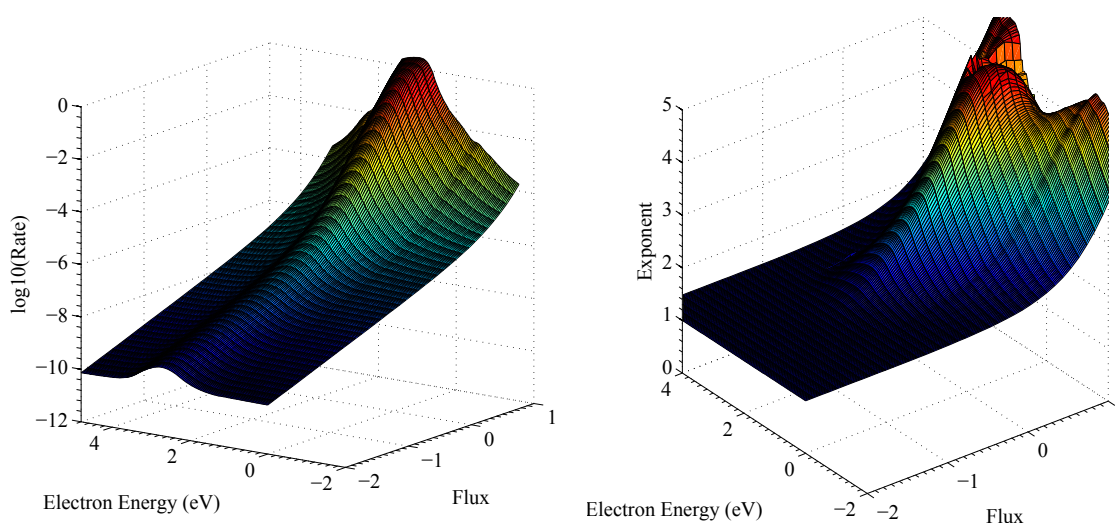


Figure 6.14: Effect of electron energy and flux on the (a) rate and (b) exponent

The energy transfer from energetic electrons to adsorbate vibrational states is not only a function of flux, which is governing the regime of operation, it is also a function of incident hot electron energy. As we can see from Fig. 6.14, the reaction rate and exponent are strong functions of flux and incident electron energy. The hot electrons with the energy close to the resonance energy of adsorbate will give higher reaction rate and exponent as shown in Fig. 6.14. If we assume two different distribution of incident electrons, one is fully

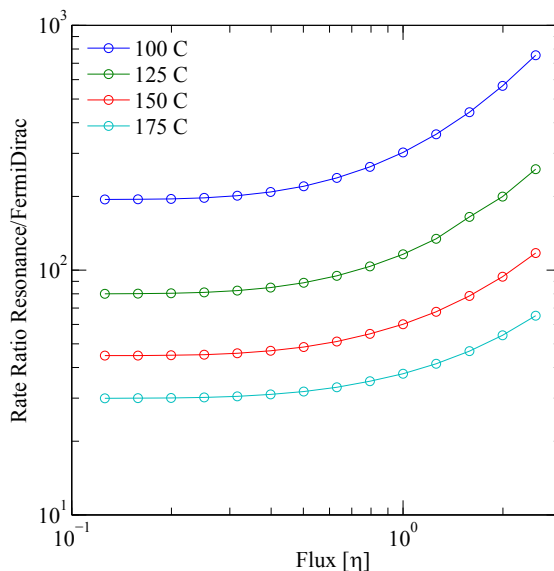


Figure 6.15: The rate enhancement due to the resonant electron distribution vs. thermalized hot electron distribution

thermalized Fermi-Dirac distribution, another is the resonance distribution measured from experimental UV-vis spectra and light source, we can calculate the reaction probability due to those two different distributions. The results are shown in Fig. 6.15. As we can see the resonance distribution of hot electrons can have  $\sim 2$  order of magnitude enhancement of the reaction rate, which can be interpreted as 2 order of magnitude lower light intensity for region transition. Together with the plasmon excitation enhanced local field 6 orders of magnitude, the resonance electron distribution can fully account for the regime transition with low intensity visible light which is only observed previously using high intensity *fs* laser pulses.

### 6.7.2 Electronic Factors Determining Resonance Energies of Simple Adsorbates

The electronic resonance energy of the adsorbate on metal surfaces is the critical factor determining the effective distribution of incident hot electrons accessible to anti-bonding orbitals for scattering. It has been shown previous [252] and in our studies that the highest probability of electron induced surface reaction can usually be obtained at the inci-

dent electron energy  $\varepsilon_a + E_a/2$ , where  $E_a$  is the activation barrier for thermal activation. The detune of the electron energy relative to electronic resonance energy results from the compromise between incident and outgoing electrons. Understanding of variations in resonance energies for diatomic molecules adsorption on metal surfaces can provide the guidance for selectively activating specific chemical bond with rationally tuned distribution of incident hot electrons from Metal-Insulator-Metal tunnel junction [242]. In this Section, we are going to identify the underlying electronic factors governing variations in resonance energies of simple diatomic molecules (CO and NO) adsorption on transition metal surfaces using linear expansion  $\Delta$ SCF-DFT method. We are going to take diatomic molecule  $N_2$ , CO and NO on metal and alloy surfaces as an example. The activation of those molecular bonds (usually the rate-limiting step) has great significance for designing more energy efficient and selective processes for F-T synthesis and ammonia synthesis, oxidation reactions, pollution controls and many others.

The  $d$ -band center of metal surface sites can be easily calculated as the first-moment of the  $d$ -DOS with respect to the Fermi level. The electronic resonance energies of  $2\pi^*$  anti-bonding orbital of diatomic molecules are obtained using linear expansion  $\Delta$ SCF-DFT method. The resonance energies vs. the  $d$ -band center of the substrate are shown in Fig. 6.16(a). We can clearly see that there is a linear correlation between the electronic resonance energy of  $2\pi^*$  anti-bonding orbital and the  $d$ -band center of the metal surface site. By tailoring the surface electronic properties, e. g. the  $d$ -band center of surface sites, we can vary not only the intrinsic chemical reactivity, but also hot-electron induced surface chemistry, which provides highly flexibility for tuning the efficiency and selectivity of surface reactions with multiple excitation sources.

The fundamental mechanism governing the linear correlation of electronic resonance energies with the surface  $d$ -band center is illustrated in Fig. 6.16(b). Hammer-Nørskov

$d$ -band model has shown that the  $d$ -band center energy is the governing parameter for the surface chemical bonding. The interaction of adsorbate valence orbitals (normalized after interaction the  $sp$ -band) with metal  $d$ -states creates anti-bonding orbital above the metal  $d$ -band. The energy level and so the occupation of this anti-bonding orbital determines the strength of chemical bonding on metal surfaces. There is direct correlation between the  $d$ -band center ( $\epsilon_d$ ) with the energy level of anti-bonding orbitals. Higher  $d$ -band center of the substrate gives rise to higher energy level of the anti-bonding states, and so less occupied which results in stronger chemical bond. In linear expansion  $\Delta$ SCD-DFT method, the electronic resonance energy is calculated by taking one-electron from the Fermi level and selectively populating this electron to be this anti-bonding orbital, which is not any of the KS orbitals of the ground state, but a linear combination. As the electron is transiently occupying the adsorbate anti-bonding orbital, the intra-adsorbate Coulomb repulsion [263], denoted as  $U$ , will shift the adsorbate/metal anti-bonding orbital upward as illustrated in Fig. 6.16(b). The energy change of the system (the electronic resonance energy of the adsorbate) is largely governed by the one-electron energy of the transiently occupied orbital since the electrostatic interaction is assumed to be constant for varying surfaces. Based on this analysis, we can write simple expression shown in Eq. 6.23.

$$(6.23) \quad \epsilon_a^{exi} \propto \epsilon_a^{gs} + U \propto \epsilon_d$$

## 6.8 Summary

Understanding of the interaction between energetic electrons and molecules adsorbed on metal surfaces is of great significance in fundamental surface science and heterogeneous catalysis. In this study, we have developed and employed a Finite-Temperature electron scattering model with first-principles calculations to investigate the energetic electron induced activation of adsorbed diatomic molecules over metal surfaces. In this model,

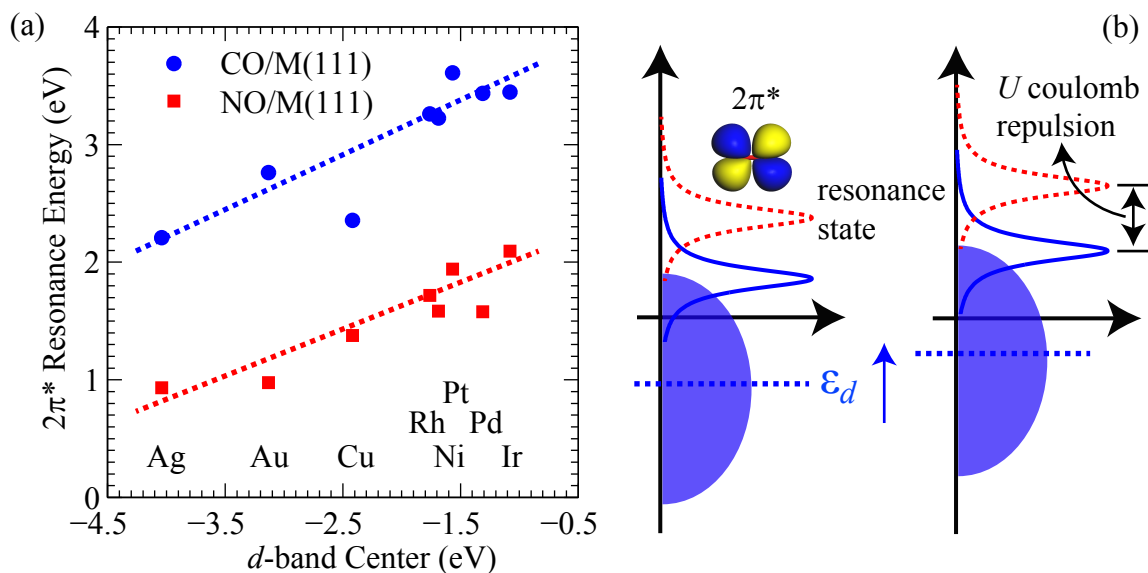


Figure 6.16: Trend of resonance energies of molecules adsorption on metal surfaces

the electronic system of the adsorbate and substrate is described by a Newns-Anderson-type Hamiltonian with the linear coupling of unoccupied resonant electronic states and vibrational modes of the adsorbate. When the resonant electronic state of the adsorbate becomes transiently occupied due to electron scattering, the adsorbate confined within the Born-Oppenheimer ground state potential well undergoes a Franck-Condon transition onto the excited state potential energy surface (PES) calculated using linear expansion  $\Delta$ SCF-DFT method implemented in GPAW. The reaction probability of the energetic electron induced surface reaction can be calculated based on the model using several parameters from density functional theory calculations. The critical feature of the model compared with previous ones is that the effect of substrate temperature has been explicitly included, and the energy transfer between excited adsorbate vibrational state and photon modes of metal substrates has been taken into account using Friction model.

We have applied the model to study energetic electron mediated oxygen activation on plasmonic silver (Ag) nanostructures. We found that the energetic electrons, generated due to surface plasmon resonance (SPR) excitation of Ag nanostructures, can induce a signifi-

cant enhancement in the rate of O-O bond activation by transient occupation of the  $O_2 2\pi^*$  anti-bonding orbital. The electron scattering induces nuclear motion along the reaction coordinate of O-O bond, thereby facilitating the dissociation step. The driving force for nuclear motion is characterized by the coupling constant obtained from the excited state PES and the normal mode frequency of O-O bond. We have shown that the model can quantitatively capture the kinetic isotope effect and the phenomenon of temperature and wavelength dependent rate enhancement of ethylene epoxidation reaction over Ag due to visible light illumination.

## CHAPTER VII

### Conclusions

In this dissertation, we have developed a general theoretical framework for the understanding of variations in the surface reactivity of transition metals with perturbed electronic properties. This unifying theoretical framework has been the guiding principle for us to unravel the physical factors governing the energetics for elementary reaction steps on perturbed metal surfaces and explore thoroughly the phase space of catalytic materials spanned by electronic and structural degrees of freedom. The perturbation of surface electronic properties and therefore the surface reactivity of transition metals can be accomplished by various means, e.g., alloying with impurity elements, doping of surface promoters, or imposing stimuli for electronic excitations. We have elaborated the fundamental mechanism of variations in the surface reactivity of transition metals with tailored electronic properties in three different applications: (i) rapid screening of multimetallic electrocatalysts for the oxygen reduction reaction in fuel cells; (ii) understanding of alkali promotion mechanisms for chemical reactions on metal surfaces; (iii) coupling of phonons and energetic electrons for photo-thermal reactions on metallic nanoparticles. The conclusions obtained from those studies are summarized as below.

Metal surfaces alloyed with impurity elements are a family of materials showing great promise in heterogeneous catalysis. Electronic communication among the constituent

metal elements results in unique active sites that can perform desired chemical transformations. It has been generally accepted that the *d*-band model of chemisorption, developed by Hammer and Nørskov, can predict the trend in chemisorption energies of various adsorbates on metal surfaces. The model correlates the central moment of the *d*-band projected on surface atoms with the surface reactivity. In general, for a given adsorption geometry adsorbates bind to the surface of transition or noble metals more strongly if the *d*-band center of the surface atom is higher in energies. Most adsorbates follow the trend predicted by the *d*-band model. We have used X-ray absorption spectroscopy (XAS) and quantum-chemical density functional theory (DFT) calculations to identify critical features in the electronic structure of different sites in alloys that govern the local chemical reactivity. The measurements led to a simple model relating local geometric features of a site in an alloy to its electronic structure. The central feature of the model is that the formation of alloys does not lead to significant charge transfer between the constituent metal elements in the alloys, and that the local electronic structure can be predicted based on physical characteristics of constituent metal elements in their unalloyed form. Recently we have identified a whole family of adsorbate-substrate systems exhibiting the surface properties in contradiction with the prediction from the *d*-band model. Those adsorbate-substrate systems are characterized by substrates that have nearly fully occupied *d*-band (mainly  $d^9$  and  $d^{10}$  metals) and adsorbates with almost completely filled valence shell (O, OH, F, Cl). We have studied the underlying mechanism of this exception by analyzing hydroxyl (OH) adsorption on a series of Pt and Pd alloys. This exception is important since OH adsorption on metal surfaces is crucial for the understanding of various catalytic, electro-catalytic and photo-catalytic reactions including oxygen reduction and water splitting reactions. We have shown that this surface phenomenon can be fully understood in terms of the repulsive interactions between adsorbate states and metal *d*-states governed by adsorbate-substrate

bond length. By establishing the underlying parameters governing the variations in surface electronic structure of *d*-band and the adsorbate-substrate bond length upon alloy formation, we have developed a model with the incorporation of both the *d*-band center and the bond distance dependence of chemisorption energies. The presented model has been successfully employed to search for optimal multicomponent Pt alloys for low temperature polymer electrolyte membrane (PEM) fuel cells cathode and identified interesting systems showing improved catalytic performance for oxygen reduction reaction. The ability to rapidly screen for new alloy catalysts along with rapid developments of synthetic chemistry approaches used to synthesize the desired alloy materials with a high degree of control of their geometry (composition as well as the atomic placement of elements) has the great potential to significantly facilitate the design of heterogeneous catalysts. In summary, by using various experimental techniques and computational tools, we have developed a fundamental knowledge-base that is sufficient to a priori predict whether the metal surface with certain perturbation alloying will exhibit an improved catalytic performance in chemical transformations based on the information which can be looked up in textbook.

Metal surfaces doped with alkali promoters are another family of catalytic materials which have exhibited dramatically improved catalytic performance for many chemical processes, such as ammonia synthesis, Fisher-Tropsch synthesis, alcohol synthesis, water-gas shift reactions, olefin epoxidation, and automotive three-way catalytic converters. Physical mechanisms governing this important phenomenon remain unclear. In this project, we have investigated the role of alkali (e.g., Cs) promoters in the dissociation reaction of oxygen on the Ag(111) model surface. We choose the Cs-O/Ag system since it is well established that alkali promoters enhance the activity and/or selectivity in many olefin epoxidation reactions on Ag catalysts, and the O-O bond activation has been suggested

to be the rate limiting step. In combination of DFT calculations and the developed theoretical framework, we have illustrated that the dominant mode of Cs promotion for the activation of O-O bond on the Ag(111) surface is electrostatic in nature. Understanding dominant modes of promotion provides a path for rational manipulation of the catalyst surface to improve its catalytic performance. Industrial catalytic processes take place at elevated temperature and pressure. Fundamental understanding of the promotion mechanism of alkali metals under reaction conditions requires the knowledge of the structural properties of alkali-modified substrates. DFT calculations are computationally expensive and usually limited by the system size to be hundreds of atoms. To map out free energies of the system under realistic operating conditions, we have used Cluster Expansion method, which employs systematic coarse-graining of DFT calculated energies. Essentially, effective interaction potentials of various clusters are obtained from limited number of DFT calculations, and these interaction parameters are then utilized to calculate the energies of any arbitrary configurations. One of the novelties of this project is the development of the Cluster Expansion scheme with the inclusion of subsurface species, which allows us to investigate the phenomenon of surface oxidation. Grand Canonical Monte Carlo simulations combined with the Cluster Expansion method have been used to extend the insight from DFT calculations to relevant catalytic conditions. We have shown that Cs can significantly enhance the surface oxidation by the formation of subsurface oxygen. The development of Cluster Expansion method, together with Monte Carlo simulations, has given us the capability to probe the structural properties of the system under realistic conditions, which are not easily accessible from other approaches.

Chemical reactions on metal surfaces are typically driven by phonons, i. e., the coupling of adsorbates vibrational degree of freedom (the reaction coordinate) with the infinite heat bath of the substrate. The intrinsic activation barrier separating reaction intermedi-

ates can only be surmounted if adsorbates gain enough energy from vibrational excitations. Identical chemical transformations on metal surfaces can proceed via the coupling of adsorbates with the other excitation sources, such as electrons. Understanding of the interaction between energetic electrons and molecules adsorbed on metal surfaces is of great significance in fundamental surface science and heterogeneous catalysis. In this study, we have developed a Finite-Temperature Electron Scattering Model based on first-principles DFT calculations. The main feature of the model is that it can describe the kinetics of the surface reactions which are coupled to the bath of multiple excitation sources (phonons and electrons) with the consideration of microscopic events occurring on the surface. We have applied the model to study energetic electron mediated oxygen activation on plasmonic silver (Ag) nanostructures. We found that the energetic electrons, generated due to surface plasmon resonance (SPR) excitation of Ag nanostructures, can induce a significant enhancement in the rate of O-O bond activation by transient occupation of the O<sub>2</sub> 2 $\pi^*$  anti-bonding orbital. The electron scattering induces nuclear motion along the reaction coordinate of O-O bond, thereby facilitating the dissociation step. The driving force for nuclear motion is characterized by the coupling constant obtained from the excited state PES and the normal mode frequency of O-O bond. We have shown that the model can quantitatively capture the phenomenon of temperature and wavelength dependent rate enhancement of ethylene epoxidation reaction over Ag due to visible light illumination. Targeted electron attachment of resonance states can potentially induce selective surface chemistry which can not be obtained using homogeneous heating. We have elaborated the underlying electronic factors governing the variations in resonance energies of simple adsorbates on metal and alloy surface, which can be used as guideline for selective surface chemistry using electron and phonon stimuli.

The theoretical framework established in this dissertation have dramatically improved

the fundamental insights into the elementary reaction steps on metal surfaces, and provided a further step towards rational design of catalytic materials with utmost energy efficiency and minimal environmental impact.

## Bibliography

- [1] Rutger A. Santen and Matthew Neurock. *Molecular heterogeneous catalysis: a conceptual and computational approach*. Wiley-VCH, 2006.
- [2] I. Chorkendorff and J. W. Niemantsverdriet. *Concepts of Modern Catalysis and Kinetics*. John Wiley & Sons, December 2003.
- [3] Henry Eyring. The activated complex in chemical reactions. *The Journal of Chemical Physics*, 3:107, 1935.
- [4] Paul Sabatier. *La catalyse en chimie organique*. C. Beranger, Paris et Liege, 2. ed., rev. et augm. edition, 1920.
- [5] Jeff Greeley, Jens K. Nørskov, Ludwig A. Kibler, Ahmed M. El-Aziz, and Dieter M. Kolb. Hydrogen evolution over bimetallic systems: Understanding the trends. *ChemPhysChem*, 7(5):1032–1035, May 2006.
- [6] J. Greeley, I. E. L. Stephens, A. S. Bondarenko, T. P. Johansson, H. A. Hansen, T. F. Jaramillo, J. Rossmeisl, Ib Chorkendorff, and J. K. Nørskov. Alloys of platinum and early transition metals as oxygen reduction electrocatalysts. *Nature Chemistry*, 1(7):552–556, October 2009. PMID: 21378936.
- [7] Martin P. Andersson, Thomas Bligaard, Arkady Kustov, Kasper E. Larsen, Jeffrey Greeley, Tue Johannessen, Claus H. Christensen, and Jens K. Nørskov. Toward

- computational screening in heterogeneous catalysis: Pareto-optimal methanation catalysts. *Journal of Catalysis*, 239(2):501–506, April 2006.
- [8] Jeff Greeley, Thomas F. Jaramillo, Jacob Bonde, Ib Chorkendorff, and Jens K. Nørskov. Computational high-throughput screening of electrocatalytic materials for hydrogen evolution. *Nat Mater*, 5(11):909–913, November 2006.
- [9] Suljo Linic, Jerome Jankowiak, and Mark A. Barteau. Selectivity driven design of bimetallic ethylene epoxidation catalysts from first principles. *Journal of Catalysis*, 224(2):489–493, June 2004.
- [10] Jeff Greeley and Jens K. Nørskov. Combinatorial density functional Theory-Based screening of surface alloys for the oxygen reduction reaction. *The Journal of Physical Chemistry C*, 113(12):4932–4939, March 2009.
- [11] K. Honkala, A. Hellman, I. N. Remediakis, A. Logadottir, A. Carlsson, S. Dahl, C. H. Christensen, and J. K. Nørskov. Ammonia synthesis from First-Principles calculations. *Science*, 307(5709):555–558, 2005.
- [12] Claus J. H. Jacobsen, Soren Dahl, Bjerne S. Clausen, Sune Bahn, Ashildur Logadottir, and Jens K. Nørskov. Catalyst design by interpolation in the periodic table: Bimetallic ammonia synthesis catalysts. *Journal of the American Chemical Society*, 123(34):8404–8405, 2001.
- [13] Felix Studt, Frank Abild-Pedersen, Thomas Bligaard, Rasmus Z. Sorensen, Claus H. Christensen, and Jens K. Nørskov. Identification of Non-Precious metal alloy catalysts for selective hydrogenation of acetylene. *Science*, 320(5881):1320–1322, June 2008.
- [14] F. Besenbacher, I. Chorkendorff, B. S. Clausen, B. Hammer, A. M. Molenbroek,

- J. K. Nørskov, and I. Stensgaard. Design of a surface alloy catalyst for steam reforming. *Science*, 279(5358):1913–1915, March 1998.
- [15] Anand Nilekar, Ye Xu, Junliang Zhang, Miomir Vukmirovic, Kotaro Sasaki, Radoslav Adzic, and Manos Mavrikakis. Bimetallic and ternary alloys for improved oxygen reduction catalysis. *Topics in Catalysis*, 46(3):276–284, December 2007.
- [16] Phillip Christopher and Suljo Linic. Engineering selectivity in heterogeneous catalysis: Ag nanowires as selective ethylene epoxidation catalysts. *J. Am. Chem. Soc.*, 130(34):11264–11265, 2008.
- [17] Phillip Christopher and Suljo Linic. Shape- and Size-Specific chemistry of ag nanostructures in catalytic ethylene epoxidation. *ChemCatChem*, 2:78–83, January 2010.
- [18] J. N. Bronsted. Acid and basic catalysis. *Chem. Rev.*, 5(3):231–338, 1928.
- [19] M. G. Evans and M. Polanyi. Further considerations on the thermodynamics of chemical equilibria and reaction rates. *Trans. Faraday Soc.*, 32:1333–1360, 1936.
- [20] Louis P. Hammett. The effect of structure upon the reactions of organic compounds. benzene derivatives. *J. Am. Chem. Soc.*, 59(1):96–103, 1937.
- [21] T. Bligaard, J.K. Nørskov, S. Dahl, J. Matthiesen, C.H. Christensen, and J. Sehested. The Brønsted–Evans–Polanyi relation and the volcano curve in heterogeneous catalysis. *Journal of Catalysis*, 224(1):206–217, May 2004.
- [22] P. Ferrin, D. Simonetti, S. Kandai, E. Kunkes, J. A. Dumesic, J. K. Nørskov, and M. Mavrikakis. Modeling ethanol decomposition on transition metals: A combined application of scaling and BrnstedEvansPolanyi relations. *Journal of the American Chemical Society*, 131(16):5809–5815, April 2009.

- [23] F. Abild-Pedersen, J. Greeley, F. Studt, J. Rossmeisl, T. R. Munter, P. G. Moses, E. Skulason, T. Bligaard, and J. K. Nørskov. Scaling properties of adsorption energies for Hydrogen-Containing molecules on Transition-Metal surfaces. *Physical Review Letters*, 99(1):016105–4, July 2007.
- [24] Eva M. Fernández, Poul G. Moses, Anja Toftelund, Heine A. Hansen, Jos I. Martínez, Frank Abild-Pedersen, Jesper Kleis, Berit Hinnemann, Jan Rossmeisl, Thomas Bligaard, and Jens K. Nørskov. Scaling relationships for adsorption energies on transition metal oxide, sulfide, and nitride surfaces. *Angewandte Chemie International Edition*, 47(25):4683–4686, 2008.
- [25] G. Jones, T. Bligaard, F. Abild-Pedersen, and J. K. Nørskov. Using scaling relations to understand trends in the catalytic activity of transition metals. *Journal of Physics: Condensed Matter*, 20(6):064239, 2008.
- [26] Sidney William Benson. *Thermochemical kinetics: methods for the estimation of thermochemical data and rate parameters*. Wiley, 1976.
- [27] Jeremy Kua, Francesco Faglioni, and William A. Goddard. Thermochemistry for hydrocarbon intermediates chemisorbed on metal surfaces:  $\text{CH}_{n-m}(\text{CH}_3)_m$  with  $n = 1, 2, 3$  and  $m \leq n$  on Pt, Ir, Os, Pd, Rh, and Ru. *J. Am. Chem. Soc.*, 122(10):2309–2321, 2000.
- [28] M. Saliccioli, Y. Chen, and D. G. Vlachos. Density functional Theory-Derived group additivity and linear scaling methods for prediction of oxygenate stability on metal catalysts: Adsorption of Open-Ring alcohol and polyol dehydrogenation intermediates on Pt-Based metals. *J. Phys. Chem. C*, 114(47):20155–20166, October 2011.

- [29] Jens K. Nørskov, Frank Abild-Pedersen, Felix Studt, and Thomas Bligaard. Density functional theory in surface chemistry and catalysis. *Proceedings of the National Academy of Sciences*, 108(3):937–943, January 2011.
- [30] Robert G Parr and Weitao Yang. *Density-Functional Theory of Atoms and Molecules*. Number 16 in International series of monographs on chemistry. Oxford University Press, New York, 1989.
- [31] Wolfram Koch. *A Chemist's Guide to Density Functional Theory*. Wiley-VCH Verlag GmbH, 3rd edition, July 2008.
- [32] Philip Hofmann. *Solid state physics: an introduction*. Wiley-VCH, 2008.
- [33] Charles Kittel. *Introduction to Solid State Physics*. Wiley, 7 edition, July 1995.
- [34] Neil W. Ashcroft and N. David Mermin. *Solid State Physics*. Brooks Cole, 1 edition, January 1976.
- [35] Roald Hoffmann. How chemistry and physics meet in the solid state. *Angewandte Chemie International Edition in English*, 26(9):846–878, September 1987.
- [36] Roald Hoffmann. A chemical and theoretical way to look at bonding on surfaces. *Reviews of Modern Physics*, 60(3):601, July 1988.
- [37] Roald Hoffmann. *Solids and surfaces: a chemist's view of bonding in extended structures*. VCH Publishers, 1988.
- [38] B. Hammer, J. K. Nørskov, and Helmut Knozinger Bruce C. Gates. Theoretical surface science and catalysis-calculations and concepts. In *Impact of Surface Science on Catalysis*, volume Volume 45, pages 71–129. Academic Press, 2000.

- [39] Jeff Greeley, Jens K. Nørskov, and Manos Mavrikakis. Electronic structure and catalysis on metal surfaces. *Annual Review of Physical Chemistry*, 53(1):319–348, 2002.
- [40] Claus Hviid Christensen and Jens K. Nørskov. A molecular view of heterogeneous catalysis. *The Journal of Chemical Physics*, 128(18):182503–8, May 2008.
- [41] E. Schrödinger. An undulatory theory of the mechanics of atoms and molecules. *Physical Review*, 28(6):1049, December 1926.
- [42] M. Born and R. Oppenheimer. Zur quantentheorie der molekeln. *Annalen der Physik*, 389(20):457–484, January 1927.
- [43] P. Hohenberg and W. Kohn. None. *Phys. Rev. B*, 136:864, 1964.
- [44] R. G. Parr and W. Yang. *Density-Functional Theory of Atoms and Molecules*. Oxford Science, 1998.
- [45] W. Kohn and L. J. Sham. Self-Consistent equations including exchange and correlation effects. *Physical Review*, 140(4A):A1133, November 1965.
- [46] J. P. Perdew, J. A. Chevary, S. H. Vosko, Koblar A. Jackson, Mark R. Pederson, D. J. Singh, and Carlos Fiolhais. Atoms, Molecules, Solids, and Surfaces: Applications of the Generalized Gradient Approximation for Exchange and Correlation. *Phys. Rev. B*, 46(11):6671–6687, Sep 1992.
- [47] Wei-Xue Li, Catherine Stampfl, and Matthias Scheffler. Insights into the function of silver as an oxidation catalyst by ab initio atomistic thermodynamics. *Physical Review B*, 68:165412, 2003.
- [48] Arvi Rauk. *Orbital interaction theory of organic chemistry*. John Wiley and Sons, 2001.

- [49] Anders Nilsson, Lars G.M. Pettersson, and Jens Nørskov. *Chemical Bonding at Surfaces and Interfaces*. Elsevier Science, October 2007.
- [50] P. W. Anderson. Localized magnetic states in metals. *Physical Review*, 124(1):41, October 1961.
- [51] D. M. Newns. Self-Consistent model of hydrogen chemisorption. *Physical Review*, 178(3):1123, February 1969.
- [52] B. Hammer. Special sites at noble and late transition metal catalysts. *Topics in Catalysis*, 37(1):3–16, March 2006.
- [53] Jens Hagen. *Industrial catalysis: a practical approach*. Wiley-VCH, 2006.
- [54] Peter Strasser, Qun Fan, Martin Devenney, W. Henry Weinberg, Ping Liu, and Jens K. Nørskov. High throughput experimental and theoretical predictive screening of materials a comparative study of search strategies for new fuel cell anode catalysts. *The Journal of Physical Chemistry B*, 107(40):11013–11021, October 2003.
- [55] D. M. Newns. Self-consistent model of hydrogen chemisorption. *Phys. Rev.*, 178(3):1123–1135, Feb 1969.
- [56] Felix Bloch. ber die quantenmechanik der elektronen in kristallgittern. *Zeitschrift fr Physik*, 52:555–600, July 1929.
- [57] W. A. Harrison. Tight-binding theory of molecules and solids. *Pure and Applied Chemistry*, 61:2161–2169, 1989.
- [58] Walter A. Harrison. *Electronic Structure and the Properties of Solids: The Physics of the Chemical Bond*. Dover Publications, July 1989.

- [59] C. M. Varma and A. J. Wilson. Systematics of the binding energy of oxygen and hydrogen on transition-metal surfaces. i. *Physical Review B*, 22(8):3795, October 1980.
- [60] A. J. Wilson and C. M. Varma. Systematics of the binding energy of oxygen and hydrogen on transition-metal surfaces. II. *Physical Review B*, 22(8):3805, October 1980.
- [61] J. K. Nørskov and N. D. Lang. Effective-medium theory of chemical binding: Application to chemisorption. *Physical Review B*, 21(6):2131, March 1980.
- [62] J. K. Nørskov. Covalent effects in the effective-medium theory of chemical bonding-hydrogen heats of solution in the 3d-metals. *Physical Review B*, 26(6):2875–2885, 1982.
- [63] B. Hammer and J. K. Nørskov. Electronic factors determining the reactivity of metal surfaces. *Surface Science*, 343(3):211–220, December 1995.
- [64] P. C. Hohenberg, W. Kohn, and L. J. Sham. None. *Adv. Quantum Chem.*, 21:7, 1990.
- [65] K. W. Jacobsen, J. K. Nørskov, and M. J. Puska. Interatomic interactions in the effective-medium theory. *Physical Review B*, 35(14):7423, May 1987.
- [66] J. K. Nørskov, S. Holloway, and N. D. Lang. Adsorbate–surface and adsorbate–adsorbate interactions and their role in surface reactions. *Journal of Vacuum Science & Technology A: Vacuum, Surfaces, and Films*, 3(3):1668–1672, May 1985.
- [67] A. Ruban, B. Hammer, P. Stoltze, H. L. Skriver, and J. K. Nørskov. Surface electronic structure and reactivity of transition and noble metals. *Journal of Molecular Catalysis A-Chemical*, 115(3):421–429, February 1997.

- [68] H. Hellmann. A new approximation method in the problem of many electrons. *The Journal of Chemical Physics*, 3:61, 1935.
- [69] J. Harris. Simplified method for calculating the energy of weakly interacting fragments. *Physical Review B*, 31(4):1770, February 1985.
- [70] J. F. Janak. Proof that  $\partial e/\partial n_i = \epsilon_i$  in density-functional theory. *Physical Review B*, 18(12):7165, December 1978.
- [71] R. F. W. Bader. Atoms in molecules. *Accounts of Chemical Research*, 18(1):9–15, 1985.
- [72] John R. Kitchin, Karsten Reuter, and Matthias Scheffler. Alloy surface segregation in reactive environments: First-principles atomistic thermodynamics study of  $\text{ag}_{\text{sub 3}}\text{Pd}(111)$  in oxygen atmospheres. *Physical Review B*, 77(7):075437–12, February 2008.
- [73] J. J. Mortensen, Y. Morikawa, B. Hammer, and J. K. Nørskov. Density Functional Calculations of  $\text{N}_2$  Adsorption and Dissociation on a  $\text{Ru}(0001)$  Surface. *J. Catal.*, 169:85, 1997.
- [74] G. A. Somorjai. *Introduction to Surface Chemistry and Catalysis*. Wiley: New York, 1994.
- [75] Gordon R. Sheffer and Terry S. King. Potassium's promotional effect of unsupported copper catalysts for methanol synthesis. *Journal of Catalysis*, 115(2):376–387, February 1989.
- [76] Charles T. Campbell and Bruce E. Koel. A model study of alkali promotion of water-gas shift catalysts:  $\text{Cs}/\text{Cu}(111)$ . *Surface Science*, 186(3):393–411, August 1987.

- [77] C. T. Campbell. Model studies of selective ethylene oxidation catalysis. *Journal of Physical Chemistry*, 89:5789–5795, 1985.
- [78] P. Vernoux, A. -Y. Leinekugel-Le-Cocq, and F. Gaillard. Effect of the addition of Na to Pt/Al<sub>2</sub>O<sub>3</sub> catalysts for the reduction of NO by C<sub>3</sub>H<sub>8</sub> and C<sub>3</sub>H<sub>6</sub> under lean-burn conditions. *Journal of Catalysis*, 219(1):247–257, October 2003.
- [79] Junliang Zhang, Miomir B. Vukmirovic, Ye Xu, Manos Mavrikakis, and Radoslav R. Adzic. Controlling the catalytic activity of Platinum-Monolayer electrocatalysts for oxygen reduction with different substrates. *Angew. Chem. Int. Ed.*, 44(14):2132–2135, March 2005.
- [80] Ifan E. L. Stephens, Alexander S. Bondarenko, Francisco J. Pérez-Alonso, Federico Calle-Vallejo, Lone Bech, Tobias P. Johansson, Anders K. Jepsen, Rasmus Fryden-dal, Brian P. Knudsen, Jan Rossmeisl, and Ib Chorkendorff. Tuning the activity of Pt(111) for oxygen electroreduction by subsurface alloying. *J. Am. Chem. Soc.*, 133(14):5485–5491, April 2011.
- [81] Z.P. Liu and P. Hu. An insight into alkali promotion: A density functional theory study of dissociation on K/Rh(111). *Journal of the American Chemical Society*, 123:12596–12604, 2001.
- [82] J. J. Mortensen, B. Hammer, and J. K. Nørskov. Alkali promotion of N<sub>2</sub> dissociation over Ru(0001). *Physical Review Letters*, 80:4333–4336, 1998.
- [83] J. J. Mortensen, B. Hammer, and J. K. Nørskov. A theoretical study of adsorbate-adsorbate interactions on Ru(0001). *Surface Science*, 414(3):315–329, September 1998.

- [84] Sergey Stolbov and Talat S. Rahman. Alkali-Induced enhancement of surface electronic polarizability. *Physical Review Letters*, 96(18):186801–4, May 2006.
- [85] R. L. Toomes and D. A. King. The coadsorption of CO and K on Co100. *Surface Science*, 349(1):19–42, March 1996.
- [86] Per Hyldgaard and Mats Persson. Long-ranged adsorbate-adsorbate interactions mediated by a surface-state band. *Journal of Physics: Condensed Matter*, 12(1):L13–L19, 2000.
- [87] J. Gilbert Kaufman and Elwin L. Rooy. *Aluminum Alloy Castings: Properties, Processes And Applications*. ASM International, illustrated edition edition, December 2004.
- [88] M. J. Gladys, O. R. Inderwildi, S. Karakatsani, V. Fiorin, and G. Held. Synergistic effects of the Cu/Pt110 surface alloy: Enhanced reactivity of water and carbon monoxide. *Journal of Physical Chemistry C*, 112(16):6422–6429, April 2008.
- [89] E. Nikolla, A. Holewinski, J. Schwank, and S. Linic. Controlling carbon surface chemistry by alloying: Carbon tolerant reforming catalyst. *Journal of the American Chemical Society*, 128(35):11354–11355, September 2006.
- [90] Jeff Greeley and Manos Mavrikakis. Alloy catalysts designed from first principles. *Nat Mater*, 3(11):810–815, November 2004.
- [91] Eranda Nikolla, Johannes Schwank, and Suljo Linic. Comparative study of the kinetics of methane steam reforming on supported ni and Sn/Ni alloy catalysts: The impact of the formation of ni alloy on chemistry. *Journal of Catalysis*, 263(2):220–227, April 2009.

- [92] Hiroshi Yano, Mikihiro Kataoka, Hisao Yamashita, Hiroyuki Uchida, and Masahiro Watanabe. Oxygen reduction activity of Carbon-Supported PtM (M = V, Ni, Cr, Co, and Fe) alloys prepared by nanocapsule method. *Langmuir*, 23(11):6438–6445, May 2007.
- [93] Vojislav Stamenkovic, Bongjin Simon Mun, Karl J.J. Mayrhofer, Philip N. Ross, Nenad M. Markovic, Jan Rossmeisl, Jeff Greeley, and Jens K. Nørskov. Changing the activity of electrocatalysts for oxygen reduction by tuning the surface electronic structure. *Angewandte Chemie International Edition*, 45(18):2897–2901, 2006.
- [94] Eranda Nikolla, Johannes Schwank, and Suljo Linic. Direct electrochemical oxidation of hydrocarbon fuels on SOFCs: improved carbon tolerance of ni alloy anodes. *Journal of The Electrochemical Society*, 156(11):B1312–B1316, November 2009.
- [95] Vojislav R. Stamenkovic, Ben Fowler, Bongjin Simon Mun, Guofeng Wang, Philip N. Ross, Christopher A. Lucas, and Nenad M. Markovic. Improved oxygen reduction activity on Pt<sub>3</sub>Ni(111) via increased surface site availability. *Science*, 315(5811):493–497, 2007.
- [96] Vojislav Stamenković, Bongjin Simon Mun, Karl J. J. Mayrhofer, Philip N. Ross, Nenad M. Marković, Jan Rossmeisl, Jeff Greeley, and Jens K. Nørskov. Changing the activity of electrocatalysts for oxygen reduction by tuning the surface electronic structure. *Angew. Chem. Int. Ed.*, 45(18):2897–2901, April 2006.
- [97] Vojislav R. Stamenković, Bongjin Simon Mun, Karl J. J. Mayrhofer, Philip N. Ross, and Nenad M. Marković. Effect of surface composition on electronic structure, stability, and electrocatalytic properties of Pt-Transition metal alloys: Pt-Skin versus Pt-Skeleton surfaces. *J. Am. Chem. Soc.*, 128(27):8813–8819, July 2006.

- [98] Herv Toulhoat and Pascal Raybaud. Kinetic interpretation of catalytic activity patterns based on theoretical chemical descriptors. *Journal of Catalysis*, 216(1-2):63–72, May 2003.
- [99] Eranda Nikolla, Johannes Schwank, and Suljo Linic. Measuring and relating the electronic structures of nonmodel supported catalytic materials to their performance. *Journal of the American Chemical Society*, 131(7):2747–2754, February 2009.
- [100] D. Vanderbilt. Soft self-consistent pseudopotentials in a generalized eigen value formalism. *Physical Review B*, 41(11):7892–7895, 1990.
- [101] M. D. Segall. Applications of ab initio atomistic simulations to biology. *Journal of Physics: Condensed Matter*, 14(11):2957–2973, 2002.
- [102] S. Gao, C. J. Pickard, A. Perlov, and V. Milman. Core-level spectroscopy calculation and the plane wave pseudopotential method. *Journal of Physics: Condensed Matter*, 21(10):104203, 2009.
- [103] David A. Muller, David J. Singh, and John Silcox. Connections between the electron-energy-loss spectra, the local electronic structure, and the physical properties of a material: A study of nickel aluminum alloys. *Physical Review B*, 57(14):8181, April 1998.
- [104] B. Hammer and J. K. Nørskov. Why gold is the noblest of all the metals. *Nature*, 376(6537):238–240, July 1995.
- [105] B. Hammer and M. Scheffler. Local chemical reactivity of a metal alloy surface. *Physical Review Letters*, 74(17):3487, April 1995.

- [106] B. Hammer, Y. Morikawa, and J. K. Nørskov. CO chemisorption at metal surfaces and overlayers. *Physical Review Letters*, 76(12):2141, March 1996.
- [107] J. K. Nørskov, T. Bligaard, A. Logadottir, S. Bahn, L. B. Hansen, M. Bollinger, H. Benggaard, B. Hammer, Z. Sljivancanin, M. Mavrikakis, Y. Xu, S. Dahl, and C. J. H. Jacobsen. Universality in heterogeneous catalysis. *Journal of Catalysis*, 209(2):275–278, July 2002.
- [108] D. G. Pettifor. *Bonding and Structure of Molecules and Solids*. Oxford University Press, USA, December 1995.
- [109] J. R. Kitchin, J. K. Nørskov, M. A. Barteau, and J. G. Chen. Role of strain and ligand effects in the modification of the electronic and chemical properties of bimetallic surfaces. *Physical Review Letters*, 93(15):156801, October 2004.
- [110] Ph. Durussel, R. Massara, and P. Feschotte. Le systeme binaire Pt-Sn. *Journal of Alloys and Compounds*, 215(1-2):175–179, November 1994.
- [111] J. O. Linde. Röntgenographische und elektrische untersuchungen des CuPt-Systems. *Annalen der Physik*, 422(2):151–164, 1937.
- [112] A. N. Mansour, J. W. Cook, and D. E. Sayers. Quantitative technique for the determination of the number of unoccupied d-electron states in a platinum catalyst using the  $l_{2,3}$  x-ray absorption edge spectra. *The Journal of Physical Chemistry*, 88(11):2330–2334, May 1984.
- [113] A. L. Ankudinov, J. J. Rehr, J. J. Low, and S. R. Bare. Pt  $l$ -edge XANES as a probe of Pt clusters. *Journal of Synchrotron Radiation*, 8(2):578–580, 2001.
- [114] A. I. Nesvizhskii and J. J. Rehr. L-edge XANES of 3d-transition metals. *Journal of Synchrotron Radiation*, 6(3):315–316, 1999.

- [115] A. L. Ankudinov, A. I. Nesvizhskii, and J. J. Rehr. Hole counts from x-ray absorption spectra. *Journal of Synchrotron Radiation*, 8(2):92–95, March 2001.
- [116] Jorge E. Möller and John W. Wilkins. Band-structure approach to the x-ray spectra of metals. *Physical Review B*, 29(8):4331, April 1984.
- [117] Maggie Teliska, Vivek S. Murthi, Sanjeev Mukerjee, and David E. Ramaker. Correlation of water activation, surface properties, and oxygen reduction reactivity of supported Pt–M/C bimetallic electrocatalysts using XAS. *Journal of The Electrochemical Society*, 152(11):A2159–A2169, November 2005.
- [118] J. R. Kitchin, J. K. Nørskov, M. A. Barteau, and J. G. Chen. Modification of the surface electronic and chemical properties of pt(111) by subsurface 3d transition metals. *The Journal of Chemical Physics*, 120(21):10240–10246, June 2004.
- [119] W. Tang, E. Sanville, and G. Henkelman. A grid-based bader analysis algorithm without lattice bias. *Journal of Physics: Condensed Matter*, 21(8):084204, 2009.
- [120] A. R. Denton and N. W. Ashcroft. Vegard’s law. *Physical Review A*, 43:3161–3164, March 1991.
- [121] J. K. Nørskov, T. Bligaard, J. Rossmeisl, and C. H. Christensen. Towards the computational design of solid catalysts. *Nat Chem*, 1(1):37–46, April 2009.
- [122] Nenad Markovic, Hubert Gasteiger, and Philip N. Ross. Kinetics of oxygen reduction on Pt(hkl) electrodes: Implications for the crystallite size effect with supported Pt electrocatalysts. *Journal of The Electrochemical Society*, 144(5):1591–1597, May 1997.
- [123] Akira Yamakata, Taka aki Ishibashi, and Hiroshi Onishi. Kinetics of the photocatalytic water-splitting reaction on TiO<sub>2</sub> and Pt/TiO<sub>2</sub> studied by time-resolved in-

- frared absorption spectroscopy. *Journal of Molecular Catalysis A: Chemical*, 199(1-2):85–94, May 2003.
- [124] R. A. van Santen and G. J. Kramer. Reactivity theory of zeolitic broensted acidic sites. *Chemical Reviews*, 95(3):637–660, May 1995.
- [125] J. R. Schrieff. Theory of chemisorption. *Journal of Vacuum Science & Technology*, 9(2):561–&, 1972.
- [126] Neil Schweitzer, Hongliang Xin, Eranda Nikolla, Jeffrey T. Miller, and Suljo Linic. Establishing relationships between the geometric structure and chemical reactivity of alloy catalysts based on their measured electronic structure. *Topics in Catalysis*, 53:348–356, February 2010.
- [127] Hongliang Xin, Neil Schweitzer, Eranda Nikolla, and Suljo Linic. Communications: Developing relationships between the local chemical reactivity of alloy catalysts and physical characteristics of constituent metal elements. *Journal of Chemical Physics*, 132(11):111101–111101–4, March 2010.
- [128] J. X. Wang, N. M. Marković, and R. R. Adzic. Kinetic analysis of oxygen reduction on Pt(111) in acid solutions: intrinsic kinetic parameters and anion adsorption effects. *J. Phys. Chem. B*, 108(13):4127–4133, April 2004.
- [129] N. M. Marković, T. J. Schmidt, V. Stamenković, and P. N. Ross. Oxygen reduction reaction on Pt and Pt bimetallic surfaces: A selective review. *Fuel Cells*, 1(2):105–116, 2001.
- [130] J. K. Nørskov, J. Rossmeisl, A. Logadottir, L. Lindqvist, J. R. Kitchin, T. Bligaard, and H. Jonsson. Origin of the overpotential for oxygen reduction at a Fuel-Cell cathode. *J. Phys. Chem. B*, 108(46):17886–17892, November 2004.

- [131] Alexander S. Bondarenko, Ifan E. L. Stephens, Heine A. Hansen, Francisco J. Pérez-Alonso, Vladimir Tripkovic, Tobias P. Johansson, Jan Rossmeisl, Jens K. Nørskov, and Ib Chorkendorff. The Pt(111)/Electrolyte interface under oxygen reduction reaction conditions: An electrochemical impedance spectroscopy study. *Langmuir*, 27(5):2058–2066, March 2011.
- [132] A. V. Ruban, H. L. Skriver, and J. K. Nørskov. Surface segregation energies in transition-metal alloys. *Phys. Rev. B*, 59(24):15990, June 1999.
- [133] R. R. Adzic, J. Zhang, K. Sasaki, M. B. Vukmirovic, M. Shao, J. X. Wang, A. U. Nilekar, M. Mavrikakis, J. A. Valerio, and F. Uribe. Platinum monolayer fuel cell electrocatalysts. *Top Catal*, 46(3-4):249–262, November 2007.
- [134] Shirlaine Koh and Peter Strasser. Electrocatalysis on bimetallic surfaces: modifying catalytic reactivity for oxygen reduction by voltammetric surface dealloying. *J. Am. Chem. Soc.*, 129(42):12624–12625, October 2007.
- [135] Hongliang Xin, Neil Schweitzer, Eranda Nikolla, and Suljo Linic. Communications: Developing relationships between the local chemical reactivity of alloy catalysts and physical characteristics of constituent metal elements. *J. Chem. Phys.*, 132(11):111101–111101–4, March 2010.
- [136] B. Hammer and J. K. Nørskov. Why gold is the noblest of all the metals. *Nature*, 376(6537):238–240, July 1995.
- [137] Mahlon S. Wilson and Shinichi Ichikawa. Comparison between the geometric and harmonic mean electronegativity equilibration techniques. *The Journal of Physical Chemistry*, 93(8):3087–3089, April 1989.

- [138] R. M. Lambert and G. Pacchioni. *Chemisorption and reactivity on supported clusters and thin films*. Springer, 1997.
- [139] Nilay İnođlu and John R. Kitchin. New solid-state table: estimating d-band characteristics for transition metal atoms. *Molecular Simulation*, 36(7):633, 2010.
- [140] Nilay İnođlu and John R. Kitchin. Simple model explaining and predicting coverage-dependent atomic adsorption energies on transition metal surfaces. *Phys. Rev. B*, 82(4):045414, July 2010.
- [141] C. D. Gelatt and H. Ehrenreich. Charge transfer in alloys: AgAu. *Phys. Rev. B*, 10(2):398, July 1974.
- [142] Tanushree Ghosh, Miomir B. Vukmirovic, Francis J. DiSalvo, and Radoslav R. Adzic. Intermetallics as novel supports for Pt monolayer O<sub>2</sub> reduction electrocatalysts: Potential for significantly improving properties. *J. Am. Chem. Soc.*, 132(3):906–907, January 2010.
- [143] Kuanping Gong, Dong Su, and Radoslav R. Adzic. Platinum-Monolayer shell on AuNi<sub>0.5</sub>Fe nanoparticle core electrocatalyst with high activity and stability for the oxygen reduction reaction. *J. Am. Chem. Soc.*, 132(41):14364–14366, October 2010.
- [144] Yangchuan Xing, Yun Cai, Miomir B. Vukmirovic, Wei-Ping Zhou, Hiroko Karan, Jia X. Wang, and Radoslav R. Adzic. Enhancing oxygen reduction reaction activity via PdAu alloy sublayer mediation of pt monolayer electrocatalysts. *J. Phys. Chem. Lett.*, 1(21):3238–3242, November 2010.
- [145] Uichiro Mizutani. *Hume-Rothery Rules for Structurally Complex Alloy Phases*. CRC Press, November 2010.

- [146] Zhi-Pan Liu and P. Hu. An Insight into Alkali Promotion: A Density Functional Theory Study of CO Dissociation on K/Rh(111). *J. Am. Chem. Soc.*, 123:12596, 2001.
- [147] Suljo Linic and Mark A. Barteau. On the mechanism of cs promotion in ethylene epoxidation on ag. *J. Am. Chem. Soc.*, 126:8086, 2004.
- [148] V. S. Stepanyuk, A. N. Baranov, D. V. Tsvilin, W. Hergert, P. Bruno, N. Knorr, M. A. Schneider, and K. Kern. Quantum interference and long-range adsorbate-adsorbate interactions. *Physical Review B*, 68(20):205410, November 2003.
- [149] M. C. Tringides and Robert Gomer. Adsorbate-adsorbate interaction effects in surface diffusion. *Surface Science*, 265(1-3):283–292, April 1992.
- [150] KarlJ.J. Mayrhofer, Viktorija Juhart, Katrin Hartl, Marianne Hanzlik, and Matthias Arenz. Adsorbate-Induced surface segregation for Core-Shell nanocatalysts. *Angewandte Chemie International Edition*, 48(19):3529–3531, April 2009.
- [151] D. M. Bird. Effects of coadsorbates in dissociative chemisorption of hydrogen on metallic surfaces. *Faraday Discussions*, pages 335–346, 1998.
- [152] Davy L. S. Nieskens, Daniel Curulla Ferr, and J. W. Niemantsverdriet. The influence of promoters and poisons on carbon monoxide adsorption on Rh(100): a DFT study. *Chemphyschem: A European Journal of Chemical Physics and Physical Chemistry*, 6(7):1293–1298, July 2005.
- [153] D. A. King and D. P. Woodruff. *The Chemical Physics of Solid Surfaces*. Elsevier Science Pub Co, April 1993.
- [154] Davy L S Nieskens, Daniel Curulla-Ferr, and J W Niemantsverdriet. Atom-molecule interactions on transition metal surfaces: a DFT study of CO and several

- atoms on Rh(100), Pd(100) and Ir(100). *Chemphyschem A European Journal Of Chemical Physics And Physical Chemistry*, 7(5):1075–1080, 2006.
- [155] H. P. Bonzel, Alexander M. Bradshaw, and Gerhard Ertl. *Physics and chemistry of alkali metal adsorption*. Elsevier, Amsterdam, 1989.
- [156] B.C. McCline and R.J. Davis. Isotopic transient kinetic analysis of Cs-promoted Ru/MgO during ammonia synthesis. *Journal of Catalysis*, 210:387–396, 2004.
- [157] A. Nielsen. Ammonia-synthesis-exploratory and applied-research. *Catalyst Reviews-Science and Engineering*, 23:17–71, 1981.
- [158] Ertl G. Lee S.B Paal, Z. Interactions of potassium, oxygen, nitrogen with polycrystalline iron surfaces. *Applied Surface Science*, 8:231–249, 1981.
- [159] D. R. Stogin, Bare S. R., and Samorjai G. A. The importance of  $c_7$  sites and surface-roughness in the ammonia-synthesis reaction over iron. *Journal of Catalysis*, 103:213–215, 1987.
- [160] K. Aika, K. Shimazaki, Y. Hattori, A. Ohya, S. Ohshima, K. Shirota, and A. Ozaki. Support and promoter effect of ruthenium alumina catalysts for ammonia-synthesis. *Journal of Catalysis*, 92:296–304, 1985.
- [161] Y. Aika, K., A. Ohya, A. Ozaki, Y. Inoue, and I. Yasumori. Support and promoter effect of ruthenium catalyst: Ruthenium alkaline-earth catalyst for activation of dinitrogen. *Journal of Catalysis*, 95:305–311, 1985.
- [162] B. C. McClaine and R. J. Davis. Importance of product readsorption during isotopic transient analysis of ammonia synthesis on ba-promoted Ru/BaX catalyst. *Journal of Catalysis*, 211:379–386, 2002.

- [163] M. E. Dry. "the Fischer-Tropsch synthesis" in (eds.) Anderson J. R. and Boudart, M. *Catalysis Reviews-Science and Technology*, 23:265–278, 1981.
- [164] G. Henrici-Olive and S. Olive. Mechanism of Fischer-Tropsch synthesis-CH<sub>2</sub> polymerization versus CO insertion. *Journal of Molecular Catalysis*, 16:111–115, 1982.
- [165] K. T. Park and J. Kong. Chemistry and physics of alkali metals on MoS<sub>2</sub> surfaces. *Topics in Catalysis*, 18:175–181, 2002.
- [166] R. B. Grant and R. M. Lambert. Ethylene oxide isomerization on single crystal Ag(111) in atomically clean and Cs-moderated conditions. *Journal of Catalysis*, 93:92–99, 1985.
- [167] I. V. Yentekakis, R. M. Lambert, M. Konsolakis, and N. Kallithrakas-Kontos. On the effects of residual chloride and of barium promotion on Pt/gamma-Al<sub>2</sub>O<sub>3</sub> catalysts in the reduction of NO by propene. *Catalysis Letters*, 81:181–185, 2002.
- [168] D. A. King and D. P. Woodruff. *The Chemical Physics of Surfaces: Coadsorption, Promoters and Poisons*. Elsevier, Amsterdam, 1993.
- [169] C. J. H. Jacobsen. Novel class of ammonia synthesis catalysts. *Chemical Communications*, 12:1057–1058, 2000.
- [170] S. Dahl, A. Logadottir, C. J. H. Jacobsen, and J. K. Nørskov. Electronic factors in catalysis: the volcano curve and the effect of promotion in catalytic ammonia synthesis. *Applied Catalysis A-General*, 222:19–29, 2000.
- [171] J. K. Nørskov. *Physics and chemistry of alkali metal adsorption*. Elsevier, Amsterdam, 1989.
- [172] G. A. Somorjai and E. L. Gurfunkel. *Physics and chemistry of alkali metal adsorption*. Elsevier, Amsterdam, 1989.

- [173] J. J. Mortensen, B. Hammer, and J. K. Nørskov. Alkali promotion of N<sub>2</sub> dissociation over Ru(0001). *Physical Review Letters*, 80(19):4333, May 1998.
- [174] Marta C.N. Amorim de Carvalho, F. B. Passos, and M. Schmal. Study of the Active Phase of Silver Catalysts for Ethylene Epoxidation. *J. Catal.*, 248:124–129, 2007.
- [175] M. Atkins, J. Couves, M. Hague, B. H. Sakakini, and K. C. Waugh. On the role of cs, cl and subsurface o in promoting selectivity in Ag/ $\alpha$ -Al<sub>2</sub>O<sub>3</sub> catalysed oxidation of ethene to ethene epoxide. *Journal of Catalysis*, 235(1):103–113, October 2005.
- [176] J. G. Serafin, A. C. Liu, and S. R. Seyedmonir. Surface Science and the Silver-catalyzed Epoxidation of Ethylene: an Industrial Perspective. *J. Mol. Catal. A: Chem.*, 131:157, 1998.
- [177] Suljo Linic, Jerome Jankowiak, and Mark A. Barteau. Selectivity Driven Design of Bimetallic Ethylene Epoxidation Catalysts from First Principles. *J. of Catal.*, 224:489–493, 2004.
- [178] S. Linic, Hong Piao, Keveh Abid, and Mark A. Barteau. Ethylene epoxidation on ag: Identification of the crucial surface intermediate by experimental and theoretical investigate of its electronic structure. *Angew. Chem. Int. Ed.*, 1:1, 2003.
- [179] S. Linic and M. A. Barteau. Formation of a stable surface oxametallacycle that produces ethylene oxide. *Journal of American Chemical Society*, 124:310–317, 2002.
- [180] K. Reuter and M. Scheffler. Composition and structure of the RuO<sub>2</sub>(110) surface in an O<sub>2</sub> and CO environment: Implications for the catalytic formation of CO<sub>2</sub>. *Physical. Review B*, 68:045407(1–11), 2003.

- [181] Q. Sun, K. Reuter, and M. Scheffler. Effect of a humid environment on the surface structure of RuO<sub>2</sub>(110), journal = *Physical Review B*, year = 2003, volume = 67, pages = 205424(1-7).
- [182] C. Stampfl, M.V. Ganduglia-Pirovano, K. Reuter, and M. Scheffler. Catalysis and corrosion: the theoretical surface-science context. *Surface Science*, 500:368–394, 2002.
- [183] K. Reuter and M. Scheffler. First-principles atomistic thermodynamics for oxidation catalysis: Surface phase diagrams and catalytically interesting regions. *Physical Review Letters*, 90:046103 (1–4), 2003.
- [184] P. Kratzer and M. Scheffler. Surface knowledge: Toward a predictive theory of materials. *Computing in Science & Engineering*, 3:16–25, 2001.
- [185] B. Hammer, L. Hansen, and J. Nørskov. Improved adsorption energetics within density-functional theory using revised Perdew-Burke-Ernzerhof functionals. *Physical Review B*, 59(11):7413–7421, March 1999.
- [186] H. J. Monkhorst and J. D. Pack. Special points for brillouin-zone integrations. *Physical Review B*, 13(12):5188, June 1976.
- [187] G. Henkelman, B. P. Uberuaga, and H. Jonsson. A Climbing Image Nudged Elastic Band Method for Finding Saddle Points and Minimum Energy Paths. *J. Chem. Phys.*, 113:9901, 2000.
- [188] A. Van der Ven, M. K. Aydinol, G. Ceder, G. Kresse, and J. Hafner. First-principles investigation of phase stability in LiCoO<sub>2</sub>. *Physical Review B*, 58:2975–2987, 1998.
- [189] D. deFontaine. Cluster approach to order-disorder transformations in alloys. *Solid State Physics-Advances in Research and Applications*, 47:33–174, 1994.

- [190] C. Wolverton. First-principles prediction of equilibrium precipitate shapes in al-cu alloys. *Philosophical Magazine Letters*, 79:683–690, 1999.
- [191] V. Ozolins, C. Wolverton, and A. Zunger. Cu-au, ag-au, cu-ag and ni-au intermetallics: First-principles study of temperature-composition phase diagrams and structures. *Phys. Rev. B*, 57:6427–6443, 1998.
- [192] C. Wolverton. First-principles theory of 250000 atom coherent alloy microstructure. *Mod. & Sim. in Mat. Sci. & Eng.*, 8:323–333, 2000.
- [193] H. R. Tang, A. Van der Ven, and B. L. Trout. Phase diagram of oxygen adsorbed on platinum (111) by first-principles investigation. *Phys. Rev. B*, 70:045420, 2004.
- [194] Richard M. Lambert, Federico J. Williams, Rachael L. Cropley, and Alejandra Palermo. Heterogeneous alkene epoxidation: past, present and future. *Journal of Molecular Catalysis A: Chemical*, 228(1-2):27–33, March 2005.
- [195] L. Surnev. *Physics and chemistry of alkali metal adsorption*. Elsevier, Amsterdam, 1989.
- [196] M. R. Salazar, J. D. Kress, and A. Redondo. Dissociation of molecular oxygen on unpromoted and cesium-promoted Ag(111) surfaces. *Catalysis Letters*, 64:2–4, 2000.
- [197] S. Gunther, H. Marbach, R. Imbihl, Lizzit S. Baraldi, A, and M. Kiskinova. Core level spectroscopy and reactivity of coadsorbed K-O layers on reconstructed Rh(110) surfaces. *Journal of Chemical Physics*, 119:12503–12509, 2003.
- [198] G. S. Leatherman and R. K. Diehl. None. *Surf. Sci.*, 380:455, 1997.
- [199] K. M. Ho and K. P. Bohnen. Stability of missing-row reconstruction of fcc(110) transition-metal surfaces. *Physical Review Letters*, 59:1883–1836, 1987.

- [200] K. W. Jacobsen and J. K. Nørskov. Theory of alkali-metal induced reconstruction of fcc(110) surfaces. *Physical Review Letters*, 61:1396–1399, 1988.
- [201] Roald Hoffmann. *Solids and Surfaces: A chemist's view of bonding in extended structures*. Wiley, New York, 1988.
- [202] B. Hammer and J. K. Nørskov. *Theory of adsorption and surface reactions*. Kluwer Academic Publishers, Dordrecht, 1997.
- [203] B. I. Lundqvist, O. Gunnarsson, H. Hjelmberg, and J. K. Nørskov. Theoretical description of molecule-metal interaction and surface reactions. *Surface Science*, 89(1-3):196–225, 1979.
- [204] B. Hammer and J. K. Nørskov. *Chemisorption and Reactivity on Supported Clusters and Thin Films*. NATO ASI Series, 1996.
- [205] M. S. Ma, M. R. Ji, W. W. Cai, J. X. Wu, J. S. Zhu, X. M. Liu, B. F. Yang, P. S. He, B. K. Jin, and Y. Z. Ruan. Potassium-promoted oxidation of beta -SiC. *Physical Review B*, 56(8):4913, 1997.
- [206] B. Hellsing. Electronic mechanism for alkali-metal-promoted oxidation of semiconductors. *Physical Review B*, 40(6):3855, 1989.
- [207] H. I. Starnberg, P. Soukiassian, and Z. Hurych. Alkali-metal-promoted oxidation of the Si(100)2×1 surface: Coverage dependence and nonlocality. *Physical Review B*, 39(17):12775, June 1989.
- [208] J. J. Mortensen and B. Hammer. A Theoretical Study of Adsorbate-adsorbate Interactions on Ru(0001). *Surf. Sci.*, 414:315, 1998.
- [209] S. C. Chuang, J. G. Goodwin, and I. Wender. The effect of alkali promotion on CO hydrogenation over Rh/TiO<sub>2</sub>. *Journal of Catalysis*, 95(2):435–446, October 1985.

- [210] Burcu Mirkelamoglu and Gurkan Karakas. The role of alkali-metal promotion on CO oxidation over PdO/SnO<sub>2</sub> catalysts. *Applied Catalysis A: General*, 299:84–94, January 2006.
- [211] L. Savio, L. Vattuone, and M. Rocca. From adsorption at the surface to incorporation into subsurface sites: the role of steps for O/Ag. *Applied Physics A: Materials Science & Processing*, 87(3):399–404, June 2007.
- [212] X. Bao, M. Muhler, B. Pettinger, R. Schlögl, and G. Ertl. On the nature of the active state of silver during catalytic oxidation of methanol. *Catalysis Letters*, 22(3):215–225, 1993.
- [213] X. Bao, M. Muhler, Th. Schedel-Niedrig, and R. Schlögl. Interaction of oxygen with silver at high temperature and atmospheric pressure: A spectroscopic and structural analysis of a strongly bound surface species. *Physical Review B*, 54(3):2249–2262, July 1996.
- [214] R. W. Joyner and M. W. Roberts. A study of the adsorption of oxygen on silver at high pressure by electron spectroscopy. *Chemical Physics Letters*, 60(3):459–462, January 1979.
- [215] Jingfa Deng, Xinhua Xu, Jinhai Wang, Yuanyan Liao, and Bifeng Hong. In situ surface raman spectroscopy studies of oxygen adsorbed on electrolytic silver. *Catalysis Letters*, 32(1):159–170, March 1995.
- [216] A. I. Boronin, S. V. Koscheev, K. T. Murzakhmetov, V. I. Avdeev, and G. M. Zhidomirov. Associative oxygen species on the oxidized silver surface formed under o<sub>2</sub> microwave excitation. *Applied Surface Science*, 165(1):9–14, September 2000.

- [217] V. I. Bukhtiyarov, M. Hävecker, V. V. Kaichev, A. Knop-Gericke, R. W. Mayer, and R. Schlögl. Atomic oxygen species on silver: Photoelectron spectroscopy and x-ray absorption studies. *Physical Review B*, 67(23):235422, June 2003.
- [218] V. I. Bukhtiyarov, M. Hvecker, V. V. Kaichev, A. Knop-Gericke, R. W. Mayer, and R. Schlögl. X-Ray absorption and photoemission studies of the active oxygen for ethylene epoxidation over silver. *Catalysis Letters*, 74(3):121–125, July 2001.
- [219] C. Backx, J. Moolhuysen, P. Geenen, and R. A. van Santen. Reactivity of oxygen adsorbed on silver powder in the epoxidation of ethylene. *Journal of Catalysis*, 72(2):364–368, December 1981.
- [220] K. Weissermel and H.-J. Arpe. *Industrial Organic Chemistry*. Weinheim, New York, 1993.
- [221] W.X. Li, C. Stampfl, and M. Scheffler. Why is a noble metal catalytically active? the role of the O-Ag interaction in the function of silver as an oxidation catalyst. *Physical Review Letters*, 90:256102(1–4), 2003.
- [222] K. A. Fichthorn and M. Scheffler. *Collective Diffusion on Surfaces: Collective Behaviour and the Role of Adatom Interactions*. Kluwer, Dordrecht, 2001.
- [223] Y. C. Hot, S. J. Jenkins, and D. A. King. Surface infra-red emission during alkali-metal incorporation at an oxide surface. *Surface Science Letters*, 550:L27–K32, 2004.
- [224] D. Tomanek and K. H. Bennemann. Total-energy calculations fro N<sub>2</sub> dissociation on Fe(111)-characterization of precursor and dissociated state. *Physical Review B*, 31:488–490, 1985.

- [225] J. Schnadt, A. Michaelides, J. Knudsen, R. T. Vang, K. Reuter, E. Laegsgaard, M. Scheffler, and F. Besenbacher. Revisiting the structure of the  $p(4 \times 4)$  surface oxide on  $ag(111)$ . *Physical Review Letters*, 96(14):146101–4, April 2006.
- [226] M. Schmid, A. Reicho, A. Stierle, I. Costina, J. Klikovits, P. Kostelnik, O. Dubay, G. Kresse, J. Gustafson, E. Lundgren, J. N. Andersen, H. Dosch, and P. Varga. Structure of  $Ag(111)-p(4 \times 4)-O$ : No silver oxide. *Physical Review Letters*, 96(14):146102–4, April 2006.
- [227] M. Todorova, W. X. Li, M. V. Ganduglia-Pirovano, C. Stampfl, K. Reuter, and M. Scheffler. Role of subsurface oxygen in oxide formation at transition metal surfaces. *Physical Review Letters*, 89(9):096103, 2002.
- [228] Karsten Reuter and Matthias Scheffler. Composition, structure, and stability of  $RuO_2(110)$  as a function of oxygen pressure. *Physical Review B*, 65(3):035406, December 2001.
- [229] Karsten Reuter and Matthias Scheffler. Composition and structure of the  $RuO_2(110)$  surface in an  $O_2$  and  $CO$  environment: Implications for the catalytic formation of  $CO_2$ . *Physical Review B*, 68(4):045407, July 2003.
- [230] R. Drautz, H. Reichert, M. Fhnle, H. Dosch, and J. M. Sanchez. Spontaneous  $L1_2$  order at  $Ni_{90}Al_{10}(110)$  surfaces: An X-Ray and First-Principles-Calculation study. *Physical Review Letters*, 87(23):236102, November 2001.
- [231] Hairong Tang, Anton Van Der Ven, and Bernhardt L. Trout. Lateral interactions between oxygen atoms adsorbed on platinum (111) by first principles. *Molecular Physics*, 102(3):273, 2004.
- [232] B. C. Han, A. Van der Ven, G. Ceder, and Bing-Joe Hwang. Surface segregation

- and ordering of alloy surfaces in the presence of adsorbates. *Physical Review B (Condensed Matter and Materials Physics)*, 72(20):205409–9, November 2005.
- [233] A. van de Walle and G. Ceder. Automating first-principles phase diagram calculations. *J. Phase Eq.*, 23:348–359, 2002.
- [234] G. L. W. Hart, V. Blum, M. J. Walorski, and A. Zunger. Evolutionary approach for determining first-principles hamiltonians. *Nature materials*, 4:391, 2005.
- [235] D. D. Zarkevich, N. A. & Johnson. Reliable first-principles alloy thermodynamics via truncated cluster expansions. *Phys. Rev. Lett.*, 92:255702, 2004.
- [236] A. Zunger, L. G. Wang, G. L. W. Hart, and M. Sanati. Obtaining ising-like expansions for binary alloys from first principles. *Mod. & Sim. in Mat. Sci. & Eng.*, 10:685–706, 2002.
- [237] A. van de Walle and G. Ceder. Automating first-principles phase diagram calculations. *Journal of Phase Equilibria and Diffusion*, 23(4):348–359, 2002.
- [238] M. Ziegler, J. Kroger, R. Berndt, A. Filinov, and M. Bonitz. Scanning tunneling microscopy and kinetic monte carlo investigation of cesium superlattices on ag(111). *Physical Review B (Condensed Matter and Materials Physics)*, 78(24):245427–7, December 2008.
- [239] Y. Xu, J. Greeley, and M. Mavrikakis. Effect of Subsurface Oxygen on the Reactivity of the Ag(111) Surface. *J. Am. Chem. Soc.*, 127:12823, 2005.
- [240] Gabor A. Somorjai and Yimin Li. *Introduction to Surface Chemistry and Catalysis*. John Wiley and Sons, June 2010.
- [241] W. Ho. Reactions at metal surfaces induced by femtosecond lasers, tunneling elec-

- trons, and heating. *The Journal of Physical Chemistry*, 100(31):13050–13060, January 1996.
- [242] J. W. Gadzuk. Resonance-Assisted hot electron femtochemistry at surfaces. *Physical Review Letters*, 76(22):4234, May 1996.
- [243] Sergei I. Anisimov and Baerbel Rethfeld. Theory of ultrashort laser pulse interaction with a metal. In Vitali I. Konov and Mikhail N. Libenson, editors, *Nonresonant Laser-Matter Interaction (NLMI-9)*, volume 3093, pages 192–203, St. Petersburg, Russia, April 1997. SPIE.
- [244] F.-J. Kao, D. G. Busch, D. Cohen, D. Gomes da Costa, and W. Ho. Femtosecond laser desorption of molecularly adsorbed oxygen from Pt(111). *Physical Review Letters*, 71(13):2094, 1993.
- [245] D. G. Busch, Shiwu Gao, R. A. Pelak, M. F. Booth, and W. Ho. Femtosecond desorption dynamics probed by Time-Resolved velocity measurements. *Physical Review Letters*, 75(4):673, July 1995.
- [246] Ki Hyun Kim, Kazuo Watanabe, Dietrich Menzel, and Hans-Joachim Freund. Photoinduced abstraction reactions within NO dimers on Ag(111). *Journal of the American Chemical Society*, 131(5):1660–1661, February 2009.
- [247] Thomas Olsen and Jakob Schiøtz. Origin of power laws for reactions at metal surfaces mediated by hot electrons. *Physical Review Letters*, 103(23):238301, November 2009.
- [248] Ned S. Wingreen, Karsten W. Jacobsen, and John W. Wilkins. Inelastic scattering in resonant tunneling. *Physical Review B*, 40(17):11834, December 1989.

- [249] J. W. Gadzuk. Inelastic resonance scattering, tunneling, and desorption. *Physical Review B*, 44(24):13466, December 1991.
- [250] Dietrich Menzel and Robert Gomer. Desorption from metal surfaces by Low-Energy electrons. *The Journal of Chemical Physics*, 41:3311, 1964.
- [251] J. A. Misewich, T. F. Heinz, and D. M. Newns. Desorption induced by multiple electronic transitions. *Physical Review Letters*, 68(25):3737, June 1992.
- [252] Thomas Olsen, Jeppe Gavnholt, and Jakob Schiøtz. Hot-electron-mediated desorption rates calculated from excited-state potential energy surfaces. *Physical Review B*, 79(3):035403, January 2009.
- [253] Phillip Christopher, Hongliang Xin, and Suljo Linic. Visible-light-enhanced catalytic oxidation reactions on plasmonic silver nanostructures. *Nat Chem*, 3(6):467–472, June 2011.
- [254] Phillip Christopher, David B. Ingram, and Suljo Linic. Enhancing photochemical activity of semiconductor nanoparticles with optically active Ag nanostructures: Photochemistry mediated by Ag surface plasmons. *The Journal of Physical Chemistry C*, 114(19):9173–9177, May 2010.
- [255] David J. Griffiths. *Introduction to Quantum Mechanics*. Benjamin Cummings, 2 edition, April 2004.
- [256] Philip Morse. Diatomic molecules according to the wave mechanics. II. vibrational levels. *Physical Review*, 34:57–64, July 1929.
- [257] Leticia Gonzalez, Daniel Escudero, and Luis Serrano-Andrés. Progress and challenges in the calculation of electronic excited states. *Chemphyschem: A European Journal of Chemical Physics and Physical Chemistry*, September 2011. PMID: 21922624.

- [258] Jeppe Gavnholt, Thomas Olsen, Mads Engelund, and Jakob Schitz.  $\delta$  self-consistent field method to obtain potential energy surfaces of excited molecules on surfaces. *Physical Review B*, 78(7):075441, 2008.
- [259] F. Buatier de Mongeot, A. Cupolillo, U. Valbusa, and M. Rocca. Anharmonicity of the o[<sub>2</sub>]Ag(001) chemisorption potential. *The Journal of Chemical Physics*, 106(22):9297, 1997.
- [260] Zhibin Lin, Leonid V. Zhigilei, and Vittorio Celli. Electron-phonon coupling and electron heat capacity of metals under conditions of strong electron-phonon nonequilibrium. *Physical Review B*, 77(7):075133, February 2008.
- [261] S. Funk, M. Bonn, D. N. Denzler, Ch. Hess, M. Wolf, and G. Ertl. Desorption of CO from ru(001) induced by near-infrared femtosecond laser pulses. *The Journal of Chemical Physics*, 112(22):9888–9897, June 2000.
- [262] M. Bonn, S. Funk, Ch. Hess, D. N. Denzler, C. Stampfl, M. Scheffler, M. Wolf, and G. Ertl. Phonon- versus Electron-Mediated desorption and oxidation of CO on ru(0001). *Science*, 285(5430):1042–1045, August 1999.
- [263] M. Plihal and David Langreth. Role of intra-adsorbate coulomb correlations in energy transfer at metal surfaces. *Physical Review B*, 58:2191–2206, July 1998.